



**HAL**  
open science

# Effective shallow water models for complex flood flow patterns in urban areas

Shangzhi Chen

► **To cite this version:**

Shangzhi Chen. Effective shallow water models for complex flood flow patterns in urban areas. Fluids mechanics [physics.class-ph]. Université de Strasbourg, 2018. English. NNT : 2018STRAD012 . tel-01862813

**HAL Id: tel-01862813**

**<https://theses.hal.science/tel-01862813>**

Submitted on 27 Aug 2018

**HAL** is a multi-disciplinary open access archive for the deposit and dissemination of scientific research documents, whether they are published or not. The documents may come from teaching and research institutions in France or abroad, or from public or private research centers.

L'archive ouverte pluridisciplinaire **HAL**, est destinée au dépôt et à la diffusion de documents scientifiques de niveau recherche, publiés ou non, émanant des établissements d'enseignement et de recherche français ou étrangers, des laboratoires publics ou privés.

*ÉCOLE DOCTORALE MSII*

Département Mécanique

**THÈSE** présentée par :

**Shangzhi CHEN**

soutenue le : 04 Juin 2018

pour obtenir le grade de : **Docteur de l'université de Strasbourg**

Discipline/ Spécialité : Génie Civil / Mécanique des fluides

**Modèle effectif par une approche de  
Saint-Venant pour les écoulements  
complexes lors d'inondations urbaines**

**THÈSE dirigée par :**

**M GHENAIM Abdellah**

**M TERFOUS Abdellali**

Professeur, INSA de Strasbourg

Maître de conférences, INSA de Strasbourg

**THÈSE encadrée par :**

**M FINAUD-GUYOT Pascal**

**M GARAMBOIS Pierre-André**

Maître de conférences, ENGEES

Maître de conférences, INSA de Strasbourg

**RAPPORTEURS :**

**Mme ROUX Hélène**

**M GUINOT Vincent**

Maître de conférences, INP Toulouse

Professeur, Université de Montpellier



# Modèle effectif par une approche de Saint-Venant pour les écoulements complexes lors d'inondations urbaines

Présentation des résultats majeurs de la thèse

## 1 Introduction

Les inondations représentent le premier risque naturel sur chaque continent et ont causé en Europe environ 100 milliards d'euros de dommage entre 1986 et 2006 (Moel et al. (2009)). Dans le contexte du changement climatique et de ses effets potentiels sur les régimes hydrologiques, une urbanisation sans précédent dans les plaines inondables a accru la vulnérabilité sociale. L'amélioration de la prévision des inondations et de la ré-analyse combinée à des analyses d'incertitudes, notamment en zone urbaine, est ainsi une priorité pour l'aide à la décision en matière de protection civile et pour les politiques d'assurance.

Des données fiables mesurées lors d'inondations urbaines qui sont nécessaires pour améliorer la compréhension des phénomènes d'inondation urbaine, élaborer de nouveaux modèles ou calibrer les modèles existants sont rares et complexes à obtenir. Les jeux de données obtenus sur des plateformes expérimentales d'étude des inondations urbaines sont donc précieuses voire essentielles (voir par exemple Mignot et al. (2006); Schubert and Sanders (2012); Finaud-Guyot et al. (2018)). Par ailleurs, il apparaît que les interactions entre des écoulements fortement énergétiques et les obstacles contrôlent l'hydrodynamique 3D (comme cela apparaît dans les carrefours Mignot et al. (2006)) ce qui implique qu'une représentation réaliste de ces phénomènes peut nécessiter la résolution d'un modèle 3D complet basé sur les équations de Navier-Stokes. Les débits injectés dans le modèle, qui peuvent provenir de données in-situ (impliquant généralement les incertitudes sur les courbes de tarage employées) ou de simulation hydro-météorologique impliquant des incertitudes météorologiques et sur le modèle hydrologique employé, constituent également une source connue d'incertitudes notamment dans le cas d'écoulements complexes en zone urbaine.

Les cartes d'inondation, de hauteurs de submersion et de vitesse d'écoulement sont généralement produites à partir de modèles 'shallow water 2D' correspondant à une moyenne sur la hauteur d'eau des équations de Navier-Stokes. En conséquence, la paramétrisation des phénomènes de dissipation d'énergie dans un modèle simplifié (tel qu'un modèle '2D shallow water') peut dépendre de l'échelle de modélisation considérée pour la représentation des pertes de charge localisées ou du frottement pariétal sur des micro ou macro rugosités dans des géométries complexes (Guinot (2012)). Cependant si la taille du domaine augmente de quelques blocs à l'échelle de tout un quartier voire une ville, le coût de simulations 2D reste élevé. Face à cela, des couplages 1D2D (Finaud-Guyot (2009); Finaud-Guyot et al. (2010a)) et des méthodes macroscopiques (Guinot and Soares-Frazão (2006); Sanders et al. (2008); Guinot (2012); Guinot et al. (2017a)) apparaissent comme des compromis avantageux pour réduire le coût de calcul des modélisations en utilisant la précision correcte du 2D au niveau des intersections hydrauliques telles que les carrefours et des modélisations 1D dans les portions d'écoulement plus simples comme les rues.

Dans le contexte de la modélisation effective des inondations urbaines et en vue de proposer un nouveau modèle 1D2D, les questions suivantes sont étudiées dans cette thèse :

1. Quelles sont les zones d'écoulement clé et quelles caractéristiques doivent être reproduites par un modèle simplifié 1D2D sur un réseau maillé ?
2. Comment paramétriser un tel modèle par exemple dans des rues où des structures d'écoulement 3D telles que des recirculations peuvent apparaître à l'aval des carrefours ?
3. Quelles sont les sensibilités paramétriques des modèles 2D SW et 1D2D dans le cas de crues urbaines dans des réseaux maillés ?
4. Quelle complexité de modélisation et quelle paramétrisation doivent être employées pour permettre une représentation effective des écoulements lors d'inondations urbaines sur de grands domaines avec un coût de calcul raisonnable en vue d'applications opérationnelles ?

Ce travail de thèse est proposé en vue d'améliorer la compréhension des mécanismes d'écoulement en jeu lors de crues urbaines et leur modélisation équivalente à un coût de calcul réduit - un nouveau code C/C++ *Flood1D2D* est présenté. Le manuscrit est organisé de la manière suivante : la section 1 présente une étude bibliographique ; les équations et leur discrétisation sont présentées en section 2 ; la section 3 illustre la validation sur des cas synthétiques du nouveau modèle *Flood1D2D* proposé dans ces travaux ; la sensibilité du modèle SW 2D à ses paramètres d'entrée est étudié avec des méthodes de décomposition de la variance au chapitre 4 ; l'application du nouveau modèle *Flood1D2D* sur plusieurs configurations hydrauliques complexes incluant un réseau des rues et carrefours est détaillée au chapitre 5.

## 2 Présentation de *Flood1D2D*

Le modèle *Flood1D2D* proposé dans cette thèse vise à modéliser les inondations urbaines en se basant sur le caractère parcimonieux des modélisations 1D et incluant des zooms 2D dans les zones à plus fortes complexités de l'écoulement tels que les zones de confluences / défluences.

### 2.1 Couplage 1D2D

Les rues sont donc modélisées par une approche 1D et les carrefours par une approche 2D (voir figure 1). La distinction 1D - 2D n'est toutefois pas liée à une quelconque contrainte sur le jeu d'équations résolues. Dans les deux cas, les équations 2D de Saint-Venant impliquant la hauteur d'eau et les deux composantes horizontales de la vitesse sont employées sans aucune orientation privilégiée de la vitesse dans les mailles 1D. La distinction réside dans le fait que les rues sont modélisées avec une unique maille sur la largeur.

Les équations résolues sont les suivantes :

$$\frac{\partial \mathbf{U}}{\partial t} + \frac{\partial \mathbf{F}}{\partial x} + \frac{\partial \mathbf{G}}{\partial y} = \mathbf{S} \quad (1a)$$

$$\mathbf{U} = \begin{bmatrix} \phi h \\ \phi q \\ \phi r \end{bmatrix} \quad \mathbf{F} = \begin{bmatrix} \phi q \\ \phi \frac{q^2}{h} + \frac{1}{2} g \phi h^2 \\ \phi \frac{qr}{h} \end{bmatrix} \quad \mathbf{G} = \begin{bmatrix} \phi r \\ \phi \frac{qr}{h} \\ \phi \frac{r^2}{h} + \frac{1}{2} g \phi h^2 \end{bmatrix} \quad \mathbf{S} = \begin{bmatrix} 0 \\ g \phi h (S_{0,x} - S_{f,x}) + \frac{1}{2} g h^2 \frac{\partial \phi}{\partial x} \\ g \phi h (S_{0,y} - S_{f,y}) + \frac{1}{2} g h^2 \frac{\partial \phi}{\partial y} \end{bmatrix} \quad (1b)$$

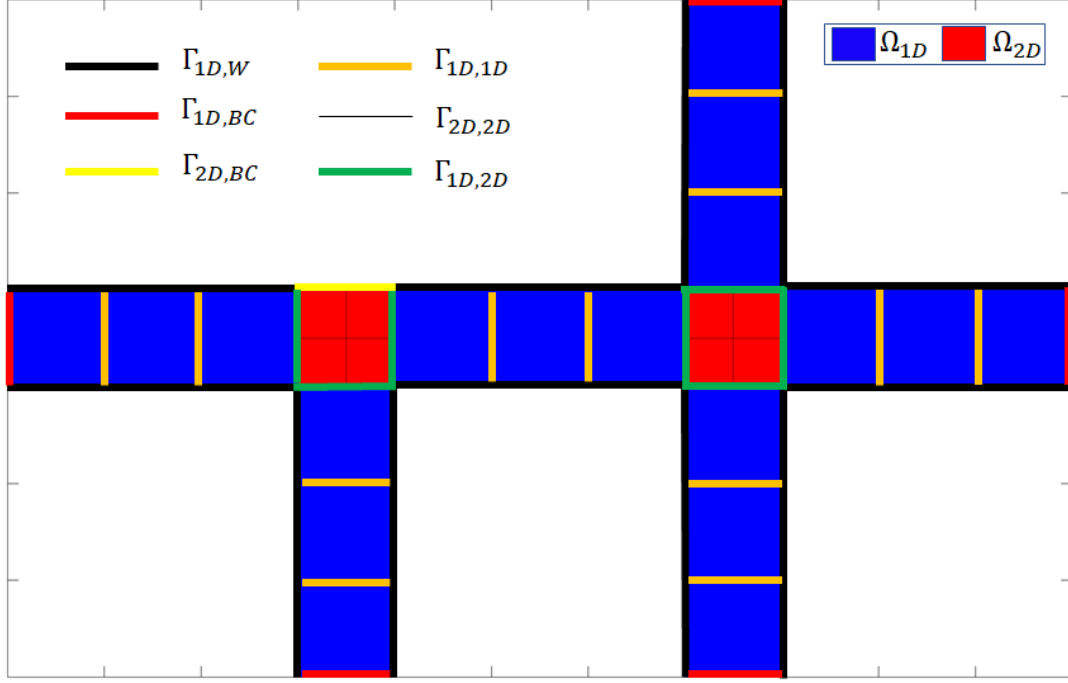


FIGURE 1 – Topologie du maillage 1D2D considéré

où  $\mathbf{U}$  représente le vecteur des variables conservées,  $\mathbf{F}$  et  $\mathbf{G}$  les composantes selon  $x$  et  $y$  du flux de  $\mathbf{U}$  et  $\mathbf{S}$  le terme source;  $h$  est la hauteur d'eau,  $q = hu$  et  $r = hv$  sont les composantes du débit unitaire (avec  $u$  et  $v$  les composantes du vecteur vitesse);  $g$  est l'accélération gravitationnelle,  $S_{0,x} = -\frac{\partial z_b}{\partial x}$  ( $S_{0,y} = -\frac{\partial z_b}{\partial y}$ ) et  $S_{f,x} = \frac{u\sqrt{u^2+v^2}}{K_x^2 h^{4/3}}$  ( $S_{f,y} = \frac{v\sqrt{u^2+v^2}}{K_y^2 h^{4/3}}$ ) sont la pente du fond et la pente de la ligne des frottements dans la direction  $x$  (respectivement  $y$ );  $z_b$  est la cote du fond et  $\phi$  est la porosité qui traduit le fait que la surface en plan d'un élément de calcul n'est pas totalement disponible pour l'eau.

L'équation (1a) est discrétisée sur chaque maille (1D ou 2D) par une méthode aux volumes finis :

$$\mathbf{U}_i^{n+1} = \mathbf{U}_i^n - \frac{\Delta t}{\phi_i A_i} \sum_{k \in N(i)} w_k \mathbf{P}_k \mathbf{F}_k^n + \Delta t \mathbf{S}(\mathbf{U}_i^n) \quad (2)$$

où  $\mathbf{U}_i^n$  représente l'état hydraulique du système dans la maille  $i$  à l'instant  $n$ ,  $\Delta t$  le pas de temps de calcul,  $\phi_i A_i$  la surface en plan de la maille  $i$  disponible pour l'eau,  $N(i)$  l'ensemble des interfaces délimitant la maille  $i$ ;  $w_k$  la longueur de l'interface  $k$ ,  $\mathbf{P}_k$  la matrice de passage permettant de passer du référentiel global au référentiel attaché à chaque interface et  $\mathbf{F}_k^n = \mathbf{F}_k(\mathbf{U}^n)$  le flux de  $\mathbf{U}$  à travers l'interface  $k$ .

En considérant les différents types d'interfaces pouvant exister du fait de la topologie du maillage considéré (voir figure 1), on a  $N(i) = N_{1D,W}(i) \cup N_{1D,BC}(i) \cup N_{1D1D}(i) \cup N_{2D,BC}(i) \cup N_{2D2D}(i) \cup N_{1D2D}(i)$  qui regroupe les interfaces 1D correspondant à des murs, à des conditions limites ou entre deux mailles 1D; les interfaces 2D correspondant à des conditions limites ou entre deux mailles 2D; et les interfaces entre mailles 1D et 2D. Les flux  $\mathbf{F}_k^n$  entre deux mailles (pour les ensembles  $N_{1D1D} \cup N_{2D2D} \cup N_{1D2D}$ ) sont calculés en utilisant un solveur de Riemann

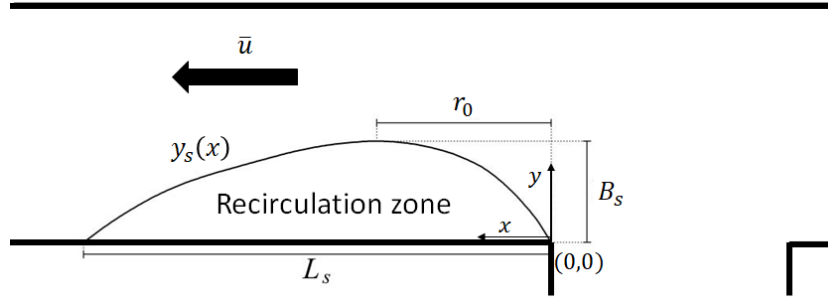


FIGURE 2 – Définition des dimensions de la zone de séparation d’après Schindfessel et al. (2017) :  $\bar{u}(x)$  est la vitesse longitudinale ;  $y_s(x)$  est la taille de la zone de recirculation comptée à partir du mur ;  $L_s$  est la longueur totale de la zone de recirculation (où  $y_s(x) > 0$  et  $L_s = \max_x y_s(x)$ ,  $\forall x \in [0, L_s]$ ) ;  $r_0$  est la distance depuis le bord du carrefour jusqu’à l’endroit où la taille de la zone de recirculation est maximale et vaut  $B_s$ .

(HLLC Soares-Frazão and Guinot (2007) ou PorAS Finaud-Guyot et al. (2010b)) afin de garantir le caractère *well-balanced* du schéma numérique. Le solveur de Riemann calcule le flux  $\mathbf{F}_k^n$  à partir des grandeurs dans les mailles gauche et droite de l’interface  $k$ . Les flux  $\mathbf{F}_k^n$  à la limite d’une maille (pour les ensembles  $N_{1D,W} \cup N_{1D,BC} \cup N_{2D,BC}$ ) sont calculés de manière similaire en utilisant une estimation des variables hydrauliques au niveau de la limite à partir des spécifications de l’utilisateur et des invariants de Riemann le long de la caractéristique entre la maille et la limite (Araud (2012)).

## 2.2 Prise en compte des recirculations dans les mailles 1D

La bibliographie (par exemple Best and Reid (1984); Gurram et al. (1997); Mignot et al. (2006)) et les expériences menées sur le pilote d’inondation urbaine d’Icube montrent la présence de zones de recirculation dans les biefs à l’aval des carrefours qui contractent l’écoulement et peuvent de ce fait jouer un effet significatif sur la répartition des débits dans un ou plusieurs carrefours (voir figure 2). Une topologie de maillage 1D permet de prendre en compte ces zones de recirculations. Il convient donc de prendre en compte leur effet sur l’hydrodynamique modélisée et qui n’est pas représenté dans les équations résolues (1a).

Dans les rues (modélisées par des mailles 1D), une paramétrisation complémentaire est donc introduite. Sur ces mailles, on considère que la veine d’écoulement effective est contractée par la présence de la zone de recirculation apparaissant à l’aval du carrefour. Les mailles 1D, définies pour représenter l’ensemble de la largeur de la rue, contiennent donc deux domaines  $\Omega_{1D} = \Omega_u \cup \Omega_v$  avec  $\Omega_u$  la zone d’écoulement inefficace située dans la recirculation pour laquelle il n’y a en moyenne pas d’écoulement et  $\Omega_v$  la veine d’écoulement par laquelle tout le débit circulant dans la rue transite (voir figure 3).

Le partage de la maille 1D est basé sur la fonction  $\omega$  qui prend en compte les effets de la recirculation.  $\omega$  mesure la proportion de la largeur de la rue disponible pour l’écoulement :  $\omega = L_v/L$  où  $L = L_u + L_v$  représente la largeur totale de la maille 1D,  $L_u$  (respectivement  $L_v$ ) est la largeur de la recirculation (respectivement veine d’écoulement). On peut démontrer que  $\omega = \Omega_v/\Omega_{1D}$ . Cette nouvelle définition de  $\omega$  est similaire à la notion de porosité définie dans Lhomme (2006). La porosité des mailles 2D est donc prise égale à 1 et pour toutes les mailles, elle est conservée constante dans le temps (et fixée *a priori* par le modélisateur). Cela suppose que le régime permanent dans un réseau maillé d’écoulement à surface libre ne dépend pas du régime

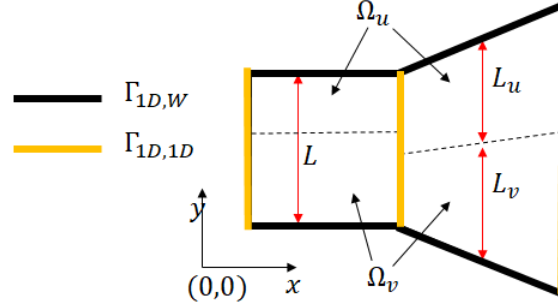


FIGURE 3 – Représentation schématique de la prise en compte des recirculations dans les mailles 1D

transitoire ayant conduit à cet état. Cette hypothèse, qui devra être étudiée de manière plus exhaustive sur le pilote d'inondation urbaine d'Icube, permet de négliger les effets de couplage entre l'hydrodynamique et la porosité.

De par la topologie du maillage, les flux  $\mathbf{F}_k^n$  dont le calcul doit prendre en compte la nouvelle paramétrisation  $\omega$  sont calculés à travers les interfaces dans l'ensemble  $N_{uv} = N_{1D,W} \cup N_{1D,1D} \cup N_{1D,2D} = N_{1D,W_u} \cup N_{1D,W_v} \cup N_{1D,1D,u} \cup N_{1D,1D,v} \cup N_{1D,2D,u} \cup N_{1D,2D,v}$ . Pour ces ensembles d'interface, on écrit :

$$\sum_{k \in N_{uv}} w_k \mathbf{P}_k \mathbf{F}_k^n = \sum_{k \in N_{uv}} \mathbf{P}_k (w_{k,u} \mathbf{F}_{k,u}^n + w_{k,v} \mathbf{F}_{k,v}^n) \quad (3)$$

où  $w_{k,u}$  (respectivement  $w_{k,v}$ ) est la longueur de l'interface  $k$  le long de la zone de recirculation (respectivement la veine d'écoulement) telle que  $w_k = w_{k,u} + w_{k,v} = (1 - \phi_k) w_k + \phi_k w_k$  et  $\mathbf{F}_{k,u}^n$  (respectivement  $\mathbf{F}_{k,v}^n$ ) est le flux à travers  $w_{k,u}$  (respectivement  $w_{k,v}$ ).

TABLE 1 –

Type	Ensemble	Domaine		$\mathbf{U}_L$	$\mathbf{U}_R$	$\phi_k$
		Gauche 1D	Droit 2D			
1D/1D	$N_{1D,1D,u}$	$\Omega_{1D,u}$	$\Omega_{1D,u}$	$[h \ 0 \ 0]^T$	$[h \ 0 \ 0]^T$	$\frac{\phi_G + \phi_R}{2}$
1D/1D	$N_{1D,1D,v}$	$\Omega_{1D,v}$	$\Omega_{1D,v}$	$[h \ q/\phi \ r/\phi]^T$	$[h \ q/\phi \ r/\phi]^T$	$\frac{\phi_G + \phi_R}{2}$
1D/BC	$N_{1D,W_u}$	$\Omega_{1D,u}$	Mur	$[h \ 0 \ 0]^T$	BC	1
1D/BC	$N_{1D,W_v}$	$\Omega_{1D,v}$	Mur	$[h \ q/\phi \ r/\phi]^T$	BC	1
1D/2D	$N_{1D,2D,u}$	$\Omega_{1D,u}$	$\Omega_{2D}$	$[h \ 0 \ 0]^T$	$[h \ q \ r]^T$	$\phi_{1D}$
1D/2D	$N_{1D,2D,v}$	$\Omega_{1D,v}$	$\Omega_{2D}$	$[h \ q/\phi \ r/\phi]^T$	$[h \ q \ r]^T$	$\phi_{1D}$

### 2.3 Validation

Le code *Flood1D2D* a été validé à l'aide de différents cas tests. La capacité du modèle 1D2D à modéliser des écoulements très transitoires a été évaluée sur l'expérience de rupture de barrage dans un canal avec un coude (Soares-Frazão and Zech (2002)).

La géométrie de l'expérience est composée d'un réservoir alimentant un canal avec un angle de  $90^\circ$  terminé par une chute d'eau (voir figure 4). Au début de l'expérience, la porte du réservoir est ôtée permettant l'écoulement de l'eau du réservoir (initialement 0.25m au dessus du fond du canal). L'expérience mesure les niveaux d'eau en différents endroit du canal jusqu'à la vidange totale du réservoir.

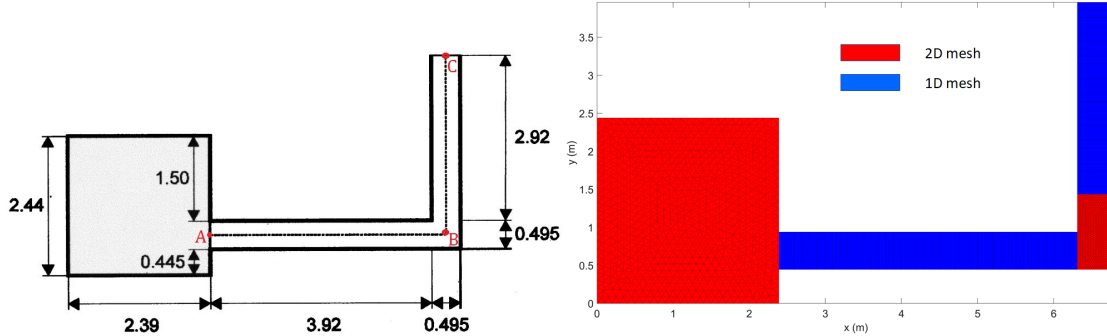


FIGURE 4 – Gauche : schéma du dispositif expérimental (dimensions en m d'après Soares-Frazão and Zech (2002)) ; Droite : maillage 1D2D utilisé pour la modélisation avec *Flood1D2D*

La configuration expérimentale est modélisée avec *Flood1D2D*. Les paramètres expérimentaux sont repris et la valeur du coefficient de Manning employée par les auteurs est conservée ( $n = 0.011\text{m}^{-1/3}.\text{s}$ ). Le maillage employé est 1D dans les parties rectilignes et 2D dans le réservoir, dans et immédiatement à l'aval du coude (voir figure 4). Les profils de hauteur d'eau obtenus à différents instants avec *Flood1D2D* (en utilisant le maillage 1D2D ou seulement un maillage 2D fin) est comparés à l'expérimental (voir figure 5). Les résultats montrent une bonne adéquation entre l'expérimental et la modélisation 1D2D ou 2D. Les caractéristiques hydrodynamiques de l'écoulement (hauteur et position des fronts, vitesse de déplacement) sont bien représentées par le modèle 1D2D.

### 3 Propagation d'incertitudes dans les modélisations d'inondations urbaines

Le but de la modélisation hydraulique est de prévoir le comportement d'écoulements à surface libre sur un domaine donné, l'évolution spatio-temporelle des hauteurs d'eau et débits y est simulée. Selon la quantité de données disponibles et les objectifs de modélisation, différentes complexités et paramétrisations hydrauliques peuvent être choisies. Ainsi, l'incertitude dans les sorties de modèles peut provenir de plusieurs sources : le type de données et erreurs d'observation, les incertitudes structurelles de modélisation ou encore les incertitudes paramétriques.

La modélisation hydraulique est utilisée pour prédire l'hydrodynamique des crues, comme ici dans le contexte de réseaux urbains maillés. Cette partie s'intéresse à l'analyse de sensibilité d'un modèle SW 2D. Le but est d'analyser comment la répartition des écoulements et la distribution des hauteurs d'eau peuvent être influencées par la structure du modèle, les conditions aux limites et les paramètres. Les sources d'incertitude en modélisation hydraulique incluent typiquement les conditions aux limites amont (ex : débits entrants) et aval (ex : hauteur, courbe de tarage), rugosité, topographie... Dans cette partie, plusieurs sources d'incertitude sont étudiées afin d'évaluer leur influence sur la variance des sorties du modèle à l'aide d'une méthode d'analyse de sensibilité

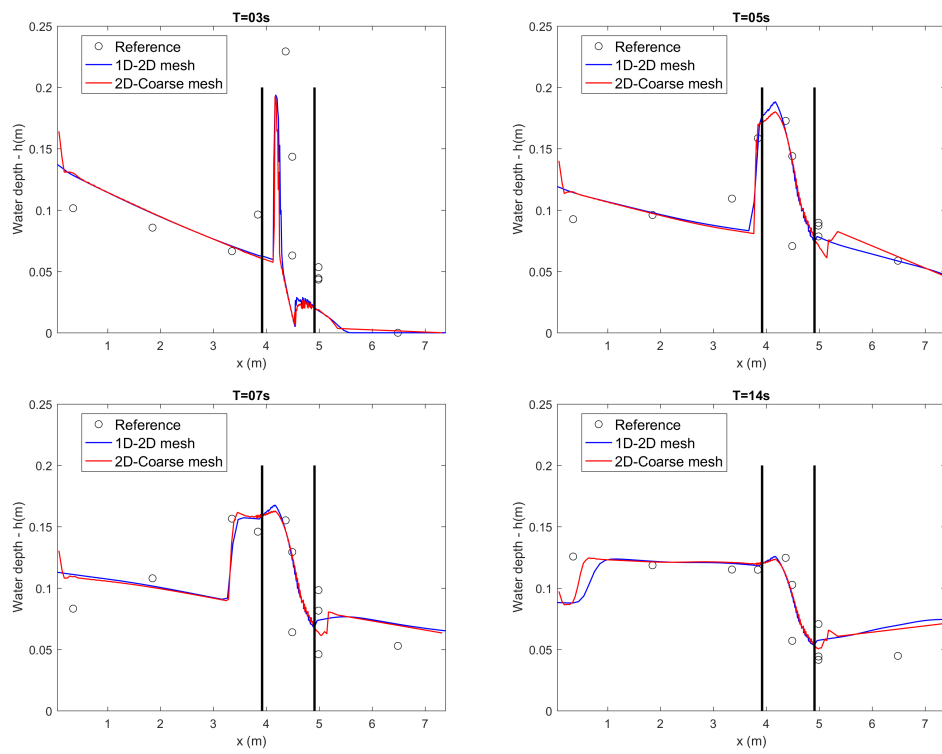


FIGURE 5 – Comparison des résultats issus de *Flood1D2D* (avec un maillage 2D ou 1D2D) avec les expériences réalisées par Soares-Frazão and Zech (2002). Ligne d'eau le long du profil A-B-C (voir figure 4). La zone 2D du maillage 1D2D est localisée entre les deux barres verticales noires.

globale (GSA).

### 3.1 Modélisation 2D SW

Des simulation 2D en régime permanent sont réalisées sur le pilote inondation Icube, représentant un réseau urbain (5m\*5m), en vue de reproduire des structures d'écoulement complexes (cf. Arrault et al. (2016)). Les conditions aux limites sont basées sur un jeu de données expérimental. Des débits et hauteurs d'eau constants sont fixés aux entrées et sorties du domaine, à fond plat horizontal, ainsi qu'un coefficient de frottement uniforme ( $K_{2D} = 100m^{1/3}.s^{-1}$ ) puisqu'il est simplement calibré sur la distribution des débits mesurée en sortie. Notons qu'une analyse de convergence des résultats par rapport à la finesse du maillage a été réalisée pour des mailles de taille variant de 0.01 à 0.0025m - la taille de maille retenue est de 0.005m. Les analyses de sensibilité sont réalisées pour un débit entrant total de  $80m^3.h^{-1}$ , correspondant à un fort débit de crue d'occurrence rare dans la réalité, réparti de manière différente entre les faces ouest et nord (50-50%, 80-20%). Sur une face le débit est réparti proportionnellement à la largeur de rue.

La distribution spatiale des hauteur d'eau et nombres de Froude est présentée sur la figure (6). La hauteur d'eau décroît des faces amont vers les faces aval, du coin nord-ouest au coin sud-est. L'écoulement est partout sous-critique sauf dans la rue 1 à l'aval du dernier carrefour entre les rues 1 et G, où une zone d'écoulement supercritique apparaît. La répartition de débit asymétrique dans le cas 80-20% a tendance à augmenter la hauteur d'eau au coin sud-est et réduire la région d'écoulement supercritique. Il est intéressant de noter que la répartition de débit simulée dans les deux configurations (50-50% et 80-20%) est très similaire et correspond bien aux mesures expérimentales. Ces résultats mettent en avant l'effet filtrant de la géométrie urbaine sur l'hydrogramme entrant comme démontré dans Finaud-Guyot et al. (2018).

### 3.2 GSA sur les hauteurs d'eau

La sensibilité d'un modèle 2D à ses quatre paramètres principaux,  $Q_{west}$  et  $Q_{north}$  les débits d'entrée sur la face ouest et nord, la hauteur d'eau en sortie  $h_{out}$  et un coefficient de frottement uniforme  $K$ , est testée à l'aide d'une méthode d'analyse de sensibilité globale (GSA). Elle permet d'évaluer la contribution des différents paramètres testés sur la variance des sorties du modèle (hauteurs d'eau et débits de sortie). Les gammes de variations des paramètres sont déterminés à partir des incertitudes expérimentales ( $Q_{north}^{cal} \pm 5\%$ ,  $Q_{west}^{cal} \pm 5\%$ ;  $h_{out}^{cal} \pm 10\%$  et  $K^{cal} \pm 50\%$ ). Un ensemble de  $N_s = 2000$  jeux de paramètres permet une bonne estimation a des indices de Sobol d'ordre 1 dans cette configuration avec la méthode de Ratto et al. (2007).

Les cartes de sensibilité de la hauteur d'eau modélisée aux paramètres sont présentées sur la figure (6) avec les cartes de nombre de Froude  $F_r$  locaux pour 2 répartitions de débit entrant. La somme des indices de Sobol  $\Sigma S_i$  est proche de 1 pour les zones d'écoulement sub-critiques (correspondant à un nombre de Froude  $F_r < 1$ ) indiquant que la variance du modèle est bien expliquée par les paramètres testés.  $\Sigma S_i$  est inférieure à 1 pour la zone où apparaît une zone d'écoulement supercritique pour certains jeux de paramètres.

Les cartes de sensibilité de la hauteur d'eau aux quatre paramètres sont présentées sur les figures 6b, c, d, e. Pour la configuration de débits entrants équi-répartis, la rugosité  $K$  et la hauteur d'eau aval  $h_{out}$  sont les paramètres les plus importants expliquant la variance des hauteurs d'eau. La sensibilité à  $K$  et  $h_{out}$  évolue globalement dans la direction nord-ouest vers sud-est excepté dans le cercle correspondant aux écoulements supercritiques : décroissance (resp. croissance) de la sensibilité à  $K$  (resp.  $h_{out}$ ). La sensibilité au débit entrant décroît le long de cette direction effective d'écoulement, elle est quasiment nulle à l'aval.

Les histogrammes présentés sur la figure 7 montrent la sensibilité de la hauteur d'eau aux paramètres testés pour quelques intersections hydrauliques - carrefours. Elles sont présentées selon la distance hydraulique à partir du coin nord-ouest et décrivent quantitativement la décroissance de l'effet des contrôles amonts  $Q_{west}$ ,  $Q_{north}$ ,  $K$ .

La figure 6 présente les cartes de sensibilité pour la configuration 80-20% des débits entrant. Les tendances des sensibilités spatiales sont similaires à la configuration 50-50%. Pour la configuration 80-20%, ces cartes montrent que la sensibilité des hauteurs d'eau à  $Q_{west}$  est quasiment deux fois plus grande que celle à  $Q_{north}$ . L'indice de Sobol de  $Q_{north}$  décroît vers l'aval alors que celui de  $Q_{west}$  augmente et explique 2% de la variance des hauteurs d'eau pour les rues 1 à 4. Dans ce cas l'influence du contrôle aval ( $h_{out}$ ) est plus faible pour la région située près des faces nord et ouest. La région d'écoulement supercritique est également réduite puisqu'un débit moins grand provient de la face nord.

## 4 Modélisation de configurations urbaines avec *Flood1D2D*

### 4.1 Modélisation d'un carrefour isolé

La modélisation des écoulements à l'échelle d'un carrefour avec le modèle Flood1D2D a été étudiée sur la configuration expérimentale proposée par Nania et al. (2004). Le carrefour étudié expérimentalement est maillé avec l'approche 1D2D proposée : le carrefour est 2D, les rues sont 1D (voir figure 8). Des conditions aux limites symétriques ( $Q_{in,x} = Q_{in,y} = 0.075\text{m}^3.\text{s}^{-1}$  et hauteur d'eau aval  $h_{out} = 0.1\text{m}$ ) permettent de garantir une symétrie des écoulements dans les rues de sorties et seules les résultats d'une rue sont donc présentés. La simulation est menée en régime permanent et confrontée à une simulation avec le logiciel Telemac 2D qui sert de référence (voir figure 9).

*Flood1D2D* est paramétrisé avec une porosité dans les rues aval :

$$B(s) = as^2 + bs + c \quad (4)$$

où  $B$  est la largeur de la recirculation,  $s$  est l'abscisse le long de la rue aval ( $s = 0$  est positionné arbitrairement à l'amont de la rue et orienté dans le sens de l'écoulement).  $a$ ,  $b$  et  $c$  sont trois coefficients calculés tels que  $B(0) = B(L_s) = 0$  et  $B(L_s/2) = B_s$  avec  $L_s$  la longueur de la recirculation et  $B_s$  la largeur maximale de la recirculation. La modélisation de référence (Telemac2D) permet de déterminer les valeurs de  $L_s = 3.3\text{m}$  et  $B_s = 0.52\text{m}$ . La modélisation est réalisée avec Flood1D2D avec un coefficient de Strickler uniforme  $K = 100\text{m}^{1/3}.\text{s}^{-1}$  et  $B_s = \{0; 0.2; 0.26; 0.3; 0.52\}$ .

Les résultats de modélisation 1D2D sont comparés à la référence pour déterminer dans quelle mesure le modèle proposé peut reproduire les caractéristiques 2D de l'écoulement (voir figure 10). La référence montre que le niveau d'eau passe par un minimum dans la rue aval ( $x \approx 5.15\text{m}$ ) qui est lié à la présence d'une zone de recirculation (visible à partir de la carte des vecteurs vitesses - non présentées ici). La modélisation d'une telle configuration en utilisant une approche 1D2D paramétrisée uniquement avec un coefficient de frottement ( $B_s = 0\text{m}$ ) ne permet pas de reproduire ce minimum dans le niveau d'eau modélisé. Cette constatation peut être généralisée : l'analyse des termes sources de l'équation SW modélisée montre que ce type de profil des hauteurs d'eau ne peut être obtenu même avec un coefficient de frottement non-uniforme. Pour une porosité  $B_s = \{0.2; 0.26; 0.3\}$ , le profil de référence est relativement bien reproduit. Les écarts entre la modélisation 1D2D et la référence dépendent de la fonction de paramétrisation employée. Pour une porosité  $B_s = 0.52\text{m}$  (correspondant à la valeur calculée à partir des résultats de référence), la contraction de la veine d'écoulement est suffisamment importante pour que l'écoulement modélisé

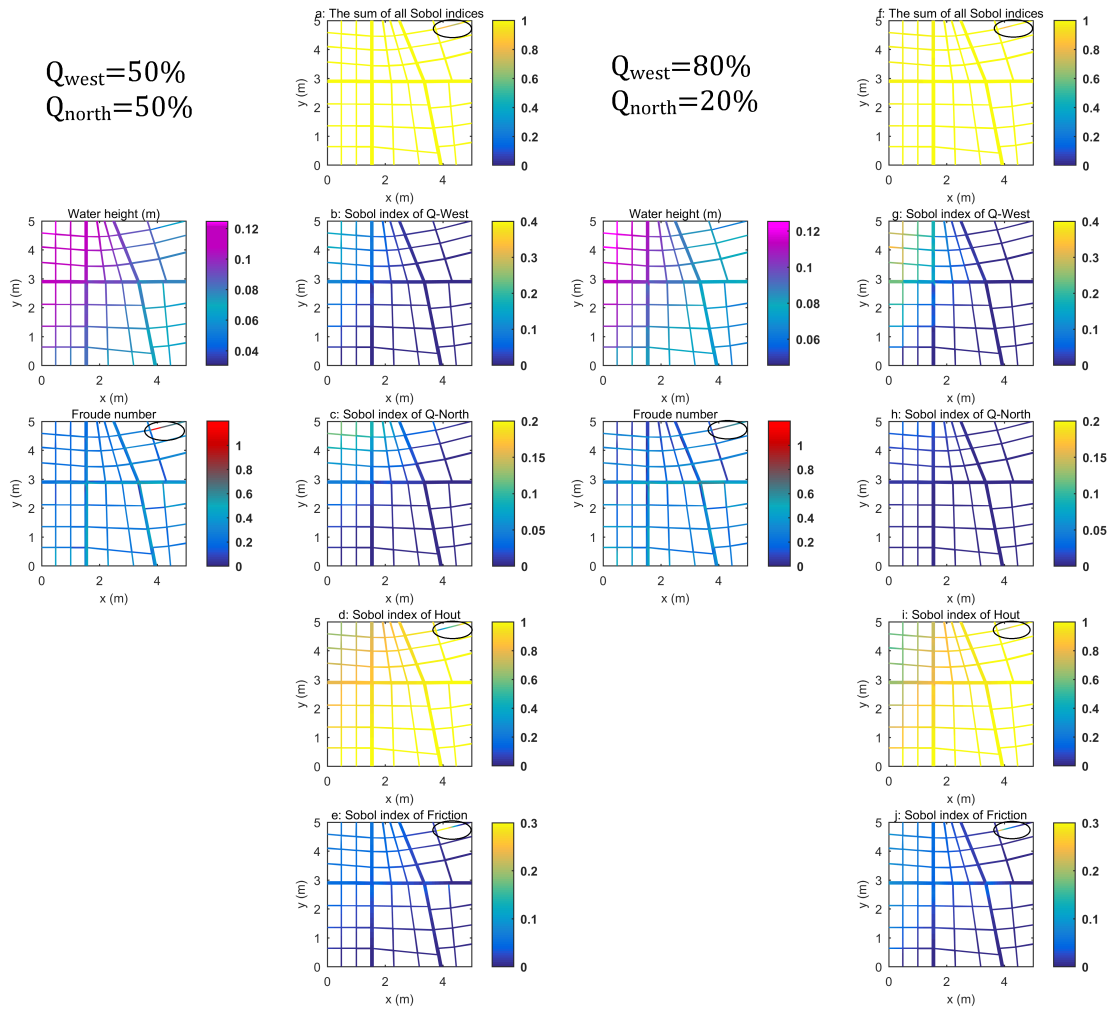


Figure 6 – Cartes de sensibilités paramétriques 2D pour un débit entrant total de  $80\text{ m}^3/\text{h}$  : gauche, débit entrant équi-réparti (50-50%) entre faces nord et ouest, droite configuration 80-20%. Les cercles repèrent les zones d'écoulement supercritique ( $Fr > 1$ ).

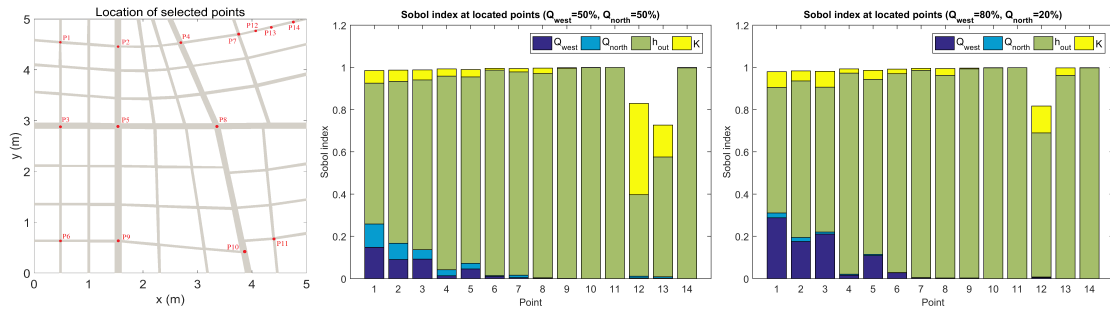


Figure 7 – Décomposition des sensibilités locales des hauteurs d'eau aux quatre paramètres testés - expérience sans pente. Numérotation des points en fonction de la distance hydraulique au coin nord-ouest.

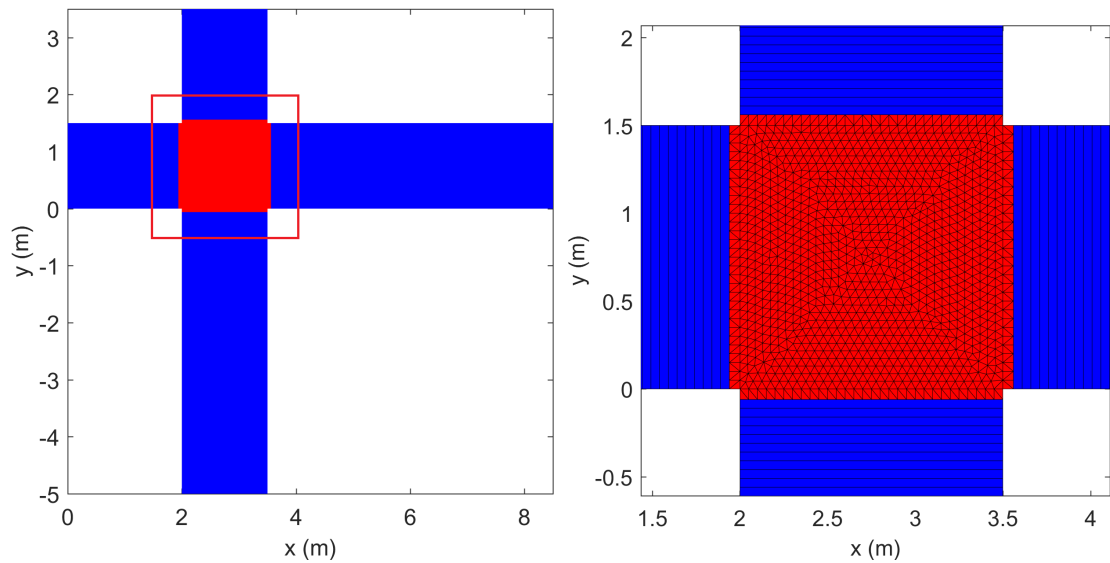


FIGURE 8 – Représentation du maillage 1D2D employé avec un zoom sur le carrefour (1D en bleu et 2D en rouge).

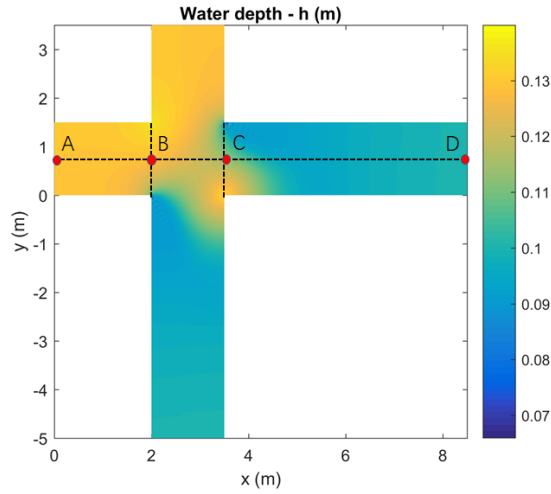


FIGURE 9 – Carte des hauteurs d’eau obtenues avec Telemac 2D

avec *Flood1D2D* devient localement torrentiel et faisant donc apparaître un ressaut hydraulique à l’aval. Ce ressaut hydraulique n’apparaît pas dans les résultats de référence. Cette différence est imputée à l’effet différent d’un même coefficient de Strickler entre une modélisation 1D et une modélisation 2D.

## 4.2 Application de *Flood1D2D* à l’échelle d’un réseau de carrefours

Comme illustré précédemment, la modélisation de la ligne d’eau d’une rue en 1D avec une paramétrisation prenant en compte seulement la friction ne permet pas de rendre compte de l’accélération locale de l’écoulement où la veine d’eau est contractée par la zone de recirculation. L’ajout d’une nouvelle paramétrisation prenant en compte la réduction de la veine d’eau permet de palier ces difficultés et montre une influence sur la répartition des débits à l’aval d’une intersection hydraulique. Cette section montre les effets d’une distribution de porosité sur l’écoulement modélisé à l’échelle de plusieurs carrefours.

### 4.2.1 Présentation de la configuration étudiée

La réponse de *Flood1D2D* est étudiée sur une sous partie du pilote d’inondation urbaine d’Icube afin d’utiliser toute la complexité d’un jeu de données expérimental tout en limitant les coûts de calcul et le nombre de paramètres. La sous partie choisie comprend 4 carrefours connectés par des rues de largeurs et orientations variables, au centre du dispositif expérimental (voir figure 11). La largeur d’une « rue large » (F et 4) est 12.5cm et 5cm pour les plus petites. Un carrefour est identifié par le nom des deux rues le formant (ex. 'E3'). Une sous partie d’une rue est nommée en utilisant les noms des carrefours amont et aval (ex. 'E3E4').

Les données expérimentales en régime permanent (Araud (2012); Finaud-Guyot et al. (2018)) permettent de connaître le débit et les hauteurs d’eau dans chaque rue, ces dernières étant mesurées de chaque côté de la rue. Le réseau est modélisé en utilisant un modèle 1D2D sur un maillage non structuré avec un pas d’espace  $\Delta x = 0.025\text{m}$  (figure 11). Les rues sont modélisées avec des mailles 1D et les carrefours en 2D. Les conditions aux limites consistent en des débits amonts pour les rues E, F, 3 et 4 (correspondant aux valeurs expérimentales) et des courbes de tarage expérimentales pour chaque condition limite aval. Le solveur de Riemann PorAS est utilisé

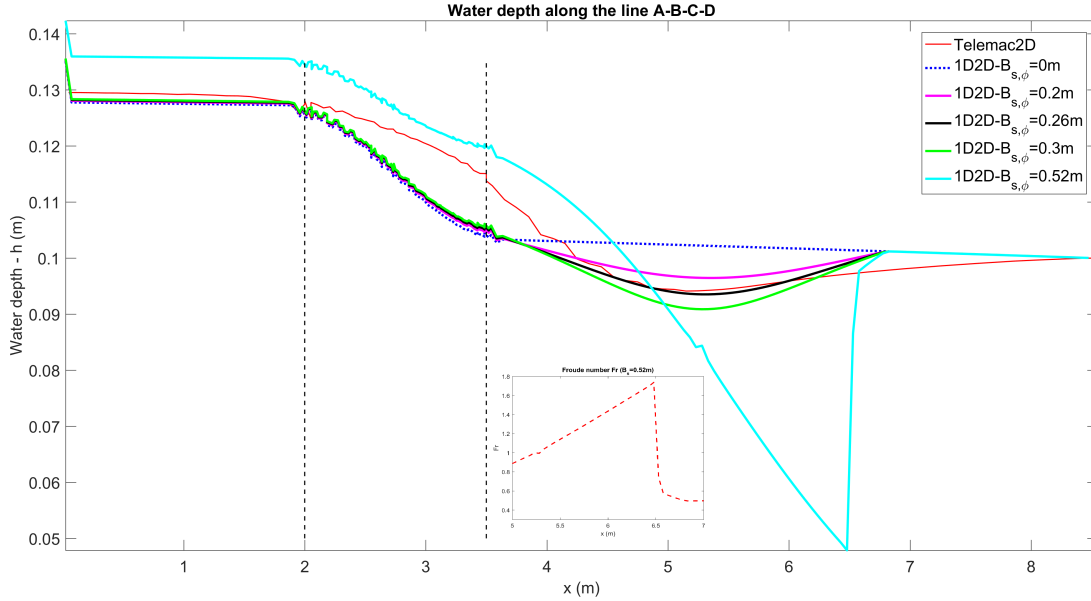


FIGURE 10 – Comparaison entre les hauteurs d’eau de référence (Telemac2D) et celles simulées avec *Flood1D2D* pour différentes paramétrisations de la porosité

pour le calcul des flux. Dans chaque configuration une simulation de 1000s permet d’atteindre un régime permanent sur tout le domaine.

Cette configuration est utilisée pour tester la réponse de *Flood1D2D* à deux paramétrisations différentes :

**Config 1** Coefficient de Strickler uniforme en espace ( $K_{street}$  et  $K_{cross}$ ) sans porosité ( $\phi = 1$  partout);

**Config 2** Coefficient de Strickler uniforme sur tout le domaine et une porosité distribuée basée sur la largeur de rue.

**Config 1 : Surface de réponse à  $K_{street}$  et  $K_{cross}$**  Le modèle est paramétrisé avec deux coefficients de Strickler uniformes :  $K_{street}$  dans les rues et  $K_{cross}$  dans les carrefours. Chaque paramètre est pris parmi les valeurs [25, 50, 75, 100, 125, 150] et toutes les combinaisons sont testées.

Les débits simulés dans les rues de sorties sont comparés aux valeurs expérimentales sur la figure 12. Pour chaque rue, la première barre correspond à la mesure expérimentale. Quelque soit la paramétrisation du modèle, chaque débit simulé pour les rues E et F (respectivement 3 et 4) sous- (respectivement sur-)estime la valeur expérimentale.  $K_{street}$  semble imposer un débit moyen dans la rue (noter par exemple le saut de débit pour la rue F quand  $K_{street}$  varie de 25 à 50).  $K_{cross}$  a un impact plus réduit sur la répartition des débits de sorties avec une influence toujours similaire autour de la valeur imposée par  $K_{street}$ .

Il apparaît donc que *Flood1D2D* paramétrisé uniquement avec un coefficient de Strickler est incapable de reproduire la ligne d’eau mesurée et la répartition expérimentale des débits.

**Config 2 : Surface de réponse à  $K_{unif}$ ,  $\phi_{large}$  et  $\phi_{narrow}$**  Le modèle est paramétrisé avec un coefficient de Strickler uniforme  $K = 75\text{m}^{1/3}.\text{s}^{-1}$  dans la mesure où la sensibilité à  $K_{street}$  et

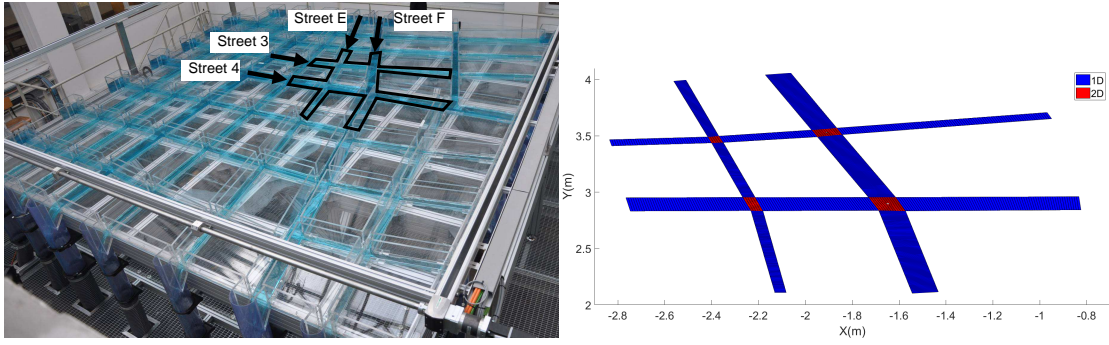


FIGURE 11 – Dispositif expérimental et illustration de la zone modélisée (gauche) et maillage 1D2D (droite).

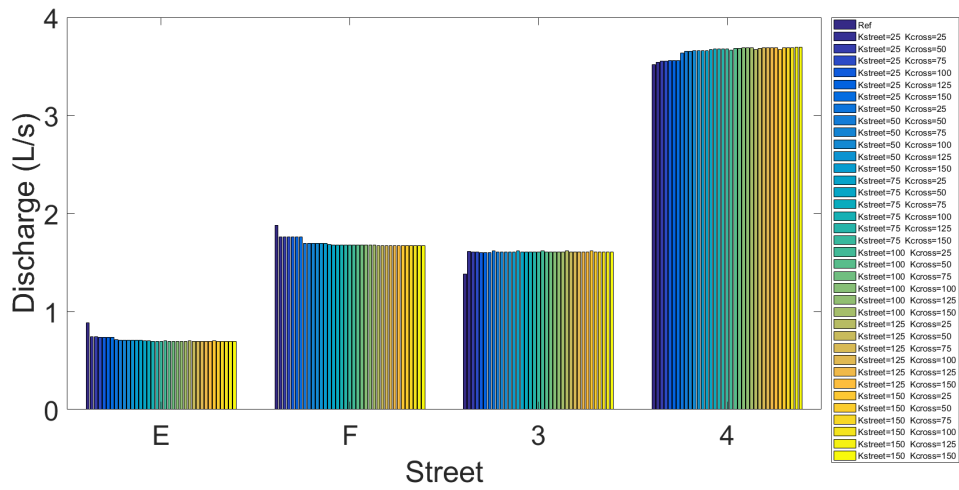


FIGURE 12 – Sensibilité du débit dans les rues aval à  $K_{street}$  et  $K_{cross}$

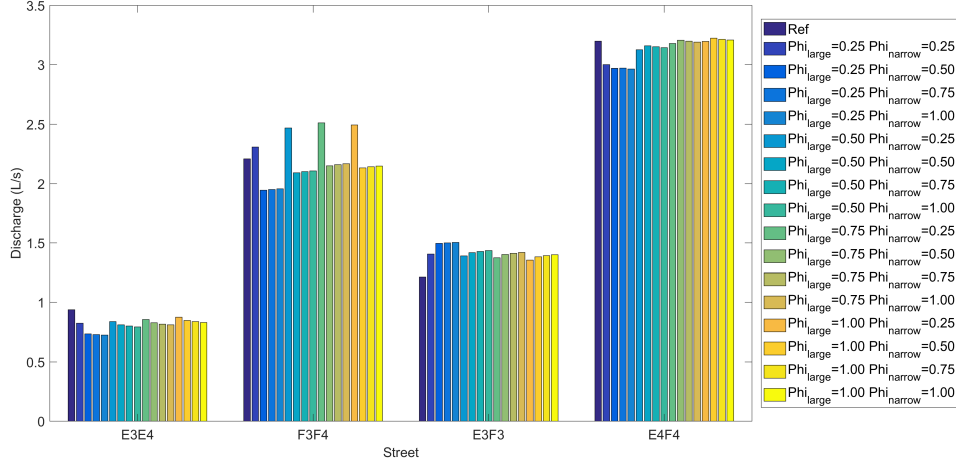


FIGURE 13 – Sensibilité du débit dans les rues à  $\phi_{r,n}$  et  $\phi_{r,l}$

$K_{cross}$  est faible. La porosité dans chaque rue à l’aval d’un carrefour est définie avec une fonction parabolique de la position :

$$\phi(s) = \begin{cases} as^2 + bs + c & \text{pour } 0 \leq s \leq 0.5 \\ 1 & \text{ailleurs} \end{cases} \quad \text{avec } \phi(0) = \phi(1/2) = 1 \quad \text{et} \quad \phi(1/4) = \phi_r \quad (5)$$

où  $s$  est l’abscisse curviligne adimensionnée (0 (respectivement 1) à l’amont (respectivement aval) de chaque rue. Le modèle est paramétrisé en ajustant les valeurs de  $a$ ,  $b$  et  $c$ , avec  $\phi_{r,l}$  dans les rues larges (F et 4) et  $\phi_{r,n}$  dans les rues étroites (E et 3). La surface de réponse de *Flood1D2D* est tracée pour toutes les combinaisons de  $\phi_{r,l}$  et  $\phi_{r,n}$  dans  $[0.25, 0.50, 0.75, 1.00]$ .

Les débits simulés dans les rues de sorties et dans les rues intermédiaires sont comparés aux valeurs expérimentales 13 et 14. Pour chaque rue, la première barre correspond aux valeurs expérimentales. Pour chaque rue, on obtient des simulations sur- et sous-estimant la valeur expérimentale (contrairement à ce qui était obtenu dans le cas de la configuration 1 avec seulement  $K_{street}$  et  $K_{cross}$ ). Malgré l’échantillonnage grossier de l’espace des paramètres (en raison du coût de chaque simulation), la surface de réponse est pratiquement centrée autour de la valeur expérimentale ce qui laisse supposer qu’il existe au moins un jeu de paramètres permettant de retrouver les valeurs expérimentales.

## 5 Conclusions et perspectives

Cette thèse propose une approche effective basée sur les équations Shallow water modifiées pour inclure une paramétrisation adaptée à la modélisation des inondations urbaines à l’échelle locale et du quartier. Ce travail de thèse est basé sur un nouveau code C/C++ *Flood1D2D* et sur les jeux de données expérimentales du pilote inondation Icube à Strasbourg. Une attention particulière est portée sur les zones de recirculations à l’aval des carrefours, leur prise en compte effective sur la modélisation des écoulements à échelle du quartier. Le jeu d’équations est présenté ainsi que leur discrétisation et l’algorithme de résolution. La validation du code sur de nombreux cas tests est réalisée.

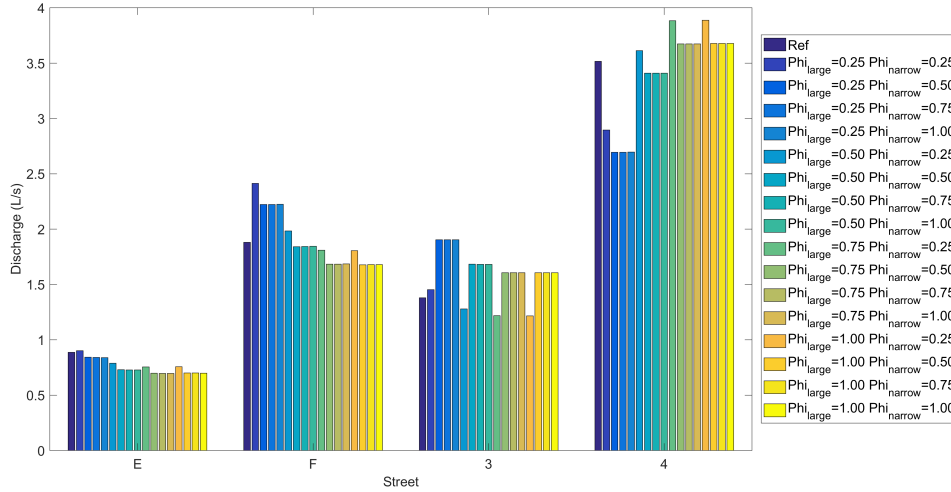


FIGURE 14 – Sensibilité du débit dans les rues aval à  $\phi_{r,n}$  et  $\phi_{r,l}$

Une analyse de sensibilité de la réponse des modèles classiques 1D et 2D shallow water à leurs paramètres d'entrée dans le cas de configuration urbaine est réalisé avec une méthode GSA. La variation spatiale et temporelle des indices de Sobol de la hauteur d'eau et du débit aux paramètres d'entrée met en évidence la position des principaux contrôles hydrauliques et leur variation au cours de la crue. Le rôle du réseau de rue sur la répartition des débits est mis en évidence.

L'intérêt de la nouvelle paramétrisation pour la modélisation effective des inondations urbaines est mise en évidence à travers la modélisation d'un carrefour. L'ajout du paramètre permet la reproduction des lignes d'eau observées en 2D dans la veine d'écoulement - chose impossible avec une paramétrisation uniquement avec un coefficient de frottement même distribué. Une analyse de sensibilité montre que la porosité a une influence majeure sur la répartition des débits. *Flood1D2D* est également appliqué à l'échelle d'un quartier du pilote inondation Icube. Les paramétrisations testées montrent que la nouvelle paramétrisation utilisant à la fois un coefficient de frottement et une porosité influence la répartition des hauteurs d'eau et des débits à échelle globale permettant ainsi de reproduire les mesures expérimentales.

La poursuite des travaux sur des configurations plus étendues (par exemple l'ensemble du pilote inondation Icube) doit être réalisée et une méthode de paramétrisation *a priori* doit être proposée tout en considérant les problématiques d'équifinalité. La question des effets transitoires avec l'évolution des zones de recirculation au cours d'une crue doit être étudiée et *Flood1D2D* doit être modifié pour pouvoir intégrer la variabilité temporelle de la porosité en fonction de l'hydrodynamique.

## References

- Araud, Q., 2012. Simulations des écoulements en milieu urbain lors d'un événement pluvieux extrême. Ph.D. thesis, Université de Strasbourg.
- Arrault, A., Finaud-Guyot, P., Archambeau, P., Bruwier, M., Erpicum, S., Pirotton, M., Dewals,

- B., 2016. Hydrodynamics of long-duration urban floods: experiments and numerical modelling. *Natural Hazards and Earth System Sciences* 16 (6), 1413–1429.
- Best, J. L., Reid, I., 1984. Separation zone at open-channel junctions. *Journal of Hydraulic Engineering* 110 (11), 1588–1594.
- Finaud-Guyot, P., 2009. Modélisation macroscopique des inondations fluviales et urbaines-prise en compte des écoulements directionnels et des échanges lit majeur-lit mineur. Ph.D. thesis, Université Montpellier II-Sciences et Techniques du Languedoc.
- Finaud-Guyot, P., Delenne, C., Guinot, V., 2010a. Coupling of 1d and 2d models for river flow modelling. In: *SimHydro 2010: Hydraulic modeling and uncertainty*.
- Finaud-Guyot, P., Delenne, C., Lhomme, J., Guinot, V., Llovel, C., 2010b. An approximate-state Riemann solver for the two-dimensional shallow water equations with porosity. *International Journal for Numerical Methods in Fluids* 62 (12), 1299–1331.
- Finaud-Guyot, P., Garambois, P.-A., Araud, Q., Lawniczak, F., François, P., Vazquez, J., Mosé, R., 2018. Experimental insight for flood flow repartition in urban areas. *Urban Water Journal*, 1–9.
- Guinot, V., 2012. Multiple porosity shallow water models for macroscopic modelling of urban floods. *Advances in Water Resources* 37, 40–72.
- Guinot, V., Sanders, B. F., Schubert, J. E., 2017a. Dual integral porosity shallow water model for urban flood modelling. *Advances in Water Resources* 103, 16–31.
- Guinot, V., Soares-Frazão, S., 2006. Flux and source term discretization in two-dimensional shallow water models with porosity on unstructured grids. *International Journal for Numerical Methods in Fluids* 50 (3), 309–345.
- Gurram, S. K., Karki, K. S., Hager, W. H., 1997. Subcritical junction flow. *Journal of Hydraulic Engineering* 123 (5), 447–455.
- Lhomme, J., 2006. Modélisation des inondations en milieu urbain: approches unidimensionnelle, bidimensionnelle et macroscopique. Ph.D. thesis, Université Montpellier II-Sciences et Techniques du Languedoc.
- Mignot, E., Paquier, A., Haider, S., 2006. Modeling floods in a dense urban area using 2d shallow water equations. *Journal of Hydrology* 327 (1), 186–199.
- Moel, H. D., Alphen, J. V., Aerts, J., 2009. Flood maps in Europe—methods, availability and use. *Natural Hazards and Earth System Sciences* 9 (2), 289–301.
- Nanía, L. S., Gómez, M., Dolz, J., 2004. Experimental study of the dividing flow in steep street crossings. *Journal of Hydraulic Research* 42 (4), 406–412.
- Ratto, M., Pagano, A., Young, P., 2007. State dependent parameter metamodelling and sensitivity analysis. *Computer Physics Communications* 177 (11), 863–876.
- Sanders, B. F., Schubert, J. E., Gallegos, H. A., 2008. Integral formulation of shallow-water equations with anisotropic porosity for urban flood modeling. *Journal of Hydrology* 362 (1), 19–38.

- Schindfessel, L., Creëlle, S., De Mulder, T., 2017. How different cross-sectional shapes influence the separation zone of an open-channel confluence. *Journal of Hydraulic Engineering* 143 (9), 04017036.
- Schubert, J. E., Sanders, B. F., 2012. Building treatments for urban flood inundation models and implications for predictive skill and modeling efficiency. *Advances in Water Resources* 41, 49–64.
- Soares-Frazão, S., Guinot, V., 2007. An eigenvector-based linear reconstruction scheme for the shallow-water equations on two-dimensional unstructured meshes. *International Journal for Numerical Methods in Fluids* 53 (1), 23–55.
- Soares-Frazão, S., Zech, Y., 2002. Dam break in channels with 90° bend. *Journal of Hydraulic Engineering* 128 (11), 956–968.

# Acknowledgment

This PhD thesis is performed in the hydraulic lab of INSA-Strasbourg under the direction of Abdallah Ghenaim and Abdelali Terfous. In this acknowledgment, I want to express my gratitude to all the people that provide help to finish this thesis.

I thank my supervisors, Abdallah Ghenaim and Abdelali Terfous, who provide this opportunity that I can study in French. In the past three and half years, they have given me a lot of help both in study and life, which is really appreciated.

I want to thank Pierre-André Garambois and Pascal Finaud-Guyot, who teach me how to make research and encourage me when I depressed in the study, The support they have given to me is cherished and I have really enjoyed the time when working with you. I think words is not enough to express my thanks to your guys. Without the help, I can't finish the thesis like this.

I want to thank two reviewers of the thesis, H el ene Roux and Vincent Guinot, for accepting review my work, and also for the advices provided.

I want to thank Mrs Sandra Soares-Frazao for the validation data provided in the thesis.

I also want to thank all the members in the laboratory for their support during all my PhD career, and the help from calculation center of University of Strasbourg.

I'm really grateful to China Scholarship Council for the financial supporting in the past three and half years, also I'd like to thank INSA de Strasbourg for providing me a wonderful research place.

At last not the least, I want to express my gratitude to my family, especially my father, my mother, my old sister and my brother in law, for their selfless support on my study career.

# Contents

<b>1</b>	<b>General introduction</b>	<b>1</b>
1.1	Context and problematics . . . . .	1
1.2	Outline of the thesis . . . . .	2
<b>2</b>	<b>Literature review</b>	<b>3</b>
2.1	Water cycle and flooding . . . . .	3
2.1.1	Water cycle . . . . .	3
2.1.2	Flood types . . . . .	4
2.1.3	Urban floods . . . . .	5
2.2	Hydraulic intersections at the “local scale” . . . . .	7
2.2.1	Three branch confluences . . . . .	8
2.2.2	Three branch bifurcations . . . . .	12
2.2.3	Four branch intersections . . . . .	14
2.2.4	Conclusion on hydraulic intersections . . . . .	16
2.3	Hydrodynamic investigations at district/city scale . . . . .	16
2.4	Numerical models applied to urban floods . . . . .	19
2.4.1	Review on 1D2D coupling . . . . .	19
2.4.2	Review on shallow water (SW) models with macroscopic porosity approaches	21
2.4.3	Conclusion . . . . .	26
2.5	Numerical model sensitivity analysis . . . . .	26
2.5.1	Uncertainty analysis (UA) and sensitivity analysis (SA) . . . . .	26
2.5.2	Sensitivity analysis applied to shallow water models . . . . .	28
2.6	Bibliography synthesis and scientific questions . . . . .	30
<b>3</b>	<b>Material and methods</b>	<b>31</b>
3.1	Derivation of the governing equations . . . . .	31
3.1.1	3D Navier-Stokes equations . . . . .	31
3.1.2	Derivation of the 2D shallow water equations . . . . .	37
3.1.3	2D shallow water equations with isotropic and constant porosity . . . . .	42
3.2	1D2D coupling model . . . . .	46
3.2.1	Topology of the coupled 1D2D model . . . . .	46
3.2.2	Finite volume method . . . . .	48
3.2.3	Discretisation . . . . .	49
3.2.4	Time splitting . . . . .	50
3.3	New hydrodynamic reconstruction . . . . .	52
3.3.1	Physical considerations on flow downstream crossroads . . . . .	52
3.3.2	Modified topology of the edge - hyperbolic part . . . . .	54
3.4	Conclusions/modeling methodology . . . . .	56

<b>4</b>	<b><i>Flood1D2D</i> validation</b>	<b>57</b>
4.1	Introduction . . . . .	57
4.2	Flux computation . . . . .	57
4.2.1	Water at rest with variable porosity and bottom elevation (T01) . . . . .	57
4.2.2	One-dimensional flow through a variable porosity zone (T02) . . . . .	59
4.2.3	One-dimensional flow over a bump (T03) . . . . .	60
4.2.4	One-dimensional flow with porosity and bottom bump (T04) . . . . .	64
4.2.5	One-dimensional dambreak without porosity (T05) . . . . .	69
4.2.6	One dimensional velocity dambreak without porosity (T06) . . . . .	69
4.2.7	One-dimensional dambreak with variable porosity (T07) . . . . .	71
4.2.8	One-dimensional dambreak with porosity discontinuity (T08) . . . . .	71
4.2.9	Two-dimensional dambreak with variable porosity (T09) . . . . .	76
4.3	Friction handling . . . . .	76
4.3.1	Backwater curve comparison (T10) . . . . .	78
4.3.2	Normal depth computation (T11) . . . . .	79
4.4	Cut cell technique . . . . .	79
4.4.1	Water at rest over variable bottom elevation and porosity (T12) . . . . .	81
4.4.2	Steady-state flow in a variable width rectangular channel (T13) . . . . .	83
4.4.3	Steady-state flow in a rectangular channel with various 1D2D junction orientation (T14) . . . . .	84
4.4.4	Dambreak in channels with 90° bend (T15) . . . . .	87
4.5	Conclusions . . . . .	89
<b>5</b>	<b>Sensitivity analysis of 1D and 2D shallow water models</b>	<b>93</b>
5.1	Chen, S., Garambois, P.-A., Finaud-Guyot, P., Dellinger, G., Mose, R., Terfous, A., Ghenaim, A., 2018. Variance based uncertainty quantification for 1d and 2d hydraulic modeling: an experimental urban flood case. Under review for Environmental Modelling & Software. . . . .	94
5.1.1	Introduction . . . . .	94
5.1.2	Methods and models . . . . .	96
5.1.3	Results . . . . .	98
5.1.4	Discussion . . . . .	105
5.1.5	Conclusions . . . . .	110
5.2	Variance based sensitivity analysis of 2D unsteady flood flow hydraulic model . . . . .	114
5.2.1	Calibration of the rating curve . . . . .	114
5.2.2	Transient 2D modeling . . . . .	115
5.2.3	Analysis of the direct run . . . . .	115
5.2.4	Global sensitivity analysis . . . . .	118
5.2.5	Conclusions on temporal sensitivities . . . . .	121
5.3	Sensitivity of global flow pattern to street blockage . . . . .	123
5.4	Conclusions . . . . .	124
<b>6</b>	<b>Model applications</b>	<b>127</b>
6.1	Influence of the friction effect parameterization . . . . .	128
6.1.1	Approximations of hydraulic radius . . . . .	128
6.1.2	Sensitivity of the $S_f$ computation to porosity . . . . .	129
6.1.3	Sensitivity of the $S_f$ computation to hydraulic radius . . . . .	131
6.2	Response surface of existing three branches recirculation laws . . . . .	133
6.3	2D hydrodynamic analysis of a four branch crossroad . . . . .	135

6.3.1	Classical 2D modeling of a four branch crossroad . . . . .	136
6.3.2	Characterization of the recirculation zone . . . . .	138
6.4	GSA of a full 2D SW model applied to crossroad modeling . . . . .	140
6.4.1	Variation range of input parameters . . . . .	140
6.4.2	GSA on the four branch crossroad flow . . . . .	140
6.4.3	Variation range of the recirculation dimensions . . . . .	143
6.5	Application of the <i>Flood1D2D</i> model . . . . .	144
6.5.1	Parameterisation of the code <i>Flood1D2D</i> . . . . .	145
6.5.2	Results comparison using <i>Flood1D2D</i> with and without porosity . . . . .	145
6.5.3	Conclusion . . . . .	150
6.6	GSA of <i>Flood1D2D</i> using porosity parameterization . . . . .	150
6.6.1	GSA on main controls and recirculation dimensions . . . . .	150
6.6.2	GSA on recirculation dimensions and roughness . . . . .	154
6.7	Application of <i>Flood1D2D</i> at the district scale . . . . .	154
6.7.1	Modeled crossroads network . . . . .	156
6.7.2	Characterization in $K_{street}/K_{cross}$ . . . . .	157
6.7.3	Parameterization in $K_{unif}/\phi_{large}/\phi_{narrow}$ . . . . .	158
6.7.4	Parameterization in $K_{unif}/\phi_{large}/\phi_{narrow}/Ratio$ . . . . .	160
6.8	Conclusions . . . . .	161
<b>7</b>	<b>General conclusions and perspectives</b>	<b>163</b>
7.1	General conclusions . . . . .	163
7.2	Perspectives . . . . .	164
	<b>Bibliography</b>	<b>165</b>
	<b>A Appendix</b>	<b>175</b>

# Chapter 1

## General introduction

### 1.1 Context and problematics

Flooding represents the first natural hazard on each continent, and it caused in Europe around 100 billion euros of damage between 1986 and 2006 (e.g. Moel et al. (2009)). In the context of climate change and its possible effects on rainfalls regimes and extremes (Pachauri et al. (2014)), an unprecedented urbanization of floodplains increases the vulnerability of human societies to floods. They are generally caused by intense rainfalls which can lead to a temporary saturation of the urbanized catchment and drainage systems. Such floods can propagate through streets and underground networks resulting in complex flow path depending on the topology of a city (Paquier et al., 2015). Flood effects can be exacerbated by existing paved streets and roads, which increase the speed of flowing water. The submersion levels and flow velocities constitute a hazard to both the population and infrastructure related to flood nature and urban networks configuration. Therefore it is of paramount importance to improve risk assessment based on flow physics understanding and predictive models both at the local and city scales. However real time forecasts of urban flood hydrodynamics, with an accurate and robust estimation of the spatio-temporal evolution of water levels and flow velocities, and their associated uncertainties, remains a real scientific challenge.

The predictive performances of a model generally depend on its complexity and the misfit to the real (nonlinear) physical processes complexity but also of the availability of constraining data. Nevertheless, reliable flood measurements, that are required to improve (urban) flood mechanism understanding, elaborate models and calibrate them are difficult to perform. That is why urban flood datasets obtained on densely instrumented laboratory scale experimental devices are precious (e.g. Mignot et al. (2006); Schubert and Sanders (2012); Finaud-Guyot et al. (2018), among others). Fine 3D hydrodynamic models, based on Navier-Stokes equations, can also be used in order to investigate hardly measurable complex turbulent flow patterns such as those involved at the local scale of hydraulic intersections (e.g. Momplot et al. (2017)) or even flow repartition at the scale of branched networks (Finaud-Guyot et al. (2018)). Such calculations, generally requiring a turbulent closure and wall function parameterization, yet remain very computationally expensive and flood models dedicated to operational use are commonly depth averaged (2D or 1D shallow water -SW- equations). Inundation maps, submersion levels and flow velocities are generally performed with a 2D SW model which is a good compromise in terms of realism and computational efficiency between 3D and cross sectional averaged 1D. However if the domain size increases from building blocks to a whole district or city, 2D simulations remain very computationally demanding. Facing this, 1D2D coupling (Finaud-Guyot (2009); Finaud-Guyot et al. (2010a)) and macroscopic (Guinot and Soares-Frazão (2006); Sanders et al. (2008); Guinot

(2012a); Guinot et al. (2017a)) methods appear to be promising approaches to reduce flood modeling computational costs but taking advantage of the relative accuracy of 2D on hydraulic intersections such as crossroads and of cheaper 1D models on street channels. Such simplified models, aiming at preserving essential flow features for an effective flood modeling with sufficient accuracy on key hydraulic variables, would also be parsimonious in terms of parameterization.

In the context of urban flood effective modeling and in view to propose an effective 1D2D model, the following questions arise and are tackled in this PhD:

1. What are the key local flow zones and features that need to be reproduced by a simplified 1D2D model of a branched network?
2. How to parameterize such a model for example in streets where 3D flow features such as recirculation zones downstream of crossroads can appear?
3. What are the sensitivity of 2D SW or 1D2D models to their parameters for urban flood flows in a branched network?

## 1.2 Outline of the thesis

In this PhD, a 1D2D model, *Flood1D2D*, is proposed with a new parameterisation adapted to the main flow features of a urban district configuration - ICube urban flood experimental rig. An isotropic porosity is implemented in *Flood1D2D* in order to be able to take into account the flow contractions due to the effect of recirculations. Sensitivity analysis of a state of the art 2D SW model and of the proposed 1D2D model to their input parameters are performed using global sensitivity analysis (GSA). Input parameters are sampled in ranges defined from typical uncertainties observed in experiments.

This PhD thesis is organized in 5 chapters plus the present general introduction and a conclusion. Chapter 1 presents a bibliography synthesis on urban floods at local and urban district scales using experimental and numerical approaches. Some shallow water models applied to urban flood are presented including 1D2D couplings and sub-grid methods like porosity function; some sensitivity analysis are also presented. Chapter 2 presents the derivation of the shallow water equations (depth-averaged) with porosity and their discretization with a finite volume method, but also the proposed numerical method and parameterization implemented in *Flood1D2D*. The model is validated in chapter 3 on reference flow cases including synthetic test cases and experimental datasets with various combinations of porosity, bottom elevation, friction and flux computation between 1D and 2D cells. Chapter 4 presents the application of GSA of classical shallow water models applied at the urban district scale using datasets of the ICube urban flood experimental rig. Chapter 5 tests the ability of *Flood1D2D* in reproducing local flow features at the street scale and their influence on discharge repartition at the block scale. The influence of input parameters like recirculation dimensions on local scale flow patterns is also quantified using GSA.

## Chapter 2

# Literature review

This PhD deals with urban flood modeling at the street and city scale. This chapter presents a bibliography synthesis of research works related to urban floods, including numerical and experimental investigations along with sensitivity analysis. It begins with a general description of the continental water cycle and the hydrological contextualization of urban floods. Then, major hydrodynamic features involved in urban flood flows are presented, and especially “local” scale hydraulic intersections. Next, the numerical methods commonly used for urban flood modeling are introduced including a review of works with different paradigms (1D, 2D and 3D), with 1D2D couplings and sub-grid scale methods. Sensitivity analysis (mainly variance based global sensitivity analysis) is introduced and its application in hydrology and hydrodynamic is also briefly reviewed. Finally, some problematics are formulated and manuscript objectives are presented.

### 2.1 Water cycle and flooding

#### 2.1.1 Water cycle

The great water cycle driven by the thermal energy of the sun describes the fluxes of water within the so-called hydrosphere on earth including oceans and continents. The quantity of water on earth (around 1,386,000,000 km<sup>3</sup>) is nearly constant since about 4 billion years (<https://water.usgs.gov/edu/earthhowmuch.html>, access on April 03, 2018) whereas its partitioning into the oceans, the atmosphere, the cryosphere and the continental surface and underground water is variable in time and space. The continental water cycle, also known as the hydrological cycle, describes the movement of water on, above and below continental surfaces as illustrated in figure 2.1. Hydrology is the scientific field, at the confluence of meteorology and fluid mechanics, focused on the continental water cycle. The main physical processes involved in water repartition are evaporation, condensation, precipitation, infiltration, surface runoff, sub-surface flow, groundwater flow. These vertical and lateral hydrometeorological processes are non linear and coupled, characterized by various relaxation times.

Soil atmosphere exchanges, including evaporation, evapotranspiration, precipitations, snow and ice melt represent the main drivers, also called forcing of surface runoff and groundwater flows. In hydrology, rainfall-runoff transformation is generally studied at the topographic basin scale whose properties (topography, soil occupation and nature, bedrock, etc) influence the spatio-temporal variability of flow processes along with the variability of the forcings. It is of particular interest to improve the understanding and predictive performances of models of those hydrological processes at various spatial and temporal scales for:

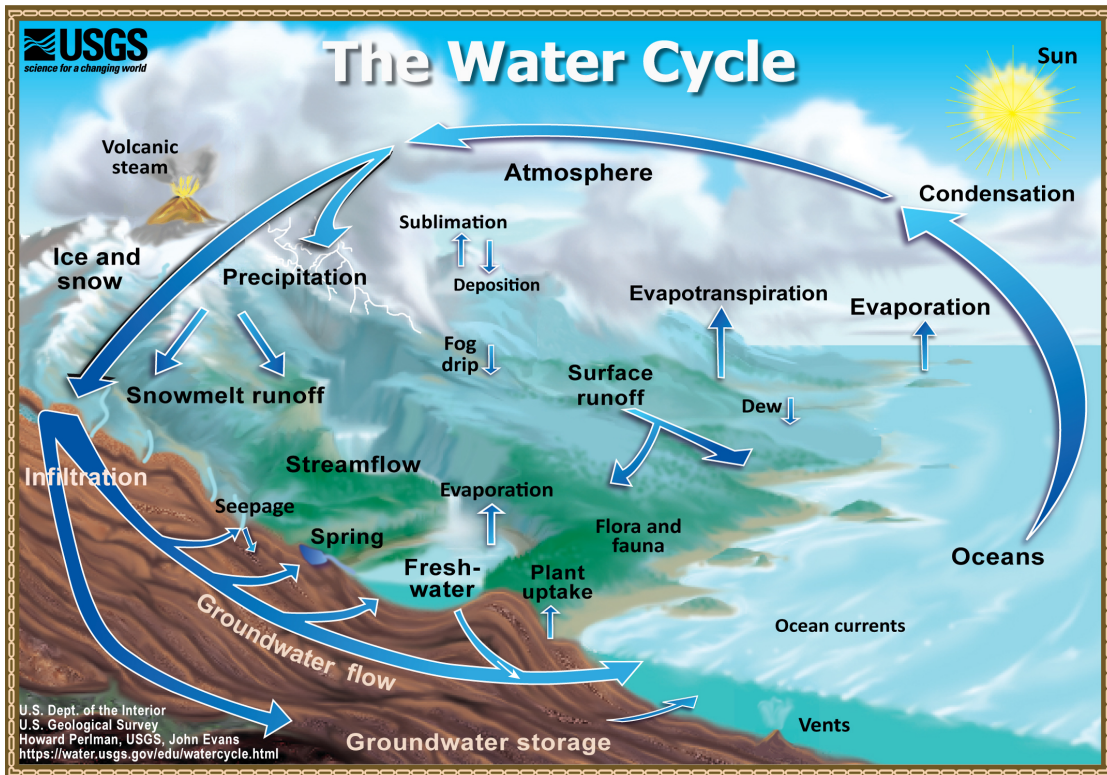


Figure 2.1: Schematic view of the great water cycle with an emphasis on the continental one (source: <https://water.usgs.gov/edu/watercycle.html>, access on April 03, 2018).

- Improving our understanding of the water cycle on earth and reach its closure in terms of quantitative water balance between ocean, continents, atmosphere and cryosphere.
- Building sustainable water management and engineering techniques in a context of climate change (Pachauri et al. (2014)).

Water management includes many problematics involving different spatio-temporal scales. Hydrological extremes such as floods may occur at short time scales and their predictivity represent an important challenge. Indeed, weather related disasters seem to become increasingly frequent and especially storm-floods which represent nowadays 47% of weather-related disasters worldwide over the period 1995-2015 (Pachauri et al. (2014); Wahlstrom and Guha-Sapir (2015)). Depending on storm and catchment properties various flood types can occur as detailed in the following section.

### 2.1.2 Flood types

#### General classification

A flood is a natural hazard that can occur in many places worldwide due to the combination of several factors that can include: precipitation, soil (and/or underground networks) saturation, ocean storm surge, dam/breach breaking, debris chocked rivers. It is commonly defined as the

overflow of water over land and built-up areas that are usually dry. Flooding can be classified as follows:

- Coastal floods generally occurring along the coastline where land can be submerged by seawater because of a storm surge due to a hurricane or tsunami and/or overwhelming rainfall.
- River (or fluvial) flooding occurring after long (oceanic) rainfall events of generally moderate intensity on large catchments (area greater than 500km<sup>2</sup> for instance). The river or stream is unable to convey the excedent of runoff drained by its upstream catchment and slowly floods its major bed (floodplains). The submersion duration can reach several days or even such as for the flood in Paris in 1910 which lasted 10 days, with a measured water level of 8.62m at Paris-Austerlitz gauging station where the water level is usually around 2.5m.
- Floods due the groundwater level rise due to a long rainfall period over the refilling area(s) of an aquifer. This kind of events were badly known until the events in the Somme catchment (France) in 2000 and 2001. The plains in Picardie (Northern France) have know submersion levels of about 15m at some places.
- Flash floods that are extreme and quick catchment responses typically smaller than 24h with high peak discharge often produced by severe localized thunderstorms on catchment headwaters (area smaller than 500km<sup>2</sup> for instance) (Garambois et al. (2013, 2015); Douinot et al. (2017)). Various definitions of flash floods are given in the literature but five criteria can be used (Garambois (2012)): flashiness of the hydrological response, river slope, Froude number, debris transport, flood effects/damages. Due to high flow power those floods can significantly modify a river geometry and are consequently highly morphogenic. Let us cite some catastrophic floods in the south of France: the Ouvèze River in 1992, the Aude River in 1999, the 2002 floods in the Gard region and the 2010 and 2016 floods in the Var department.
- Urban flooding consisting in significant submersion of densely populated and often highly impermeable areas. It can be caused by the combination of various factors including upstream runoff and river flooding, storm surge or tsunامي, rainfall localized on the urban area and the saturation of the capacity of drainage systems such as storm sewers (Mignot et al. (2006); Sattar et al. (2008)).

### **2.1.3 Urban floods**

Urban flooding is defined as the inundation of land or property in a more or less densely built and populated environment. Such hydrological events can be due to various combinations of hydro-meteorological factors as presented above and also site specific features such as topography, soil occupation and properties and antecedent wetness. Urban floods are generally caused by rainfalls overwhelming the infiltration capacity of a (urban) catchment and the storage and conveyance capacities of drainage systems, such as storm sewers as in figure 2.2.

#### **2.1.3.1 Physical phenomena involved in urban hydrology**

Urban hydrology is a science investigating the hydrological cycle (see figure 2.3) and its changes, water regime and quality within the urbanized landscape and its impacted zones . The hydrological process in urbanized catchments consist in (Fletcher et al. (2013); Salvatore et al. (2015)):



Figure 2.2: Pictures of urban flooding during severe flood

- Meteorological forcing: the accurate prediction of rainfall-runoff interaction highly depend on rainfall measurement over an urban area and its upstream catchment (e.g. with meteorological radars, or new techniques based on cell phones networks for example), rainfall forecasting and rainfall modelling (Skamarock et al. (2005); Seity et al. (2011)).
- Surface runoff process: the urbanization is accompanied with the replacement from natural/cultivated soil to impervious surface, which has profound impacts on urban hydrology. The volume of surface runoff can increase dramatically due to impervious surfaces where infiltration hence water storage is impossible.
- Subsurface flow processes: subsurface flows in urban sewers and water supply networks, underground networks (Ishigaki et al. (2003); Noh et al. (2016)).

The accumulation of overland flow in urban areas caused by excedent rainfall, due to imperious surface and inappropriately designed drainage systems can be the main reasons for urban flooding.

### 2.1.3.2 Urban flood flows physics and risk to people

The increase of flood damages is particularly marked in urbanized areas representing an increasing percentage of the world population. Both an increasing urbanization and the potential rise of high to extreme rainfall events should lead to more frequent urban flooding. In urban areas, flood effects can be exacerbated by existing paved streets and roads, which increase the speed of flowing water. The flood flow in urbanized areas constitutes a hazard to both the population and infrastructure. Important features of this hazard are the variability of water depth and velocities (Mignot et al. (2006); Yu and Lane (2006a)).

In urban area flood flow paths are quite complex and related to the topology of the city. From a hydraulic point of view, the structure of the city formed of building blocks is organized on the basis of networks (Paquier et al. (2015)): the hydrographic network including the rivers, underground sewer network and street networks (Finaud-Guyot et al. (2018)). During urban flooding, the streets can become the main flow paths while remaining the only means for emergency services and evacuation of the population.

The hydrodynamics of urban flood flows can be viewed at two different scales of interest:

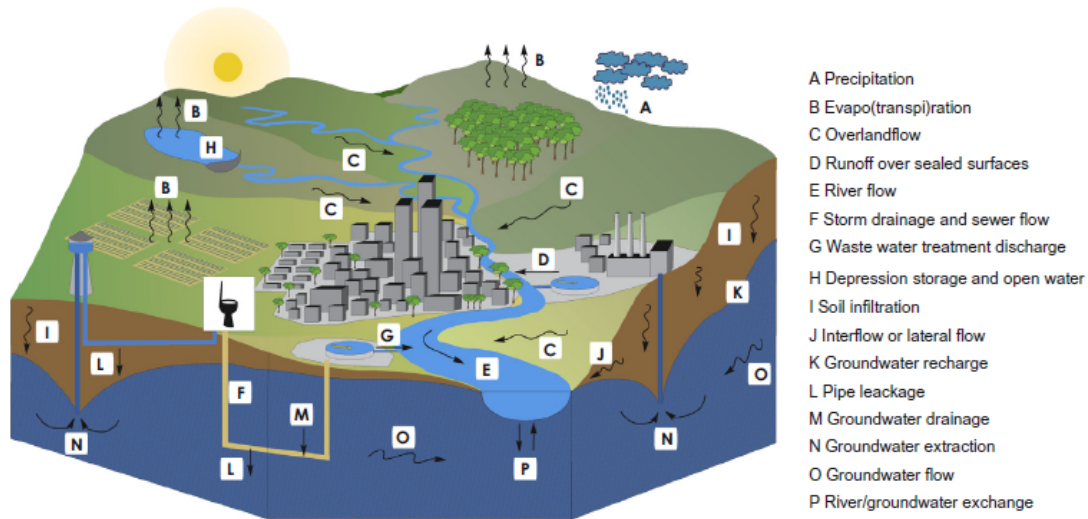


Figure 2.3: Hydrological processes about physical phenomena involved in an urbanized catchment taken from Salvadore et al. (2015)

- Local scale: the study is focused on the properties of the flow (velocity and cross section/submersion depths) at local scale in a portion of street or at a crossroad involving confluences/defluences;
- District/city scale: the studied domain is composed of several streets and crossroads hence forming a branched network.

Therefore it is of paramount importance to improve risk assessment based on flow physics and prediction tools efficient both at the local and the city scale. A bibliography synthesis of local phenomena at hydraulic intersections is presented in the next section followed by a synthesis on flow studies at the district and city scales.

## 2.2 Hydraulic intersections at the “local scale”

Open channel intersections are commonly encountered in natural rivers (deltas, floodplains) and anthropized channels (irrigation networks and sewerage, urban street networks). In the literature mainly three types of hydraulic intersections are documented:

- Three branch confluence flow: two upstream reaches feeding one downstream reach;
- Three branch dividing flow: one upstream reach feeding two downstream reaches;
- Four branch intersection flow: two upstream reaches feeding two downstream reaches.

The basic intersections are three branch intersections including confluence flow or bifurcation flow. Both types of hydraulic intersections involve modifications in the mass and momentum repartition:

**Dividing flow** The continuity equation imposes that upstream discharge is splitted into two downstream discharges. The momentum is also splitted into the downstream branches but energy losses can appear due to basal friction, turbulence dissipation (e.g. flow in zones with complex hydrodynamics such as recirculation or vortex).

**Junction** The mass continuity imposes that the downstream discharge is the sum of the two upstream ones. Similarly the downstream momentum is the sum of the two upstream minus the energy losses mentioned above.

Due to flow physics and the variability of flow regimes in each branch, there is not the same number of hydraulic unknowns (depth, discharges) for a confluence and a dividing flow. In the case of the four branches flow, the hydraulic problem can even be more complex. Ming (2017) among others, considers that a four branch intersections (with two inlet and outlets) can be seen as the combination of a confluence flow and a bifurcation flow. Street intersections when city is flooded are the typical examples of free surface flows at hydraulic intersections. The local and global flow features of those intersections have been thoroughly reviewed by Ming (2017). In this thesis, we make a more detailed review on local flow feature and especially the separation zone.

### 2.2.1 Three branch confluences

#### General introduction

The general flow pattern is summarized in figure 2.4 based on the experiment of Weber et al. (2001) and numerical modeling by Huang et al. (2002). A three branch confluence flow is generally characterized, depending on flow regimes, by complex flow patterns. The general features are:

- A shear plane which delimitates the separation between the two upstream incoming flows (identified as “mixing layer” in figure 2.4). A mixing layer exists between main channel flow and tributary inflow. The velocity difference between them causes shear forces and coherent structures into the mixing layer (Thanh et al. (2010); Mignot et al. (2014)).
- A separation zone that occurs due to the tributary branch momentum causing the flow to detach at the downstream corner of the crossroad (Best and Reid (1984)). The separation zone is characterized by low flow pressure, which causes the separation streamline to deflect towards the branch-side bank further downstream, forming a three-dimensional separation zone (Hsu et al. (1998)). A recirculation zone may appear into the separation zone with flow circulation.
- A flow contraction due to the recirculation. The combined flow accelerates as it passes through this part of the channel, where water height decreases and velocity increases for subcritical flow.
- A stagnation zone that is characterized by a low velocity close to the upstream corner between two incoming flows. The dimensions of the stagnation zone are influenced by the incoming discharge ratios.

Among others, Schindfessel et al. (2017) propose a schematic representation of a recirculation zone as presented in figure 2.5. Two methods are used to delineate the dimensions of a separation zone, which is based on the 2D flow field. The first method is named as the *isovel method* proposed that the isoline of zero longitudinal velocity is used to delineate the separation zone (Qing-Yuan et al. (2009)). The second method is referred as the *zero-discharge method* that a zero discharge in the direction of the main flow defined the longitudinal extent of the separation flow (Schindfessel et al. (2017)) (see figure 2.5):

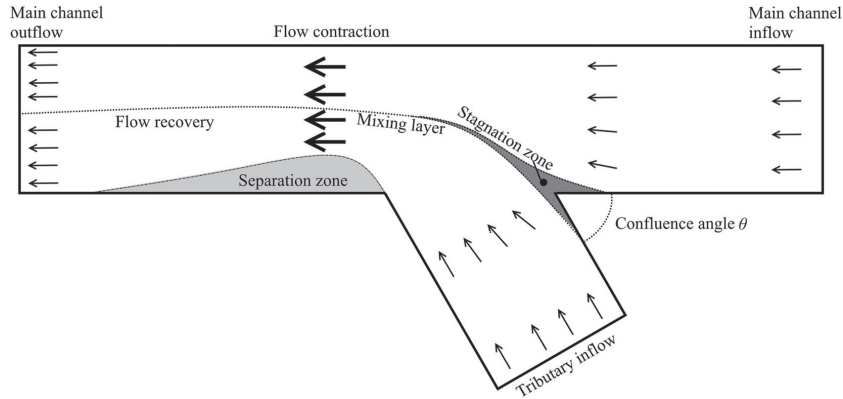


Figure 2.4: Illustration of a general conceptual model for an open channel confluence (Creëlle et al. (2016))

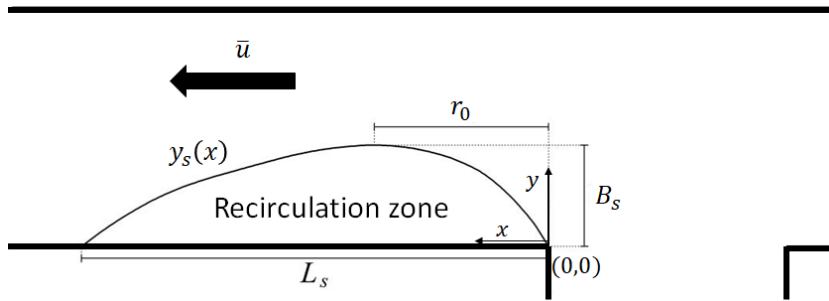


Figure 2.5: Definition of the dimensions of the separation zone adapted from Schindfessel et al. (2017)

$$\int_0^{y_s(x)} \bar{u}(x) dy = 0 \quad (2.1)$$

where  $\bar{u}(x)$  is the longitudinal velocity;  $y_s(x)$  is the distance of the recirculation limit to the wall.  $L_s$  is defined as the length of separation zone (for which  $y_s(x) > 0$ ) and  $B_s$  is defined as the maximum value of  $y_s(x)$  for all  $x$  between 0 and  $L_s$ . The length  $r_0$  corresponds to the distance from the downstream corner to the  $x$ -coordinate where  $B_s$  is found.

### Flow features on separation zone

A first comprehensive study of open channel confluence flows is proposed in Taylor (1944). The experiment proposed consists in a rectangular channel of uniform width with junction angles of  $45^\circ$  and  $135^\circ$  without bottom slope, in subcritical flow conditions. An analytical relationship is obtained based on momentum considerations and compared with experimental results for confluence flow. A reasonable agreement between model and experiment is found for the  $45^\circ$  junction, but not for that at  $135^\circ$ .

Several studies have been conducted on three branch confluence flow (Webber and Greated (1966); Modi et al. (1981); Best and Reid (1984); Hager (1987, 1989); Mamedov (1989); Gurram et al. (1997); Hsu et al. (1998); Weber et al. (2001); Huang et al. (2002); Schindfessel et al.

(2017)). The research is focused on local flow patterns like flow separation, secondary current and mixing layers, global flow features like upstream and downstream depth ratio and energy loss at a flow crossroad based on momentum and energy balance.

Webber and Greated (1966) perform experimental studies on three branch confluence flow with varied angle  $30^\circ$ ,  $60^\circ$  and  $90^\circ$  using equal width on horizontal plan. Theoretical flow patterns are derived using free-streamline theory and conformal mapping to define a theoretical flow pattern throughout the junction and compared with experiment. The location of stagnation point at the upstream corner of the channel junction and delineation of separation zone are also presented. No attempt of quantifying the dimensions of separation zone is conducted. Modi et al. (1981) uses a conformal mapping technique to predict the geometry of the separation zone.

Best and Reid (1984) conduct experimental studies on separation zones in the case of an open channel junction of equal width and an empirical relationship is derived for the maximum width  $B_s$  and length  $L_s$  of recirculation zone based on the ratio between lateral and downstream discharge with angles of  $15^\circ$ ,  $45^\circ$ ,  $70^\circ$  and  $90^\circ$ . The results show that the width and length of the flow separation zone at open-channel confluences increases with both junction angle and the contribution of the tributary to the total discharge. The shape of the separation zone remains more or less constant. The ratio between maximum width and length is  $\frac{B_s}{L_s} = 0.19$ . The recirculation zone grows at the expense of the channel width ("flow vein") occupied by the combined streams. For combined flows a relation is presented by Best and Reid (1984) for a  $90^\circ$  angle to determine  $B_s$  and  $L_s$  and writes:

$$B_s = B \times (0.506 + 0.205 \ln q) \quad (2.2a)$$

$$L_s = B \times (2.587 + 1.025 \ln q) \quad (2.2b)$$

where  $B$  is channel width,  $q = \frac{Q_L}{Q_d}$ ,  $Q_L$  and  $Q_d$  are lateral and downstream discharges.

Best and Reid (1984) also compared his relationship to the dataset of Modi et al. (1981). It shows that predicted width of the separation zone is overestimated and the fraction of the channel occupied by the flow vein is therefore underestimated. Hager (1989) expressed the upstream to downstream water depth ratio and the contraction coefficient as functions of the junction angle and the discharge ratio, assuming critical flow conditions at the maximum flow constriction downstream of the junction. To quantify the dimensions of separation zone, an empirical relationship is proposed by Mamedov (1989) which relates the length and width of the separation zone to the confluence angle, the momentum ratio, the inflow velocity ratio, and a factor depending on the inflow conditions.

Gurram et al. (1997) provide a detailed study on subcritical three-branch junction flows using an experimental device with angles of  $30^\circ$ ,  $60^\circ$  and  $90^\circ$  and uniform width. Then, an empirical relationship is provided for maximum separation width  $B_s$  and length  $L_s$ ,

$$B_s = B \times \left[ \frac{1}{2} \times \left( F_d - \frac{2}{3} \right)^2 + 0.45 \times q^{1/2} \times \left( \frac{\delta}{90^\circ} \right) \right] \quad (2.3a)$$

$$L_s = B \times \left[ 3.8 \times \sin^3 \delta \times \left( 1 - \frac{1}{2} \times F_d \right) \times q^{1/2} \right] \quad \text{for } F_d < 1 \quad (2.3b)$$

$$L_s = B \times \left[ 0.26 \times \left( 1 + \frac{3 \times \delta}{90^\circ} \right) \times q^{1/2} \right] \quad \text{for } F_d = 1 \quad (2.3c)$$

where  $B$  is channel width,  $F_d$  is the downstream Froude number,  $q = \frac{Q_L}{Q_d}$ ,  $Q_L$  and  $Q_d$  are lateral and downstream discharges and  $\delta$  is junction angle.

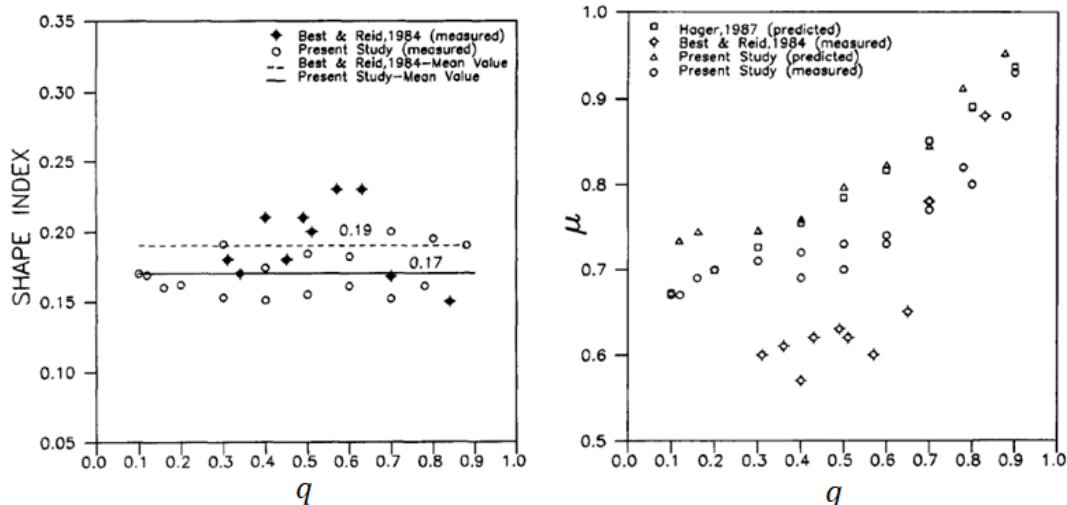


Figure 2.6: Shape index and maximum contraction coefficient  $\mu$  on separation zone: left, shape index of separation zone; right, contraction coefficient at maximum flow constriction taken from Hsu et al. (1998)

Gurram et al. (1997) also proposed an empirical model of the shape of the recirculation:

$$Y_s = [\sin(90^\circ X_s)]^{2/3} \quad (2.4)$$

where  $Y_s = y_s(x)/B_s$  and  $X_s = x/(L_s/2)$ , leading to a symmetrical profile.  $y_s(x)$  and  $x$  are defined in figure 2.5.

Hsu et al. (1998) conducted T-branch ( $90^\circ$  angle) confluence for subcritical flows in the upstream main and branch channels, with Froude numbers lower than 0.45. The maximum width and length of the separation zone were determined by averaging three plane observations of dye traces that were injected near the water surface at the downstream corner. Shape index and contraction coefficient at maximum flow constriction  $\mu$  are obtained and compared with Best and Reid (1984) and Hager (1987) (see figure 2.6). Shape index keeps constant as 0.17 with the variation of discharge ratio  $q$  compared with 0.19 provided by Best and Reid (1984).  $\mu$  increases when discharge ratio  $q$  changes from 0.1 to 1.

Weber et al. (2001) conducted experiments on a T-branch confluence. Separation zones with 3D flow features are observed. Recirculation inside the separation zone is highlighted as reverse flows are identified. The separation zone is larger near the surface than at the bottom, both in length and width. As presented by Best and Reid (1984); Gurram et al. (1997), the separation zone grows as the discharge ratio  $q = \frac{Q_L}{Q_d}$  increases. However, the growth of the separation zone has a limitation observed by Weber et al. (2001). Depending on  $q$  a reflection of the lateral inflow on the opposite wall can appear and reduce the length of the recirculation zone.

Weber et al. (2001) also show that a smaller inflow angle at the bottom resulted in a lower lateral momentum, which caused a narrower separation zone near the bottom than at the surface. Due to a negative  $v$ -component of the flow (crossflow horizontal velocity component), the flow near the bottom is the first portion of the junction flow that enters the separation zone along the junction-adjacent wall. The flow is reflected off by the wall opposite to the junction and comes to the bottom from the surface. It is shown that the upper portion of the separation zone can

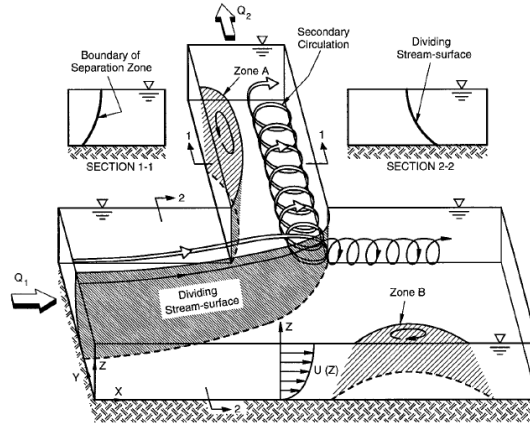


Figure 2.7: Illustration of a general concept model for a dividing open channel flow from Neary et al. (1999)

be filled by the vertical flow, but not lateral flow. When flow near the bottom approaches the junction adjacent wall, it is redirected like the surface flow at the junction-opposite wall. Some of this is in the downstream direction but the bed flow is also deflected upward into the zone of separation (Weber et al. (2001)).

Except experiments conducted on three-branch crossroad flows, 3D numerical approaches are also adopted to delineate the separation zone. Huang et al. (2002) simulated T-confluence flow using 3D Reynolds-averaged Navier-Stokes equations (cf. next chapter, equation (3.32)) to reproduce the features of separation zone observed by Weber et al. (2001). Schindfessel et al. (2017) used validated large-eddy simulation (LES) to study the flow in confluences with four different cross-sectional shapes. Results show that the dimensions of the separation zone are significantly influenced by the cross-sectional shapes.

## 2.2.2 Three branch bifurcations

### General introduction

Three branch bifurcations can be seen in irrigation networks or in the separation of a river around an island with one incoming flow and two unknown downstream discharges. The main difference between confluence flow and bifurcation flow is that discharge distribution at crossroad is unknown. Mass conservation is kept for the whole domain, therefore only an extra variable is introduced to the problem. The general flow patterns of three branches bifurcation in subcritical flow conditions is summarized in figure 2.7 by Neary and Odgaard (1993); Neary et al. (1999):

- A separation zone highlighted as zone A in figure 2.7 occurs in the branch channel just downstream of the crossroad for the transformation of momentum from main channel to the branch. The size of the separation zone is related to the discharge ratio  $\frac{Q_L}{Q_{total}}$  between lateral discharge in the branch and total inflow discharge. As previously presented, this separation zone can cause a reduction of the effective flow vein and thus locally increase the flow velocity up to a potential transition from subcritical to supercritical flow.
- Flow contraction: as previously presented, due to the existence of a separation zone at branch channel, can cause the reduction of effective flow vein and increase the flow velocity,

which can cause the transition from subcritical to supercritical flow.

- Separation zone in the main channel (zone B in figure 2.7): several studies have identified this separation zone in the main channel downstream of a crossroad (Neary and Odgaard (1993); Neary et al. (1999)). Its dimensions mainly depended on the discharge ratio  $\frac{Q_L}{Q_{total}}$ .
- Dividing stream surface: the dividing stream surface is composed of stream lines connected to the downstream corner representing the splitting of the inlet discharge (Neary and Odgaard (1993); Momplot et al. (2017)).

For three branch bifurcation flows, the research is mainly focused on the prediction of discharge distribution at a crossroad. As presented by Taylor (1944), this problem can't be solved only using momentum balance to provide the solution. Therefore, an extra equation is needed to close the system and provide the full solution like energy equation, analogously to other flow phenomena and dimensional analysis.

### Flow features on separation zone in the branch channel

Kasthuri and Pundarikanthan (1987), who discuss Best and Reid (1984), provide an empirical relationship for the maximum separation width  $B_s$  and length  $L_s$  based on the ratio between the lateral and total inlet discharge for three branch dividing flow with right angle:

$$B_s = B \times \left[ 0.504 \times \left( \frac{Q_L}{Q} \right)^2 - 0.893 \times \left( \frac{Q_L}{Q} \right) + 0.861 \right] \quad (2.5a)$$

$$L_s = B \times \left[ 6.49 \times \left( \frac{Q_L}{Q} \right)^2 - 8.44 \times \left( \frac{Q_L}{Q} \right) + 4.45 \right] \quad (2.5b)$$

where  $Q_L$  and  $Q$  are lateral and total inlet discharges. This formula is more deeply studied in section 6.2.

The flow structure at a 90° open channel bifurcation flow is investigated experimentally by Neary and Odgaard (1993). Experimental data on velocity shows that the flow at an open channel bifurcation is three-dimensional, which is similar to river bend flows. Results show that roughness of the main channel bed and the ratio of diversion flow velocity to main flow velocity key parameters to determine the three-dimensional flow features, like flow dividing and secondary currents. The flow separation is characterized by low velocities, eddies, and recirculation. The separation zone is larger at the surface than at the bottom. Neary et al. (1999) developed a three-dimensional (3D) numerical model for predicting turbulent flows through lateral intakes with rough walls. Reynolds-averaged Navier-Stokes equations are solved with the isotropic turbulence closure model of  $k - \omega$ . The complexity of flow in the branch is increased with the increase of bed roughness, which induced the increased number of eddies and the width of the separation zone.

Hsu et al. (2002) conducted an experiment for a subcritical open channel dividing flow over a horizontal bed equipped with equal width in angle 90°. Based on experimental observations, the contraction coefficient  $\mu = \frac{B_s}{B}$  at maximum width-contracted section in the separation region is almost linearly related to  $q$ , the branch to main channel upstream discharge ratio (see figure 2.8), which resulted in a small effective width in the separation zone at branch channel when  $q$  is small.

Ramamurthy et al. (2007) study T-branch dividing flows experimentally and numerically using 3D Navier-Stokes (NS) equations with  $k - \omega$  turbulence model. A qualitatively correct

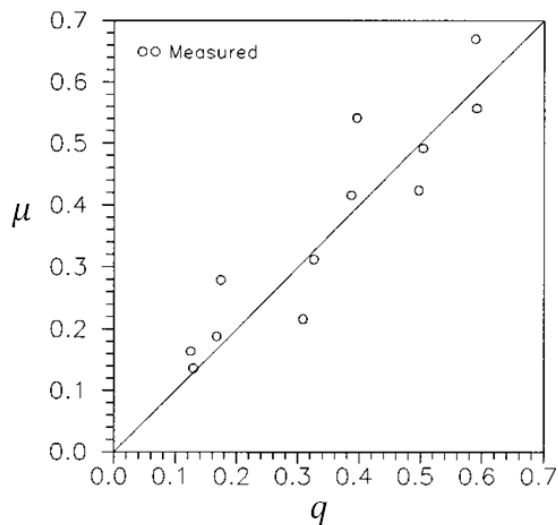


Figure 2.8: Contraction coefficient in branch channel taken from Hsu et al. (2002)

fit is obtained between model results and experiment. With a decrease of branch to upstream discharge ratio, the width and length of this separation zone increase. Li and Zeng (2009) simulate the T-branch dividing flows using 3D NS equations and a one-equation turbulence closure model. They investigate the flow phenomena with or without vegetation. The overall agreement between the computed results and the experimental data from Ramamurthy et al. (2007) is good. The largest discrepancy occurs at the recirculation zone, which may due to the isotropic assumption of turbulence in one-equation models (e.g., Spalart–Allmaras model) or two-equation models (e.g.,  $k$ - $\epsilon$  or  $k$ - $\omega$  models). In complex hydraulic zones, this assumption may be invalid.

### 2.2.3 Four branch intersections

Among the various configurations of inlet and outlet street in four branch intersections (Araud (2012)), the more deeply studied is the configuration with two inlets and two outlets shown as in figure 2.9. As suggested by Ming (2017), such configuration can be seen as a combination of confluence flow and bifurcation flow, leading to a more complex problem. The general flow patterns are similar to the three branch intersections with shear plane and separation zone in two outlet channels.

Nanía et al. (2004) studied experimentally supercritical flows in a four branch intersection with slope. It has been found that the flow distribution as well as the flow pattern can be predicted by a non-dimensional parameter, the inflow power ratio at the entrance of the crossroad. The inflow power is defined as  $\gamma \times Q \times \left( z + \frac{U^2}{2g} \right)$ , where  $\gamma$  the specific weight of flow,  $Q$  the discharge,  $z$  the water surface elevation,  $U$  the velocity and  $g$  the acceleration of gravity. Two types of flow patterns had been identified according to the presence and location of hydraulic jumps. The third type of flow pattern with two oblique jumps is observed and defined by Mignot et al. (2008b) in the intersection as illustrated in figure 2.10. Theoretical explanations to three flow types are also provided.

Except supercritical flow mentioned above, subcritical four-branch junction flow is studied experimentally by Rivière et al. (2006, 2011); Nanía et al. (2011). The intersection and channels are all horizontal and flow depths are controlled by vertical weirs at the downstream end of outlet

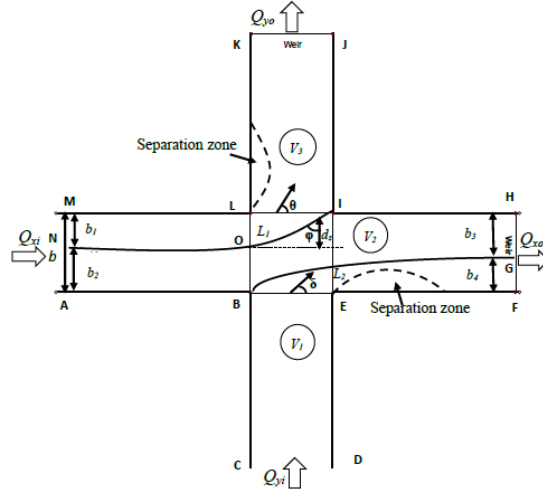


Figure 2.9: Illustration of a general conceptual model for a four-branch intersection from Rivière et al. (2011)

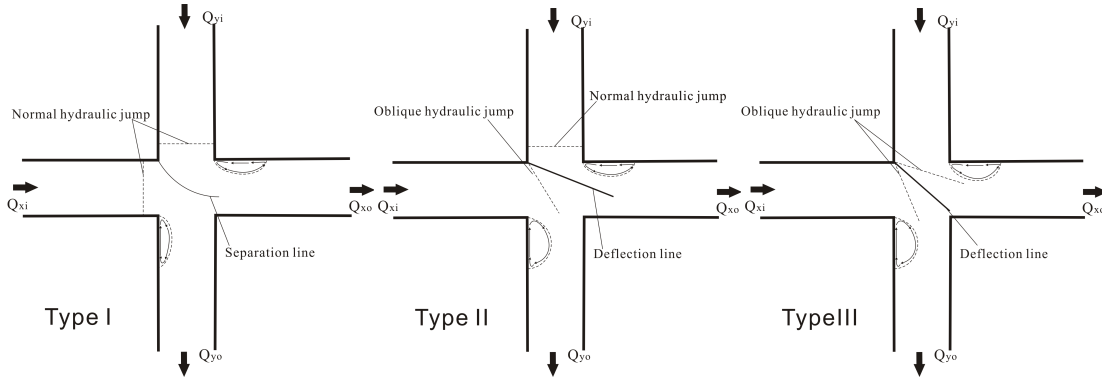


Figure 2.10: General schemes of the different flow types observed in supercritical flows in a four branch intersection: left, Type I; middle, Type II; right, Type III (Mignot et al. (2008b))

channels, where empirical relationship for discharge distribution at crossroad is studied. Nanía et al. (2011) conducted four branch subcritical junction flow on horizontal plane with derived empirical relationship for discharge distribution at crossroads. A complementary work for open channel transcritical flows at three and four branch channel intersections can be found in Rivière et al. (2013). They point out that the existence of a critical section in the lateral outflow channel is not sufficient to isolate flow in the intersection from the downstream control in the lateral channel.

Li and Zeng (2010) conducted 3D simulations at a channel crossing in subcritical or supercritical flow conditions. Using numerical models validated on T-branch junction flow, the dimensions of recirculation zone are quantified. Results show that under the identical outlet conditions, the contraction coefficient  $\mu = \frac{B-B_s}{B}$  is only dependent on the input flow ratio  $\frac{Q_{yi}}{Q_{xi}}$  ( $Q_{xi}$  and  $Q_{yi}$  are the inlet discharges in  $x$  and  $y$  channels). For asymmetrical outlet conditions, a higher value of the ratio of the inlet flow rates  $\frac{Q_{yi}}{Q_{xi}}$  leads to a larger recirculation zone in the  $x$ -channel and

smaller recirculation zone in the  $y$ -channel. A larger exit weir height always leads to a smaller recirculation in both the  $x$ - and  $y$ -channels.

#### 2.2.4 Conclusion on hydraulic intersections

In this section, scientific research concerning hydraulic intersections at “local scale” has been reviewed. Several points can be raised:

- For three branch confluence flows: the separation zone downstream of a crossroad has been extensively studied both experimentally and numerically. 2D flow velocity fields could be used to quantify the dimensions of separation zone for different flow conditions. 3D experimental data provided by Weber et al. (2001) gives insight into the mechanism of the separation zone interacting with the main flow. 3D simulation appears to be an appropriate tool to provide 3D flow features of separation zone. The studies are mainly focused on flows configured with equal channel width without slope under steady state.
- For three branch bifurcation flow: the separation zone at bifurcation flow has been studied experimentally and numerically. The researches are mainly focused on subcritical flows. The studies are mainly focused on flows configured with equal channel width in subcritical flow regime without slope under steady state.
- For four branch intersections: few studies have been conducted on four branch intersections mainly on supercritical flows. The function of recirculation zone on flow patterns (water height and discharge distribution) still needs to be explored. The studies are mainly focused on flows with two inlets and two outlets in equal channel width under steady state, whereas no studies have been performed with one inlet and three outlets or one outlet and three inlets.

### 2.3 Hydrodynamic investigations at district/city scale

This section presents research works related to the study of hydrodynamic at the district/city scale explored using experimental or numerical approaches.

An experimental model of Kyoto city is constructed by Ishigaki et al. (2003) to study the interaction between surface flows and underground spaces like the subway network. The water height and velocity at different locations are measured. The measurements consist in water depth distribution over the whole domain and velocity around the breach. Results show that in the tested configurations, about 50% of total inflow discharge is flowing into the underground space.

Mignot et al. (2006) used 2D shallow water equations to simulate the severe October 1988 flood in the Richelieu urban locality of the French city of Nimes (see figure 2.11). Detailed description of the street network and of the cross-sections of the streets with sensitivity analysis of various topographical and numerical parameters have been conducted. Results show the ability of the 2D model for planning mitigation measures in a dense urban area after calibration. Assessment of the 2D models for flash flood simulation from local scale to field scale is conducted based on two experimental and two field datasets (Abderrezzak et al. (2009)). Sensitivity analysis of uncertainty sources on crossroad obstacles and sewer networks is studied by Paquier et al. (2015).

A model of Toce valley with idealized urban area has been constructed during the project IMPACT (Zech and Soares-Frazão (2007); Testa et al. (2007)). The urban area is made of cubic concrete blocks (aligned or staggered) to represent the buildings (see figure 2.12). The time-varied water depth forced by an inflow hydrograph is recorded at ten locations using probes into

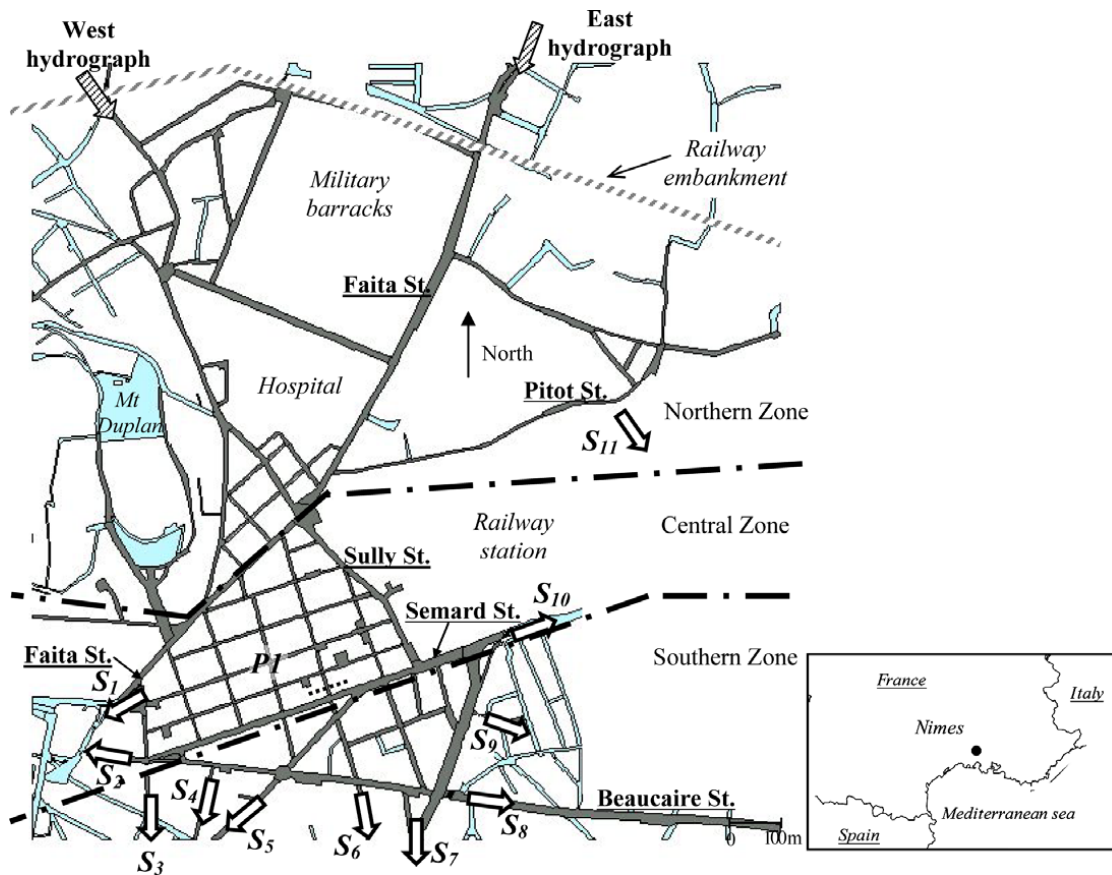


Figure 2.11: “Richelieu” area of the city of Nîmes with  $S_1$  to  $S_{11}$  the outlets from the area (Mignot et al. (2006))

and outside the urban district. Results show that the water depth pattern is sensitive to the local block patterns.

Sudden transient flow caused by a dam-break flowing in an idealised city is studied experimentally and numerically by Soares-Frazão and Zech (2008). The street orientation aligned or not with the approaching flow velocity direction is configured in order to investigate the effects on flow depth and velocity.

A model of the New Orleans 17th street is constructed to reproduce a levee breach which caused by the Hurricane Katrina (Sattar et al. (2008); Jia et al. (2010); Van Emelen et al. (2012)). The hydraulic model is at the scale 1:50 and conserves the Froude similarity. Various procedures are studied to close the breach and reduce inundation extent.

Moderate to extreme flooding are tested on the **ICube urban flood experimental rig** presented by Araud (2012); Finaud-Guyot et al. (2018) in steady state. It represents an idealized urban geometry at the scale 1/200 (as illustrated in figure 2.13). Inlet discharge is distributed based on the width of the street at each face (west and north face). Results show that the upstream Froude numbers are independent of the total discharge and in the range 0.2 to 0.35. At the downstream ends of the streets, the Froude numbers correspond to supercritical flows.

An analysis of the discharge distribution at the city scale is proposed. At the scale of the dis-



Figure 2.12: Upstream part of the physical model where the model city has been implemented (aligned city layout) (Testa et al. (2007))

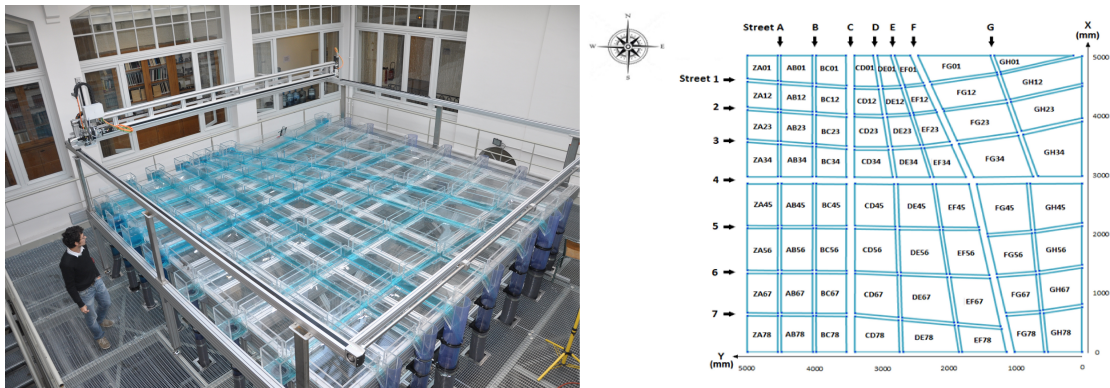


Figure 2.13: Schematic of experiment device for urban flood (Araud (2012))

trict the flow distribution is barely independent of the total discharge injected and the upstream discharge distribution at two inlet faces. Three types of streets are identified based on the outlet discharge evolution with the inlet discharge distribution at upstream between two inlet faces.

Arrault et al. (2016) used a 2D shallow water (SW) model to simulate the idealized city configuration constructed by Araud (2012) with/ without porosity like approach, where the influence of roughness parameter, grid size and turbulence model are tested. They show that roughness parameter has very little influence on the discharge partition and for turbulence model, except some local flow patterns.

A local experimental study consisting in a rainfall simulator, ground surface, and sewer pipe system is conducted by Noh et al. (2016). Based on the Froude similarity law, the scale is assumed to be 1/20 between the experimental rig and the real-world. An ensemble method is proposed to consider the interaction effect among a manhole, a sewer pipe and surface flow for urban flood modeling. Numerical results are compared with experimental data and parameters uncertainty to model output is analyzed. Results show that ensemble simulation using interaction models based on the weir and orifice formulas can reproduce experimental data with high accuracy both for steady and unsteady conditions. At the same time, the identifiability of model parameters is also detected.

As a conclusion, several experimental and numerical models have been proposed to simulate urban floods from transient dambreak due to a flash flood to quasi steady state for long-duration flood events. The models sizes range from several building to small European city with variable street widths and angles. However, detailed data of sufficient quality about real-world city flooding still lacks for numerical model improvement and validation.

## 2.4 Numerical models applied to urban floods

Numerical modeling is nowadays widely used in fluid mechanics and especially hydrodynamic modeling in the field of water management. Hydrodynamic modeling can be used in view to better understand and forecast urban flood flows to protect property and people's life. Flood inundation models have been reviewed by Teng et al. (2017) who list their advantages and limitations (see table 2.1).

Hydrodynamic models are mathematical models that attempt to replicate fluid motion by solving the continuity and momentum equations. Depending on their modeling paradigm and especially their spatial representation of a flooded domain for instance, models can be dimensionally grouped into 1D, 2D and 3D models:

- 1D shallow water models (SW) are very efficient in terms of computation, but their hypothesis do not allow to simulate complex flow features (2D, or even 3D) as discussed in the present work.
- 2D shallow water models (SW), widely used in urban flood modeling, are a good compromise between 1D and 3D (relatively limited computational resources but correct flow simulation accuracy).
- 3D simulation generally based on Reynolds averaged Navier-Stokes equations with a turbulent closure, are generally applied at the local scale like the crossroad scale (Bradbrook et al. (1998); Neary et al. (1999); Huang et al. (2002); Ramamurthy et al. (2007); Li and Zeng (2009, 2010)). 3D models are too expensive for systematic simulations at the district/city scale and hard to calibrate - wall function and turbulence model parameters. 3D models are not used in this thesis.

### 2.4.1 Review on 1D2D coupling

Integrated 1D2D models consisting in mixing 1D and 2D SW models when needed have been presented in the literature (Ghostine et al. (2015)). Using such a method, less computation points are required in simple flow zones leading to a reduced computation time and memory.

The 1D quasi 2D model as extensions of existing 1D models was first proposed by Cunge (1975). 1D shallow water equations are solved on the looped channel flow (using Preissmann scheme) and the domains are linked using a storage cell algorithm based on mass conservation. However, the ability of 1D-quasi 2D schemes in determining the front wave advance and recession process over a floodplain is always limited (Ghostine et al. (2015)). The 1D2D coupling between sewer and street networks is also conducted by different authors (Seyoum et al. (2011); Fan et al. (2017)).

For river flow modeling with lateral flood plains, Finaud-Guyot et al. (2010a, 2011) developed a new 1D2D coupling methodology. The mass and momentum exchanges between the 1D and 2D models are taken into account for momentum transfer whereas generally neglected.

Based on finite volume method, a new 1D2D coupling method is proposed by Bladé et al. (2012) between river and floodplain. The connection between 1D and 2D mesh is divided into:

Table 2.1: Some well known software/models that are capable of modeling flood inundation taken from Teng et al. (2017)

Developer	1D	2D	1D + 2D	3D	Simplified	Status	Note
Ambiental Australian National University & Geoscience Australia		Flowroute-i ANUGA Hydro				Commercial Open	<a href="https://anuga.anu.edu.au/">https://anuga.anu.edu.au/</a> source
BMT WBM	TUFLOW Classic 1D	TUFLOW Classic 2D TUFLOW GPU TUFLOW FV	TUFLOW Classic	TUFLOW FV		Commercial	
Cardiff University	FASTER	DIVAST DIVAST-TVD				Research	Is the foundation of ISIS 2D.
CH2M Hill (formerly Halcrow Group)	Flood Modeller Pro 1D solvers	Flood Modeller Pro 2D solvers	Flood Modeller Pro		Flood Modeller Pro 2D FAST solver	Commercial	Flood Modeller Pro is the successor of the ISIS suite.
CSIRO				SPM	TVD	Research	
DELTAES	SOBEK Suite	SOBEK Suite DELFT3D	SOBEK Suite	DELFT3D		Commercial	DELFT3D is open source <a href="http://oss.deltares.nl/web/delft3d/get-started">http://oss.deltares.nl/web/delft3d/get-started</a> .
DHI	MIKE11/MIKE HYDRO River	MIKE21	MIKE Flood	MIKE 3		Commercial	
Électricité de France	MASCARET	TELEMAC 2D		TELEMAC 3D		Open source	
HR-Wallingford Innovyze	InfoWorks RS	InfoWorks 2D	InfoWorks ICM		RFSM	Commercial	Commercial Use ISIS flow simulation engine.
JBA Nottingham University		JFLOW TRENT	TRENT			Commercial Research	
Svašek Hydraulics		FINEL 2D		FINEL 3D		Commercial	
Tokyo University		CaMa-Flood				Research	Global-scale model.
University of Bristol		LISFLOOD-FP	LISFLOOD-FP			Research	
University of California		BreZo				Research	
University of Exeter	SIPSON	UIM	UIM + SIPSON			Research	
US Army Corps of Engineers	HEC-RAS	HEC-RAS 2D				Free	<a href="http://www.hec.usace.army.mil/software/hec-ras">http://www.hec.usace.army.mil/software/hec-ras</a>
XP Solutions		XP2D	XP2D			Commercial	
ANSYS			XP2D	CFX, Fluent		Commercial	
Autodesk				Bifrost		Commercial	As part of Maya
Blender				Blender		Open source	<a href="https://www.blender.org">https://www.blender.org</a>
Chaos Group				PHEONIX FD		Commercial	
DPIT				Navié Effex		Commercial	
Kyushu University				Flip3D		Open source	<a href="https://code.google.com/p/flip3d/">https://code.google.com/p/flip3d/</a>
Maxon				Cinema 4D		Commercial	
Next Limit				RealFlow		Commercial	
Red Giant				Psunami		Commercial	
Side Effects Software				Houdini		Commercial	
TU München & ETH Zürich				Mantaflow		Open source	<a href="http://mantaflow.com">http://mantaflow.com</a>

connection in flow direction and lateral connections. For 1D2D integration, a flux-based method (FB) is proposed using numerical fluxes for connection between 1D and 2D. The results are compared with Source Term-based (STB) connection which no momentum transfer is considered. The ability of new flux-based method to predict velocity field is proved, compared to fine 2D results.

For supercritical flow simulation at four-branch crossroads, a comparison between a coupled 1D2D model and a fully 2D model is conducted by Ghostine et al. (2015). The 1D Saint-Venant equations are applied in the two upstream branches up to a distance of  $2B$  (channel width) from the junction to ensure that the flow is one-dimensional in this area. In the other areas, the 2D Saint-Venant equations are applied for the flow is two-dimensional. The coupling between 1D and 2D model is conducted using flux computation between the interface using Roe's solver. The averaged variables are used on 2D side for flux computation.

Except classical domain decomposition approach, a superposition approach for the coupling

between 1D and 2D models is proposed by Gejadze and Monnier (2007); Marin and Monnier (2009). The coupling term in 1D equations are source terms derived from the 3D Navier-Stokes equations. The coupling terms in the 2D equations are the incoming characteristics at open boundaries. The coupling algorithm is based on an optimal control process. The superposition and coupling between 1D and 2D equations with non-flat topographies is solved by Fernandez-Nieto et al. (2010).

#### 2.4.2 Review on shallow water (SW) models with macroscopic porosity approaches

Among the possibilities explored in the literature to tailor shallow water models for complex geometries such as those encountered in urban areas, macroscopic approaches involving a parametrisation of sub-grid features have been proposed. Such approaches adapted to an operational context. The idea is to solve SW equations on a grid adapted to data availability, while preserving the predictive capacity of such model. This can lead to a reduced computational cost. However an additional parameterisation is required at the sub-grid scale with the so-called porosity function. Depending on the complexity considered, the porosity function can be either isotropic (Defina (2000); Hervouet et al. (2000); Guinot and Soares-Frazão (2006); Lhomme (2006); Soares-Frazão et al. (2008); Guinot (2012a); Velickovic et al. (2017)) or anisotropic (Sanders et al. (2008); Guinot (2012a); Chen et al. (2012a,b); Lhomme (2006); Özgen et al. (2016a,b); Guinot et al. (2017a); Bruwier (2017); Bruwier et al. (2017)).

##### 2.4.2.1 Origin of the porosity-based approach

The concept of the porosity is a measure of the void (i.e. "empty") spaces in a material as a fraction of the volume of voids over the total volume thus comprised between 0 and 1 originally. The porosity is initially introduced in the porous media field (see for instance Bachmat and Bear (1986)). The approach substitutes, on a representative elementary volume (REV), the heterogeneous medium constituted by the fluid and the solid matrix by a fictitious homogeneous medium with parameters that have to be globally representative of the pore scale variables (see Figure 2.14).

##### 2.4.2.2 Isotropic porosity method

To our best knowledge, Defina (2000) is the first to propose to modify the shallow water equations with porosity (introduced as a "*h-dependent storativity coefficient*") to statistically account for partially wet and very irregular domain (such as bottom irregularity). Assuming a hydrostatic approximation, the three-dimensional Reynolds-averaged equations are first averaged over a representative elementary domain including porosity and then integrated over the depth. The proposed model is shown to significantly improve the hydraulic results in modeling wetting-drying problems.

Following that, Hervouet et al. (2000) modify the shallow water equations with time-varied porosity to represent a local density of buildings for urban flood modeling. In these modified equations the porosity accounts for the presence of buildings, structures, etc. that restrict the area available to water flow. The new set of equations are used to model various test cases and the gap between reference and numerical results is claimed to be due to the miss-fit of the porosity estimation.

Guinot and Soares-Frazão (2006); Lhomme (2006) present a detailed derivation of the shallow water equations with porosity for urban flood modeling using an isotropic porosity function and complementary head loss parametrisation to take into account the urban singularities effect.

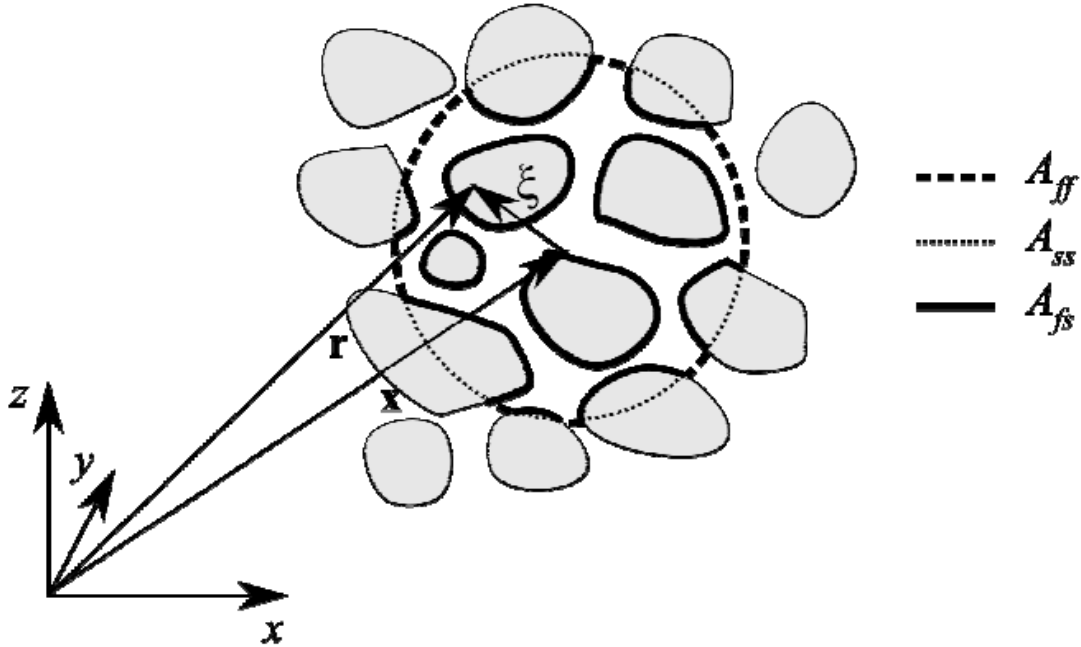


Figure 2.14: REV in a 3D porous medium and definition of bounding surfaces  $A_{ff}$  (surface between fluid and fluid),  $A_{fs}$  (surface between fluid and solid) and  $A_{ss}$  (surface between solid and solid) taken from Velickovic et al. (2012)

Guinot and Soares-Frazão (2006) use a unique parameter for the mass and momentum equations and propose the corresponding discretisation using a classical finite volume method involving a HLL-based Riemann solver modified to account the effect of porosity. Various analytical test cases with porosity are proposed and used to validate the proposed implementation. Comparison to experiments shown fairly good results. Lhomme (2006) introduces storage (respectively conveyance) isotropic porosity for the mass (respectively momentum) shallow water equations. Storage porosity induces an increase of the water depth due to the reduction of the plan area of the computational domain. The conveyance porosity corresponds to the reduction of the cross section available to the flow. A detailed analysis is proposed in Lhomme (2006) to characterize the singular head loss parameters proposed in Guinot and Soares-Frazão (2006); Lhomme (2006). Concerning the porosity, Lhomme (2006) considers, except in the continuous model, that the proposed porosity parameterisation is identical for all the different tested configurations of urban flooding. Soares-Frazão et al. (2008), using the same numerical model as Guinot and Soares-Frazão (2006); Lhomme (2006) to model experimental configurations representing the Italian Toce valley, highlight the interest of using the porosity for an accurate flow representation without detailed accounting of the urbanized area in the mesh.

Later, Guinot (2012a) proposes a multiple porosity shallow water model for macroscopic modeling of urban floods with flow considered as isotropic also called the “*dual porosity model for isotropic flow*”. The computational cells are indeed assumed to include building, mobile and stagnant water (see figure 2.15). This new model is assessed on various test cases showing a significant improvement of the numerical results compared to a classical simple porosity model and a significant reduction of the computational cost compared to a classical 2D model without

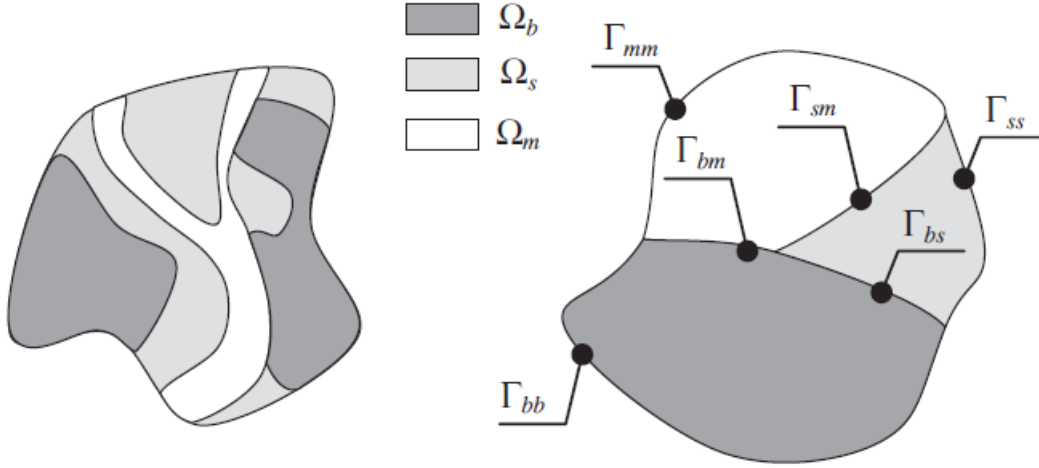


Figure 2.15: Left: Schematic urban geometry involving buildings ( $\Omega_b$ ), flow vein ( $\Omega_m$ ) and stagnant water ( $\Omega_s$ ). Right: Equivalent representation in a computational cell. Illustration from Guinot (2012a)

porosity. As highlighted by Sanders et al. (2008), the representativity of a representative elementary volume (theoretically required to define any porosity approach) is hard to obtain in a real-world urban flooding configuration. Guinot (2012a) provides a detailed discussion showing that porosity-based approaches in urban flood modeling defined at a smaller scale than the one required to define a representative elementary volume remains valid.

Velickovic et al. (2017) presents a steady-state experimental data-set of structured anisotropic urban layout. The single isotropic porosity model (presented by Guinot and Soares-Frazão (2006); Lhomme (2006); Soares-Frazão and Zech (2008)) is modified using a drag tensor to allow representing preferential flow despite the isotropic porosity. The drag tensor is calibrated using experimental data and is shown to allow reproducing satisfactorily either the preferential flow or the anisotropic configurations but not both.

### 2.4.2.3 Anisotropic porosity method

Sanders et al. (2008) proposed anisotropic porosity function in integral form as volume porosity (storage) and areal porosity (connectivity) as illustrated in figure 2.16. The volume porosity is defined to account for the storage effect of buildings, whereas areal porosity is used to calculate flux across the cell edges, which is anisotropic. Drag coefficient formulation is proposed for the calculation of source term on friction. The integral porosity (IP) model has been applied to several cases of urban flood modeling. Compared to the classical isotropic porosity model, the new integral porosity model allows for a better representation of preferential flow in anisotropic building configurations.

Guinot (2012a) also proposed a multiple porosity shallow water model for preferential flow. As highlighted on figure 2.17, such model involves several sub-domains with various characteristics:  $\Omega_b$ ,  $\Omega_s$  and  $\Omega_m$  defined as for the “*dual porosity model for isotropic flow*”,  $\Omega_{\{1,\dots,M\}}$  corresponding to  $M$  domains with mobile water for which the flow is oriented in a given predefined direction and  $\Omega_i$  corresponding to mobile water with no preferential direction connecting two anisotropic mobile water zones. Several test cases highlight the ability of this proposed model to accurately reproduce the flow characteristics without detailed accounting of the urbanized area in the mesh.

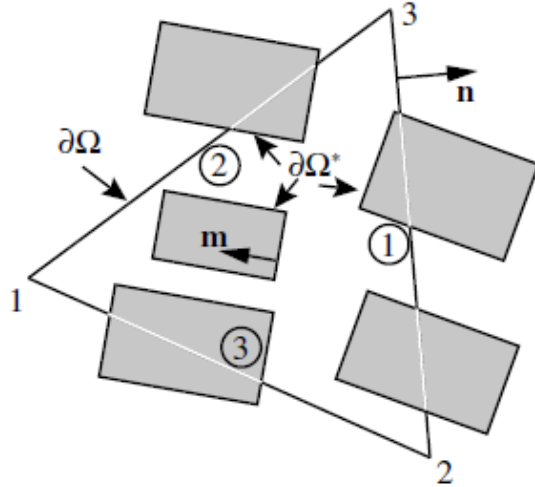


Figure 2.16: Schematic representation of the computational cell highlighting the non-isotropic conveyance porosity defined as the void portion of each edge. Illustration from Sanders et al. (2008)

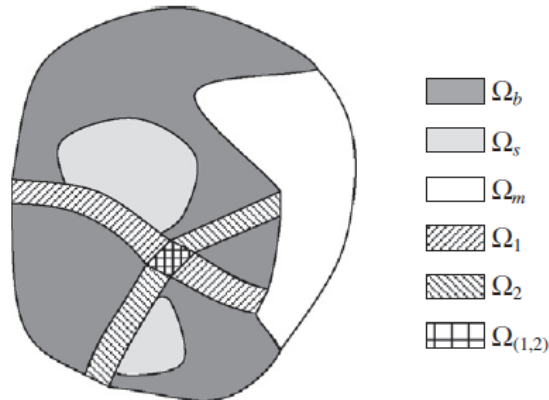


Figure 2.17: Multiple porosity model with preferential directions. Definition sketch for the isotropic and anisotropic flow regions.  $\Omega$ : region area. Subscript  $b$ : building,  $s$ : stagnant water,  $m$ : mobile water and 1 or 2: anisotropic water region. Illustration from Guinot (2012a)

Guinot (2012a) also highlights how the multiple porosity model is able to account for reduction of the momentum without head loss model just due to the flow exchanges between immobile and mobile water zones. Finally, a general comparison between differential and integral porosity model presents the interest of the two writings.

Chen et al. (2012a) present a sub-grid parametrisation using an anisotropic porosity for urban flood modeling based on a 2D Saint-Venant equations without inertial terms. A building coverage ratio and two conveyance reduction factors (similar to the storage and conveyance porosity defined by Lhomme (2006)) are computed to parameterise the hydrodynamic model from a fine grid coherent with a typical GIS digital elevation model. Chen et al. (2012b) propose an extension of the single layered approach (presented in Chen et al. (2012a)) in the so-called

“*multi-layered approach*”. Those methods allow to account the effect on the flow of sub-grid scale buildings.

Özgen et al. (2016a,b) generalize the IP model proposed by Sanders et al. (2008) with a depth-dependent porosity function. Mathematical description (Özgen et al. (2016a)) and numerical discretization (Özgen et al. (2016b)) for urban flood modeling are provided. The porosity terms are thus varying as the water depth evolves along the simulation time. Test cases highlights the relative inaccuracy of this method with important slope and the dependence of the results to the mesh.

In multiple porosity models (thus involving both storage and conveyance porosity), same definition of the velocity within and at the boundary of the computation appears to be ambiguous Guinot et al. (2017a). To cope with that Guinot et al. (2017a) introduces two velocity (defined respectively in the computational domain and its boundary) in the set of equations leading to the so-called “*Dual integral porosity model*”. The continuity equation, written between the cell and its boundary, introduces a sufficient closure equation to insure the solution unicity. The friction is taken into account using a depth-dependent tensor-based writing of the building drag model introduced in Sanders et al. (2008). Various test cases including real-world configurations highlight the improvement of the results obtained using the DIP model compared to the classical IP.

Bruwier (2017); Bruwier et al. (2017) introduce improvement for the integral porosity shallow water model for Cartesian grids. It is highlighted that due to the Cartesian grid, porosity in some computational cells could be very small and that the computational timestep has to be decreased accordingly to insure the CFL criterion. Such problem does not appear for unstructured grid as it is possible to define the mesh such as avoid too small porosity values. Bruwier et al. (2017) thus propose to suppress the cell with smallest porosity and to distribute the storage / conveyance porosity to one (or more) neighboring cell(s) and their corresponding edges. One can wonder what produces this algorithm if the smallest porosity cell is only surrounded by fully empty cells (with thus a porosity of 1). Would it leads to computational cells with a storage porosity bigger than 1? The classical definition of the conveyance porosity, applied to Cartesian grids, might lead to overestimation of this parameter (Chen et al. (2012a); Özgen et al. (2016b) cited by Bruwier et al. (2017)). Bruwier et al. (2017) thus propose a new method for computing the conveyance porosity that leads to results with a similar accuracy than using the classical conveyance porosity computation method but without requiring to calibrate complementary drag force term. Finally the numerical results using the anisotropic porosity shallow water model are compared using various parameter values.

#### 2.4.2.4 Comparison of the different porosity methods

Schubert and Sanders (2012) present the first field-scale application of the anisotropic IP method and offer insight into its practical utility. Four different methods to account for the effect of buildings on the flow are proposed: setting the limit of the building as impervious boundary conditions (BH), increasing the topography of the cell including building (BB), increasing the friction coefficient without modifying the topography (BR) or using porosity approach (BP). All those approaches are compared to data available (Baldwin Hills, CA urban dam break scenario). BR and BB methods are shown to be easy to implement. However, the first method fails to reproduce accurately the flow features close to buildings as they are not represented and the second one can leads to computationally expensive models due to refined mesh close to buildings. BH method allows for the same level of details than the BB method with coarser mesh but the model is difficult to prepare. Finally BP method is shown to be the best compromise between accuracy and computational cost.

Kim et al. (2015) studied the errors associated with porosity models applied in urban flood modeling. Three different types of errors are identified: “structural error” due to the limitations of the employed equations, “scale error” produced by relatively too coarse grid, and “porosity error” corresponding to inadequation between the porosity equations employed and modeled sub-grid scale obstructions. Porosity errors are shown to be greater than scale errors but less than structural errors. Isotropic porosity model compared to anisotropic models leads to bigger error on the computed water depth and velocity. The later being barely as accurate that the fine grid shallow water models.

Guinot (2017b) proposes a comparison of three types of porosity models: Single porosity model (SP), Integral porosity model (IP) and Dual Integral porosity model (DIP) against various periodic computational domains. The DIP model is shown to produce the most accurate results compared to both the SP and the IP model. However, all the tested porosity models are shown to reproduce the flux closure when the wave propagates in direction not aligned with the streets. The conveyance porosity thus appears to be insufficient and should be associated with a flow direction indicator. Finally, Guinot (2017b) details research direction both for improving the DIP model but also to design experiments able to validate the shallow water porosity model.

Guinot (2017c) presents a consistency analysis and a determination of the wave propagation properties of both the IP and DIP model. The sensitivity of the porosity models to the mesh is highlighted and criteria are proposed to reduce the mesh dependence.

### 2.4.3 Conclusion

In this section, numerical models on urban flood modeling have been reviewed, including integration between 1D and 2D models and sub-grid method to account for sub-grid features (buildings and blocks). 1D2D coupling methods reveal to be a good compromise between simple 1D and relatively costly 2D. Porosity models are a promising approach for urban flood modeling at rather large scale - e.g. city scale. Porosity functions are used to account for the influence of street/buildings on urban flood propagation, whereas its application to account for sub-scale flow features still needs to be studied.

## 2.5 Numerical model sensitivity analysis

### 2.5.1 Uncertainty analysis (UA) and sensitivity analysis (SA)

The goal of a numerical model is generally to predict the behavior of a (physical) system. The chosen and affordable complexity of a model depends on the modeling goals and the data availability. For a given model it is of prior interest to understand and quantify the links between its outputs and inputs. The uncertainty in model outputs may be related to different sources: data type and observation errors, model structural uncertainties, parametric uncertainties.

Therefore it is important to systematically assess the uncertainty associated with a model and its sensitivity to input parameters. Let us distinguish two definitions:

- Uncertainty quantification (UQ) is the forward propagation of uncertainty to predict the overall uncertainty in model outputs.
- Sensitivity analysis (SA) is the study of how the uncertainty in model output can be apportioned to different sources of uncertainty in model inputs (Saltelli et al. (2008); Pianosi et al. (2016)). Sensitivity analysis can be based on various techniques including the analysis of local gradients or of a whole region of a parameter space (cf. section 5.1.1).

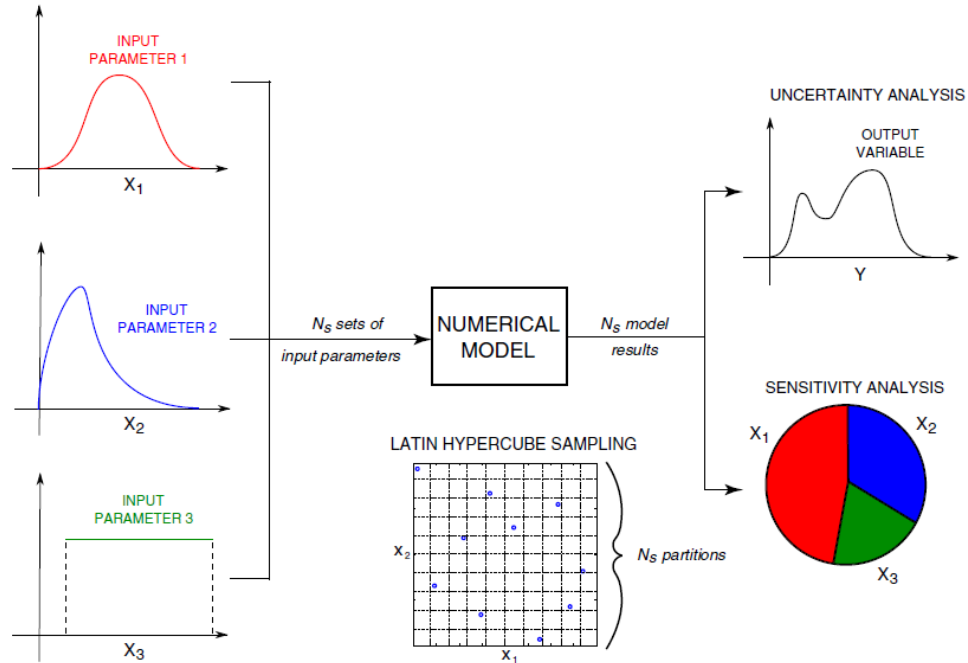


Figure 2.18: Schematic illustration of uncertainty quantification (UQ) and sensitivity analysis (SA) taken from Vitturi et al. (2016). Please note that  $N_s$  refers to the number of different input parameter sets (number of simulations performed), sampled here on a latin hypercube

Both methods are based on a sampling of model input parameter space. The result of multiple model evaluations on this sample of parameter sets can be represented in terms of probability distributions of the output values (UQ) or relative weights of the input parameters in explaining the variability of model output (SA) (cf. figure 2.18).

Sensitivity analysis methods can be classified based on their scope, applicability, and characteristics (Song et al. (2015)). A general workflow for the application of sensitivity analysis is presented in figure 2.19. The simplest and most common classifications are local SA and global SA. Local sensitivity analysis is focused on the effects of uncertain inputs around a point in parameter space (or base case), whereas global sensitivity analysis is focused more on the influences of uncertain inputs over the whole input space. Currently, various global sensitivity analysis techniques such as screening methods, regression analysis or variance-based method have been widely used to analyze hydrological models (Song et al. (2015)):

- One-at-a-time (OAT) method is changing one factor at a time, to see what effect this produces on the output. Such a sequential method is not recommended in the case of non linear models and potentially correlated parameters.
- Screening methods consist in identifying which input variables are contributing significantly to the model output uncertainty.

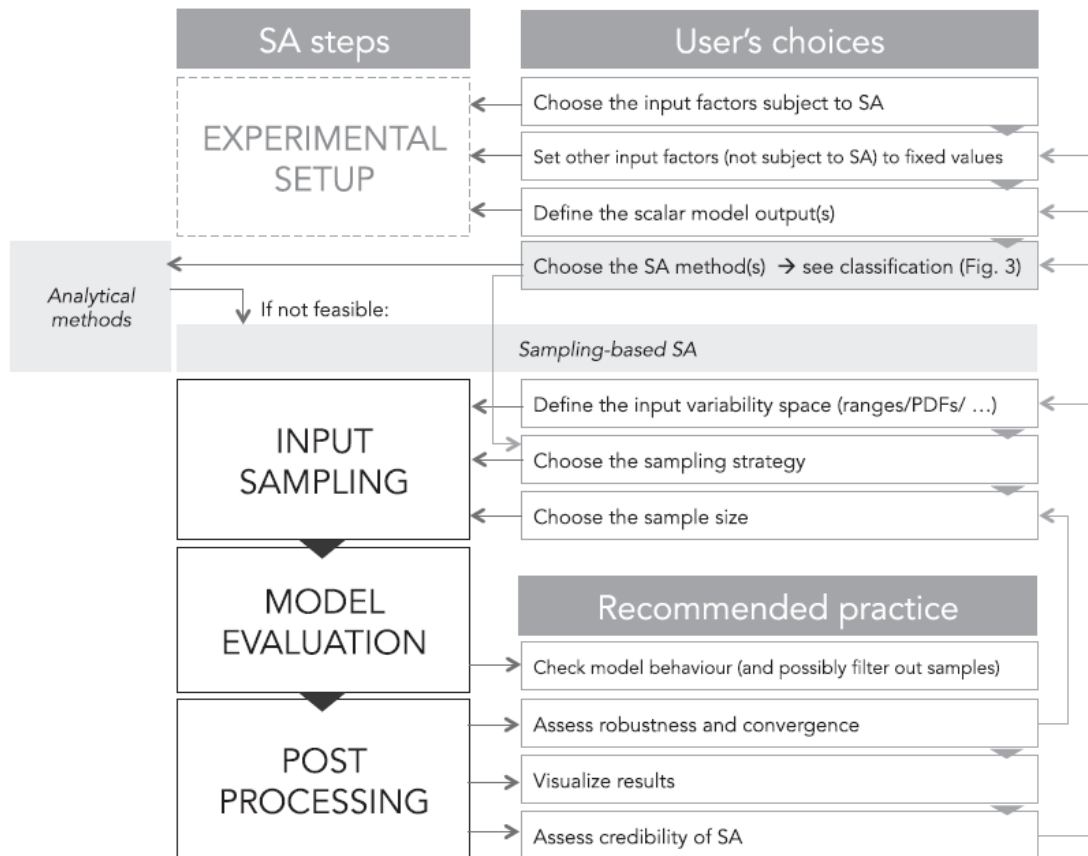


Figure 2.19: Workflow for the application of sensitivity analysis (SA), choices to be made and recommended practice for their revision made by Pianosi et al. (2016)

- Regression models consist in fitting a linear regression on the model response with respect to parameters and use standardized regression coefficients as direct measures of sensitivity.
- Variance-based methods are a class of probabilistic approaches which quantify the input and output uncertainties as probability distributions, and decompose the output variance into parts attributable to input variables and combinations of variables (Saltelli et al. (2008)).

A review of application of sensitivity analysis on environmental models has been provided by Pianosi et al. (2016), which summarizes and classifies the concepts and methods in sensitivity analysis (SA) and provides a general workflow (cf. figure 2.19).

### 2.5.2 Sensitivity analysis applied to shallow water models

Flood inundation maps are commonly generated with a 2D shallow water (SW) model consisting in depth averaged Navier-Stokes equations ( Hervouet (2007); Arrault et al. (2016); Monnier et al. (2016)) where uncertainty sources can be model structure and parameterization (e.g. basal friction), initial and boundary conditions (bathymetry and source terms). A full shallow water model including inertia terms may be required to capture small scale features and rapidly varying

flows over “rural” floodplains (Neal et al. (2012)), along with appropriate numerical methods for shock capture and wet dry front treatments (Monnier et al. (2016)). As a matter of facts, the interaction of high energy flows with obstacles triggers 3D flow processes such as crossroads junctions (Mignot et al. (2006)) - which for a realistic representation generally require to solve the Navier-Stokes equations in 3D. Consequently, flow resistance parameterization for a 2D SW model, which is an effective representation of 3D (turbulent) free surface flow structures, may depend on its scale for localized head losses in complex geometries (Guinot (2012a)) or parietal friction on smooth or macro roughness (Cassan et al. (2015, 2017)). Another boundary condition that is a well known source of uncertainty is inflow discharge especially in complex urban flood configurations - which can be provided by in situ measurements (involving rating curve uncertainty Delrieu et al. (2005); Paris et al. (2016); Savage et al. (2016)) or simulated by a hydro-meteorological chain involving meteorological model uncertainties (Vié et al. (2011)) and hydrological model uncertainties (Douinot et al. (2017)).

Flood simulation accuracy is not necessarily improved by increasing model complexity and resolution (Dottori et al. (2013)) but uncertainty sources may also vary (even interact) as the amount of data required to constrain the model. Sensitivity analysis, that assesses how the uncertainty in the output of a model can be apportioned to different sources of uncertainty in the model input (Saltelli et al. (2004)), has become a popular tool in environmental modeling (Pianosi et al. (2016)). SA is used in catchment hydrology to explore high dimensional parameter spaces, assess parameter identifiability and understand uncertainty sources (Hornberger and Spear (1981); Beven and Binley (1992); Pushpalatha et al. (2011); Garambois et al. (2013, 2015) among others). Temporal variations of distributed rainfall runoff and simplified hydraulic model parameters sensitivities are analyzed and ranked in the case of Mediterranean flash floods (Garambois et al. (2013)) or large scale conceptual model of the Amazon river (Emery et al. (2016)). Temporal sensitivities of simulated flood response highlight phases and locations of higher sensitivities to runoff production parameters and/or runoff routing depending on rainfall forcing variabilities and drainage network shape among other parameters.

Among the few SA studies in the field of river hydraulic modeling, Roux and Dartus (2008) propose a generalized sensitivity analysis of a 1D Saint Venant model with simplified geometry adapted to remote sensing and ungauged rivers, in the case of flood scenario on the Lèze River, France. The authors show the importance of downstream flow depth in controlling flood extent for a 1.5 km reach of a small river (around 100m bankfull width). Guinot and Cappelaere (2009a) propose local sensitivity equations for the 2D steady state SW equations without shocks and provide some guidelines for model calibration and validation. These sensitivity equations are also derived and implemented for 1D Saint Venant model (Delenne et al. (2011)). Local sensitivities derived with the adjoint method (2D SW DassFlow model), and involving a cost function, are presented in the case of a high resolution model of a flood on a 2km reach of the Lèze River (Monnier et al. (2016)). The authors find higher sensitivities of water depth to bathymetry and roughness downstream (subcritical regime) of the observation points in the floodplain and in the main channel, roughness sensitivities are higher in the main channel.

Recently variance based SA has been applied to 2D hydraulic models in flooding conditions (Abily et al. (2016); Savage et al. (2016)). Abily et al. (2016) present a spatial SA approach of a 2D SW model based on high resolution digital elevation model (DEM). Sensitivity maps of simulated water depth to uncertain parameters including topography are presented for the last 5km of the Var valley, France - November 1994 flood. For a 50km<sup>2</sup> rural floodplain in Sicily, Savage et al. (2016) highlight the sensitivity of simulated flood extent to inflow discharge during flood rising limb then the channel friction parameter during flood peak and the floodplain friction parameter during recession. First order sensitivity of both maximal water depth and flood extent to topography and model resolution is limited whereas interactions of those parameters

with others (hydrographs and roughness) increases at the end of the flood given their influence on floodplain flow pathways in this case. A methodology for quantifying the parametric uncertainty due to friction in urban flooding simulations is proposed by Bellos et al. (2017). Due to the fact that quantification of uncertainty in urban flood modeling is often computationally expensive they propose a method based on a model surrogate obtained with polynomial chaos expansion. They investigate the sensitivity due to roughness parameter.

Variance based methods will be applied to the various SW models used in this PhD.

## 2.6 Bibliography synthesis and scientific questions

From the bibliography synthesis above on urban flood modeling involving either classical or porosity approaches and local features on hydraulic intersections, or the few studies at the city scale, several scientific questions arise:

- Is it possible to propose an effective model for urban floods at a reduced complexity (coherent with operational costs) and computational cost?
  - Which modeling paradigm could be used?
  - Given a modeling paradigm which parameterization is affordable (with respect to calibration problems) and effective for describing main physical processes involved in urban floods?
- What would be the predictive capacity of such a simplified model compared to a reference hydrodynamic model and/or experimental datasets?
- What would be the sensitivity of such a simplified model output with respect to its inputs?

In the light of these questions, this thesis aims to develop a new effective model based on SW equations adapted to simulate the main operational features of urban flood flows at the local scale and the district scale. This work is based on ICube urban flood experimental rig presented above (see figure 2.13) and aims at studying flood flows in a real-like street network. A particular attention is paid to recirculation areas downstream of crossroads, their local effective modeling and their effect on the flow pattern at the district scale. This PhD work is based on the development of a new C code *Flood1D2D*. The next chapter presents the flow governing equations and their discretization.

## Chapter 3

# Material and methods

This PhD aims to propose a coupled and effective 1D2D approach adapted to simulate urban flood flows with a reasonable computational cost. Based on the conclusions of the bibliography study and observations made on ICube urban flood experimental rig, this new model aims at:

- taking advantage of the relative accuracy of a 2D shallow water model for describing the main aspects of flood flows patterns;
- taking advantage of low computational cost of 1D in streets, assuming that an accurate representation of velocity field in 2D in streets is already simplified with respect to the real physics and unnecessary for operation forecasts of water levels and discharge distribution in urban area.

This chapter presents the derivation of the 2D shallow water equations from 3D Navier-Stokes that are assumed to be valid in urban flood flows patterns. Then 2D shallow water equations with porosity (isotropic- and constant in time) are derived (cf. Guinot and Soares-Frazão (2006); Lhomme (2006); Finaud-Guyot (2009)) as they are implemented in *Flood1D2D* and validated in this PhD (cf. chapter 4). Finally a new numerical approach is introduced for coupling 1D-like shallow water model for streets and 2D shallow water model for crossroads with the help of a porosity-like parameter (cf. section 3.3). It will be shown in chapter 5 that such a model is able to simulate realistic discharge and water surface patterns, including water surface shape in flow veins contracted by 3D recirculations in streets downstream of some crossroads.

### 3.1 Derivation of the governing equations

#### 3.1.1 3D Navier-Stokes equations

The 3D Navier-Stokes equations are derived using a mass and momentum balance on a control volume.

##### 3.1.1.1 Derivation of the continuity equation

First of all, we consider a fixed control volume of volume  $V$  and surface  $S$  as in figure 3.1. A small area  $dS$  of the surface has a outward normal unit vector  $\vec{n}$ . Let us define the fluid velocity  $\vec{U}$ , and its density  $\rho$ . The infinitesimal mass flux  $q$  through this small area is:

$$q = \rho \vec{U} \cdot \vec{n} dS \tag{3.1}$$

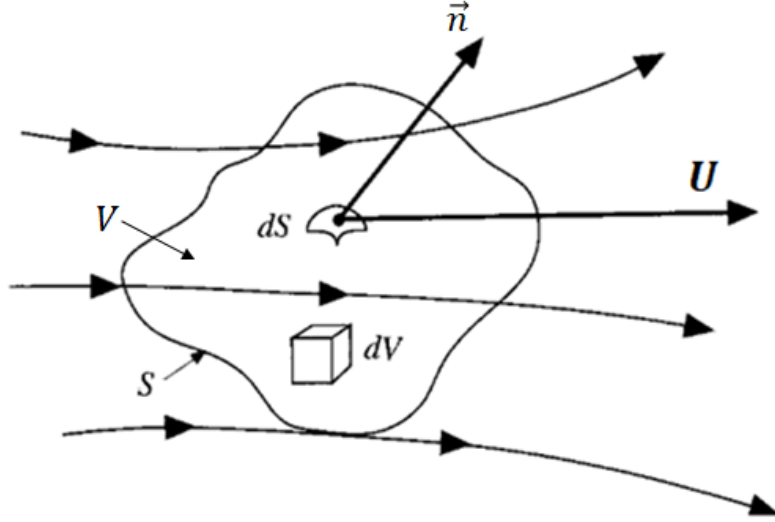


Figure 3.1: Finite control volume fixed in space from Anderson and Wendt (1995)

and the whole flux through the surface  $S$  is  $Q = \int_S \rho \vec{U} \cdot \vec{n} dS$ . According to the divergence theorem:

$$\begin{aligned} Q &= \int_S \rho \vec{U} \cdot \vec{n} dS \\ &= \int_V (\vec{\nabla} \cdot \rho \vec{U}) dV \end{aligned} \quad (3.2)$$

Knowing that the mass flux  $Q$  through the surface  $S$  is just equal to the mass change in the control volume  $\int_V \frac{\partial \rho}{\partial t} dV$ , which lead to:

$$\begin{aligned} \int_V (\vec{\nabla} \cdot \rho \vec{U}) dV &= - \int_V \frac{\partial \rho}{\partial t} dV \\ \int_V (\vec{\nabla} \cdot \rho \vec{U}) dV + \int_V \frac{\partial \rho}{\partial t} dV &= 0 \\ \int_V \left( \vec{\nabla} \cdot \rho \vec{U} + \frac{\partial \rho}{\partial t} \right) dV &= 0 \end{aligned} \quad (3.3)$$

Because the equation must hold for any small arbitrary control volume anywhere in the fluid, the previous integrand is also equal to zero. So we get the local form of continuity equation:

$$\vec{\nabla} \cdot (\rho \vec{U}) + \frac{\partial \rho}{\partial t} = 0 \quad (3.4)$$

Expansion of the second term yields:

$$\frac{\partial \rho}{\partial t} + \vec{U} \cdot \vec{\nabla} (\rho) + \rho \vec{\nabla} \cdot \vec{U} = 0 \quad (3.5)$$

Introducing the material derivative defined as  $\frac{D}{Dt} \equiv \frac{\partial}{\partial t} + \vec{U} \cdot \vec{\nabla}$  in equation (3.5) gives:

$$\frac{D\rho}{Dt} + \rho \vec{\nabla} \cdot \vec{U} = 0 \quad (3.6)$$

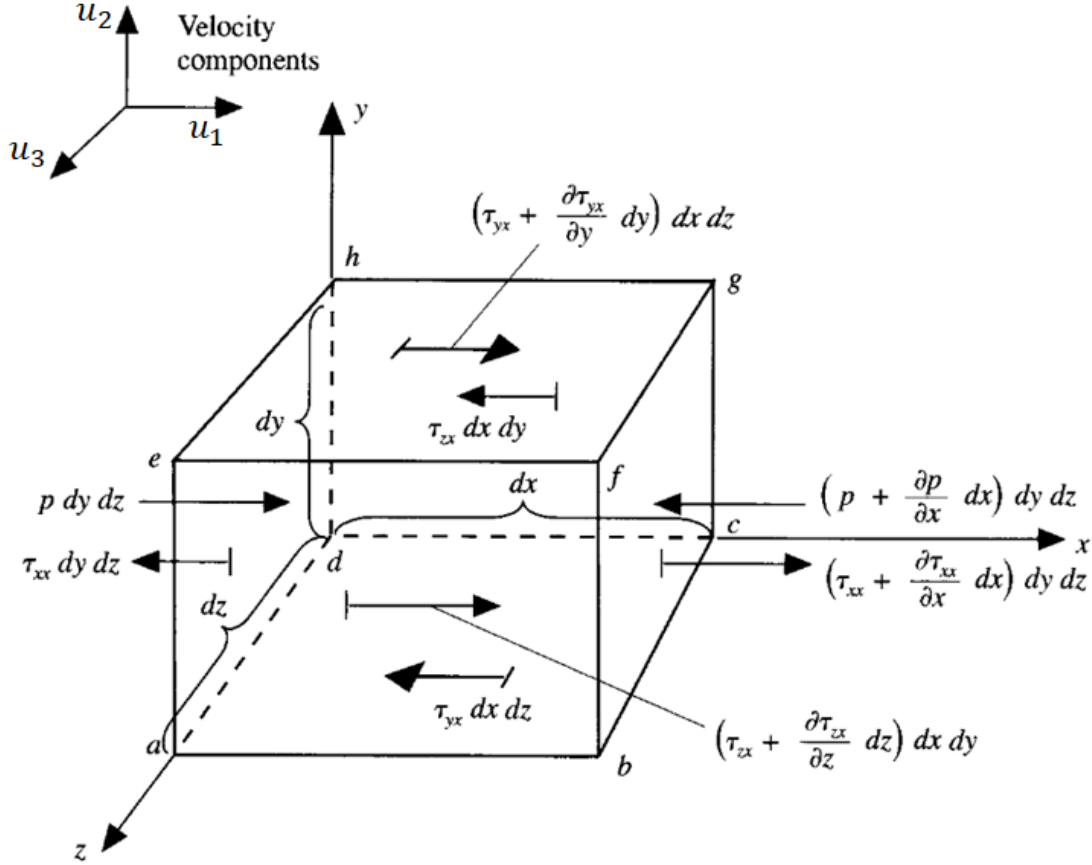


Figure 3.2: Infinitesimally small volume of moving fluid. Only the forces in the  $x$  direction are shown. Model used for the derivation of the  $x$  component of the momentum equation from Anderson and Wendt (1995)

### 3.1.1.2 Momentum equation

Let us consider an infinitesimal control volume  $V$  with a surface  $S$  in a Cartesian coordinates system (figure 3.2). For the sake of simplicity, the control volume is considered to be a cuboid. This is not contradictory with the control volume used in section 3.1.1.1 as equation (3.6) is valid for any infinitesimal control volume. The material derivative of the momentum in the control volume  $V$  is  $D(\rho \vec{U})/Dt$ . It is the sum of the accumulation of the momentum  $\rho \vec{U}$  per unit volume  $dV$  within the control volume  $V$  and of the change of the momentum across the control-surface boundaries:

$$\frac{D(\rho \vec{U})}{Dt} = \frac{\partial}{\partial t} \int_V \rho \vec{U} dV + \int_S \rho \vec{U} (\vec{U} \cdot \vec{n}) dS \quad (3.7)$$

This change in the momentum, according to Newton's second law, is equal to the sum of forces  $\sum \vec{F}$  applied to the fluid inside this control volume:

$$\frac{D(\rho \vec{U})}{Dt} = \sum \vec{F} \quad (3.8)$$

The forces acting on the fluid in the control volume in the  $\vec{x}_i$  direction  $(\sum \vec{F})_i$  are either the volumic integral of the body forces  $\rho f_i$  per unit volume or the surface integral of the surface forces  $n_j \sigma_{ij}$  per unit area giving:

$$\left(\sum \vec{F}\right)_i = \int_V \rho f_i dV + \int_S n_j \sigma_{ij} dS \quad (3.9)$$

where  $n_j$  is the  $j$ th component of the unit normal vector  $\vec{n}$  that points outward from the control volume and  $\sigma_{ij}$  is the component of stress tensor  $\boldsymbol{\sigma}$ . By substituting equations (3.7) and (3.9) into equation (3.8), we obtain the integral form of the momentum equation in the  $i$  direction, where  $\vec{U} = (u_1, u_2, u_3)$ :

$$\frac{\partial}{\partial t} \int_V \rho u_i dV + \int_S \rho u_i (\vec{U} \cdot \vec{n}) dS = \int_V \rho f_i dV + \int_S n_j \sigma_{ij} dS \quad (3.10)$$

Applying the divergence theorem to the surface integral terms of equation (3.10) yields:

$$\int_V \left[ \frac{\partial}{\partial t} (\rho u_i) + \vec{\nabla} \cdot (\rho u_i \vec{U}) - \rho f_i - \frac{\partial \sigma_{ij}}{\partial x_j} \right] dV = 0 \quad (3.11)$$

Because this integral holds for any arbitrary small control volume, the integrand must be zero, and therefore:

$$\frac{\partial}{\partial t} (\rho u_i) + \vec{\nabla} \cdot (\rho u_i \vec{U}) = \rho f_i + \frac{\partial \sigma_{ij}}{\partial x_j} \quad (3.12)$$

Expanding the left-hand side of equation (3.12) and using the continuity equation we get:

$$\begin{aligned} \frac{\partial}{\partial t} (\rho u_i) + \vec{\nabla} \cdot (\rho u_i \vec{U}) &= u_i \left( \frac{\partial \rho}{\partial t} + \vec{\nabla} \cdot \rho \vec{U} \right) + \rho \left[ \frac{\partial u_i}{\partial t} + \vec{U} \cdot \vec{\nabla} (u_i) \right] \\ &= \frac{D \rho u_i}{Dt} \end{aligned} \quad (3.13)$$

that is the fluid acceleration given by the material derivative of velocity  $\frac{D u_i}{Dt} = \frac{\partial u_i}{\partial t} + \vec{U} \cdot \vec{\nabla} (u_i)$ . So after substituting this expression of the acceleration term into equation (3.12), we find that the local form of the momentum equation is:

$$\frac{D \rho \vec{U}}{Dt} \cdot \vec{x}_i = \rho f_i + \frac{\partial \sigma_{ij}}{\partial x_j} \quad (3.14)$$

The stress tensor  $\boldsymbol{\sigma}$  is often decomposed into two terms of interest: the volumetric stress tensors which tends to change the volume of the body (contribution of pressure force) and the stress deviator tensor which determines body deformation and movement (composed of shear stresses). The stress tensor components as represented on an infinitesimal cuboid fluid element (figure 3.2) can be summarized in matrix form as follows:

$$\boldsymbol{\sigma} = - \begin{bmatrix} p & 0 & 0 \\ 0 & p & 0 \\ 0 & 0 & p \end{bmatrix} + \begin{bmatrix} \sigma_{11} + p & \tau_{12} & \tau_{13} \\ \tau_{21} & \sigma_{22} + p & \tau_{23} \\ \tau_{31} & \tau_{32} & \sigma_{33} + p \end{bmatrix} = -p \mathbf{I} + \boldsymbol{\tau} \quad (3.15)$$

*Remark:* the decomposition  $\boldsymbol{\sigma} = -p\mathbf{I} + \boldsymbol{\tau}$  leads to the general form of the Navier-Stokes equations where fluid properties must be specified for a practical use:

$$\frac{D\rho\vec{U}}{Dt} = \rho\vec{f} - \vec{\nabla}(p) + \vec{\nabla}\cdot\boldsymbol{\tau} \quad (3.16)$$

The moment equilibrium results in the symmetry of the stress vector components so that  $\sigma_{ij} = \sigma_{ji}$  and for a Newtonian fluid the stress is proportional to the rate of deformation:

$$\tau_{ij} = \tau_{ji} = \mu \left( \frac{\partial u_j}{\partial x_i} + \frac{\partial u_i}{\partial x_j} \right) \quad (3.17)$$

where  $\mu$  is the dynamic viscosity of the fluid. As proposed by Stokes in 1845 (Stokes (1845)):  $\tau_{ii} = \sigma_{ii} + p$  can be combined by:

$$\tau_{ii} = \lambda \left( \vec{\nabla} \cdot \vec{U} \right) + 2\mu \frac{\partial u_i}{\partial x_i} \quad (3.18)$$

where  $\lambda$  is the second viscosity coefficient. Stokes made the commonly used hypothesis that

$$\lambda = -\frac{2}{3}\mu \quad (3.19)$$

The stress components are related to the velocity field by

$$\sigma_{ij} = \left( -p - \frac{2}{3}\mu \frac{\partial u_k}{\partial x_k} \right) \delta_{ij} + \mu \left( \frac{\partial u_i}{\partial x_j} + \frac{\partial u_j}{\partial x_i} \right) \quad (3.20)$$

the dummy variable  $k$  is summed from 1 to 3, and  $\delta_{ij}$  is the Kronecker delta function defined by:

$$\delta_{ij} \equiv \begin{cases} 1 & i = j \\ 0 & i \neq j \end{cases} \quad (3.21)$$

Substituting equation (3.20) into equation (3.14), we obtain the Navier-Stokes equations:

$$\frac{D\rho u_i}{Dt} = \rho f_i - \frac{\partial}{\partial x_i} \left( p + \frac{2}{3}\mu \vec{\nabla} \cdot \vec{U} \right) + \frac{\partial}{\partial x_j} \mu \left( \frac{\partial u_i}{\partial x_j} + \frac{\partial u_j}{\partial x_i} \right) \quad (3.22)$$

Assuming a constant viscosity coefficient  $\mu$ , equation (3.22) becomes:

$$\begin{aligned} \frac{D\rho u_i}{Dt} &= \rho f_i - \frac{\partial p}{\partial x_i} - \mu \frac{\partial}{\partial x_i} \left( \frac{2}{3} \vec{\nabla} \cdot \vec{U} \right) + \mu \frac{\partial^2 u_i}{\partial x_j^2} + \mu \frac{\partial u_j^2}{\partial x_i \partial x_j} \\ &= \rho f_i - \frac{\partial p}{\partial x_i} + \mu \left[ \frac{\partial}{\partial x_i} \left( \frac{\partial u_j}{\partial x_j} - \frac{2}{3} \vec{\nabla} \cdot \vec{U} \right) + \frac{\partial^2 u_i}{\partial x_j^2} \right] \end{aligned} \quad (3.23)$$

For  $\vec{\nabla} \cdot \vec{U} = \frac{\partial u_i}{\partial x_i}$  and  $\frac{\partial^2 u_i}{\partial x_j^2} = \Delta u_i$ , equation (3.23) yields:

$$\frac{D\rho u_i}{Dt} = \rho f_i - \frac{\partial p}{\partial x_i} + \mu \left[ \frac{1}{3} \vec{\nabla} \left( \vec{\nabla} \cdot \vec{U} \right) + \Delta u_i \right] \quad (3.24)$$

Then, by assuming an incompressible fluid (for which continuity equation becomes  $\vec{\nabla} \cdot \vec{U} = 0$ ), and considering the gravity  $\vec{g}$  as the only body force we find that equation (3.24) reduces to:

$$\rho \left( \frac{\partial \vec{U}}{\partial t} + \vec{U} \cdot \nabla \vec{U} \right) = \rho \vec{g} - \vec{\nabla} p + \mu \Delta \vec{U} \quad (3.25)$$

### 3.1.1.3 Reynolds-averaged Navier-Stokes equations and Boussinesq approximation

The Navier-Stokes equations of motion, expressed in tensor notation for an incompressible Newtonian fluid write:

$$\vec{\nabla} \cdot \vec{U} = 0 \quad (3.26a)$$

$$\rho \left( \frac{\partial \vec{U}}{\partial t} + \vec{U} \cdot \nabla \vec{U} \right) = \rho \vec{g} - \vec{\nabla} p + \mu \Delta \vec{U} \quad (3.26b)$$

Next, assuming each instantaneous quantity can be split into time-averaged and fluctuating components, like  $u_i = \bar{u}_i + u'_i$ ,  $p = \bar{p} + p'$ , yields a time-averaged equation:

$$\frac{\partial \bar{u}_i}{\partial x_i} = 0 \quad (3.27a)$$

$$\frac{\partial \bar{u}_i}{\partial t} + \bar{u}_j \frac{\partial \bar{u}_i}{\partial x_j} + \overline{u'_j \frac{\partial u'_i}{\partial x_j}} = \bar{f}_i - \frac{1}{\rho} \frac{\partial \bar{p}}{\partial x_i} + \nu \frac{\partial^2 \bar{u}_i}{\partial x_j \partial x_j} \quad (3.27b)$$

Let's introduce  $\overline{S_{ij}}$  the mean strain-rate tensor, which is:

$$\overline{S_{ij}} = \frac{1}{2} \left( \frac{\partial \bar{u}_i}{\partial x_j} + \frac{\partial \bar{u}_j}{\partial x_i} \right) \quad (3.28)$$

The momentum equation can then be written as:

$$\frac{\partial \bar{u}_i}{\partial t} + \bar{u}_j \frac{\partial \bar{u}_i}{\partial x_j} = \bar{f}_i - \frac{1}{\rho} \frac{\partial \bar{p}}{\partial x_i} + \frac{\partial}{\partial x_j} \left( 2\nu \overline{S_{ij}} - \overline{u'_i u'_j} \right) \quad (3.29)$$

The quantity  $\overline{u'_i u'_j}$  is known as the Reynolds stress tensor which is symmetric ( $\overline{u'_i u'_j} = \overline{u'_j u'_i}$ ) and thus has only six components to determine.

The Boussinesq hypothesis is commonly used to relate the Reynolds stresses to the mean velocity gradients:

$$-\overline{u'_i u'_j} = 2\nu_t \overline{S_{ij}} - \frac{2}{3} k \delta_{ij} \quad (3.30)$$

where  $k = \frac{1}{2} \overline{u'_i u'_i}$  is the turbulent kinetic and  $\nu_t$  is the kinetic eddy viscosity assumed as an isotropic quantity. Equation (3.29) becomes:

$$\begin{aligned} \frac{\partial \bar{u}_i}{\partial t} + \bar{u}_j \frac{\partial \bar{u}_i}{\partial x_j} &= \bar{f}_i - \frac{1}{\rho} \frac{\partial \bar{p}}{\partial x_i} + \frac{\partial}{\partial x_j} [2\nu \overline{S_{ij}} + 2\nu_t \overline{S_{ij}} - \frac{2}{3} k \delta_{ij}] \\ &= \bar{f}_i - \frac{\partial}{\partial x_i} \left( \frac{\bar{p}}{\rho} + \frac{2}{3} k \right) + \frac{\partial}{\partial x_j} [2(\nu + \nu_t) \overline{S_{ij}}] \end{aligned} \quad (3.31)$$

Therefore, Reynolds-averaged Navier-Stokes equations using Boussinesq approximation become:

$$\frac{\partial \bar{u}_i}{\partial x_i} = 0 \quad (3.32a)$$

$$\frac{\partial \bar{u}_i}{\partial t} + \bar{u}_j \frac{\partial \bar{u}_i}{\partial x_j} = \bar{f}_i - \frac{\partial}{\partial x_i} \left( \frac{\bar{p}}{\rho} + \frac{2}{3} k \right) + \frac{\partial}{\partial x_j} [(\nu + \nu_t) \bar{d}] \quad (3.32b)$$

where  $\bar{d} = 2\overline{S_{ij}}$ .

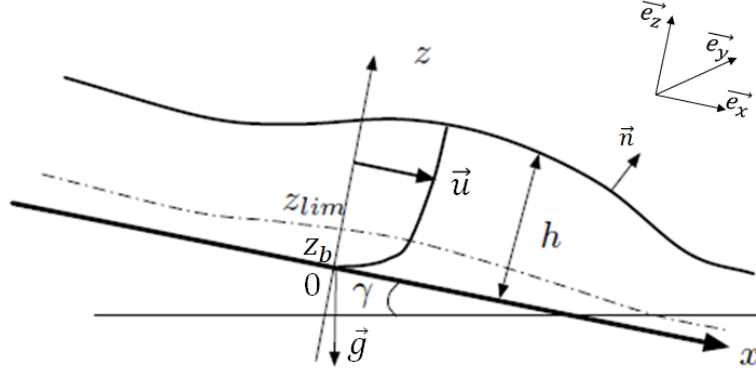


Figure 3.3: Tilted channel with a flat bottom adapted from Thual (2010)

### 3.1.2 Derivation of the 2D shallow water equations

Consider a free surface turbulent flow of an incompressible and Newtonian fluid. We start from the three-dimensional incompressible and turbulent Navier-Stokes equations (3.32).

#### 3.1.2.1 Three-dimensional Navier-Stokes equations

Let consider a three-dimensional flow on a tilted plane making an angle  $\gamma$  with the horizontal. By choosing the  $Ox$  axes to be parallel to the tilted plane, one denotes by  $(\vec{e}_x, \vec{e}_y, \vec{e}_z)$  the unit vectors of the  $(x, y, z)$  plane. The gravity vector then reads  $\vec{g} = g \sin \gamma \vec{e}_x - g \cos \gamma \vec{e}_z$ . One chooses the axes origin at the bottom so the  $z = 0$  corresponds to the tilted plane.

A turbulent flow of an incompressible and Newtonian fluid can be described by the incompressible Reynolds-averaged Navier-Stokes equations with turbulent viscosity (equation (3.32)). For the sake of simplicity, the notation  $u_i$ ,  $p$ ,  $S_{ij}$  and  $d$  are used for the Reynolds means rather than  $\overline{u_i}$ ,  $\overline{p}$ ,  $\overline{S_{ij}}$  and  $\overline{d}$ . One assumes that the turbulent viscosity  $\nu_t$  is constant in the fully turbulent flow for  $z \geq z_{lim}(x, y, t)$  where  $z_{lim}$  is the top of a bottom boundary layer (Southard (2006)). One supposes that  $\nu$  is negligible in front of  $\nu_t$  in the upper layer, which allows to write the Navier-Stokes equations under the form:

$$\vec{\nabla} \cdot \vec{U} = 0 \quad (3.33a)$$

$$\frac{\partial \vec{U}}{\partial t} + \vec{U} \cdot \nabla \vec{U} = \vec{g} - \frac{1}{\rho} \vec{\nabla} p_t + \nu_t \Delta \vec{U} \quad (3.33b)$$

where  $p_t = p + \frac{2}{3} \rho k$  is the ‘‘turbulent pressure’’ and  $\Delta u_i = \frac{\partial d}{\partial x_j} = \frac{\partial S_{ij}}{\partial x_j} = \frac{\partial}{\partial x_j} \left( \frac{\partial u_i}{\partial x_j} + \frac{\partial u_j}{\partial x_i} \right)$ .

#### 3.1.2.2 Flow boundary conditions

Assuming the free surface equation can read  $F(x, y, z, t) = z - h(x, y, t) = 0$  which excludes deformations of the breaking type (Thual (2010)). The normal  $\vec{n} = \vec{\nabla} F / \|\vec{\nabla} F\|$  to the surface is proportional to the vector  $\vec{\nabla} F = \frac{\partial F}{\partial x} \vec{e}_x + \frac{\partial F}{\partial y} \vec{e}_y + \frac{\partial F}{\partial z} \vec{e}_z$ . The kinematic boundary condition  $\frac{dF}{dt} = 0$  then reads:

$$\frac{\partial h}{\partial t} + u_1 \frac{\partial h}{\partial x} + u_2 \frac{\partial h}{\partial y} = u_3 \quad \text{for } z = h(x, y, t) \quad (3.34)$$

The dynamic boundary condition on the free surface expresses the continuity of the surface forces. If one assumes that the liquid (water) is in contact with a perfect fluid (air) of constant pressure  $p_a$ , it reads:

$$\boldsymbol{\sigma}_t \cdot \vec{n} = -p_a \cdot \vec{n} \quad \text{for } z = h(x, y, t) \quad (3.35)$$

where  $\boldsymbol{\sigma}_t(x, y, z, t)$  is the “turbulent stress tensor”.

$$\boldsymbol{\sigma}_t = -p_t \mathbf{I} + 2\rho\nu_t \mathbf{d}, \quad \text{with } \mathbf{d}(x, y, z, t) = 2\overline{S_{ij}} \quad (3.36)$$

The settlement of the boundary conditions at  $z = z_{lim}$  have to match with the bottom boundary layer. A very simple model consists in considering that  $z_{lim}$  is very small and to impose the boundary conditions such as:

$$u_3 = 0 \quad \text{and} \quad \vec{e}_x \cdot \boldsymbol{\sigma}_t \cdot \vec{e}_z = \tau_x^* \quad \text{for } z = 0, \quad (3.37a)$$

$$\vec{e}_y \cdot \boldsymbol{\sigma}_t \cdot \vec{e}_z = \tau_y^* \quad \text{for } z = 0, \quad (3.37b)$$

where  $\tau^*$  is the bottom shear stress applied by the fluid on the wall. The stress  $\tau^*$  can then be modeled as a function of the velocity, of the height as well and other parameters such as the molecular viscosity  $\nu$  of the fluid or the characteristic height  $k_s$  of the bottom roughness.

### 3.1.2.3 Derivation of the Saint-Venant equations

The Saint-Venant equations are obtained by integrating in the vertical direction the turbulent Navier-Stokes equations, assuming that the depth is small in front of the variation scale of the phenomena in the direction of the flow (Guinot (2012b)). The following sets of hypothesis can be found in Guinot (2012b) and Thual (2010):

- The shallow water approximations apply so that vertical acceleration is negligible, resulting in a vertical pressure distribution that is hydrostatic;
- The channel bed is stable, so that the bed elevation do not change with time;
- The water is assumed to be incompressible in the range of ordinary pressure and water levels. The density is constant;
- The flow is fully turbulent. The head loss due to bottom friction is proportional to the square of the velocity;
- The diffusion of momentum due to turbulence and viscosity, the Coriolis effect and shear stress due to the wind are neglected.

Neglecting the turbulence effect,  $k = 0$  and thus  $p_t = p + \frac{2}{3}\rho k = p$ . Since the pressure profile is hydrostatic,  $p_t$  writes:

$$p_t(x, y, z, t) = p_a - \rho g \cos \gamma [z - h(x, y, t)] \quad (3.38)$$

The remaining boundary conditions read:

$$\frac{\partial h}{\partial t} + u_1 \frac{\partial h}{\partial x} + u_2 \frac{\partial h}{\partial y} = u_3 \quad \text{and} \quad \frac{\partial u_1}{\partial z} = 0 \quad \text{for} \quad z = h \quad (3.39a)$$

$$w = 0, \quad \rho \nu_t \frac{\partial u_1}{\partial z} = \tau_x^* \quad \text{and} \quad \rho \nu_t \frac{\partial u_2}{\partial z} = \tau_y^* \quad \text{for} \quad z = 0 \quad (3.39b)$$

One defines the fluid layer longitudinal velocity  $u(x, y, t) = \frac{1}{h(x, y, t)} \int_0^{h(x, y, t)} u_1(x, y, t) dz$  and  $v(x, y, t) = \frac{1}{h(x, y, t)} \int_0^{h(x, y, t)} u_2(x, y, t) dz$ .

The integration along  $\vec{e}_y$  of the continuity equation (3.33a) leads to:

$$\int_0^h \frac{\partial u_1}{\partial x} dz + \int_0^h \frac{\partial u_2}{\partial y} dz + \int_0^h \frac{\partial u_3}{\partial z} dz = 0 \quad (3.40)$$

Using Leibniz's integration rule, equation (3.40) becomes:

$$\frac{\partial}{\partial x} \int_0^h u_1 dz + \frac{\partial}{\partial y} \int_0^h u_2 dz - u_{1,h} \frac{\partial h}{\partial x} - u_{2,h} \frac{\partial h}{\partial y} + u_{3,h} - u_3(x, y, 0, t) = 0 \quad (3.41)$$

Using the boundary condition equation (3.39) to eliminate last terms  $u_3(x, y, 0, t) = 0$  and  $\frac{\partial h}{\partial t} = -u_{1,h} \frac{\partial h}{\partial x} - u_{2,h} \frac{\partial h}{\partial y} + u_{3,h}$ , equation (3.41) becomes:

$$\frac{\partial}{\partial x} \int_0^h u_1 dz + \frac{\partial}{\partial y} \int_0^h u_2 dz + \frac{\partial h}{\partial t} = 0 \quad (3.42)$$

Using the definition of fluid layer longitudinal velocity  $u(x, y, t)$ ,  $v(x, y, t)$ , we get:

$$\frac{\partial}{\partial x} (hu) + \frac{\partial}{\partial y} (hv) + \frac{\partial h}{\partial t} = 0 \quad (3.43)$$

Substituting equation (3.38) into the momentum equations (3.33b) in  $x$  and  $y$  direction, we get:

$$\frac{\partial u_1}{\partial t} + u_1 \frac{\partial u_1}{\partial x} + u_2 \frac{\partial u_1}{\partial y} + u_3 \frac{\partial u_1}{\partial z} = -g \cos \gamma_x \frac{\partial h}{\partial x} + g \sin \gamma_x + \nu_t \frac{\partial^2 u_1}{\partial z^2} \quad (3.44a)$$

$$\frac{\partial u_2}{\partial t} + u_1 \frac{\partial u_2}{\partial x} + u_2 \frac{\partial u_2}{\partial y} + u_3 \frac{\partial u_2}{\partial z} = -g \cos \gamma_y \frac{\partial h}{\partial y} + g \sin \gamma_y + \nu_t \frac{\partial^2 u_2}{\partial z^2} \quad (3.44b)$$

By using the continuity equation (3.33a) in the momentum equations (3.44a) and (3.44b), one obtains:

$$\frac{\partial u_1}{\partial t} + \frac{\partial u_1^2}{\partial x} + \frac{\partial u_1 u_2}{\partial y} + \frac{\partial u_1 u_3}{\partial z} = -g \cos \gamma_x \frac{\partial h}{\partial x} + g \sin \gamma_x + \nu_t \frac{\partial^2 u_1}{\partial z^2} \quad (3.45a)$$

$$\frac{\partial u_2}{\partial t} + \frac{\partial u_1 u_2}{\partial x} + \frac{\partial u_2^2}{\partial y} + \frac{\partial u_2 u_3}{\partial z} = -g \cos \gamma_y \frac{\partial h}{\partial y} + g \sin \gamma_y + \nu_t \frac{\partial^2 u_2}{\partial z^2} \quad (3.45b)$$

Integrating momentum equations (3.45) along the direction  $\vec{e}_z$ , and using the Leibnitz formula, one then obtains:

$$\frac{\partial}{\partial t} \int_0^h u_1 dz - u_1 \frac{\partial h}{\partial t} \Big|_{z=h} + \frac{\partial}{\partial x} \int_0^h u_1^2 dz - u_1^2 \frac{\partial h}{\partial x} \Big|_{z=h} + \frac{\partial}{\partial y} \int_0^h u_1 u_2 dz - u_1 u_2 \frac{\partial h}{\partial y} \Big|_{z=h} + [u_1 u_3]_{z=0}^{z=h} =$$

$$-gh \cos \gamma_x \frac{\partial h}{\partial x} + gh \sin \gamma_x + \nu_t \left[ \frac{\partial u_1}{\partial z} \right]_{z=0}^{z=h} \quad (3.46a)$$

$$\begin{aligned} \frac{\partial}{\partial t} \int_0^h u_2 dz - u_2 \frac{\partial h}{\partial t} \Big|_{z=h} + \frac{\partial}{\partial x} \int_0^h u_1 u_2 dz - u_1 u_2 \frac{\partial h}{\partial x} \Big|_{z=h} + \frac{\partial}{\partial y} \int_0^h u_2^2 dz - u_2^2 \frac{\partial h}{\partial y} \Big|_{z=h} + [u_2 u_3]_{z=0}^{z=h} = \\ -gh \cos \gamma_y \frac{\partial h}{\partial y} + gh \sin \gamma_y + \nu_t \left[ \frac{\partial u_2}{\partial z} \right]_{z=0}^{z=h} \end{aligned} \quad (3.46b)$$

By using the boundary conditions, being  $\rho \nu_t \frac{\partial u_1}{\partial z} = \tau_x^*$ ,  $\rho \nu_t \frac{\partial u_2}{\partial z} = \tau_y^*$  for  $z = 0$ , and the definition of  $u$ , one obtains:

$$\frac{\partial u h}{\partial t} + \frac{\partial}{\partial x} \int_0^h u_1^2 dz + \frac{\partial}{\partial y} \int_0^h u_1 u_2 dz + gh \cos \gamma_x \frac{\partial h}{\partial x} = gh \sin \gamma_x - \frac{\tau_x^*}{\rho} \quad (3.47a)$$

$$\frac{\partial v h}{\partial t} + \frac{\partial}{\partial x} \int_0^h u_1 u_2 dz + \frac{\partial}{\partial y} \int_0^h u_2^2 dz + gh \cos \gamma_y \frac{\partial h}{\partial y} = gh \sin \gamma_y - \frac{\tau_y^*}{\rho} \quad (3.47b)$$

One seeks to obtain a model that only involves the  $u(x, y, t)$ ,  $v(x, y, t)$  and  $h(x, y, t)$  fields. Thus it only remains to express terms like  $\frac{\partial}{\partial x} \int_0^h u_1^2 dz$  and  $\tau_x^*$  as functions of these fields. A first modeling consists in writing, through a dimensional analysis, that

$$\begin{aligned} \int_0^h u_1^2 dz &= \alpha u^2 h \\ \int_0^h u_1 u_2 dz &= \alpha u v h \\ \int_0^h u_2^2 dz &= \alpha v^2 h \end{aligned} \quad (3.48)$$

Since the flow is turbulent,  $u_1(z)$  and  $u_2(z)$  are nearly constant along the depth and one can assume  $\alpha = 1$ .

For the modeling of the bottom shear  $\tau^*$ , one defines the dimensionless quantity  $C_f(h, u, v)$  by the dimensional relation:

$$\tau_x^* = \frac{1}{2} C_f(h, u, v) \rho u \sqrt{u^2 + v^2} \quad (3.49a)$$

$$\tau_y^* = \frac{1}{2} C_f(h, u, v) \rho v \sqrt{u^2 + v^2} \quad (3.49b)$$

The Chezy coefficient  $C_f$  in open channel hydraulics is often expressed with the Manning-Strickler formula:

$$C_f(h) = \frac{2g}{K^2 h^{1/3}} \quad (3.50)$$

where  $K$  is the ‘‘Strickler coefficient’’ ( $\text{m}^{1/3} \cdot \text{s}^{-1}$ ).

Eventually, the Saint-Venant equations read:

$$\frac{\partial h}{\partial t} + u \frac{\partial h}{\partial x} + v \frac{\partial h}{\partial y} = -h \left( \frac{\partial u}{\partial x} + \frac{\partial v}{\partial y} \right) \quad (3.51a)$$

$$\frac{\partial u}{\partial t} + u \frac{\partial u}{\partial x} + v \frac{\partial u}{\partial y} + g \cos \gamma_x \frac{\partial h}{\partial x} = g \left( \sin \gamma_x - \frac{u \sqrt{u^2 + v^2}}{K_x^2 h^{4/3}} \right) \quad (3.51b)$$

$$\frac{\partial v}{\partial t} + u \frac{\partial v}{\partial x} + v \frac{\partial v}{\partial y} + g \cos \gamma_y \frac{\partial h}{\partial y} = g \left( \sin \gamma_y - \frac{v\sqrt{u^2 + v^2}}{K_y^2 h^{4/3}} \right) \quad (3.51c)$$

where  $K_x = K_y = K$  in all the following configurations. In equation (3.51),  $g \cos \gamma_x \frac{\partial h}{\partial x}$  and  $g \cos \gamma_y \frac{\partial h}{\partial y}$  represent the pressure gradient,  $g \sin \gamma_x$  and  $g \sin \gamma_y$  the projection of the gravity in the  $x$  and  $y$  direction.

For the continuity equation (3.51a), it can be rewritten as:

$$\frac{\partial h}{\partial t} + \frac{\partial hu}{\partial x} + \frac{\partial hv}{\partial y} = 0 \quad (3.52)$$

For momentum equation (3.51b) in  $x$  direction, it can be rewritten as:

$$\frac{\partial hu}{\partial t} + \frac{\partial hu^2}{\partial x} + \frac{\partial huv}{\partial y} - u \left( \frac{\partial h}{\partial t} + \frac{\partial hu}{\partial x} + \frac{\partial hv}{\partial y} \right) + gh \cos \gamma_x \frac{\partial h}{\partial x} = gh \left( \sin \gamma_x - \frac{u\sqrt{u^2 + v^2}}{K_x^2 h^{4/3}} \right) \quad (3.53)$$

Using continuity equation (3.52) and setting  $\gamma_x \rightarrow 0$  ( $\cos \gamma_x \rightarrow 1$  and  $\sin \gamma_x = \tan \gamma_x = -\frac{\partial z_b}{\partial x}$ ), equation (3.53) can be rewritten as:

$$\begin{aligned} \frac{\partial hu}{\partial t} + \frac{\partial hu^2}{\partial x} + \frac{\partial huv}{\partial y} + \frac{\partial}{\partial x} \left( \frac{1}{2} gh^2 \right) &= gh \left( -\frac{\partial z_b}{\partial x} - \frac{u\sqrt{u^2 + v^2}}{K_x^2 h^{4/3}} \right) \\ \frac{\partial hu}{\partial t} + \frac{\partial}{\partial x} \left( hu^2 + \frac{1}{2} gh^2 \right) + \frac{\partial huv}{\partial y} &= gh (S_{0,x} - S_{f,x}) \end{aligned} \quad (3.54)$$

where  $S_{0,x} = -\frac{\partial z_b}{\partial x}$  and  $S_{f,x} = \frac{u\sqrt{u^2 + v^2}}{K_x^2 h^{4/3}}$ .

For momentum equation in  $y$  direction a similar form is obtained:

$$\frac{\partial hv}{\partial t} + \frac{\partial}{\partial x} (huv) + \frac{\partial}{\partial y} \left( hv^2 + \frac{1}{2} gh^2 \right) = gh (S_{0,y} - S_{f,y}) \quad (3.55)$$

where  $S_{0,y} = -\frac{\partial z_b}{\partial y}$  and  $S_{f,y} = \frac{v\sqrt{u^2 + v^2}}{K_y^2 h^{4/3}}$ .

The vector formulation the equations are written in conservative form as:

$$\frac{\partial \mathbf{U}}{\partial t} + \frac{\partial \mathbf{F}}{\partial x} + \frac{\partial \mathbf{G}}{\partial y} = \mathbf{S} \quad (3.56)$$

$$\mathbf{U} = \begin{bmatrix} h \\ q \\ r \end{bmatrix}, \quad \mathbf{F} = \begin{bmatrix} q \\ \frac{q^2}{h} + gh^2/2 \\ \frac{qr}{h} \end{bmatrix}, \quad \mathbf{G} = \begin{bmatrix} r \\ \frac{qr}{h} \\ \frac{r^2}{h} + gh^2/2 \end{bmatrix}, \quad \mathbf{S} = \begin{bmatrix} 0 \\ gh (S_{0,x} - S_{f,x}) \\ gh (S_{0,y} - S_{f,y}) \end{bmatrix}$$

where the unit discharge component  $q = hu$  and  $r = hv$ .

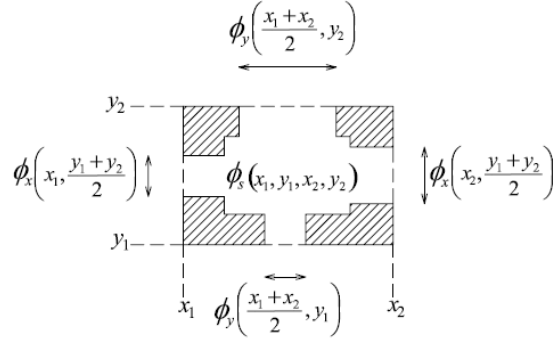


Figure 3.4: Scheme of control volume with different representation of porosity (Lhomme (2006))

### 3.1.3 2D shallow water equations with isotropic and constant porosity

#### 3.1.3.1 Introduction of general porosity function

Various formulations of shallow water models with porosity used for describing subgrid-scale geometrical features have been proposed in the literature (cf. section 2.4.2).

The most common definition of porosity is a volumetric porosity  $\phi$ , that is a fraction of a control volume occupied by voids. This fraction can itself be splitted into two parts: a storage porosity  $\phi_s$  and an anisotropic conveyance porosity formed by  $\phi_x$  and  $\phi_y$  along the two directions of the plane (Lhomme (2006)) (see figure 3.4). The storage porosity can be defined as the fraction of the plan view area available to the flow. On the other hand, the conveyance porosity is the fraction of the cross section available to the flow, which is directionally dependent on the plane orientation.

In this section, only differential formulation using isotropic and constant porosity is derived following Guinot and Soares-Frazão (2006); Lhomme (2006); Lhomme and Guinot (2007) since it is implemented in the C/C++ code: *Flood1D2D*. Such parameterization is either used to account for the impact of sub-grid scale features: geometrical obstruction or flow features such as recirculations.

#### 3.1.3.2 Derivation of shallow water equations with isotropic porosity in differential formulation (Guinot and Soares-Frazão (2006))

The equations are derived by calculating a mass and momentum balance over a rectangular infinitesimal volume  $d\Omega$  of horizontal and vertical dimensions  $\delta x$  and  $\delta y$  as illustrated in figure 3.5. The derivation of SW equations with a constant isotropic porosity  $\phi$  follows a similar procedure as 3D Navier-Stokes equations proposed in section 3.1.1.

**The continuity equation** The volume  $\Omega(t)$  of water contained in the control volume is given by:

$$\Omega(t) = \int_{y_0}^{y_0+\delta y} \int_{x_0}^{x_0+\delta x} \phi(x, y) h(x, y, t) dx dy \quad (3.57)$$

where  $(x_0, y_0)$  are the coordinates of the lower left corner of the control volume presented in figure 3.5. The volumic fluxes  $F_{V,\{N,W,E,S\}}$  (where subscripts  $N,W,E,S$  stands respectively for

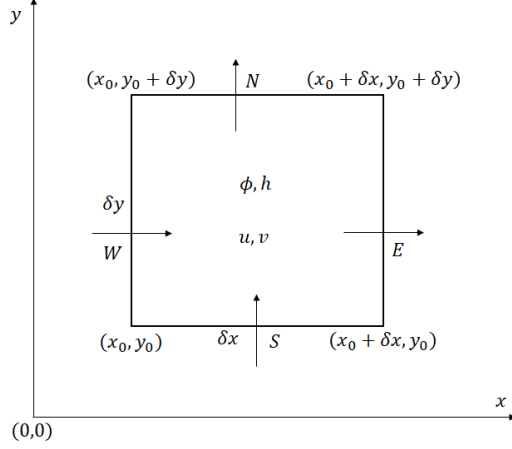


Figure 3.5: Schematic of control volume  $d\Omega$

north, west, east and south face) across the edges are respectively given by:

$$\begin{aligned} F_{V,W} &= \int_{y_0}^{y_0+\delta y} \phi(x_0, y) h(x_0, y) u(x_0, y) dy \\ &= \int_{y_0}^{y_0+\delta y} (\phi h u)(x_0, y) dy \end{aligned} \quad (3.58a)$$

$$F_{V,E} = \int_{y_0}^{y_0+\delta y} (\phi h u)(x_0 + \delta x, y) dy \quad (3.58b)$$

$$F_{V,S} = \int_{x_0}^{x_0+\delta x} (\phi h v)(x, y_0) dx \quad (3.58c)$$

$$F_{V,N} = \int_{x_0}^{x_0+\delta x} (\phi h v)(x, y_0 + \delta y) dx \quad (3.58d)$$

Using mass conservation, the continuity equation can be written as:

$$\begin{aligned} \Omega(t + dt) - \Omega(t) &= \int_t^{t+dt} (F_{V,W} - F_{V,E} + F_{V,S} - F_{V,N}) dt \\ \int_t^{t+dt} \frac{\partial \Omega}{\partial t} dt &= \int_t^{t+dt} (F_{V,W} - F_{V,E} + F_{V,S} - F_{V,N}) dt \\ \frac{\partial \Omega}{\partial t} &= F_{V,W} - F_{V,E} + F_{V,S} - F_{V,N} \end{aligned} \quad (3.59)$$

that can be written as:

$$\begin{aligned} \int_{y_0}^{y_0+\delta y} \int_{x_0}^{x_0+\delta x} \frac{\partial (\phi h)}{\partial t} (x, y) dx dy + \int_{y_0}^{y_0+\delta y} [(\phi h u)(x_0 + \delta x, y) - (\phi h u)(x_0, y)] dy \\ + \int_{x_0}^{x_0+\delta x} [(\phi h v)(x, y_0 + \delta y) - (\phi h v)(x, y_0)] dx = 0 \end{aligned} \quad (3.60)$$

When both  $\delta x$  and  $\delta y$  tend to 0:

$$(\phi hu)(x_0 + \delta x, y) - (\phi hu)(x_0, y) \underset{\delta x \rightarrow 0}{\approx} \delta x \frac{\partial}{\partial x} (\phi hu) \quad (3.61a)$$

$$(\phi hv)(x, y_0 + \delta y) - (\phi hv)(x, y_0) \underset{\delta y \rightarrow 0}{\approx} \delta y \frac{\partial}{\partial y} (\phi hv) \quad (3.61b)$$

we can get the final continuity equation with porosity:

$$\frac{\partial}{\partial t} (\phi h) + \frac{\partial}{\partial x} (\phi hu) + \frac{\partial}{\partial y} (\phi hv) = 0 \quad (3.62)$$

**The momentum equation** The total  $x$ -momentum in the control volume is given by:

$$M_x = \rho \int_{y_0}^{y_0 + \delta y} \int_{x_0}^{x_0 + \delta x} (\phi uh)(x, y, t) dx dy \quad (3.63)$$

The  $x$ -momentum fluxes across the various edges of the control volume are given by:

$$F_{M,W} = \rho \int_{y_0}^{y_0 + \delta y} (\phi hu^2)(x_0, y) dy \quad (3.64a)$$

$$F_{M,E} = \rho \int_{y_0}^{y_0 + \delta y} (\phi hu^2)(x_0 + \delta x, y) dy \quad (3.64b)$$

$$F_{M,S} = \rho \int_{x_0}^{x_0 + \delta x} (\phi huv)(x, y_0) dx \quad (3.64c)$$

$$F_{M,N} = \rho \int_{x_0}^{x_0 + \delta x} (\phi huv)(x, y_0 + \delta y) dx \quad (3.64d)$$

The external forces exerted in the  $x$ -direction on the water in the control volume are the following:

- The pressure force  $P_W$  is exerted from left to right on the western side of the control volume such as:

$$P_W = \frac{\rho g}{2} \int_{y_0}^{y_0 + \delta y} (\phi h^2)(x_0, y) dy \quad (3.65)$$

- The pressure force  $P_E$  exerted from right to left on the eastern side of the control volume writes:

$$P_E = -\frac{\rho g}{2} \int_{y_0}^{y_0 + \delta y} (\phi h^2)(x_0 + \delta x, y) dy \quad (3.66)$$

- The reaction  $W_x$  exerted by the walls on the water body owing to the variation of the porosity in the  $x$ -direction is given by:

$$W_x = \frac{\rho g}{2} \int_{y_0}^{y_0 + \delta y} \int_{x_0}^{x_0 + \delta x} \frac{\partial \phi}{\partial x} h^2 dx dy \quad (3.67)$$

- The  $x$ -reaction  $B_x$  of the bottom to the weight of the water body per unit surface is the product of the local bottom pressure, the bottom slope in the  $x$ -direction and the porosity:

$$B_x = -\rho g \int_{y_0}^{y_0+\delta y} \int_{x_0}^{x_0+\delta x} (\phi h)(x, y) \frac{\partial z_b}{\partial x} dx dy \quad (3.68)$$

- The resistance  $R_x$  due to friction is accounted for by a classical Strickler law. The friction force is exerted only at the points occupied by the water:

$$R_x = -\rho g h \int_{y_0}^{y_0+\delta y} \int_{x_0}^{x_0+\delta x} \left[ \frac{(u^2 + v^2)^{1/2}}{K_x^2 h^{4/3}} \phi u \right] (x, y) dx dy \quad (3.69)$$

The momentum balance can be written as:

$$M_x(t + dt) - M_x(t) = \int_t^{t+\delta t} (F_{M,W} - F_{M,E} + F_{M,S} - F_{M,N} + P_W - P_E + W_x + B_x + R_x) dt \quad (3.70)$$

It is first noted that in the limit of vanishing  $\delta x$  and  $\delta y$ , the differences between the fluxes and the forces at opposite edges of the control volume can be simplified as follows:

$$F_{M,W} - F_{M,E} \underset{\delta x \rightarrow 0}{\approx} -\rho \int_{y_0}^{y_0+\delta y} \int_{x_0}^{x_0+\delta x} \frac{\partial}{\partial x} (\phi u^2 h) dx dy \quad (3.71a)$$

$$F_{M,S} - F_{M,N} \underset{\delta y \rightarrow 0}{\approx} -\rho \int_{x_0}^{x_0+\delta x} \int_{y_0}^{y_0+\delta y} \frac{\partial}{\partial y} (\phi u v h) dy dx \quad (3.71b)$$

$$P_W - P_E \underset{\delta x \rightarrow 0}{\approx} -\frac{\rho g}{2} \int_{y_0}^{y_0+\delta y} \int_{x_0}^{x_0+\delta x} \frac{\partial}{\partial x} (\phi h^2) dx dy \quad (3.71c)$$

We get the final equation in  $x$  direction:

$$\frac{\partial}{\partial t} (\phi u h) + \frac{\partial}{\partial x} \left( \phi u^2 h + \frac{g}{2} \phi h^2 \right) + \frac{\partial}{\partial y} (\phi u v h) = g \frac{h^2}{2} \frac{\partial \phi}{\partial x} - g \phi h \frac{\partial z_b}{\partial x} - g h \frac{(u^2 + v^2)^{1/2}}{K_x^2 h^{4/3}} \phi u \quad (3.72)$$

A similar reasoning leads to the following equation for the  $y$ -momentum:

$$\frac{\partial}{\partial t} (\phi v h) + \frac{\partial}{\partial x} (\phi u v h) + \frac{\partial}{\partial y} \left( \phi v^2 h + \frac{g}{2} \phi h^2 \right) = g \frac{h^2}{2} \frac{\partial \phi}{\partial y} - g \phi h \frac{\partial z_b}{\partial y} - g h \frac{(u^2 + v^2)^{1/2}}{K_y^2 h^{4/3}} \phi v \quad (3.73)$$

The vector form of equations is

$$\frac{\partial}{\partial t} (\mathbf{U}_\phi) + \frac{\partial}{\partial x} (\mathbf{F}_\phi) + \frac{\partial}{\partial y} (\mathbf{G}_\phi) = \mathbf{S}_\phi \quad (3.74)$$

with

$$\mathbf{U}_\phi = \begin{bmatrix} \phi h \\ \phi q \\ \phi r \end{bmatrix}, \quad \mathbf{F}_\phi = \begin{bmatrix} \phi q \\ \phi \frac{q^2}{h} + \frac{1}{2} g \phi h^2 \\ \phi \frac{qr}{h} \end{bmatrix}, \quad \mathbf{G}_\phi = \begin{bmatrix} \phi r \\ \phi \frac{qr}{h} \\ \phi \frac{r^2}{h} + \frac{1}{2} g \phi h^2 \end{bmatrix}, \quad \mathbf{S}_\phi = \begin{bmatrix} 0 \\ g \phi h (S_{0,x} - S_{f,x}) + \frac{1}{2} g h^2 \frac{\partial \phi}{\partial x} \\ g \phi h (S_{0,y} - S_{f,y}) + \frac{1}{2} g h^2 \frac{\partial \phi}{\partial y} \end{bmatrix}$$

where  $q = hu$  and  $r = hv$  are the unit discharge components.  $S_{0,x} = -\frac{\partial z_b}{\partial x}$  (respectively,  $S_{0,y} = -\frac{\partial z_b}{\partial y}$ ) and  $S_{f,x} = \frac{u\sqrt{u^2+v^2}}{K_x^2 h^{4/3}}$  (respectively,  $S_{f,y} = \frac{v\sqrt{u^2+v^2}}{K_y^2 h^{4/3}}$ ) are the bottom slope and head slope at  $x$  (respectively,  $y$ ) direction.

The equation of (3.74) is implemented in *Flood1D2D* using a finite volume approach (see section 3.2.2) and an explicit time discretization.

## 3.2 1D2D coupling model

The numerical model *Flood1D2D* is developed to achieve effective and computationally affordable flood simulations in complex branched urban networks. It aims, with a parsimonious parameterization, to predict realistic flood flow patterns at the city scale with adapted complexities at the local scale. It is based on a full 2D shallow water model at crossroads and a much cheaper 1D effective approach in streets remaining physically coherent and sufficiently informative for operational purpose (i.e. providing the averaged water depth and velocity on the cross-section of the street).

### 3.2.1 Topology of the coupled 1D2D model

The modeling paradigm, based on the shallow water equations consists in 2D cells in the crossroad and effective 1D cells including the full street width (see figure 3.6). As introduced in Finaud-Guyot (2009) and unlike classical 1D2D approaches (see section 2.4.1), the distinction between 1D and 2D cells is not linked to any particular constraint on the set of equations. The equations on both 1D and 2D cells involves the water depth and the two components of the horizontal velocity without any assumption on the velocity orientation.

The only constraint for the junction between 1D and 2D cells is that a 1D edge (understand the edge of a 1D cell) should correspond several 2D edges (understand edges of a 2D cell) (see figure 3.7).

#### Particular case of the 1D2D width variation

The junction between 1D and 2D cells can correspond to a variation of the channel width (being either an enlargement or a narrowing). As illustrated on figures 3.8a and 3.8b, the connection of a large domain to a narrow one introduces particular boundary on the larger domain (illustrated by  $\Gamma_{2D,BC-C}$  on figure 3.8a and  $\Gamma_{1D2D}$  on figure 3.8b).

In the case of a large 2D domain connected to a narrow 1D domain, such boundary can easily be handled as they corresponds to 2D cell edges (see figure 3.8a). In the opposite case of a narrow 2D domain connected to a large 1D domain, the handling of those boundaries would require that the first 1D cell has 6 different edges: one 1D1D:  $\Gamma_{1D,1D}$ , one 1D2D:  $\Gamma_{1D,2D}$ , two classical BC:  $\Gamma_{1D,BC}$  (as the other 1D cells) and two '1D2D' BC:  $\Gamma_{1D,2D}$  (see figure 3.8b).

Such hexaedral cells cannot be handled by the meshing software (Aquaveo Surface-Water Modeling System 11.2.5) and would require a particular implementation in *Flood1D2D* to handle cells with six interfaces. Instead, two different solutions have been designed for this particular problem: deleting the nodes of the 1D cell corresponding to the channel corner (see figure 3.8c) or moving the junction between the two parts of the mesh of the width variation position (see figure 3.8d).

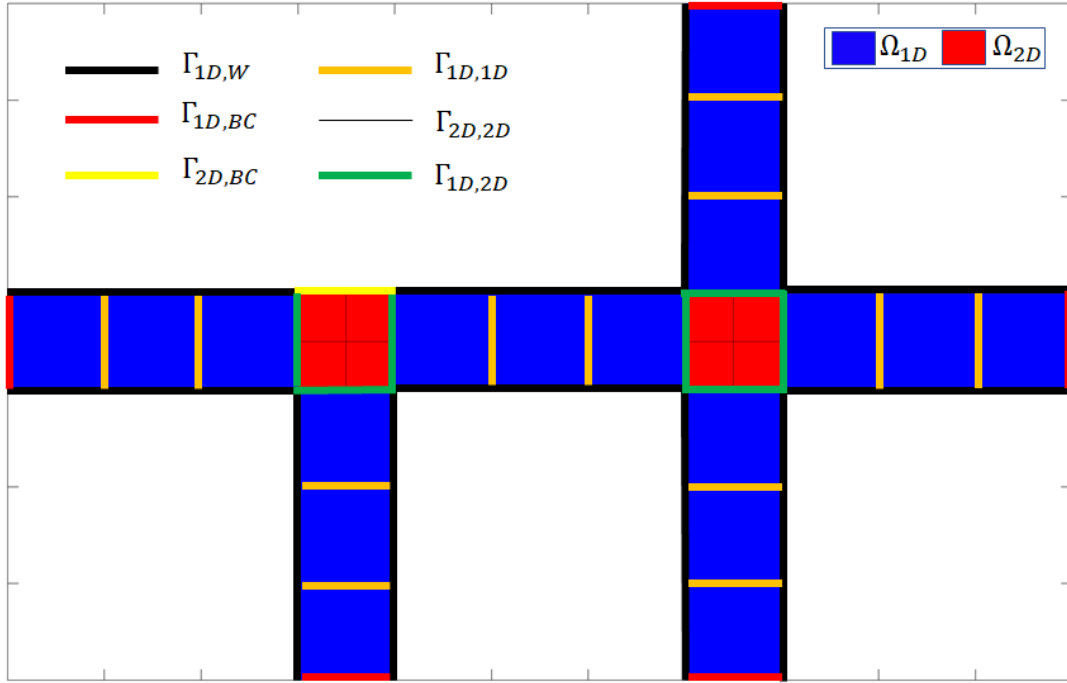


Figure 3.6: Topology of the 1D2D coupling model:  $\Gamma_{1D,W}$ , interfaces of the 1D cell corresponding to walls;  $\Gamma_{1D,BC}$ , interfaces of the 1D cell corresponding to BC;  $\Gamma_{2D,BC}$ , interfaces of the 2D cell corresponding to hydrodynamic BC;  $\Gamma_{1D,1D}$ , interfaces between two 1D cells;  $\Gamma_{2D,2D}$ , interfaces between two 2D cells;  $\Gamma_{1D,2D}$ , interfaces between 1D and 2D cells

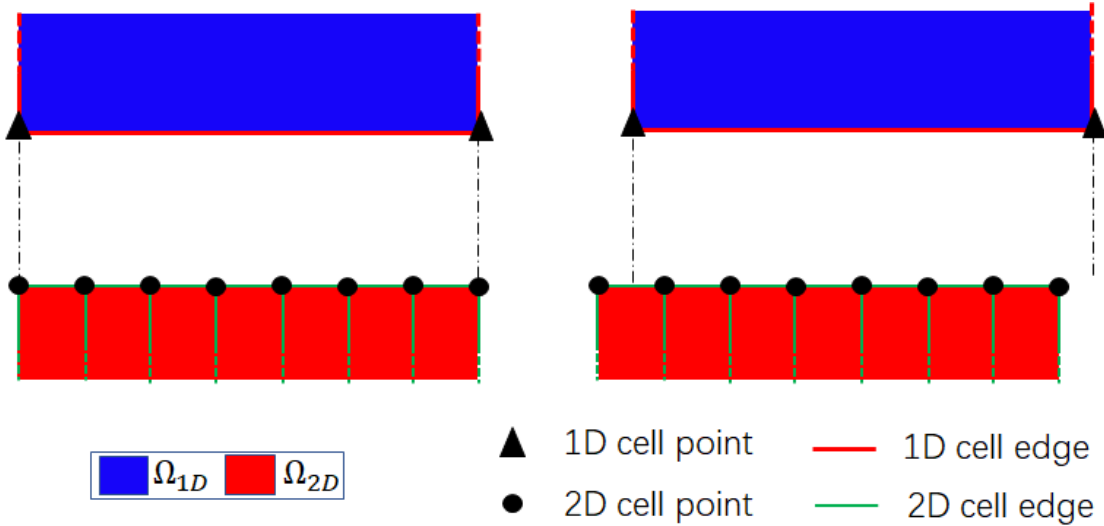


Figure 3.7: Coupling between 1D and 2D mesh: left, allowed configuration; right, forbidden configuration. Note that the 2D cell points are on the segment defined by the 1D cell points. This has not been represented for the sake of clarity

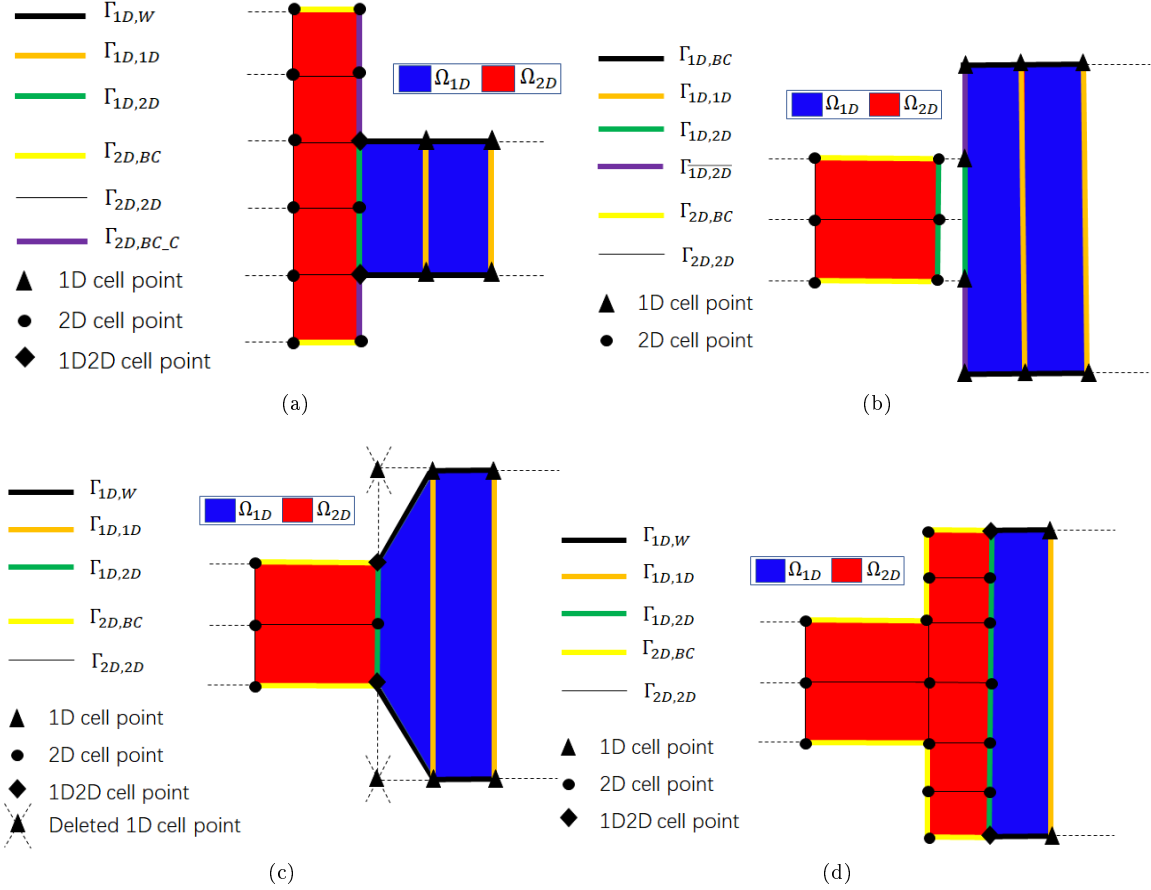


Figure 3.8: 1D2D coupling on a channel width variation. Top left: large 2D connected to narrow 1D domain. Top right: narrow 2D connected to large 1D domain - the 1D cell has 6 nodes and interfaces. Bottom left: meshing solution 1 - corner deletion. Bottom right: meshing solution 2 - 2D mesh overlapping the width variation

### 3.2.2 Finite volume method

The flow is modeled using the shallow water equations with porosity (section 3.1.3) over the whole domain, applied to both 1D effective and 2D cells. The porosity can be imposed to 1 when relevant to come back to the classical shallow water equations without porosity. The numerical tool *Flood1D2D* has been implemented to solve the governing 2D shallow water equations using a finite volume approach. The set of equations considered can be written in conservative form as:

$$\frac{\partial \mathbf{U}}{\partial t} + \frac{\partial \mathbf{F}}{\partial x} + \frac{\partial \mathbf{G}}{\partial y} = \mathbf{S} \quad (3.75)$$

where  $\mathbf{U}$  is the vector of the conserved variables,  $\mathbf{F}$  (respectively  $\mathbf{G}$ ) is the flux in the  $x$  (respectively  $y$ ) direction and  $\mathbf{S}$  is the source term. For the sake of simplicity  $\mathbf{U}_\phi$ ,  $\mathbf{F}_\phi$ ,  $\mathbf{G}_\phi$  and  $\mathbf{S}_\phi$  (defined in equation (3.74)) are written as  $\mathbf{U}$ ,  $\mathbf{F}$ ,  $\mathbf{G}$  and  $\mathbf{S}$ .

The finite volume method consists in solving the integral of equation (3.75) on a given domain  $\Omega \subset \mathbb{R}^2$ :

$$\int_{\Omega} \left( \frac{\partial \mathbf{U}}{\partial t} + \frac{\partial \mathbf{F}}{\partial x} + \frac{\partial \mathbf{G}}{\partial y} \right) d\Omega = \int_{\Omega} \mathbf{S} d\Omega \quad (3.76)$$

$\mathbf{F}$  (respectively  $\mathbf{G}$ ) being the  $x$  (respectively  $y$ ) component of the flux vector  $\vec{\mathbf{H}} = \left[ \vec{H}_1 \quad \vec{H}_2 \quad \vec{H}_3 \right]^T$   
 $\vec{H}_i = \mathbf{F}_i \vec{x} + \mathbf{G}_i \vec{y} \forall i \in [1..3]$ ,  $\frac{\partial \mathbf{F}}{\partial x} + \frac{\partial \mathbf{G}}{\partial y}$  thus represents the divergence of  $\vec{\mathbf{H}}$ :

$$\int_{\Omega} \left( \frac{\partial \mathbf{U}}{\partial t} + \text{div} \vec{\mathbf{H}} \right) d\Omega = \int_{\Omega} \mathbf{S} d\Omega \quad (3.77)$$

By additivity of the integral we get the sum of the integrals on each derivatives:

$$\int_{\Omega} \frac{\partial \mathbf{U}}{\partial t} d\Omega + \int_{\Omega} \text{div} \vec{\mathbf{H}} d\Omega = \int_{\Omega} \mathbf{S} d\Omega \quad (3.78)$$

Therefore, by applying the Green Ostrogradsky's theorem, the integral of the divergence of the flux vector ( $\text{div} \vec{\mathbf{H}}$ ) on the volume  $\Omega$  can be transformed into the integral of flux vector through  $\Gamma$  the closed border of  $\Omega$ :

$$\int_{\Omega} \frac{\partial \mathbf{U}}{\partial t} d\Omega + \int_{\Gamma} \vec{\mathbf{H}} \cdot \vec{n} d\Gamma = \int_{\Omega} \mathbf{S} d\Omega \quad (3.79)$$

where  $\vec{n}$  is the normal outward unit vector to  $\Gamma$ . The integration volume  $\Omega$  being assumed to be constant in time, equation (3.79) can be written as:

$$\frac{\partial}{\partial t} \left( \int_{\Omega} \mathbf{U} d\Omega \right) + \int_{\Gamma} \vec{\mathbf{H}} \cdot \vec{n} d\Gamma = \int_{\Omega} \mathbf{S} d\Omega \quad (3.80)$$

Introducing the integral definition of the average:  $\bar{f} = \frac{1}{\Omega} \int_{\Omega} f d\Omega$  in equation (3.80) leads to:

$$\frac{\partial \Omega \bar{\mathbf{U}}}{\partial t} + \int_{\Gamma} \vec{\mathbf{H}} \cdot \vec{n} d\Gamma = \Omega \bar{\mathbf{S}} \quad (3.81)$$

where  $\bar{\mathbf{S}}$  is the average source term  $\mathbf{S}$  in the cell.

### 3.2.3 Discretisation

Equation (3.81) is discretized on each computational cell  $\Omega_i \subset \mathcal{D}$  (see figure 3.9). The sequence  $(\Omega_i)_{1 \leq i \leq N}$  defining a mesh of the computational domain  $\mathcal{D}$  such as  $\Omega_i$  is a part of  $\mathcal{D}$ ,  $\Omega_i \cap \Omega_j = \emptyset, \forall i \neq j \in [1..N]$ , and  $\cup_{i=1}^N \Omega_i = \mathcal{D}$ . Applying this framework allows to write equation (3.81) on the cell  $\Omega_i$  as:

$$\frac{\partial \Omega_i \mathbf{U}_i}{\partial t} + \int_{\Gamma_i} \vec{\mathbf{H}} \cdot \vec{n} d\Gamma = \Omega_i \mathbf{S}(\mathbf{U}_i) \quad (3.82)$$

where  $\mathbf{U}_i$  the vector of the conserved variables in cell  $i$ .

The closed border of cell  $\Omega_i$  is  $\Gamma_i$  that corresponds to a set of edges  $N(i)$ . Using a classical Euler explicit discretisation of equation (3.82) leads to:

$$\mathbf{U}_i^{n+1} = \mathbf{U}_i^n - \frac{\Delta t}{A_i} \sum_{k \in N(i)} \mathbf{P}_k \mathbf{F}_k^n w_k + \Delta t \mathbf{S}(\mathbf{U}_i^n) \quad (3.83)$$

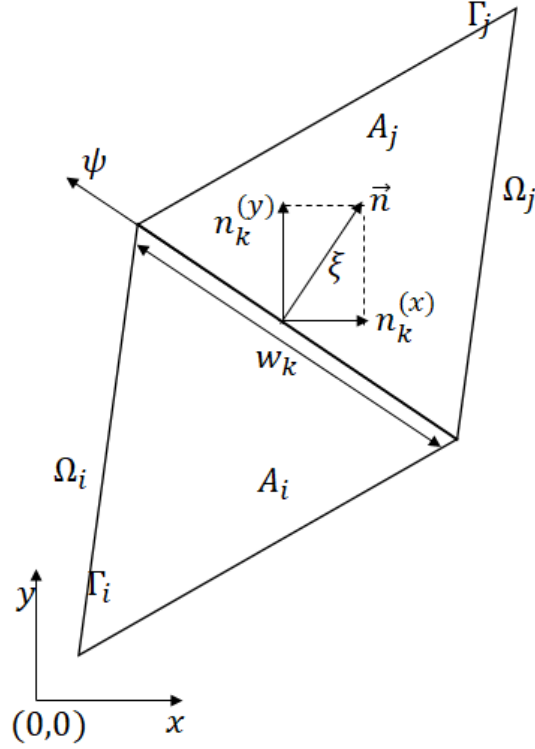


Figure 3.9: Conceptual view of the finite volume discretization: two elements  $\Omega_i$  and  $\Omega_j$  of  $\mathcal{D}$

where  $n$  is the timestep,  $N(i)$  represents all the interfaces of cell  $\Omega_i$ ,  $A_i$  the area of cell  $i$  and  $w_k$  the length of edge  $k$  between  $\Omega_i$  and  $\Omega_j$ .  $N(i)$  the numerical ensemble corresponding to  $\Gamma_i$  the mathematical ensemble.

The matrix  $\mathbf{P}_k$  expresses the rotation from the global coordinate system  $(x, y)$  to the local coordinate system  $(\xi, \psi)$  attached to each interface as illustrated in figure 3.9 for interface  $k$  between cells  $\Omega_i$  and  $\Omega_j$ . The rotation leaves the water depth invariant but acts on the unit discharges. The expression of  $\mathbf{P}_k$  is therefore:

$$\mathbf{P}_k = \begin{bmatrix} 1 & 0 & 0 \\ 0 & n_k^{(x)} & -n_k^{(y)} \\ 0 & n_k^{(y)} & n_k^{(x)} \end{bmatrix} \quad (3.84)$$

where  $n_k^{(x)}$  and  $n_k^{(y)}$  are the components along  $x$  and  $y$  directions of the normal unit vector  $\vec{n}$  between the cells  $i$  and  $j$  (pointing outward from  $i$  to  $j$ ) (see figure 3.9).

### 3.2.4 Time splitting

The source term  $\mathbf{S}(\mathbf{U}_i^n)$  of equation (3.83) can be splitted to make appear the effect of the three source terms written in equation (3.74):

$$\mathbf{U}_i^{n+1} = \mathbf{U}_i^n - \frac{\Delta t}{A_i} \sum_{k \in N(i)} \mathbf{P}_k \mathbf{F}_k^n w_k + \Delta t [\mathbf{S}_0(\mathbf{U}_i^n) + \mathbf{S}_\phi(\mathbf{U}_i^n) + \mathbf{S}_f(\mathbf{U}_i^n)] \quad (3.85)$$

where  $\mathbf{S}_0(\mathbf{U}_i^n)$ ,  $\mathbf{S}_\phi(\mathbf{U}_i^n)$  and  $\mathbf{S}_f(\mathbf{U}_i^n)$  correspond respectively to the average contribution of bottom source term, the porosity variation source term and the friction effect on cell  $\Omega_i$ .

In order to simplify the computation of the variation of  $\mathbf{U}_i$  on the time step and to allow the use of the numerical method adapted to each part of equation (3.85), a classical time splitting algorithm is used (MacCormack and Paullay (1972)). The first step is devoted to the computation of the hyperbolic part of equation (3.74) including the bottom and porosity source terms in order to achieve a well-balanced computation of the flux  $(\mathbf{F})_k^n$ . The second step focuses on the friction effect computation.

### 3.2.4.1 Step 1 - Well balanced computation of the hyperbolic part

The first computational step does not account the effect of the friction:

$$\mathbf{U}_i^{n+h} = \mathbf{U}_i^n - \frac{\Delta t}{A_i} \sum_{k \in N(i)} \mathbf{P}_k \mathbf{F}_k^n w_k + \Delta t [\mathbf{S}_0(\mathbf{U}_i^n) + \mathbf{S}_\phi(\mathbf{U}_i^n)] \quad (3.86)$$

where  $\mathbf{U}_i^{n+h}$  stands for the estimation of  $\mathbf{U}_i$  including the effect of the hyperbolic fluxes and bottom and porosity source terms on one timestep.

Considering the different types of interfaces that may exist due to the topology of the 1D2D considered mesh (see figure 3.6),  $N(i) = N_{1D,W}(i) \cup N_{1D,BC}(i) \cup N_{2D,BC}(i) \cup N_{1D1D}(i) \cup N_{2D2D}(i) \cup N_{1D2D}(i)$ . Note that depending on the considered cell  $\Omega_i$  some sets of interfaces might be empty: for a 2D cell that does not share any interface with a boundary or with a 1D cell, all the sets are empty excepts  $N_{2D2D}(i)$ . In the particular case of a 1D cell coupled to several 2D cells, the junction interface of the 1D cell is accounted as multiple edges corresponding to the edges of each 2D cell.

The fluxes  $\mathbf{F}_k^n$  between two cells (for the set of edges  $N_{1D1D}(i) \cup N_{2D2D}(i) \cup N_{1D2D}(i)$ ) are computed using a Riemann solver (either HLLC or PorAS (Finaud-Guyot et al. (2010b))). Such choice allows to preserve the well-balanced condition due to the bottom and porosity source term effect  $\mathbf{S}_0(\mathbf{U}_i^n)$  and  $\mathbf{S}_\phi(\mathbf{U}_i^n)$  across interface  $k$ . The parameters of the Riemann solver (being the values of  $\mathbf{U}$ ,  $\phi$  and  $z_b$  in the left and right cells attached to interface  $k$ ) are thus directly taken in the corresponding cells of the mesh:  $\Omega_i$  and  $\Omega_j$ .

The fluxes  $\mathbf{F}_k^n$  between one cell  $\Omega_i$  and a boundary (for the set of edges  $N_{1D,W}(i) \cup N_{1D,BC}(i) \cup N_{2D,BC}(i)$ ) are computed using an estimation of  $h_{BC}$  and  $q_{BC}$  at the boundary. The user defined boundary condition allows to determine either  $h_{BC}$ ,  $q_{BC}$  or a relationship between them and the Riemann invariants conservation along the characteristic from cell  $\Omega_i$  to the boundary allows to provide the second equation that close the system (Araud (2012)).

### 3.2.4.2 Step 2 - Friction effect computation

$$\mathbf{U}_i^{n+1} = \mathbf{U}_i^{n+h} + \Delta t \mathbf{S}_f(\mathbf{U}_i^n) \quad (3.87)$$

The friction term is solved using an ordinary differential equation in the form (Finaud-Guyot (2009)):

$$\frac{df}{dt} = -\alpha f \quad (3.88)$$

where  $f = q$  or  $f = r$ . This equation is equal to:

$$\frac{df}{f} = -\alpha dt \quad (3.89)$$

The analytical solution for this equation can be obtained by integrating equation (3.89) over the timestep:

$$\begin{aligned}
\int_{f^n}^{f^{n+1}} \frac{1}{f} df &= \int_{t^n}^{t^{n+1}} -\alpha dt \\
[\ln f]_{f^n}^{f^{n+1}} &= -\alpha \Delta t \\
\ln f^{n+1} - \ln f^n &= -\alpha \Delta t \\
\ln \left( \frac{f^{n+1}}{f^n} \right) &= -\alpha \Delta t \\
\frac{f^{n+1}}{f^n} &= \exp(-\alpha \Delta t) \\
\frac{f^n}{f^{n+1}} &= f^n \exp(-\alpha \Delta t)
\end{aligned} \tag{3.90}$$

For the 2D mesh, we can get:

$$\alpha = g \frac{\sqrt{q^2 + r^2}}{K^2 h^{7/3}} \tag{3.91}$$

Equation (3.91) can be used into equation (3.90), the variables vector  $U^{n,h}$  can be transformed as:

$$h^{n+1} = h^{n,h} \tag{3.92a}$$

$$q^{n+1} = q^n \exp \left[ -g \frac{\sqrt{(q^n)^2 + (r^n)^2}}{K_x^2 (h^n)^{7/3}} \Delta t \right] \tag{3.92b}$$

$$r^{n+1} = r^n \exp \left[ -g \frac{\sqrt{(q^n)^2 + (r^n)^2}}{K_y^2 (h^n)^{7/3}} \Delta t \right] \tag{3.92c}$$

### 3.3 New hydrodynamic reconstruction

The proposed 1D2D shallow water coupling between 1D streets and 2D crossroads achieved with a cut-cell technique allows a sufficiently informative modeling for operational purpose.

For open channel flows downstream of a crossroad, complex flow features are not finely accounted by such a 1D approach parameterized with roughness only (cf. chapter 6 section 6.5.2). In the streets, a complementary parsimonious parameterization of the shallow water equations is thus introduced.

In what follows, each computational cell representing a part of either a street or a crossroad, the full area of the modeled domain is available for water. The porosity  $\phi$  in each computational cell, representing the ratio of the cell area available for water to the total area of the cell (see section 3.3.1), is thus equal to one.

#### 3.3.1 Physical considerations on flow downstream crossroads

This parameterization takes advantage of empirical findings on the effects of 3D flow structures on local and global flow patterns in urban geometries. Modeling and experimental observations of flow hydrodynamic within complex branched networks highlight the presence of recirculation areas downstream of crossroad and their effects on global flow repartition (e.g. Mignot et al. (2008a,b); Finaud-Guyot et al. (2018), see details in section 2.2).

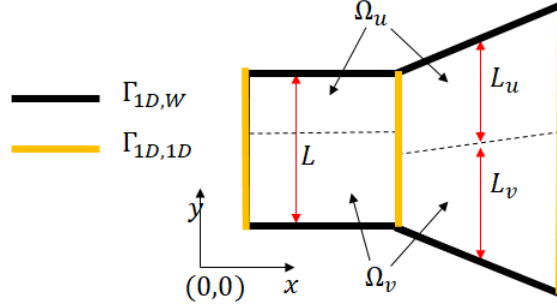


Figure 3.10: Sketch of the recirculation zone on the 1D cell

The new parameter thus aims to represent the effect of the recirculation at the local and global flow pattern. Those zones being often observed downstream of crossroads, the parametrisation is only applied on 1D cells. On those cells, an effective approach is introduced based on the idea of an equivalent flow vein narrowed by the recirculation zone downstream of a crossroad. 1D cells, defined on the whole street width (figure 3.10), contain 2 domains  $\Omega_{1D} = \Omega_u \cup \Omega_v$ :

- $\Omega_u$ : an ineffective flow area located in a recirculation zone on which there is on average no flux in the street direction;
- $\Omega_v$ : an effective flow vein.

The cell splitting is based on the function  $\omega$  used to account for recirculation effects. The variable  $\omega$  measures the proportion of the cell width that is not occupied by the recirculation:

$$\omega = \frac{L_v}{L} \quad (3.93)$$

where  $L = L_u + L_v$  represents the full width of the 1D cell and  $L_u$  (respectively  $L_v$ ) is the width of the recirculation (respectively flow vein). If  $\omega = 1$  the full street width is available for flow and no recirculation is taken into account. The variable  $\omega$  is also the area ratio of the flow vein to the full cell:  $\omega = \Omega_v / \Omega_{1D}$ . Indeed, the integration of  $L_v$  on the 1D cell along the street axis  $s$  is the area of the flow vein on the cell:

$$\begin{aligned} \Omega_v &= \int_s L_v(s) ds \\ &= \int_s \omega L(s) ds \\ &= \omega \int_s L(s) ds \\ &= \omega \Omega_{1D} \end{aligned} \quad (3.94)$$

Such a definition of  $\omega$ , corresponding to the effective flow width with respect to the full cell width, is similar to a porosity as it can be defined in Lhomme (2006). In the following, the notation  $\phi$  has been chosen instead of  $\omega$  to simplify the implementation of *Flood1D2D*. Moreover, the parameter is also defined for the 2D cells but taken equal to 1.

In the present study, the parametrisation  $\phi$  is constant in time even if all the hydraulic variables can be variable in time. This assumes that the steady-state configuration in a complex

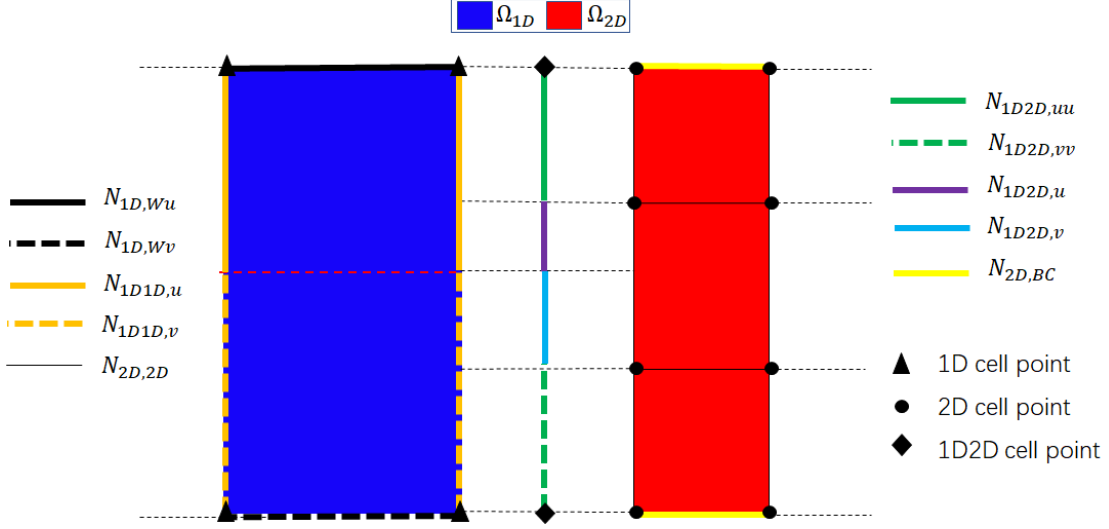


Figure 3.11: Sub-edges of 1D2D mesh for the effect of recirculation zone. For the sake of readability, a gap has been introduced between  $\Omega_{1D}$  and  $\Omega_{2D}$

branched networks is not dependent of the transient hydrodynamic that has lead to the steady-state. Such important hypothesis will have to be more deeply studied on the ICube urban flood experimental rig. This also allows to neglect the coupling between the modeled hydrodynamic and the parametrisation of  $\phi$ . In order to account for the effect of recirculation on the computed fluxes between cells, a specific numerical reconstruction is introduced in what follows.

### 3.3.2 Modified topology of the edge - hyperbolic part

Compared to the classical 1D2D model, the overall computational algorithm (see section 3.2.4) and the computation of the friction effect (see section 3.2.4.2) remains unchanged. In this section, only the computation of the hyperbolic part of the equation is thus presented.

Finally the computational domain still consists in  $\mathcal{D} = \Omega_{1D} \cup \Omega_{2D}$  and thus the discretisation equation (3.86) remains unchanged with a computation of the fluxes for  $k$  in  $N(i) = N_{1D,W}(i) \cup N_{1D,BC}(i) \cup N_{2D,BC}(i) \cup N_{1D1D}(i) \cup N_{2D2D}(i) \cup N_{1D2D}(i)$ :

$$\begin{aligned}
\mathbf{U}_i^{n+h} = & \mathbf{U}_i^n \\
& - \frac{\Delta t}{A_i} \left\{ \sum_{k \in N_{1D,BC}(i)} \mathbf{P}_k \mathbf{F}_k^n w_k \right. \\
& + \sum_{k \in N_{2D,BC}(i) \cup N_{2D2D}(i)} \mathbf{P}_k \mathbf{F}_k^n w_k \} \\
& + \sum_{k \in N_{1D,W}(i) \cup N_{1D1D}(i) \cup N_{1D2D}(i)} \mathbf{P}_k \mathbf{F}_k^n w_k \\
& + \Delta t [\mathbf{S}_0(\mathbf{U}_i^n) + \mathbf{S}_\phi(\mathbf{U}_i^n)]
\end{aligned} \tag{3.95}$$

The flux computation for  $N_{1D,BC}(i) \cup N_{2D,BC}(i) \cup N_{2D2D}(i)$  remains unchanged. However, the flux computation for the edges in  $N_{uw} = N_{1D,W}(i) \cup N_{1D1D}(i) \cup N_{1D2D}(i)$  is modified to

take into account the effect of the recirculation on the flow:

$$\sum_{k \in N_{uv}} \mathbf{P}_k \mathbf{F}_k^n w_k = \sum_{k \in N_{uv}} \mathbf{P}_k (\mathbf{F}_{k,u}^n w_{k,u} + \mathbf{F}_{k,v}^n w_{k,v}) \quad (3.96)$$

where  $w_{k,u}$  (respectively  $w_{k,v}$ ) is the length of interface  $k$  along the recirculation zone (respectively the flow vein) such as  $w_k = w_{k,u} + w_{k,v}$  and  $\mathbf{F}_{k,u}^n$  (respectively  $\mathbf{F}_{k,v}^n$ ) is the flux through  $w_{k,u}$  (respectively  $w_{k,v}$ ). Introducing the porosity definition leads to:

$$w_{k,v} = \phi_k w_k \quad w_{k,u} = (1 - \phi_k) w_k \quad (3.97)$$

where  $\phi_k$  is the porosity at the interface. Detailing each subset of  $N_{uv}$  corresponding to each different computation method leads to  $N_{uv} = N_{1D,Wu} \cup N_{1D,Wv} \cup N_{1D1D,u} \cup N_{1D1D,v} \cup N_{1D2D,uu} \cup N_{1D2D,u} \cup N_{1D2D,v} \cup N_{1D2D,vv}$  (see figure 3.11):

$N_{1D,Wu}$  is the edges subset of the wall boundary along the recirculation zone. The flux through this type of interface is computed using the Riemann invariants between the 1D cell and the boundary condition set to  $q_{BC} = 0$ . The edge being fully along a recirculation zone, the hydraulic variables in the 1D cell  $\mathbf{U}_{1D}$  are take equal to  $[h \ 0 \ 0]^T$ .

$N_{1D,Wv}$  is the edges subset of the wall boundary along the flow vein. The flux through this type of interface is computed using the Riemann invariants between the 1D cell and the boundary condition set to  $q_{BC} = 0$ . The edge being fully along a flow vein, the hydraulic variables in the 1D cell  $\mathbf{U}_{1D}$  are take equal to  $[h \ q \ r]^T$ .

$N_{1D1D,u}$  is the subset of the edges between two recirculation zones in 1D cells. The flux through this type of interface is computed using either the HLLC or the PorAS Riemann solver parameterized with  $\mathbf{U}_{1D} = [h \ 0 \ 0]^T$ . Even with only a water surface elevation variation across the interface, such Riemann solver computes a mass flux through the interface that is not coherent with the physical hypothesis that considers a nul discharge across a recirculation. The computed mass flux is thus ignored and taken equal to 0.

$N_{1D1D,v}$  is the subset of the edges between two flow veins in a 1D cells. The flux through this type of interface is computed using either the HLLC or the PorAS Riemann solver parameterized with  $\mathbf{U}_{1D} = [h \ q/\phi \ r/\phi]^T$ .

$N_{1D2D,uu}$  is the subset of edges between a 1D and a 2D cell that are fully along the recirculation zone. The flux through this type of interface is computed using either the HLLC or the PorAS Riemann solver parameterized with  $\mathbf{U}_{1D} = [h \ 0 \ 0]^T$  and  $\mathbf{U}_{2D} = [h \ 0 \ 0]^T$ . As for  $N_{1D1D,u}$ , the computed mass flux is ignored and taken equal to 0.

$N_{1D2D,u}$  is the subset of the edges between a 1D and a 2D cells that are neither fully along a recirculation zone nor the flow vein. The flux through this type of interface is computed using either the HLLC or the PorAS Riemann solver parameterized with  $\mathbf{U}_{1D} = [h \ 0 \ 0]^T$  and  $\mathbf{U}_{2D} = [h \ 0 \ 0]^T$ . As for  $N_{1D1D,u}$ , the computed mass flux is ignored and taken equal to 0.

Table 3.1: Sub-edges of 1D2D coupling with the consideration of recirculation effect

$N$	$U_{1D}$	$U_{2D}$	$\phi_k$
$N_{1D,Wu}$	$\begin{bmatrix} h & 0 & 0 \end{bmatrix}^T$		0
$N_{1D,Wv}$	$\begin{bmatrix} h & q & r \end{bmatrix}^T$		1
$N_{1D1D,u}$	$\begin{bmatrix} h & 0 & 0 \end{bmatrix}^T$		$\frac{\phi_L + \phi_R}{2}$
$N_{1D1D,v}$	$\begin{bmatrix} h & q/\phi & r/\phi \end{bmatrix}^T$		$\frac{\phi_L + \phi_R}{2}$
$N_{1D2D,uu}$	$\begin{bmatrix} h & 0 & 0 \end{bmatrix}^T$	$\begin{bmatrix} h & 0 & 0 \end{bmatrix}^T$	0
$N_{1D2D,u}$	$\begin{bmatrix} h & 0 & 0 \end{bmatrix}^T$	$\begin{bmatrix} h & 0 & 0 \end{bmatrix}^T$	$\phi_{1D}$
$N_{1D2D,v}$	$\begin{bmatrix} h & q/\phi_{1D} & r/\phi_{1D} \end{bmatrix}^T$	$\begin{bmatrix} h & q/\phi_k & r/\phi_k \end{bmatrix}^T$	$\phi_{1D}$
$N_{1D2D,vv}$	$\begin{bmatrix} h & q & r \end{bmatrix}^T$	$\begin{bmatrix} h & q & r \end{bmatrix}^T$	1

$N_{1D2D,v}$  is the subset of edges between a 1D and a 2D cells that are neither fully along a recirculation zone nor the flow vein. The flux through this type of interface is computed using either the HLLC or the PorAS Riemann solver parameterized with  $\mathbf{U}_{1D} = [h \ q/\phi_{1D} \ r/\phi_{1D}]^T$  and  $\mathbf{U}_{2D} = [h \ q/\phi_k \ r/\phi_k]^T$ .

$N_{1D2D,vv}$  is the subset of the edges between a 1D and a 2D cells that are fully along the flow vein. The flux through this type of interface is computed using either the HLLC or the PorAS Riemann solver parameterized with  $\mathbf{U}_{1D} = [h \ q \ r]^T$  and  $\mathbf{U}_{2D} = [h \ q \ r]^T$ .

For every computation using a Riemann solver, the bottom elevation value is classically parameterized i.e. the value for  $z_{bL}$  (respectively  $z_{bR}$ ) is the bottom elevation in the left (respectively right) cell attached to the considered interface and the porosity is taken equal to 1 in every configuration.

Once the fluxes are computed, the quantities exchanged between cells depend on the length of the interfaces (either  $w_k$ ,  $w_{k,u}$  or  $w_{k,v}$ ) and thus on the porosity  $\phi_k$  at the interface (see table 3.1):

$$\phi_k = \begin{cases} 0 & \text{for } k \in N_{1D,Wu} \cup N_{1D2D,uu} \\ 1 & \text{for } k \in N_{1D,Wv} \cup N_{1D2D,vv} \\ \frac{\phi_L + \phi_R}{2} & \text{for } k \in N_{1D1D,u} \cup N_{1D1D,v} \\ \phi_{1D} & \text{for } k \in N_{1D2D,u} \cup N_{1D2D,v} \end{cases} \quad (3.98)$$

$\phi_L$  (respectively  $\phi_R$ ) being the porosity in the cell on the left (respectively right) side of interface  $k$  and  $\phi_{1D}$  being the porosity of the 1D cell attached to interface  $k$ .

### 3.4 Conclusions/modeling methodology

In this chapter, a new physical model based on 2D shallow water equations including porosity has been proposed. The original finite volume discretization, using a cut-cell technique between 1D and 2D interfaces, has been implemented into the code *Flood1D2D*. In the next chapter, *Flood1D2D* model will be validated on several flow cases where reference solutions, either analytical or experimental, are available.

## Chapter 4

# *Flood1D2D* validation

### 4.1 Introduction

The numerical approach presented in chapter 3 has been implemented in a new program *Flood1D2D* developed during this PhD. This numerical tool is based on a classical finite volume approach (see section 3.2.2) and the proposed cut cell technique (see section 3.3) to solve the 2D shallow water equations with porosity (see equation (3.74)). As highlighted in section 3.3, the computation requires: (i) the computation of the flux through the interface between 2 cells while preserving the well-balancing property for both the bottom slope and the porosity variations; (ii) the computation of the friction effect; and (iii) a cut-cell technique at the junction between streets and crossroads.

First, the efficiency of the Riemann solvers are assessed on classical academic test cases, essentially to detect any mistake in their implementation. Next, the source terms computation corresponding to the friction effect is validated. Finally, the proposed cut-cell technique abilities are assessed on academic cases including porosity in view of urban flood modeling.

### 4.2 Flux computation

*Flood1D2D* being based on a finite volume approach, the hydraulic computations are based on a Riemann solver (cf. section 3.2.3) at each interface between the cells of the mesh. The code uses two classical Riemann solvers (HLLC (Guinot and Soares-Frazão, 2006) and PorAS (Finaud-Guyot et al. (2010b))) adapted to configuration of both bottom and porosity variations for computing the fluxes through interfaces while preserving the well-balancing condition. The test cases presented hereafter aim to validate the correct implementation of those Riemann solvers in all possible configurations: 1D or 2D, steady-state or transient regime, various hydraulic regimes (sub, super or transcritical), with either smooth or abrupt variation of the porosity and the bottom elevation (one of them or both).

#### 4.2.1 Water at rest with variable porosity and bottom elevation (T01)

This test case aims at validating the ability of the code to compute wetting and drying front in case of stagnant water in a partly immersed domain including a variable porosity. The modeled domain is thus a rectangular channel with no friction and a spatially varied porosity and bottom elevation along the channel. A linear variation of both the porosity and the bottom elevation starts at  $x_0 = 10\text{m}$  over  $l_0 = 20\text{m}$  (see figure 4.1 and table 4.1). An uniform water level (with no velocity) is set as an initial condition and is supposed to remain unchanged during the simulation.

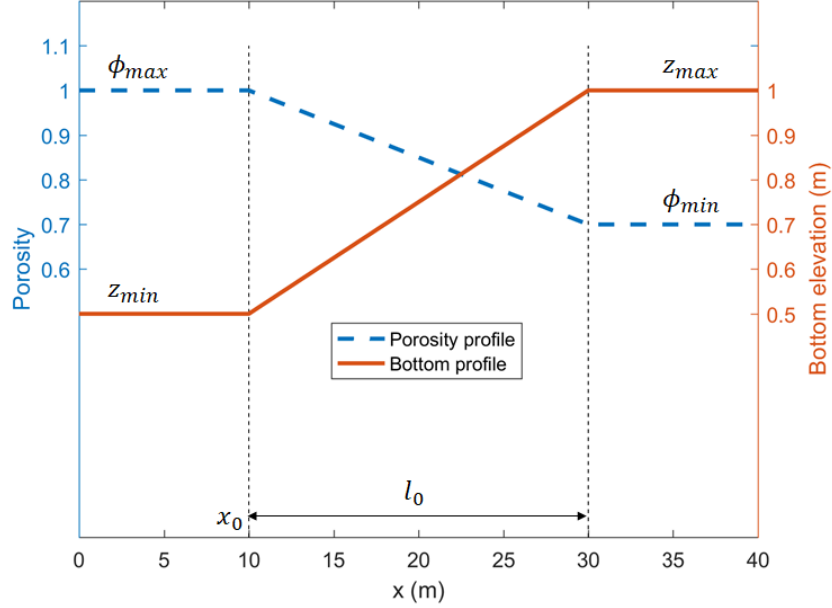


Figure 4.1: Test case T01 - Bottom and porosity variation along the channel

Table 4.1: Parameters for the test case with water at rest (T01)

Symbol	Meaning	Value
$g$	Gravitational acceleration	$9.81\text{m}\cdot\text{s}^{-2}$
$l$	Domain length	$40\text{m} \times 1\text{m}$
$l_0$	Length of the variation zone	20m
$x_0$	Position of the beginning of the variation zone	10m
$\phi_{max}$	Porosity upstream of the variation zone ( $x \leq x_0$ )	1
$\phi_{min}$	Porosity downstream of the variation zone ( $x \geq x_0 + l_0$ )	0.7
$z_{min}$	Bottom elevation upstream of the variation zone ( $x \leq x_0$ )	0.5m
$z_{max}$	Bottom elevation downstream of the variation zone ( $x \geq x_0 + l_0$ )	1.0m
$\Delta x$	Cell size	0.1m
$\Delta y$	Cell width	1m
$q$	Prescribed unit discharge at the upstream boundary ( $x = 0\text{m}$ )	$0\text{m}^2\cdot\text{s}^{-1}$
$h$	Prescribed water depth at the downstream boundary ( $x = 40\text{m}$ )	0m
$z_{ini}$	Initial water surface elevation over the domain	0.75m
$t$	Simulation time	1000s

The simulation is performed on a structured mesh of rectangular cells ( $\Delta x = 0.1\text{m}$  in the longitudinal direction of the channel and  $\Delta y = 1\text{m}$  in the transversal direction). The initial water surface elevation is set to  $z_{ini} = 0.75\text{m}$  (with no velocity) and the computation is run during 1000s, time at which the results are presented (see figure 4.2). Numerical results show that for both Riemann solver (HLLC and PorAS), the water surface elevation remains constant and equal to the initial water depth with no velocity after 1000s. This is coherent with the expected result and confirms the ability of the code to deal with wetting and drying front.

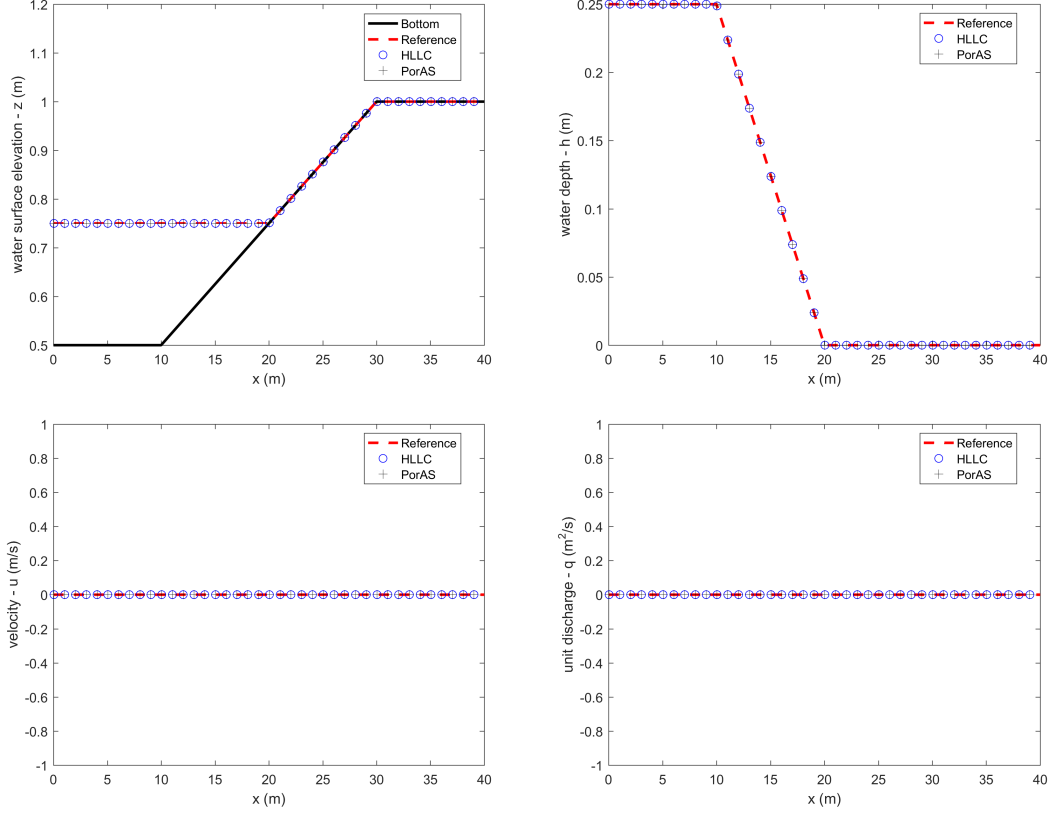


Figure 4.2: Test case T01 - Comparison of *Flood1D2D* results (using either the HLLC or the PorAS Riemann solver) with the reference. Top left: water surface elevation; top right: water depth; bottom left: velocity; bottom right: unit discharge. Note that the computed water surface elevation (for both Riemann solvers) varies for  $x > 20\text{m}$  because the elevation returned by the code is the maximal value between the bottom and the free surface elevation (i.e. the bottom elevation when the water depth is nil). Only 1 point every 10 are plotted in space for the sake of clarity

#### 4.2.2 One-dimensional flow through a variable porosity zone (T02)

This test case aims at validating the ability of the code to deal with variable porosity in steady state. A permanent flow is thus simulated in a rectangular channel without friction nor slope and with a spatially varying porosity with a parabolic profile:

$$\phi(x) = \begin{cases} ax^2 + bx + c & \text{for } x \in [x_m - l_0; x_m + l_0] \\ \phi_0 & \text{elsewhere} \end{cases} \quad (4.1a)$$

$$a = \frac{\phi_0 - \phi_m}{l_0^2}, \quad b = -2ax_m, \quad c = \phi_0 + a(x_m^2 - l_0^2) \quad (4.1b)$$

where the length of the porosity variation is  $2l_0$ ,  $x_m$  is the position of the middle of the porosity variation,  $\phi_0$  (respectively  $\phi_m$ ) is the porosity outside (respectively in the middle) of the variation

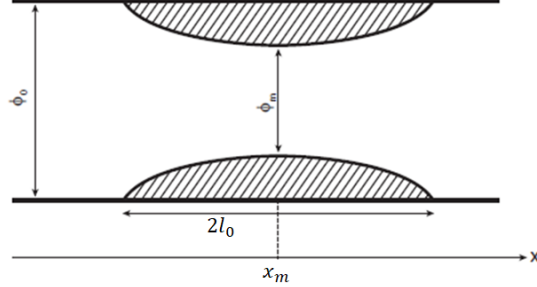


Figure 4.3: Diagram of variables definition for test case T02, top view along flow distance from Finaud-Guyot (2009)

area (see figure 4.3). The ability of the code to deal with variable porosity is tested for two different hydraulic regimes: a subcritical flow (T02a) and a transcritical flow (T02b).

As highlighted by Finaud-Guyot (2009), the reference solution for this test case is obtained by solving the steady-state momentum conservation equation in a non-prismatic rectangular channel derived from the shallow water equations with porosity and no bottom source term:

$$\phi \frac{dh}{dx} (1 - Fr^2) = h Fr^2 \frac{d\phi}{dx} \quad (4.2)$$

Equation (4.2) is discretized and solved using an Euler method on a very fine grid ( $\Delta x = 0.002\text{m}$ ) from downstream to upstream (respectively upstream to downstream) for subcritical (respectively supercritical) flow regime. The reference for test case T02a (subcritical flow) is established using  $q_{upstream} = 1\text{m}^2.\text{s}^{-1}$  and  $h_{downstream} = 1\text{m}$ . For the transcritical case (T02b), the discharge is the same as for T02a and no water depth is needed at the boundary since the flow is controlled by a critical depth (such as  $Fr = 1$ ) that appears at  $x_m$ .

For both hydraulic regimes, the domain length is  $l = 100\text{m}$  with a uniform mesh of regular cells of  $0.1\text{m} \times 1\text{m}$ . For both hydraulic regimes, the simulations are performed from an initial water surface elevation set to  $1\text{m}$  and initial velocity in  $x$  direction is set to  $0\text{m}.\text{s}^{-1}$ . The computational parameters are given in table 4.2. The simulations are carried out until steady flow conditions are reached over the computational domain (after barely 3000s).

The simulation results for subcritical and transcritical flow regimes are presented in figures 4.4 and 4.5. Numerical results show a good agreement between the computed hydraulic variables ( $h$ ,  $Fr$ ,  $q$  and  $Q$ ) using either the HLLC or the PorAS Riemann solvers and the reference whatever the hydraulic flow regime. However, in both configurations, the total discharge  $Q = \phi \times \Delta y \times q$  computed with the PorAS Riemann solver is constant and variable with the HLLC solver. As the test case corresponds to a steady-state, the total discharge computed by the HLLC Riemann solver is wrong. This is due to the fact that the total discharge is computed by a Riemann solver at the interface between two cells i.e. based on the geometrical features (bottom elevation and porosity) of both cells whereas the computed (and plotted) values are in the middle of each cell.

### 4.2.3 One-dimensional flow over a bump (T03)

This test case aims at validating the ability of the code to deal with variable bottom elevation in steady state. A permanent flow is thus simulated in a rectangular channel with a spatially

Table 4.2: Parameters for the test case with variable porosity (T02)

Symbol	Meaning	Value
$g$	Gravitational acceleration	$9.81\text{m}\cdot\text{s}^{-2}$
$l$	Domain length	$100\text{m} \times 1\text{m}$
$2l_0$	Length of the porosity variation	50m
$x_m$	Position of the minimal porosity $\phi_m$ in the domain	50m
$\phi_0$	Porosity outside of the porosity variation	1
$\phi_m$	Minimum of the porosity	0.6
$\Delta x$	Cell size	0.1m
$\Delta y$	Cell width	1m
$z_{ini}$	Initial water level over the domain	1m
$q_{upstream}$	Prescribed unit discharge at the upstream boundary ( $x = 0\text{m}$ )	$1\text{m}^2\cdot\text{s}^{-1}$
$h_{downstream}$	Prescribed water depth at the downstream boundary ( $x = 100\text{m}$ ) for subcritical flow (T02a)	1m
	for transcritical flow (T02b)	0.1m

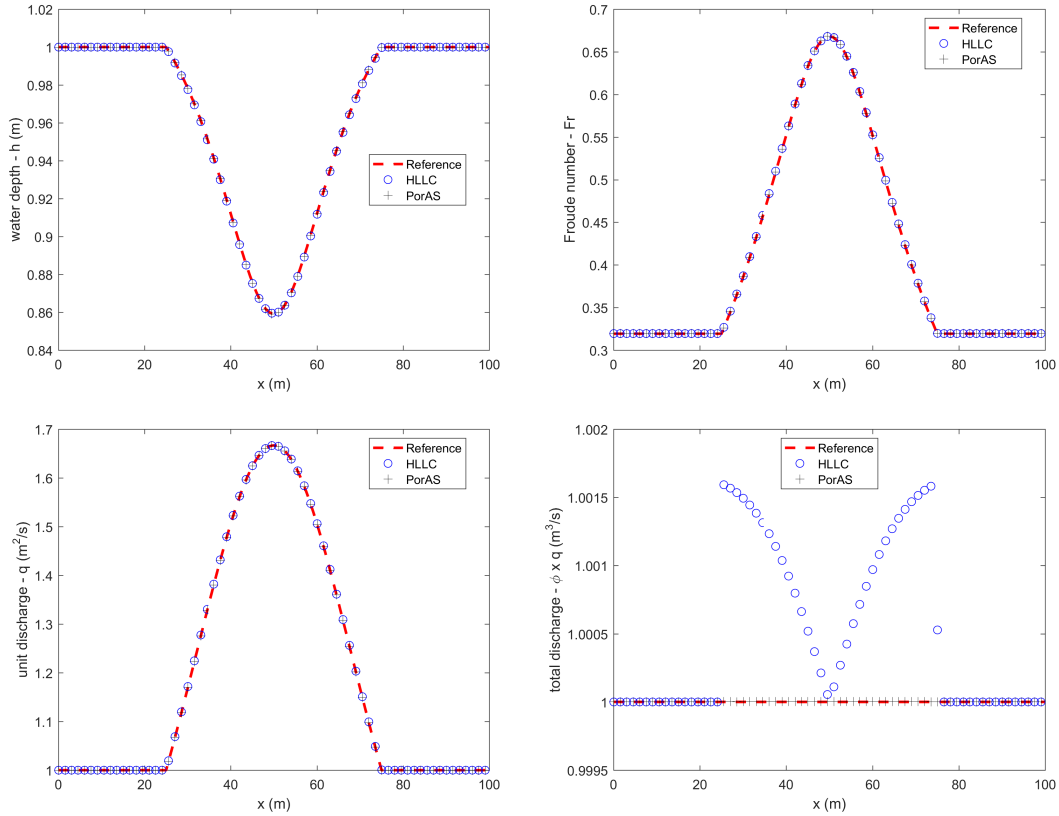


Figure 4.4: Comparison of *Flood1D2D* results (using either the HLLC or the PorAS Riemann solver) with the semi-analytical reference for the test case T02a (subcritical flow regime). Only 1 point every 15 are plotted for the sake of clarity

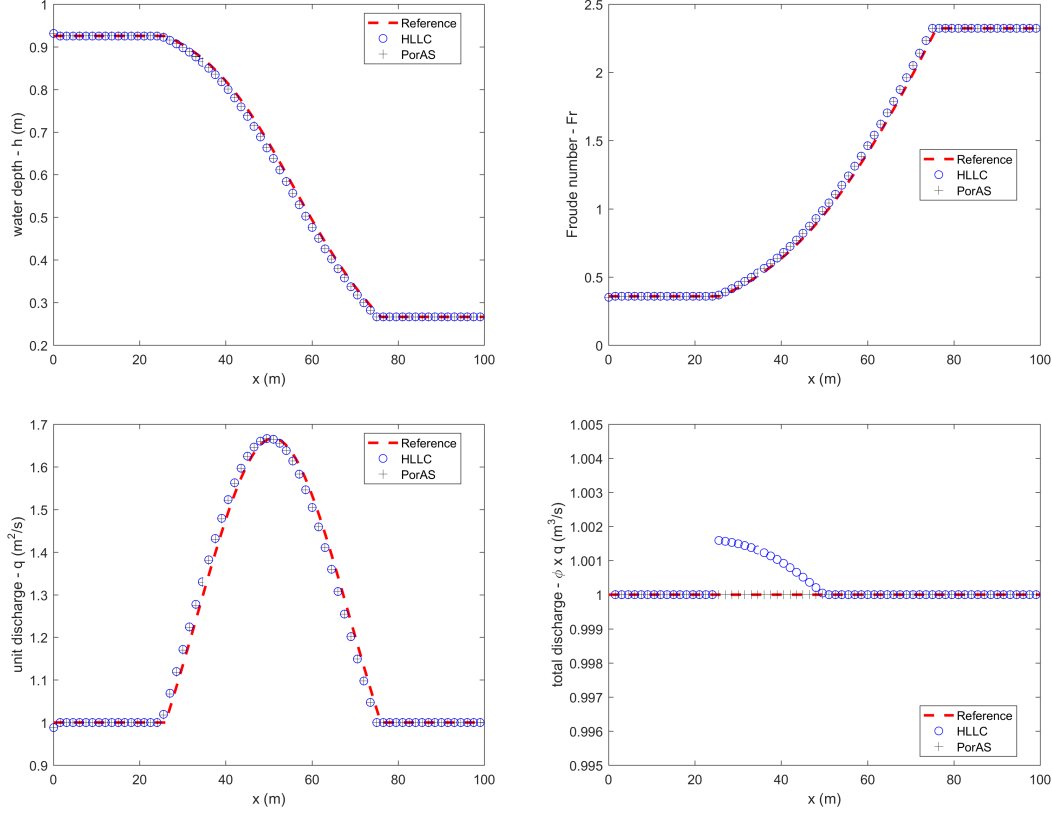


Figure 4.5: Comparison of *Flood1D2D* results (using either the HLLC or the PorAS Riemann solver) with the semi-analytical reference for the test case T02b (transcritical flow regime). Only 1 point every 15 are plotted for the sake of clarity

varying bottom elevation with parabolic profile, a uniform porosity set to 1 and without friction. The ability of the code to deal with variable bottom is tested for two different hydraulic regimes: a subcritical flow (T03a) and a transcritical flow (T03b).

As highlighted by Finaud-Guyot (2009), the reference solution for this test case is obtained by solving the steady-state momentum conservation equation in rectangular channel derived from the shallow water equations with a bottom source term:

$$\frac{dh}{dx}(1 - Fr^2) = -\frac{dz_b}{dx} \quad (4.3)$$

Equation (4.3) is discretized and solved using an Euler method on a very fine grid ( $\Delta x = 0.05\text{m}$ ) from downstream to upstream (respectively upstream to downstream) for subcritical (respectively supercritical) flow regime. The reference for test case T03a (subcritical flow) is established using  $q_{upstream} = 4.42\text{m}^2.\text{s}^{-1}$  and  $h_{downstream} = 2\text{m}$ . For the transcritical case (T03b), the discharge is  $q_{upstream} = 1.53\text{m}^2.\text{s}^{-1}$  and no water depth is necessary at the boundary since the flow is controlled by a critical depth (such as  $Fr = 1$ ) that appears at  $x_m$  (middle of the bump, see figure 4.6).

For both hydraulic regimes, the domain length is  $l = 25\text{m}$  with a mesh of uniform cell

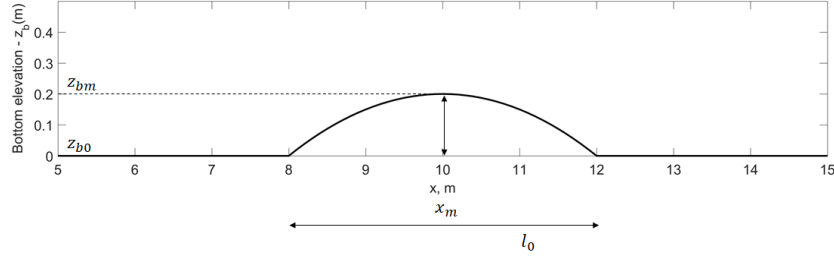


Figure 4.6: Geometry definition for test case T03, side view along flow distance

Table 4.3: Parameters for the test case over a bump (T03)

Symbol	Meaning	Value
$g$	Gravitational acceleration	$9.81\text{m}\cdot\text{s}^{-2}$
$l$	Domain length	$25\text{m} \times 1\text{m}$
$l_0$	Bump length	4m
$x_m$	Middle of bump	10m
$z_{b0}$	Minimum bottom elevation	0m
$z_{bm}$	Maximum bottom elevation	0.2m
$\Delta x$	Cell size	0.1m
$\Delta y$	Cell width	1m
$z_{ini}$	Initial water surface elevation (T03a)	2m
	Initial water surface elevation (T03b)	0.1m
$q_{upstream}$	Prescribed unit discharge at the upstream boundary ( $x = 0\text{m}$ ) for subcritical flow	$4.42\text{m}^2\cdot\text{s}^{-1}$
	for transcritical flow	$1.53\text{m}^2\cdot\text{s}^{-1}$
$h_{downstream}$	Prescribed water depth at the downstream boundary ( $x = 100\text{m}$ )	2m

0.1m  $\times$  1m. The simulation is carried out from an initial velocity in  $x$  direction set to  $0\text{m}\cdot\text{s}^{-1}$  (for both configurations: T03a and T03b) and an initial constant water surface elevation set to  $z_{ini} = 2\text{m}$  (respectively  $z_{ini} = 0.1\text{m}$ ) for test case T03a (respectively T03b). The computational parameters are given in table 4.3. The simulation is carried out until steady flow conditions are reached over the computational domain (after barely 1000s).

The simulation results for subcritical and transcritical flow are presented in figures 4.7 and 4.8. Numerical results show a good agreement between the computed hydraulic variables ( $h$ ,  $z$ ,  $Fr$  and  $q$ ) using either the HLLC or the PorAS Riemann solver and the reference whatever the hydraulic flow regime. However, in both configurations, the total discharge  $Q = \Delta y \times q$  ( $Q = 4.42\text{m}^3\cdot\text{s}^{-1}$  for test case T03a and  $Q = 1.53\text{m}^3\cdot\text{s}^{-1}$  for test case T03b) computed with the PorAS Riemann solver is constant over the whole domain but variable with the HLLC solver. As this test case corresponds to a steady-state flow, the total discharge computed by the HLLC Riemann solver is wrong. This is due to the fact that the total discharge is computed by a Riemann solver at the interface between two cells i.e. based on the geometrical features (bottom elevation and porosity) of both cells whereas the computed (and plotted) values are in the middle of each cell as explained for test case T02.

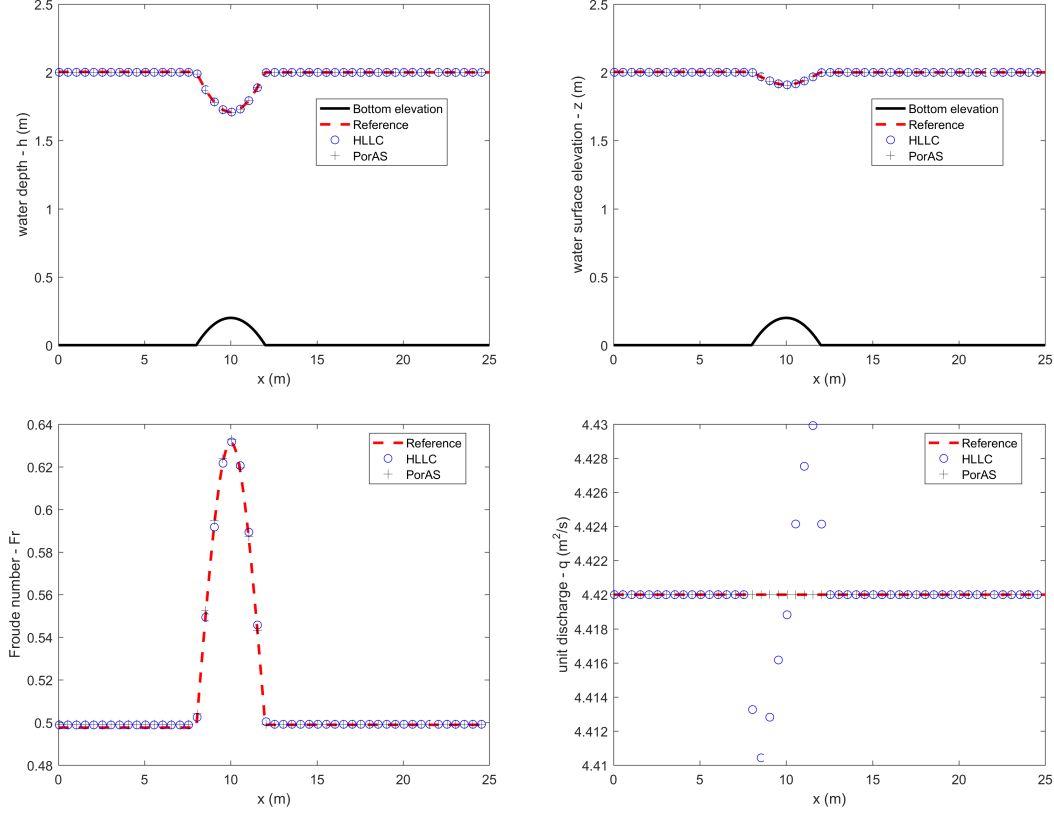


Figure 4.7: Comparison of *Flood1D2D* results (using either the HLLC or the PorAS Riemann solver) with the semi-analytical reference for the test case T03a (subcritical flow regime over a bump). Only 1 point every 5 are plotted in space for the sake of clarity

#### 4.2.4 One-dimensional flow with porosity and bottom bump (T04)

This test case aims at validating the ability of the code to deal with variable porosity and bottom bump in steady state. A permanent flow is thus simulated in a rectangular channel without friction. The evolution of porosity and bottom elevation along the channel is illustrated in figure 4.1.

As highlighted by Finaud-Guyot (2009), the reference solution of this test case is obtained by solving the steady-state momentum conservation equation in a non-prismatic rectangular channel derived from the shallow water equations with porosity and a bottom source term:

$$\phi(1 - Fr^2) \frac{dh}{dx} = hFr^2 \frac{d\phi}{dx} - \phi \frac{dz_b}{dx} \quad (4.4)$$

Equation (4.4) is discretized and solved using an Euler method on a very fine grid ( $\Delta x = 0.002\text{m}$ ) from downstream to upstream for subcritical flow regime. The reference for test case T04 is established using  $q_{upstream} = 1\text{m}^2 \cdot \text{s}^{-1}$  and  $h_{downstream} = 1\text{m}$ .

The domain length is  $l = 40\text{m}$  with a structured mesh of uniform cell size:  $1\text{m} \times 1\text{m}$  (T04a),  $0.1\text{m} \times 1\text{m}$  (T04b) and  $0.01\text{m} \times 1\text{m}$  (T04c) to test the convergence. The computational timestep is reduced accordingly to the space step  $\Delta x$  as *Flood1D2D* uses an adaptive timestep algorithm.

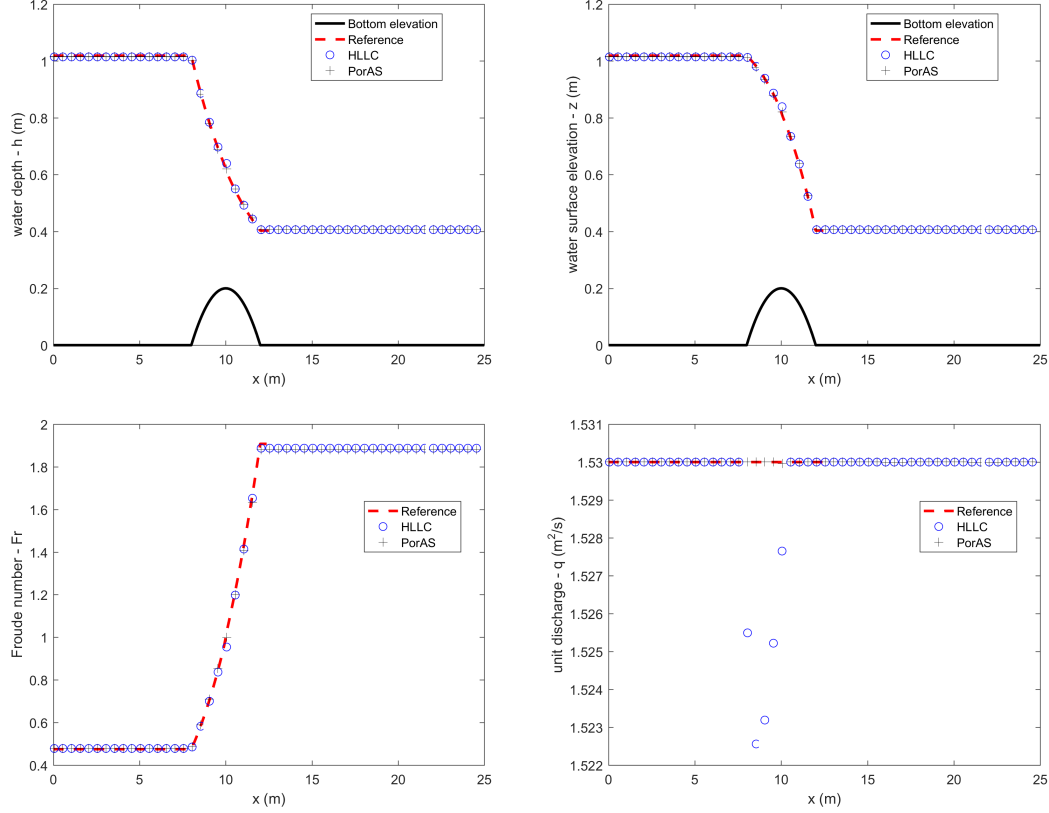


Figure 4.8: Comparison of *Flood1D2D* results (using either the HLLC or the PorAS Riemann solver) with the semi-analytical reference for the test case T03b (transcritical flow regime over a bump). Only 1 point every 5 are plotted for the sake of clarity

For all cases, the simulation is carried out from initial water surface elevation  $z_{ini} = 1\text{m}$  and an initial velocity in  $x$  direction is set to  $0\text{m}\cdot\text{s}^{-1}$ . The computational parameters are given in table 4.4. The simulation is carried out until steady flow conditions are reached over the computational domain (after barely 1000s).

The simulation results based on the different decreasing cell sizes are presented in figures 4.9, 4.10 and 4.11. For every test case, the computed hydraulic variables ( $h$ ,  $q$ ) using the PorAS Riemann solver are closer from the reference than using the HLLC Riemann solver whatever the space discretisation step  $\Delta x$ . As for the previous test cases (and for similar reasons), the total computed discharge  $Q = \phi \times q$  for the HLLC results are not constant (see figure 4.12). Logically, as the cell size decreases, the hydraulic variables (whatever the Riemann solver) get closer to the reference (see figure 4.12).

A convergence study is conducted based on the results of test case T04a, T04b and T04c. Let define the error  $\epsilon_f$  on the computed variable  $f$ :

$$\epsilon_f = \frac{1}{N} \sum_{i=1}^N (f_{i,sim} - f_{i,ref})^2 \quad (4.5)$$

where  $N$  is the total number of cell,  $f_{i,sim}$  is the computed value of the variable  $f$  in cell  $i$

Table 4.4: Parameters used for test cases T04a, T04b and T04c

Symbol	Meaning	Value
$g$	Gravitational acceleration	$9.81\text{m}\cdot\text{s}^{-2}$
$l$	Domain length	$40\text{m} \times 1\text{m}$
$l_0$	Length of the variation zone	20m
$x_0$	Position of the beginning of the variation zone	10m
$\phi_{max}$	Porosity upstream of the variation zone	1
$\phi_{min}$	Porosity downstream of the variation zone	0.7
$z_{min}$	Bottom elevation upstream of the variation zone	0.5m
$z_{max}$	Bottom elevation downstream of the variation zone	1.0m
	Cell size	
	for test case T04a	1m
$\Delta x$	for test case T04b	0.1m
	for test case T04c	0.01m
$\Delta y$	Cell width	1m
$z_{ini}$	Initial water level over the domain	1m
$q_{upstream}$	Prescribed unit discharge at the upstream boundary ( $x = 0\text{m}$ )	$1\text{m}^2\cdot\text{s}^{-1}$
$h_{downstream}$	Prescribed water depth at the downstream boundary ( $x = 40\text{m}$ )	1m

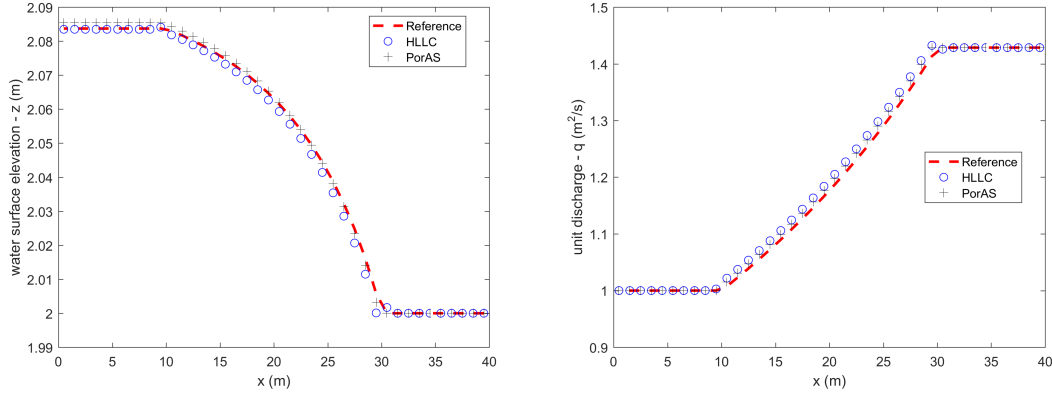


Figure 4.9: First test case for convergence analysis (T04a):  $\Delta x = 1\text{m}$ . Comparison of *Flood1D2D* results (using either the HLLC or the PorAS Riemann solver) with the semi-analytical reference (subcritical flow regime with porosity and bottom bump)

and  $f_{i,ref}$  is the reference value of the variable  $f$  at the gravity center of cell  $i$ . Figure 4.13 presents the evolution of  $\epsilon_h$  and  $\epsilon_q$  when the spatial discretization step  $\Delta x$  is changed for the results computed using the HLLC Riemann solver. Over the range of variation for  $\Delta x$ ,  $\epsilon_h$  and  $\epsilon_q$  decrease with  $\Delta x$  confirming that *Flood1D2D* converges to the reference solution.

All the previous test cases (T01 to T04) have allowed to validate the correct implementation of both HLLC and PorAS Riemann solvers in steady-state configurations. The latter allowing to avoid any miss-evaluation of the total discharge  $Q = \phi \times q$  in the computational cell (even if both solvers correctly compute the fluxes through the mesh interfaces). The following test cases are designed to assess the validity of the Riemann solvers in transient configurations.

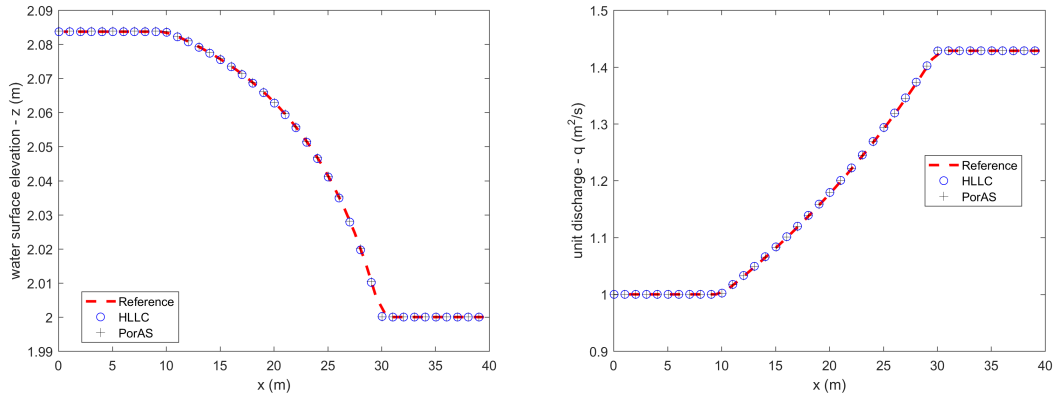


Figure 4.10: Second test case for convergence analysis (T04b):  $\Delta x = 0.1\text{m}$ . Comparison of *Flood1D2D* results (using either the HLLC or the PorAS Riemann solver) with the semi-analytical reference (subcritical flow regime with porosity and bottom bump). Only 1 point every 10 are plotted for the sake of clarity

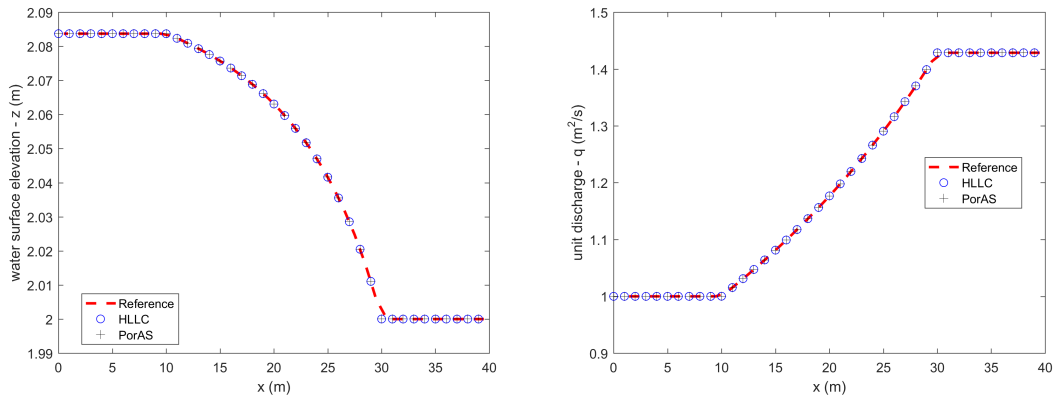


Figure 4.11: Third test case for convergence analysis (T04c):  $\Delta x = 0.01\text{m}$ . Comparison of *Flood1D2D* results (using either the HLLC or the PorAS Riemann solver) with the semi-analytical reference (subcritical flow regime with porosity and bottom bump). Only 1 point every 100 are plotted for the sake of clarity

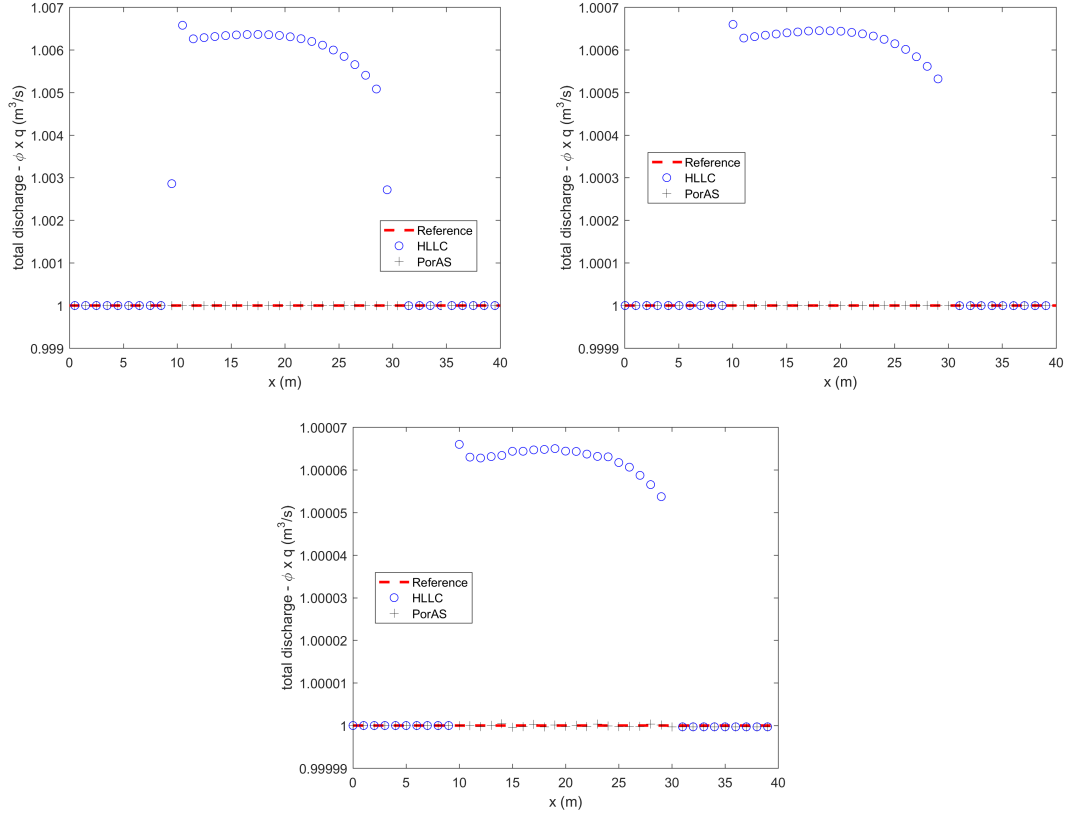


Figure 4.12: Test case for convergence analysis on total discharge (T04a, T04b and T04c). Comparison of *Flood1D2D* results (using either the HLLC or the PorAS Riemann solver) with the semi-analytical reference (subcritical flow regime with porosity and bottom bump). Top left, T04a; top right, T04b; bottom, T04c. For the sake of clarity, only 1 point every 10 (respectively 100) are plotted for T04b (respectively T04c)

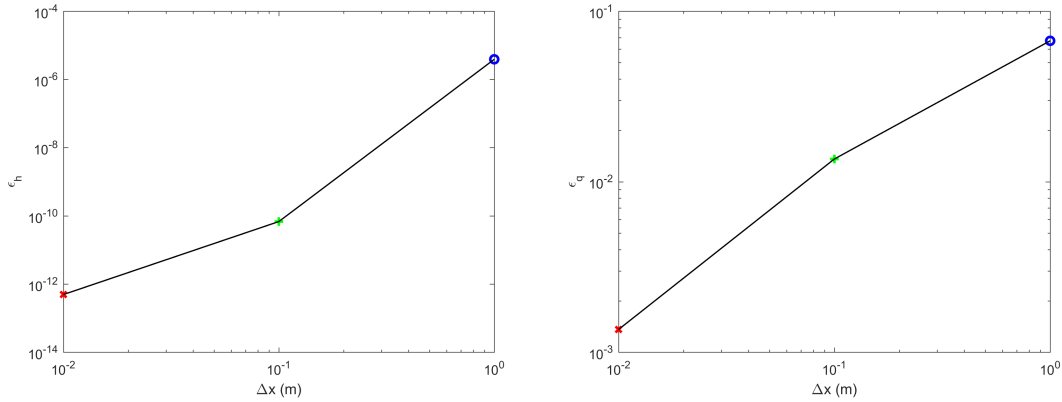


Figure 4.13: Convergence curves on grid size for the HLLC Riemann solver: left, water depth  $h$ ; right, unit discharge  $q$

### 4.2.5 One-dimensional dambreak without porosity (T05)

This test case aims at validating the ability of the code to deal with transient dambreak problem without porosity variation over a flat bottom and with no friction. Two different hydraulic regimes are tested: subcritical (T05a) and transcritical (T05b).

For both hydraulic regimes, the domain is  $l = 200\text{m}$  long with a structured mesh of uniform cell size  $0.1\text{m} \times 1\text{m}$ . The dam is located at  $x_0 = 100\text{m}$  in the middle of the channel and initially separates two zones with no velocity and a constant water level:  $h_{0,L} = 10\text{m}$  and  $h_{0,R} = 5\text{m}$  (respectively  $h_{0,R} = 1\text{m}$ ) for test T05a (respectively T05b). The dam disappears instantaneously at  $t = 0\text{s}$ . The comparison between the reference and the computational results is done at  $t = 8\text{s}$  such as the effect of the dambreak does not reach the boundary of the domain. The computational parameters are summarized in table 4.5. The reference solution for those test cases can be obtained by solving analytically the shallow water equation (Guinot and Soares-Frazão (2006)).

Table 4.5: Parameters for the one-dimensional dambreak problem (T05)

Symbol	Meaning	Value
$g$	Gravitational acceleration	$9.81\text{m}\cdot\text{s}^{-2}$
$l$	Domain length	$200\text{m} \times 1\text{m}$
$x_0$	Dam location	$100\text{m}$
$\Delta x$	Cell size	$0.1\text{m}$
$\Delta y$	Cell width	$1\text{m}$
$h_{0,L}$	Initial water depth on the left-hand side of the dam	$10\text{m}$
	Initial water depth on the right-hand side of the dam	
	For test case T05a	$5\text{m}$
$h_{0,R}$	For test case T05b	$1\text{m}$
$t$	Computation time	$8\text{s}$

The simulation results for subcritical and transcritical flows are presented in figures 4.14. Numerical results show a good agreement between the computed hydraulic variables ( $h$ ,  $q$  and  $Fr$ ) and the reference using either the HLLC or the PorAS Riemann solver whatever the hydraulic flow regime. In both cases, a slight numerical diffusion can be identified at locations where the variable value changes. Even if not presented here, the numerical diffusion can be reduced by decreasing accordingly the computational space and time step. This test case highlights the ability of both Riemann solvers to correctly localize both rarefaction and shock waves.

### 4.2.6 One dimensional velocity dambreak without porosity (T06)

The previous dambreak test case (T05) creates whatever the initial configuration of the water depth (expect  $h_{0,L} = h_{0,R}$  for which there is no test case anymore) both a rarefaction and a shock wave. The test case T06 is also a dambreak problem but the initial discontinuity is applied on the velocity allowing to obtain a solution with two rarefaction waves. In this test case, there is no variation of the porosity nor the bottom elevation and no friction is taken into account. For this test case, two different hydraulic regimes are tested: subcritical (T06a) and transcritical (T06b).

For both hydraulic regimes, the domain is  $l = 200\text{m}$  long with a structured mesh of uniform cell size  $0.1\text{m} \times 1\text{m}$ . The dam is located at  $x_0 = 100\text{m}$  in the middle of the channel and initially separates two zones with a constant water level  $h_{0,L} = h_{0,R} = 1\text{m}$  and a constant velocity  $u_{0,L} = 0\text{m}\cdot\text{s}^{-1}$  and  $u_{0,R} = 3\text{m}\cdot\text{s}^{-1}$  (respectively  $u_{0,R} = 5\text{m}\cdot\text{s}^{-1}$ ) for test T06a (respectively T06b). The dam disappears instantaneously at  $t = 0\text{s}$ . The comparison between the reference

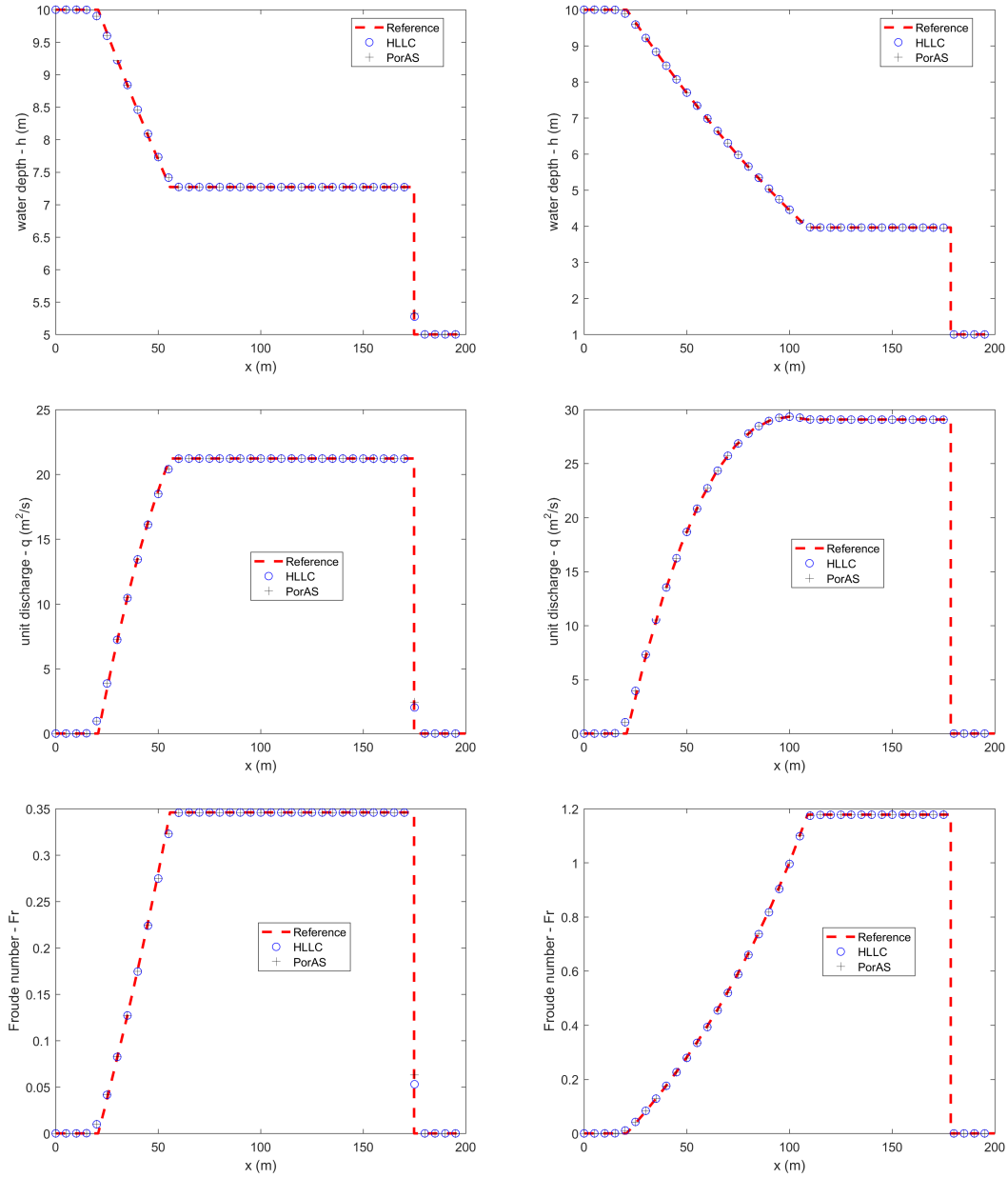


Figure 4.14: Comparison of *Flood1D2D* results (using either the HLLC or the PorAS Riemann solver) with the analytical reference for the test case T05a (subcritical flow regime, left side) and T05b (transcritical flow regime, right side). Only 1 point every 50 are plotted for the sake of clarity

Table 4.6: Parameters for the one-dimensional velocity dambreak problem (T06)

Symbol	Meaning	Value
$g$	Gravitational acceleration	$9.81\text{m}\cdot\text{s}^{-2}$
$l$	Domain length	$200\text{m} \times 1\text{m}$
$x_0$	Dam location	100m
$\Delta x$	Cell size	0.1m
$\Delta y$	Cell width	1m
$u_{0,L}$	Initial velocity on the left-hand side of the dam	$0\text{m}\cdot\text{s}^{-1}$
	Initial velocity on the right-hand side of the dam	
	For test case T06a	$3\text{m}\cdot\text{s}^{-1}$
$u_{0,R}$	For test case T06b	$5\text{m}\cdot\text{s}^{-1}$
$h_{0,L}$	Initial water depth on the left-hand side of the dam	1m
$h_{0,R}$	Initial water depth on the right-hand side of the dam	1m
$t$	Computation time	8s

and the computational results is done at  $t = 8\text{s}$  such as the effect of the dambreak does not reach the boundary of the domain. The computational parameters are summarized in table 4.6. The reference solution of those test cases can be obtained by solving analytically the shallow water equation (Guinot and Soares-Frazão (2006)).

The simulation results with subcritical and transcritical flow are presented in figures 4.15 and 4.16. Numerical results show a good agreement between the computed hydraulic variables ( $h$ ,  $q$ ,  $u$  and  $\text{Fr}$ ) and the reference using either the HLLC or the PorAS Riemann solver whatever the hydraulic flow regime. As for the case T05, a slight numerical diffusion appears close to the wave location.

#### 4.2.7 One-dimensional dambreak with variable porosity (T07)

The two previous test cases (T05 and T06) highlight the ability of *Flood1D2D* to correctly solve the shallow water equations (3.56) in highly transient configurations without porosity.

This test case aims at validating the ability of the code to deal with transient dambreak problem with a porosity varying linearly from 0 to 1 over a flat bottom with no friction. As presented in Guinot and Soares-Frazão (2006), this one-dimensional dambreak with variable porosity is equivalent to a classical circular dambreak with uniform porosity. The reference is computed as a classical dambreak over a grid with uniform cell width  $\Delta x = 10^{-3}\text{m}$ .

The domain is  $l = 100\text{m}$  long with a structured mesh of uniform cell size  $0.1\text{m} \times 1\text{m}$ . The dam is located at  $x_0 = 50\text{m}$  with an initial water depth of  $h_{0,L} = 10\text{m}$  on the left-hand side of the dam and  $h_{0,R} = 1\text{m}$  on the right hand side; the initial velocity in  $x$  direction is set to  $0\text{m}\cdot\text{s}^{-1}$ . The dam disappears instantaneously at  $t = 0\text{s}$ . The comparison between the reference and the computational results is done at  $t = 4\text{s}$  such as the effect of the dambreak does not reach the boundary of the domain. The computational parameters are given in table 4.7.

The simulation results are presented in figure 4.17. Numerical results show a good agreement between the computed hydraulic variables ( $h$ ,  $q$ ,  $u$  and  $\text{Fr}$ ) and the reference using either the HLLC or the PorAS Riemann solver.

#### 4.2.8 One-dimensional dambreak with porosity discontinuity (T08)

This test case aims at validating the ability of the code to deal with transient dambreak problem with a porosity discontinuity, which is located at the same place that the initial water height

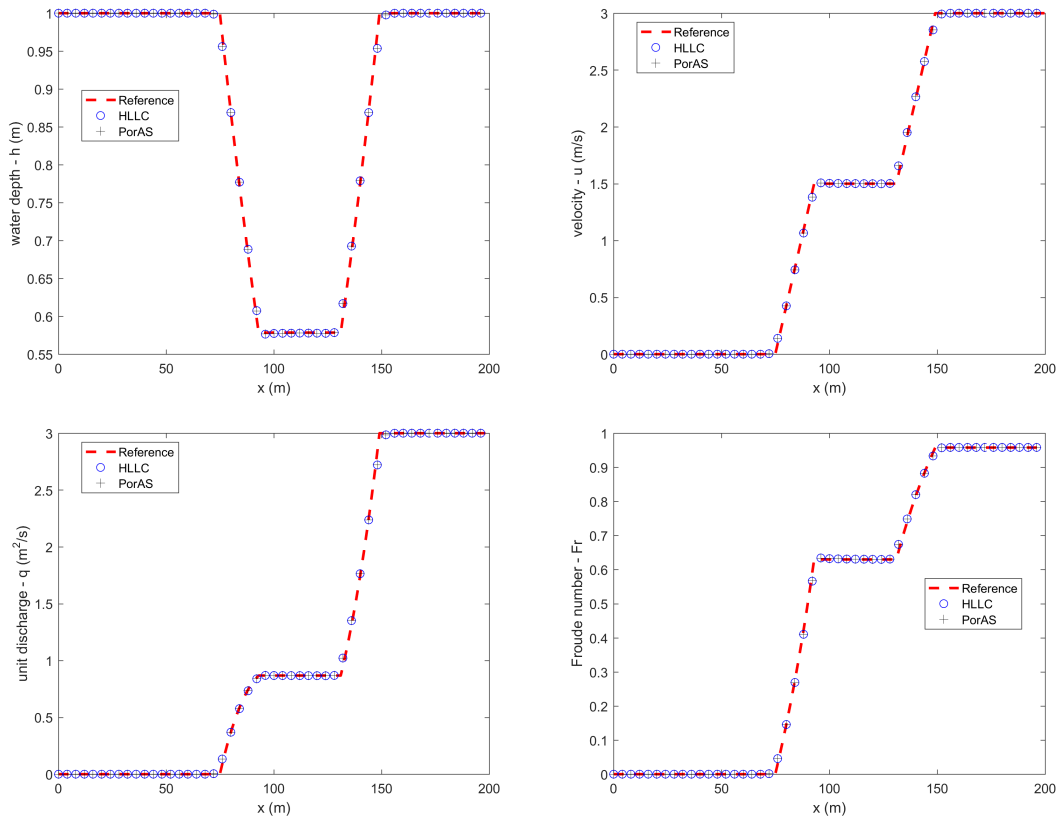


Figure 4.15: Comparison of *Flood1D2D* results (using either the HLLC or the PorAS Riemann solver) with the semi-analytical reference for the test case T06a (subcritical flow regime). Only 1 point every 40 are plotted for the sake of clarity

discontinuity over a flat bottom.

The domain length is  $l = 100\text{m}$  long with a structured mesh of uniform cell size  $1\text{m} \times 1\text{m}$  for T08a,  $0.1\text{m} \times 1\text{m}$  for T08b and  $0.01\text{m} \times 1\text{m}$  for T08c. The dam is located at  $x_0 = 50\text{m}$  in the middle of the channel and initially separates two zones with a constant porosity  $\phi_L = 1$  and  $\phi_R = 0.1$ , water level  $h_{0,L} = 10\text{m}$  and  $h_{0,R} = 1\text{m}$  and the initial velocity in  $x$  direction is set to  $0\text{m}\cdot\text{s}^{-1}$ . The dam disappears instantaneously at  $t = 0\text{s}$ . The comparison between the reference and the computational results is done at  $t = 4\text{s}$  such as the effect of the dambreak does not reach the boundary of the domain. The computational parameters are summarized in table 4.8. The reference solutions of those test cases can be obtained by solving analytically the shallow water equation with porosity (Guinot and Soares-Frazão (2006)).

For test case T08, the simulation results are presented in figures 4.18. For each mesh, numerical results show a good agreement between the computed hydraulic variables ( $h$  and  $q$ ) and the reference using either the HLLC or the PorAS Riemann solver. However, a slight difference appears between the computed velocity for  $x > 50\text{m}$  and the reference. The gap remains constant as the computational space and time step are decreased accordingly (see figure 4.19 with the velocity), which may be accounted by the Riemann solver adopted.

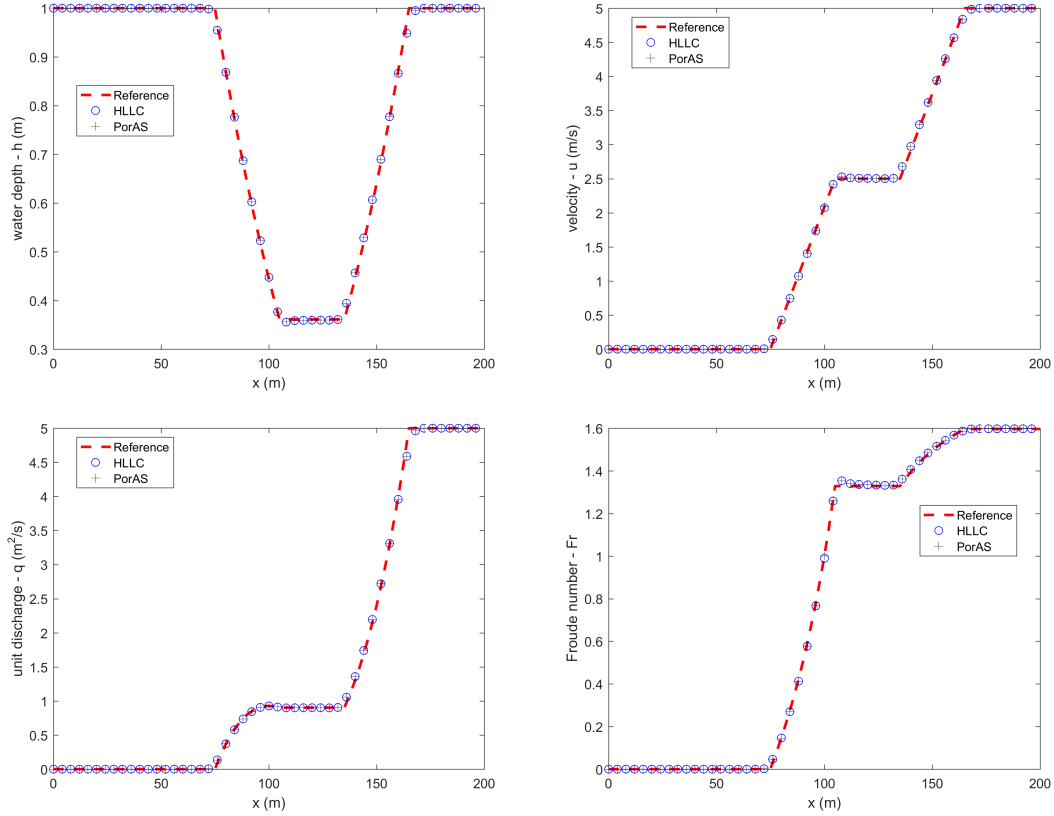


Figure 4.16: Comparison of *Flood1D2D* results (using either the HLLC or the PorAS Riemann solver) with the semi-analytical reference for the test case T06b (transcritical flow regime). Only 1 point every 40 are plotted for the sake of clarity

Table 4.7: Parameters for the one-dimensional dambreak with variable porosity (T07)

Symbol	Meaning	Value
$g$	Gravitational acceleration	$9.81\text{m}\cdot\text{s}^{-2}$
$l$	Domain length	$100\text{m} \times 1\text{m}$
$x_0$	Dam location	50m
$\frac{\partial\phi}{\partial x}$	Derivative of the porosity	$0.01\text{m}^{-1}$
$\Delta x$	Cell size	0.1m
$\Delta y$	Cell width	1m
$h_{0,L}$	Initial water depth on the left-hand side of the dam	10m
$h_{0,R}$	Initial water depth on the right-hand side of the dam	1m
$t$	Computation time	4s

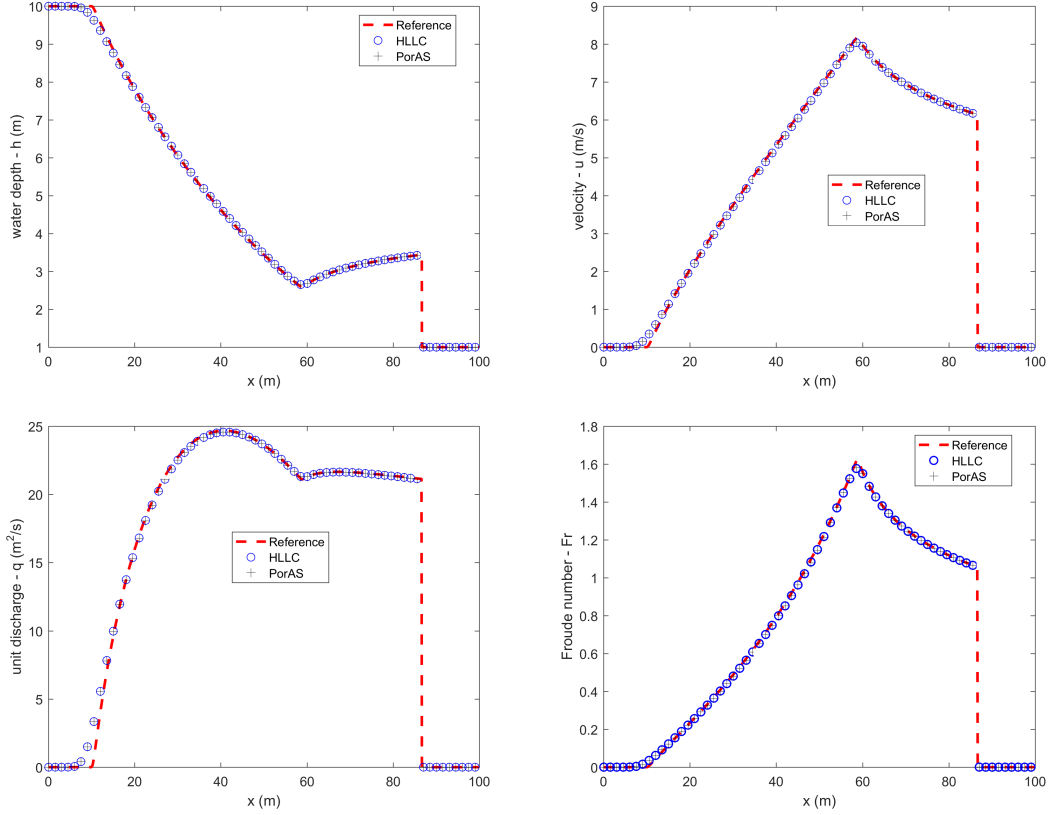


Figure 4.17: Comparison of *Flood1D2D* results (using either the HLLC or the PorAS Riemann solver) with the semi-analytical reference for the test case T07 (transcritical flow regime). Only 1 point every 15 are plotted for the sake of clarity

Table 4.8: Parameters for the one-dimensional dambreak with porosity discontinuity (T08)

Symbol	Meaning	Value
$g$	Gravitational acceleration	$9.81\text{m}\cdot\text{s}^{-2}$
$l$	Domain length	$100\text{m} \times 1\text{m}$
$x_0$	Dam location	50m
$\phi_L$	Porosity on the left-hand side of the dam	1
$\phi_R$	Porosity on the right-hand side of the dam	0.1
	Cell size	
	for test case T08a	1m
$\Delta x$	for test case T08b	0.1m
	for test case T08c	0.01m
$\Delta y$	Cell width	1m
$h_{0,L}$	Initial water depth on the left-hand side of the dam	10m
$h_{0,R}$	Initial water depth on the right-hand side of the dam	1m
$t$	Computation time	4s

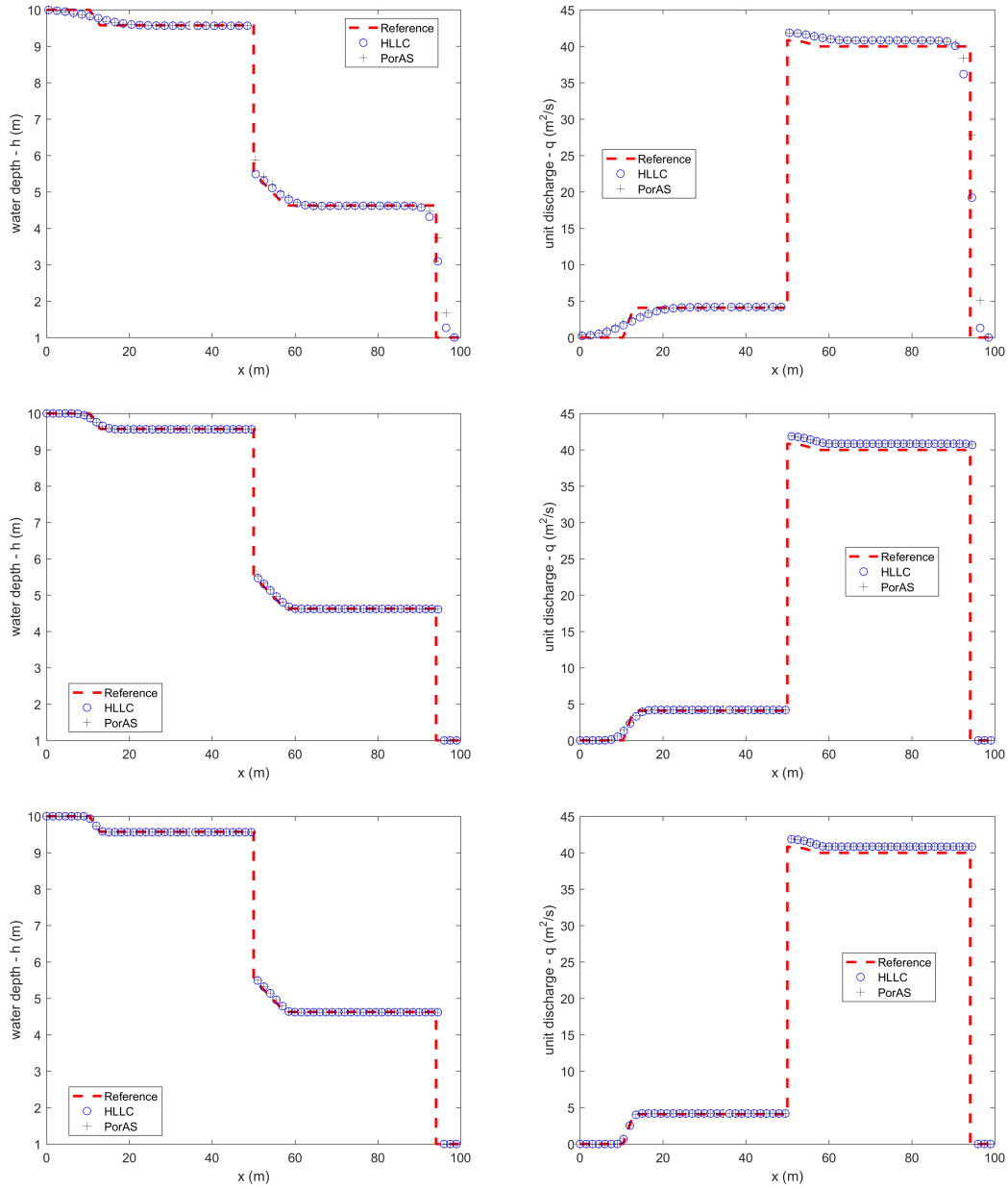


Figure 4.18: Comparison of *Flood1D2D* results (using either the HLLC or the PorAS Riemann solver) with the analytical reference for the test case T08 (transcritical flow regime): top,  $\Delta x = 1\text{m}$ ; middle,  $\Delta x = 0.1\text{m}$ ; bottom,  $\Delta x = 0.01\text{m}$ . For the sake of clarity, only 1 point every 2 (respectively, 15 and 150) are plotted for test case T08a (respectively, T08b and T08c)

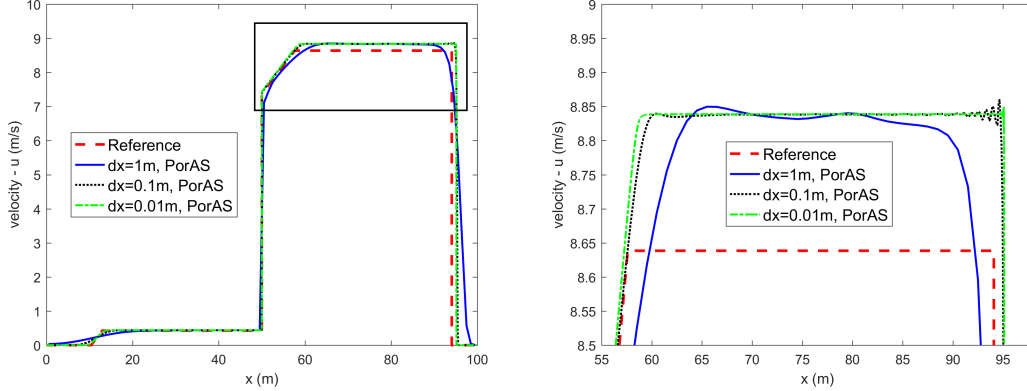


Figure 4.19: Convergence of *Flood1D2D* results (velocity  $u$ ) (using the PorAS Riemann solver) compared with the analytical reference on grid size: left, comparison on velocity; right, zoomed space on rectangular shape

#### 4.2.9 Two-dimensional dambreak with variable porosity (T09)

All the previous test cases highlight the efficiency of both the HLLC and PorAS Riemann solver in one-dimensional configurations. This test case aims at validating the ability of the code to deal with a two-dimensional dambreak problem with a variable porosity over a flat bottom without friction. As shown in Guinot and Soares-Frazão (2006), the circular dambreak problem with a porosity proportional to the inverse of the distance to the center of the dam has the same analytical solution as a classical one-dimensional dambreak with a constant porosity.

The domain length is  $200\text{m} \times 200\text{m}$  wide and the center of the circular dam (having a radius of  $R = 50\text{m}$ ) is located in the middle of the domain in  $(x_0, y_0)$ . The dam initially separates two zones with no velocity and a constant water level:  $h(r \leq R) = 10\text{m}$  and  $h(r > R) = 1\text{m}$ . The porosity is defined as:

$$\phi(x, y) = \frac{1}{r} \quad \text{where } r = \sqrt{(x - x_0)^2 + (y - y_0)^2} \quad (4.6)$$

The dam disappears instantaneously at  $t = 0\text{s}$ . The comparison between the reference and the computational results is done at  $t = 4\text{s}$  such as the effect of the dambreak does not reach the boundary of the domain. The computational parameters are given in table 4.9.

The computation is done using an unstructured mesh with triangular cells of typical dimension  $\Delta x = 1\text{m}$ . Figure 4.20 presents both the water depth and the unit-discharge profile along the radius of the dam (either aligned with the  $x$  or  $y$  direction). Numerical results show a good agreement between the computed hydraulic variables using either the HLLC or the PorAS Riemann solver and the reference. Moreover the profiles are very similar whatever the orientation chosen (either  $x$  or  $y$ ) highlighting that *Flood1D2D* does not introduce anisotropy when solving this dambreak problem.

### 4.3 Friction handling

The algorithm used in *Flood1D2D* being based on the time splitting method (see section 3.2.4), the computation of the hyperbolic fluxes is done first, then the friction effect is taken into account. The Riemann solver is only used for the hyperbolic flux computation and since both HLLC and

Table 4.9: Parameters for the two-dimensional dambreak with variable porosity (T09)

Symbol	Meaning	Value
$g$	Gravitational acceleration	$9.81\text{m}\cdot\text{s}^{-2}$
$l$	Domain length	$200\text{m} \times 200\text{m}$
$R$	Radius of the dam	50m
$\phi$	Porosity	$\frac{1}{r}$ ( $0 \leq r \leq 100$ )
$\Delta x$	Cell size in x direction	1m
$\Delta y$	Cell size in y direction	1m
$h_{0,L}$	Initial water depth on the left-hand side of the dam	10m
$h_{0,R}$	Initial water depth on the right-hand side of the dam	1m
$t$	Computation time	4s

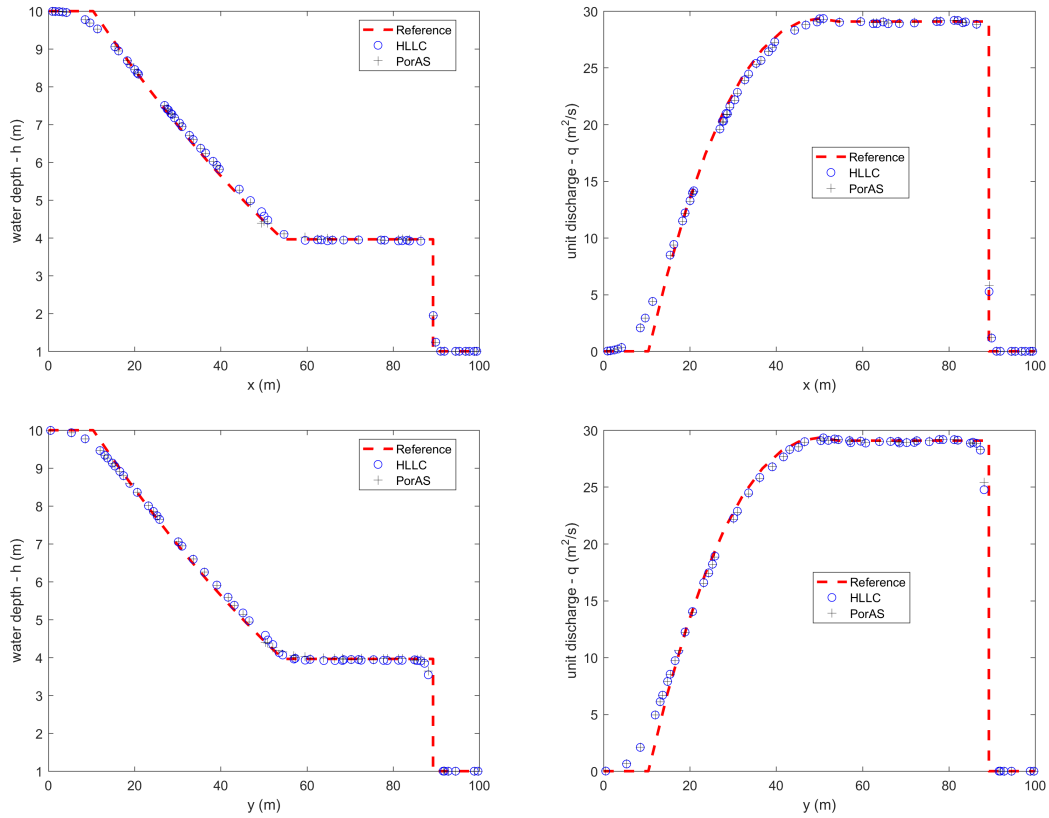


Figure 4.20: Two-dimensional dambreak with variable porosity for the test case T09 using triangular mesh elements. Comparison of *Flood1D2D* results (using either the HLLC or the PorAS Riemann solver) with the analytical reference. Top, X-axis; bottom, Y-axis. Only 1 point every 4 are plotted for the sake of clarity

PorAS solvers are validated and show similar results (see section 4.2), all the following test cases are only performed using the PorAS solver.

The friction computation is validated on two test cases: a comparison of the computed water surface profile with a classical backwater curve (T10) and a comparison between the converged water depth and the theoretical normal depth in both sub- and supercritical configurations.

### 4.3.1 Backwater curve comparison (T10)

This test case aims to check the ability of *Flood1D2D* to correctly take into account the friction effect. A steady-state flow is thus simulated in a rectangular channel of width  $B = 5\text{m}$  over a flat bottom ( $S_0 = 0\text{m.m}^{-1}$ ) and compared to the classical backwater curve:

$$\begin{aligned} \frac{dh}{dx} &= \frac{S_o - S_f}{1 - \text{Fr}^2} \\ S_f &= \left( \frac{Q}{KBh^{5/3}} \right)^2 \\ \text{Fr} &= \frac{Q}{Bh\sqrt{gh}} \end{aligned} \quad (4.7)$$

Note that the expression of  $S_f$  in equation (4.7) is written with the assumption that the hydraulic radius  $R_h$  is equal to the water depth  $h$  as it is implemented in *Flood1D2D*. Equation (4.7) is discretized and solved using an Euler method on a very fine grid ( $\Delta x = 0.001\text{m}$ ) from downstream to upstream for subcritical flow regime:

$$h_{i-1} = h_i - \Delta x \frac{S_0 - S_f(h_i)}{1 - \text{Fr}^2(h_i)} \quad (4.8)$$

The reference for test case T10 is established using  $q_{upstream} = 0.05\text{m}^2.\text{s}^{-1}$  and  $h_{downstream} = 0.1\text{m}$ .

The domain length is  $l = 100\text{m}$  long with a grid of uniform cell width  $0.1\text{m} \times 1\text{m}$ . The simulation is carried out from an initial water level  $z_{ini} = 0.1\text{m}$  and no initial velocity. The friction coefficient  $K$  is set to  $25\text{m}^{1/3}.\text{s}^{-1}$ . The computational parameters are summarized in table 4.10. The simulation is carried out until steady flow conditions are reached over the computational domain.

Table 4.10: Parameters for one-dimensional flow with friction (T10)

Symbol	Meaning	Value
$g$	Gravitational acceleration	$9.81\text{m}.\text{s}^{-2}$
$l$	Domain length	$100\text{m} \times 1\text{m}$
$B$	Channel width	$5\text{m}$
$S_0$	Bottom slope	$0\text{m}.\text{m}^{-1}$
$\Delta x$	Cell size	$0.1\text{m}$
$\Delta y$	Cell width	$1\text{m}$
$z_{ini}$	Initial water level	$0.1\text{m}$
$q_{upstream}$	Prescribed unit discharge at the upstream boundary ( $x = 0\text{m}$ )	$0.05\text{m}^2.\text{s}^{-1}$
$h_{downstream}$	Prescribed water depth at the downstream boundary ( $x = 100\text{m}$ )	$0.1\text{m}$
$K$	Strickler coefficient	$25\text{m}^{1/3}.\text{s}^{-1}$

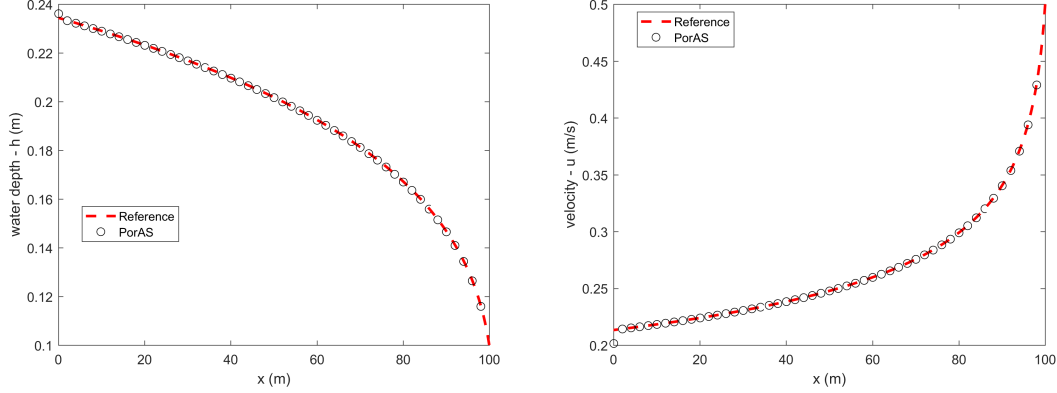


Figure 4.21: Comparison of *Flood1D2D* results (using either the HLLC or the PorAS Riemann solver) for the test case T10 (subcritical flow regime with friction). Only 1 point every 20 are plotted for the sake of clarity

The simulation results are presented in figure 4.21. Numerical results show a good agreement between the computed hydraulic variables ( $h$ , and  $u$ ) using the PorAS Riemann solver and the reference.

### 4.3.2 Normal depth computation (T11)

This test case aims to check the ability of *Flood1D2D* to correctly take into account the friction effect and the bottom slope. A steady-state flow is thus simulated in a rectangular channel of width  $B = 5\text{m}$  with bottom slope  $S_0 = 0.001\text{m.m}^{-1}$  (respectively  $S_0 = 0.005\text{m.m}^{-1}$ ) for test case T11a (respectively T11b) and compared to the classical backwater curve obtained using equation 4.7. Equation (4.7) is discretized and solved using an Euler method on a very fine grid ( $\Delta x = 0.001\text{m}$ ) from downstream to upstream for subcritical flow regime (equation (4.8)). The reference for test case T11a (respectively T11b) is established using  $q_{upstream} = 2\text{m}^2.\text{s}^{-1}$  and  $h_{downstream} = 1\text{m}$  (respectively  $h_{downstream} = 0.7\text{m}$ ).

For test case T11a (respectively T11b), the domain length is  $l = 3000\text{m}$  (respectively  $l = 500\text{m}$ ) long with a grid of uniform cell width  $3\text{m} \times 5\text{m}$  (respectively  $0.5\text{m} \times 5\text{m}$ ). The simulation is carried out from an initial water level  $z_{ini} = 1\text{m}$  (respectively  $z_{ini} = 0.5\text{m}$ ) and no initial velocity. The friction coefficient  $K$  is set to  $25\text{m}^{1/3}.\text{s}^{-1}$  (respectively  $K = 90\text{m}^{1/3}.\text{s}^{-1}$ ). The computational parameters are summarized in table 4.11 (respectively table 4.12). The simulations are carried out until steady flow conditions are reached over the computational domain.

The simulation results are presented in figures 4.22 and 4.23. Numerical results show a good agreement between the computed hydraulic variables ( $h$ , and  $Fr$ ) using the PorAS Riemann solver and the reference.

## 4.4 Cut cell technique

A novelty of the developed model *Flood1D2D* is the use of a cut cell technique. Several test cases are developed to show that this new functionality allows to simulate correctly specific hydraulic problems of flow contraction/expansions while being insensitive to mesh type change between 1D-like and 2D domains.

Table 4.11: Parameters for one-dimensional flow with friction and bottom slope (T11a)

Symbol	Meaning	Value
$g$	Gravitational acceleration	$9.81\text{m}\cdot\text{s}^{-2}$
$l$	Domain length	$3000\text{m} \times 5\text{m}$
$B$	Channel width	5m
$S_0$	Bottom slope	$0.001\text{m}\cdot\text{m}^{-1}$
$\Delta x$	Cell size	3m
$\Delta y$	Cell width	5m
$z_{ini}$	Initial water level	1m
$q_{upstream}$	Prescribed unit discharge at the upstream boundary ( $x = 0\text{m}$ )	$2\text{m}^2\cdot\text{s}^{-1}$
$h_{downstream}$	Prescribed water depth at the downstream boundary ( $x = 3234\text{m}$ )	1m
$K$	Strickler coefficient	$25\text{m}^{1/3}\cdot\text{s}^{-1}$

Table 4.12: Parameters for one-dimensional flow with friction and bottom slope (T11b)

Symbol	Meaning	Value
$g$	Gravitational acceleration	$9.81\text{m}\cdot\text{s}^{-2}$
$l$	Domain length	$500\text{m} \times 5\text{m}$
$B$	Channel width	5m
$S_0$	Bottom slope	$0.005\text{m}\cdot\text{m}^{-1}$
$\Delta x$	Cell size	0.5m
$\Delta y$	Cell width	5m
$z_{ini}$	Initial water level	0.5m
$q_{upstream}$	Prescribed unit discharge at the upstream boundary ( $x = 0\text{m}$ )	$2\text{m}^2\cdot\text{s}^{-1}$
$h_{downstream}$	Prescribed water depth at the downstream boundary ( $x = 539\text{m}$ )	0.7m
$K$	Strickler coefficient	$90\text{m}^{1/3}\cdot\text{s}^{-1}$

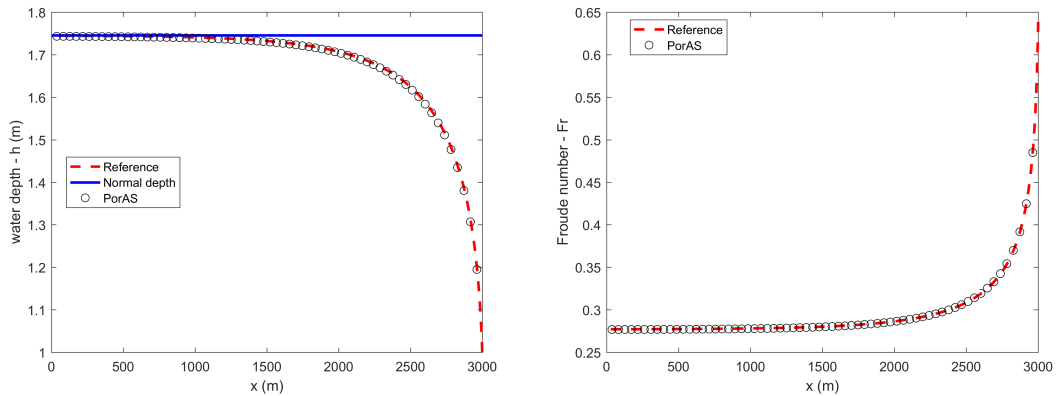


Figure 4.22: Comparison of *Flood1D2D* results (using the PorAS Riemann solver) for the test case T11a (subcritical flow regime with friction). Only 1 point every 15 are plotted for the sake of clarity

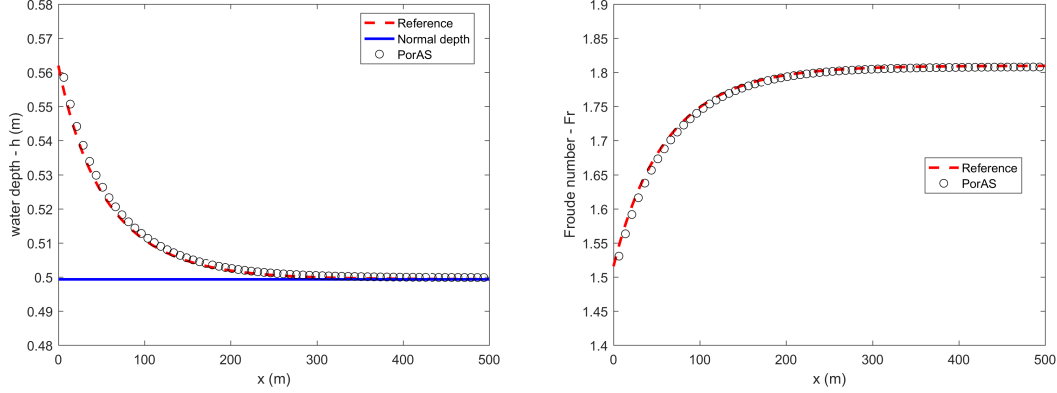


Figure 4.23: Comparison of *Flood1D2D* results (using the PorAS Riemann solver) for the test case T11b (supercritical flow regime with friction). Only 1 point every 15 are plotted

#### 4.4.1 Water at rest over variable bottom elevation and porosity (T12)

This test case aims to check that the computation at the junction between a 1D and a 2D parts of the mesh does not introduce unexpected fluxes (in case of implementation error). The domain represents a three-branch rectangular channel junction: 3 channels of 30m long and 10m large joining at  $90^\circ$  in a junction measuring  $10\text{m} \times 10\text{m}$  (see figure 4.24, top). The channels are considered as 1D parts of the mesh ( $\Delta x_{1D} = 10\text{m}$ ) and the junction is 2D ( $\Delta x_{2D} = 5\text{m}$ ). Water at rest is simulated considering a variable bottom elevation (see figure 4.24, bottom left) and porosity (see figure 4.24, bottom right).

The simulation is carried out from an initial water elevation  $z_{ini} = 10\text{m}$  and no velocity. At each channel end, a water elevation  $z_{BC} = 10\text{m}$  is set for the boundary conditions (see figure 4.24, top). The computational parameters are given in table 4.13. The simulation is carried out during 1000s, time at which the computed water depth and water surface elevation are presented (see figure 4.25, top). After 1000s, the initial water surface elevation is preserved and the water remain stagnant (in every cell:  $u = 0\text{m}\cdot\text{s}^{-1}$  and  $v = 0\text{m}\cdot\text{s}^{-1}$ , see figure 4.25, bottom). Those results highlight that the cut-cell technique implemented allows to preserve the well-balancing property of *Flood1D2D*.

Table 4.13: Parameters for 1D2D coupling cases (T12)

Symbol	Meaning	Value
$g$	Gravitational acceleration	$9.81\text{m}\cdot\text{s}^{-2}$
$l$	Domain length	$70\text{m} \times 40\text{m}$
$S_{0,x}$	Slope in x direction	$0.1\text{m}\cdot\text{m}^{-1}$
$S_{0,y}$	Slope in y direction	$-0.1\text{m}\cdot\text{m}^{-1}$
$\Delta x_{1D}$	Cell size for 1D mesh	10m
$\Delta x_{2D}$	Cell size for 2D mesh	5m
$z_{ini}$	Initial water level over the domain	10m
$u_{ini}$	Initial velocity at x direction	$0\text{m}\cdot\text{s}^{-1}$
$v_{ini}$	Initial velocity at y direction	$0\text{m}\cdot\text{s}^{-1}$
$z_{BC}$	Water surface elevation at boundary conditions	10m
$t$	Computation time	1000s

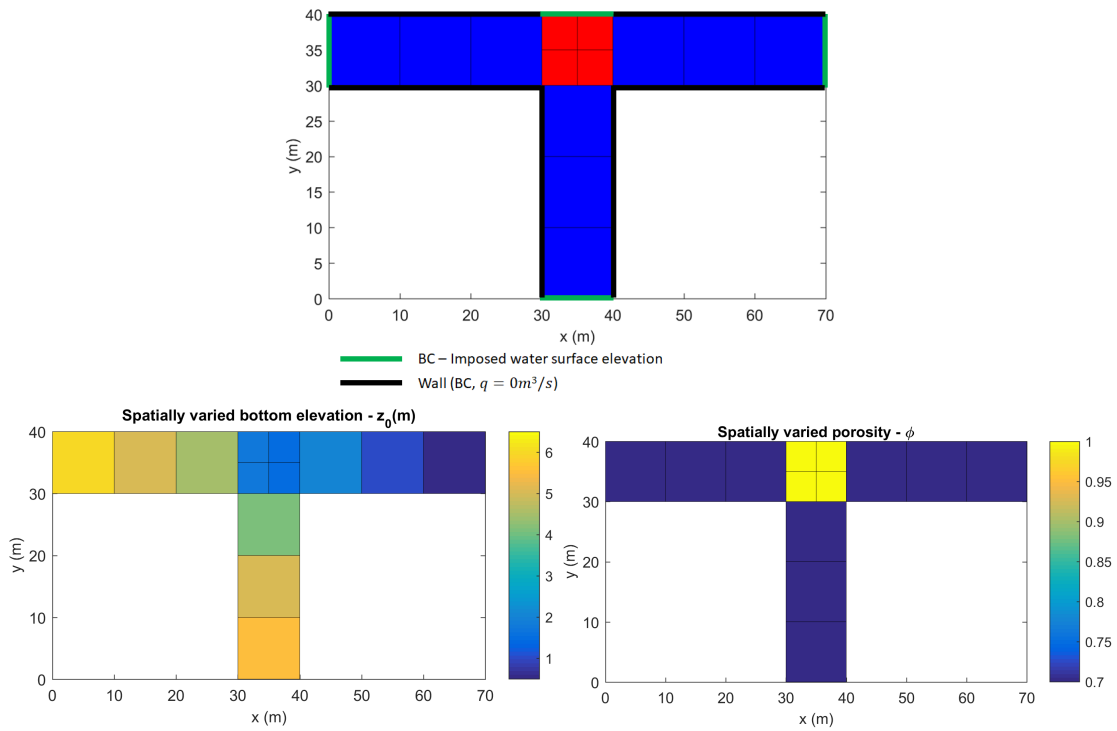


Figure 4.24: Parameterization of test case T12: top, 1D2D mesh, blue is 1D mesh and red is 2D; bottom left, spatially varied bottom elevation  $z_0$ ; bottom right, spatially varied porosity  $\phi$

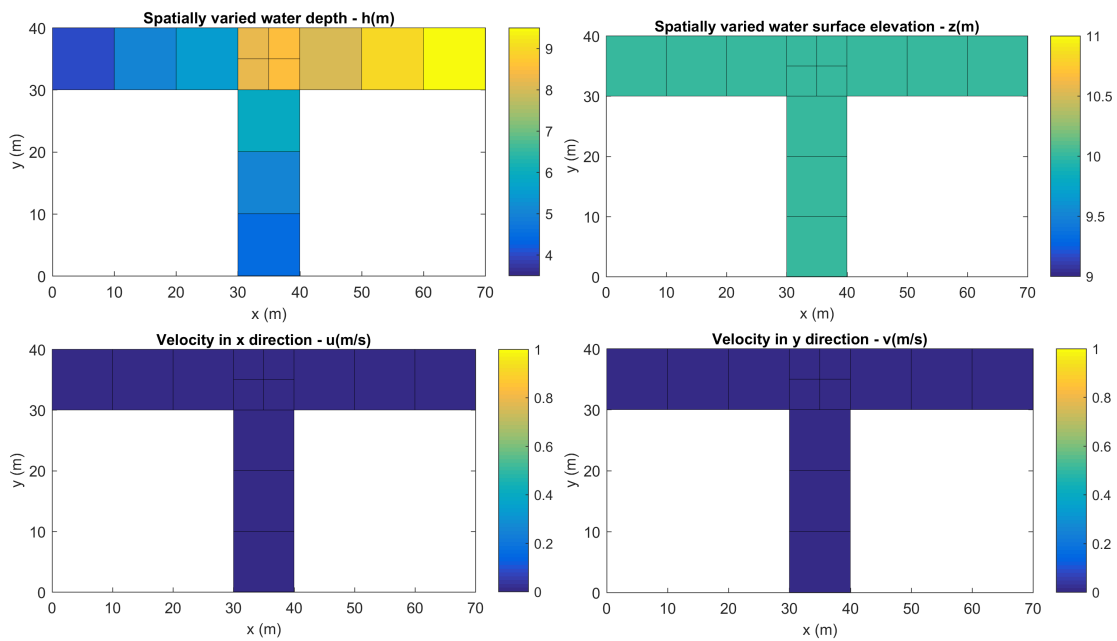


Figure 4.25: *Flood1D2D* results over variable bottom elevation and porosity for the test case T12 (1D2D coupling): top left, water depth  $h$ ; top right, water surface elevation  $z$ ; bottom left, velocity  $u$ ; bottom right, velocity  $v$

#### 4.4.2 Steady-state flow in a variable width rectangular channel (T13)

This test case aims to check that the model at the junction between a 1D and a 2D parts of the mesh correctly estimates the flux between the two parts of the mesh. The domain is a rectangular channel with a length  $l = 400\text{m}$  with 5 reaches of various widths (see table 4.14). The channel is meshed with 1D and 2D parts such as reproducing all possible configurations between 1D and 2D zones that may be encountered (see figure 4.26). Particularly, two different meshing for the junction between 1D and 2D parts of the mesh have been created: at  $x = 50\text{m}$  the junction corresponds exactly with the width variation and at  $x = 250\text{m}$ , the 2D part overlaps the width variation. Connecting a unique cell (1D part) to a larger 2D mesh does not require any meshing trick (at  $x=100\text{m}$ ) whereas connecting multiple 2D cells to a larger unique cell requires a meshing trick (cf. zoom 3, see chapter 3 section 3.2.1 for details).

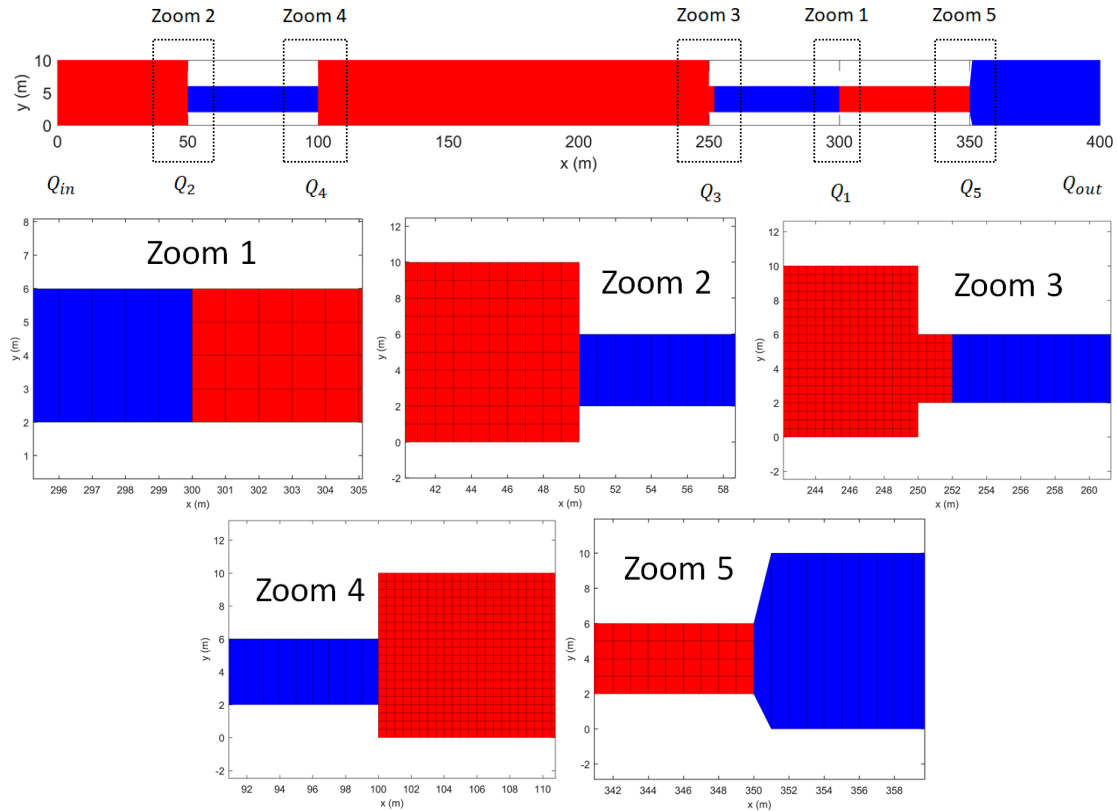


Figure 4.26: Map of the full domain with 1D and 2D mesh (blue is a 1D mesh and red is a 2D mesh) for test case T13: Zoom 1, zoom on mesh junction ( $x = 300\text{m}$ ) - 1D to 2D (same width); Zoom 2, zoom on mesh junction ( $x = 50\text{m}$ ) - 2D to narrower 1D; Zoom 3, zoom on mesh junction ( $x = 250\text{m}$ ) - 2D to narrower 1D; Zoom 4, zoom on mesh junction ( $x = 100\text{m}$ ) - 1D to larger 2D; Zoom 5, zoom on mesh junction ( $x = 350\text{m}$ ) - 2D to larger 1D

The simulation is carried out over a flat bottom without friction with an initial water surface elevation  $z_{ini} = 1\text{m}$  and the initial velocity in  $x$  and  $y$  direction is set to  $0\text{m}\cdot\text{s}^{-1}$ . The test case is established using  $q_{upstream} = 1\text{m}^2\cdot\text{s}^{-1}$  and  $h_{downstream} = 1\text{m}$ . The computational parameters

Table 4.14: Parameters for 1D2D coupling case with varied width (T13)

Symbol	Meaning	Value
$g$	Gravitational acceleration	$9.81\text{m}\cdot\text{s}^{-2}$
$l$	Domain length	$10\text{m} \times 1\text{m}$
$B_1$	Width of the channel from 0m to 50m	10m
$B_2$	Width of the channel from 50m to 100m	4m
$B_3$	Width of the channel from 100m to 250m	10m
$B_4$	Width of the channel from 250m to 350m	4m
$B_5$	Width of the channel from 350m to 400m	10m
$\Delta x_{1D}$	Cell size for 1D mesh	0.25m
$\Delta x_{2D}$	Cell size for 2D mesh	0.25m
$z_{ini}$	Initial water surface elevation over the domain	1m
$u_{ini}$	Initial velocity at x direction	$0\text{m}\cdot\text{s}^{-1}$
$v_{ini}$	Initial velocity at y direction	$0\text{m}\cdot\text{s}^{-1}$
$q_{upstream}$	Prescribed unit discharge at the upstream boundary ( $x = 0\text{m}$ )	$1\text{m}^2\cdot\text{s}^{-1}$
$h_{downstream}$	Prescribed water depth at the downstream boundary ( $x = 400\text{m}$ )	1m
$Q$	Total discharge	$10\text{m}^3\cdot\text{s}^{-1}$

are given in table 4.14. The simulation is carried out until steady flow conditions are reached over the computational domain (after barely 1500s).

The discharges at the junction between the 1D and the 2D parts and the water depth computed are presented in figure 4.27. Figure 4.27c shows the total discharge computed at the boundaries of the domain and at the junction (see figure 4.26, top) between each submesh part. The computed discharge differs from the reference (total discharge  $Q$ ) from less than 0.5%; this is explained by the simulation that is not fully converged. However, it highlights that *Flood1D2D* is able to correctly estimate the flux between the subparts of the mesh. Figures 4.27a and 4.27b plot the water depth along the channel. The water level remains barely flat on each reach of constant width even if the reach is subdivided into a 1D and a 2D mesh part. The water level changes are due to the width variations of the channel.

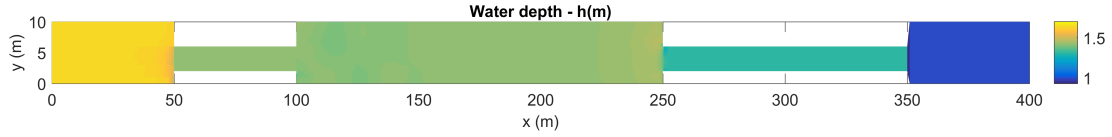
#### 4.4.3 Steady-state flow in a rectangular channel with various 1D2D junction orientation (T14)

This test case aims to check that the orientation of a junction between a 1D and a 2D part of the mesh has no impact on the flux computation. A steady state flow is thus simulated in a rectangular channel without friction nor slope.

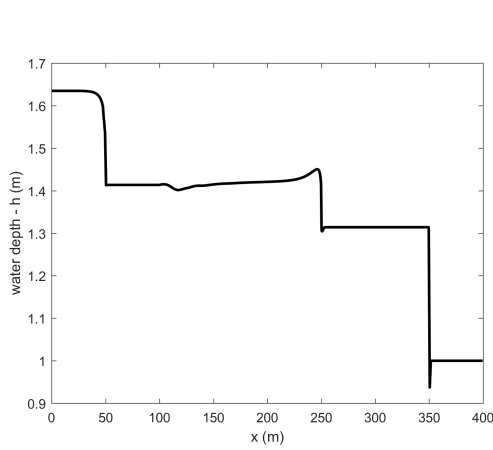
For this simulation, the domain length is  $l = 225\text{m}$  with a uniform width  $B = 10\text{m}$ . The mesh involves both 1D and 2D parts with oblique edges between cells to check if flux orientation remains unaffected through those edges (see figure 4.28). The average dimensions of the cells are:  $2\text{m} \times 10\text{m}$  for the 1D part and  $2\text{m} \times 2\text{m}$  for 2D part of the mesh.

The simulation is carried out over a flat bottom without friction with an initial water surface elevation  $z_{ini} = 5\text{m}$  and the initial velocity in  $x$  and  $y$  direction is set to  $0\text{m}\cdot\text{s}^{-1}$ . The test case is established using  $q_{upstream} = 10\text{m}^2\cdot\text{s}^{-1}$  and  $h_{downstream} = 5\text{m}$ . The computational parameters are summarized in table 4.15. The simulation is carried out until steady flow conditions are reached over the computational domain (after barely 10000s).

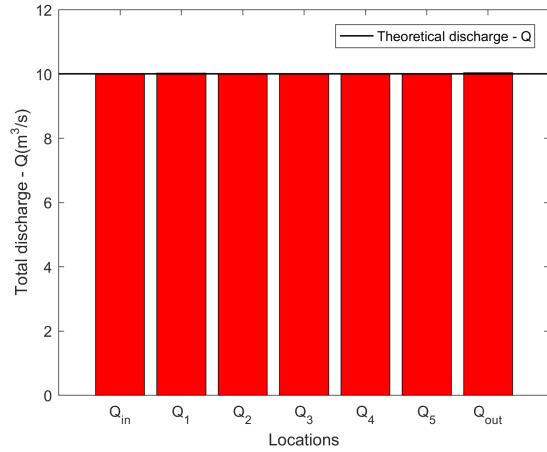
The simulation results are presented in figure 4.29. The water depth profile is constant and equal to the prescribed downstream water depth which is coherent with a computation without



(a) The map of water depth -  $h$



(b) Water depth along the channel from upstream to downstream



(c) Fluxes at boundary conditions and interfaces

Figure 4.27: *Flood1D2D* results with varied channel width for the test case T13 (1D2D coupling)

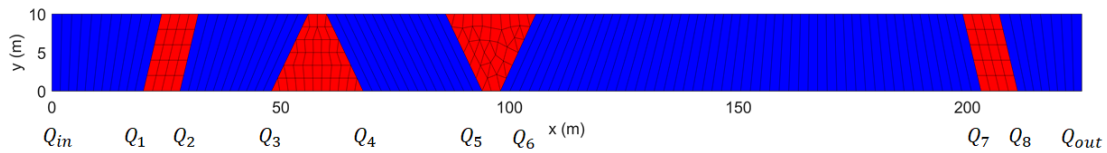
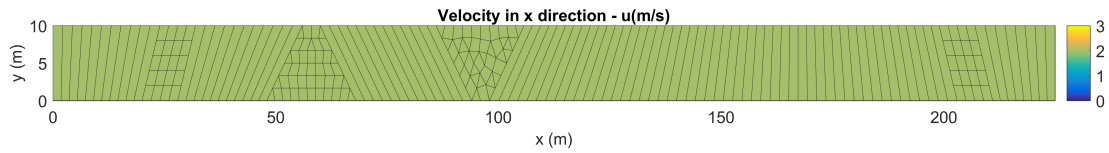


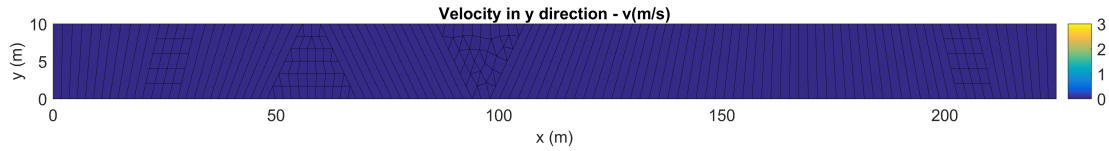
Figure 4.28: Map of the full domain with 1D and 2D mesh (blue is 1D mesh and red is 2D)

Table 4.15: Parameters for 1D2D coupling case with varied width (T14)

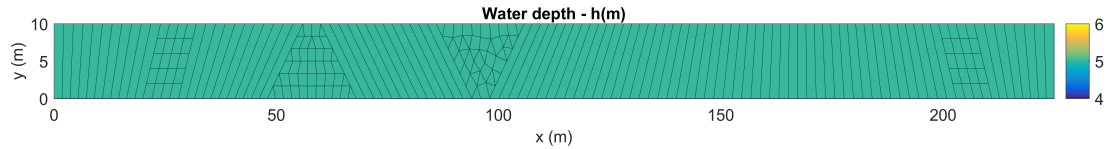
Symbol	Meaning	Value
$g$	Gravitational acceleration	$9.81\text{m}\cdot\text{s}^{-2}$
$l$	Domain length	$225\text{m} \times 10\text{m}$
$B$	Width of the channel	10m
$\Delta x_{1D}$	Cell size for 1D mesh	$2\text{m} \times 10\text{m}$
$\Delta x_{2D}$	Cell size for 2D mesh	$2\text{m} \times 2\text{m}$
$z_{ini}$	Initial water surface elevation over the domain	5m
$q_{upstream}$	Prescribed unit discharge at the upstream boundary ( $x = 0\text{m}$ )	$10\text{m}^2\cdot\text{s}^{-1}$
$h_{downstream}$	Prescribed water depth at the downstream boundary ( $x = 225\text{m}$ )	5m
$t$	Computation time	10000s



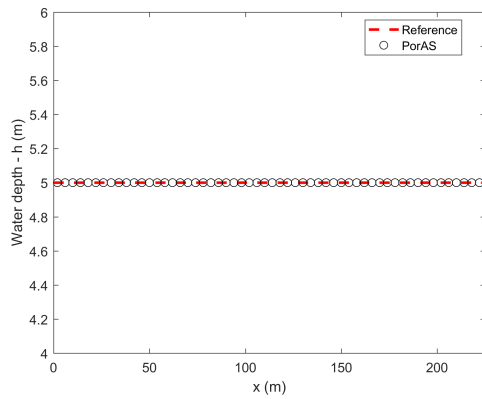
(a) The map of velocity field  $u$  over the domain



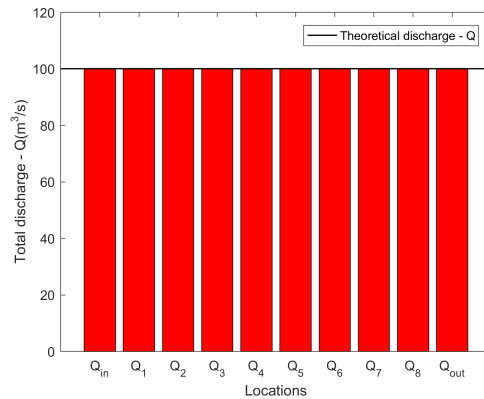
(b) The map of velocity field  $v$  over the domain



(c) The map of water depth -  $h$  over the whole domain



(d) Water depth along the channel from upstream to downstream



(e) Fluxes across the boundaries and interfaces

Figure 4.29: Comparison of *Flood1D2D* results (using the PorAS Riemann solver) for test case T13

friction (see figures 4.29c and 4.29d). The total discharge computed at the boundaries of the domain and at the junctions between the 1D and 2D part of the mesh (see figure 4.29e) is constant over the whole domain highlighting that the orientation of the junction has no impact on the flux computation. The velocity vector maps (see figures 4.29a and 4.29b) show that all velocity vectors are aligned with the channel direction; this highlights that any orientation of computational edge with respect to the flux direction allows to produce good results.

#### 4.4.4 Dambreak in channels with 90° bend (T15)

This test case aims to demonstrate the ability of the 1D2D coupling method implemented in *Flood1D2D* to correctly model a highly transient hydrodynamics. *Flood1D2D* is thus compared to an experimental dambreak in open channel with 90° bend (Soares-Frazão and Zech (2002)).

##### 4.4.4.1 Description of the experiment

The experimental geometry is composed of a rectangular channel of width  $B = 0.495\text{m}$  with a 90° bend. The canal is connected to a reservoir of dimensions  $2.44\text{m} \times 2.39\text{m}$  that is located 4m upstream of the bend and is then ended after 3m with a free fall. The channel is initially empty and the initial water level in the reservoir is  $z_{ini} = 0.25\text{m}$  above the bottom of the channel (figure 4.30, left side). At  $t = 0\text{s}$ , a flap gate is opened and the water flows out of the reservoir and reaches the bend, then changes direction abruptly. The wave reflection on the opposite wall of the bend ( $x = 6.805\text{m}$ ) causes the increase of water height in the bend. Water then propagates to upstream and downstream of the bend. During the experiment, the water level in the reservoir decreases until it reaches the level of the channel bottom. The manning roughness is  $0.011\text{m}^{-1/3}\cdot\text{s}$  as described by the authors.

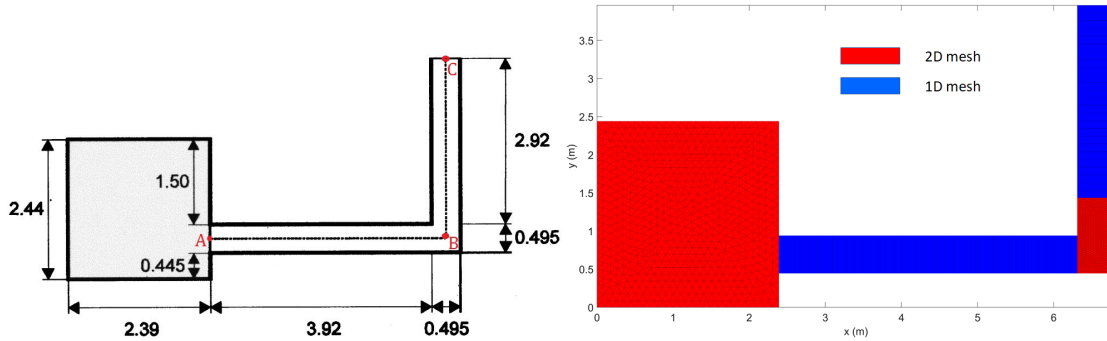


Figure 4.30: Channel with 90° bend – Top view left: dimensions in m (Soares-Frazão and Zech (2002)); Right 1D2D mesh used with *Flood1D2D*

The hydraulic configurations of the experiment is modeled using *Flood1D2D* either using only a classical structured/unstructured 2D mesh or a 1D2D coupling mesh (see figure 4.30, right side). In both cases, the reservoir is included in the mesh and the initial water surface elevation is set to  $z_{ini} = 0.25\text{m}$ . At the downstream end of the channel, the boundary condition is set as a free outlet.

As stated by the authors, the convergence of mesh size is checked successfully to 0.1m for square grids and the simulation was conducted using grid size 0.4m. In this section, the convergence of mesh size is also checked using a 2D unstructured triangular mesh and results are shown in figure 4.31. Computed water height varied with time is compared with experimental results, where the convergence is reached at grid size  $\Delta x = 0.025\text{m}$ .

##### 4.4.4.2 Sensitivity analysis of water height to mesh type and size

Before validating the ability of the code to deal with 1D2D coupling in transient state, the sensitivity to mesh type and size is conducted. Two types of mesh including triangular and quadrilateral elements are tested using grid size  $\Delta x = 0.025\text{m}$ . The parameters used are the same as stated in section 4.4.4.1 with results presented in figure 4.32. Results show that the

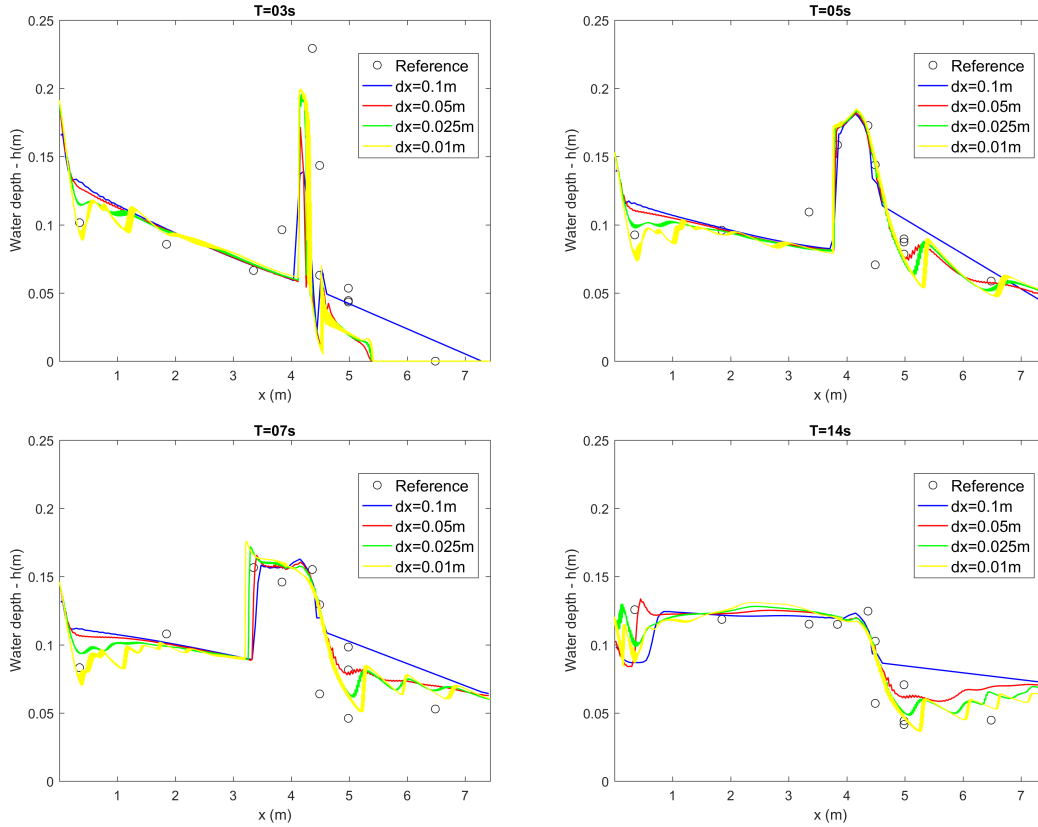


Figure 4.31: Comparison of *Flood1D2D* results using different grid sizes ( $dx = 0.1\text{m}$ ,  $dx = 0.05\text{m}$ ,  $dx = 0.025\text{m}$  and  $dx = 0.01\text{m}$ ) with the experiment data from Soares-Frazão and Zech (2002): water height along the line A-B-C as illustrated in figure 4.30

influence of mesh type to simulated water height is limited. Therefore, triangular mesh is selected for further use.

Except mesh type, the sensitivity to mesh size is also tested. Fine mesh with grid size  $\Delta x = 0.025\text{m}$  and coarse mesh with  $\Delta x = 0.1\text{m}$  ( $\Delta x = 0.025\text{m}$  around bend) are tested. Same parameter configurations are used as stated in section 4.4.4.1. Results are presented in figure 4.33 which shows that coarse mesh with refined mesh at bend is enough to reproduce the flow feature (water height) compared with fine mesh and selected for further use.

#### 4.4.4.3 Results

The 2D and 1D2D simulated water depth and flow lines along the channel centerline are presented at different time steps. The results from Soares-Frazão and Zech (2002) are also used for the comparisons presented in figures 4.31 to 4.35.

Figure 4.34 illustrates spatially varied water heights at different time steps: 3s, 5s, 7s and 14s. The simulated 2D results provided by Soares-Frazão and Zech (2002) and results calculated by the code *Flood1D2D* using 2D and 1D2D coupling mesh are compared. The results show that the code *Flood1D2D* can reproduce the water depth measurements of Soares-Frazão and Zech (2002)

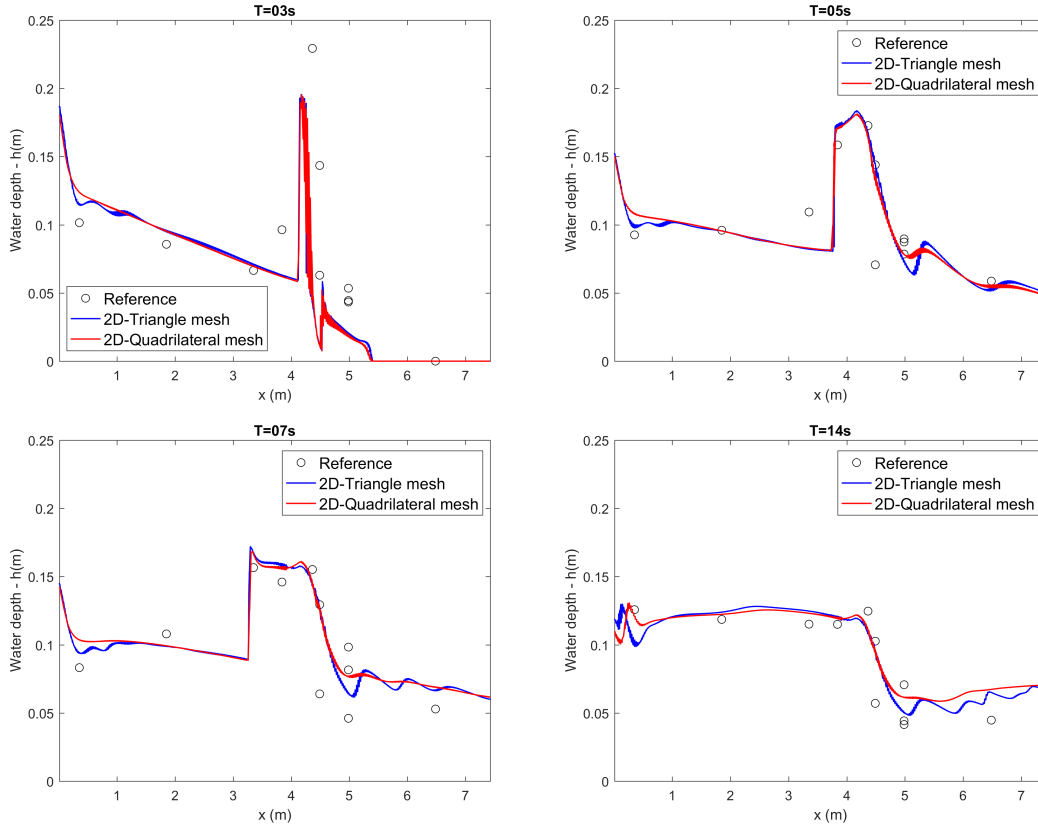


Figure 4.32: Comparison of *Flood1D2D* results (2D triangular mesh ( $\Delta x = 0.025\text{m}$ ) or 2D quadrilateral mesh ( $\Delta x = 0.025\text{m}$ )) with the experiment provided by Soares-Frazão and Zech (2002): water height along the line A-B-C as illustrated in figure 4.30

qualitatively either in 2D or in 1D2D which can be clearly observed in figures 4.34 and 4.35. The code *Flood1D2D* can reproduce spatially varied water height in the unsteady simulation.

## 4.5 Conclusions

In this chapter, the code *Flood1D2D* presented in chapter 3 is validated against various test cases. Several classical 1D and 2D test cases provided by Soares-Frazão and Zech (2002); Guinot and Soares-Frazão (2006); Finaud-Guyot et al. (2010b) are used with and without porosity. Numerical results are compared with analytical and experimental results. Several new test cases are also designed to test the 1D2D coupling functionalities and results are compared with full 2D results and experimental results when available. The ability of the code is fairly well demonstrated especially concerning:

- Open channel flows with and without porosity;
- Open channel flows in non flat bottom with and without friction effect;
- Transient dambreak problem with and without porosity in 1D and 2D scale;

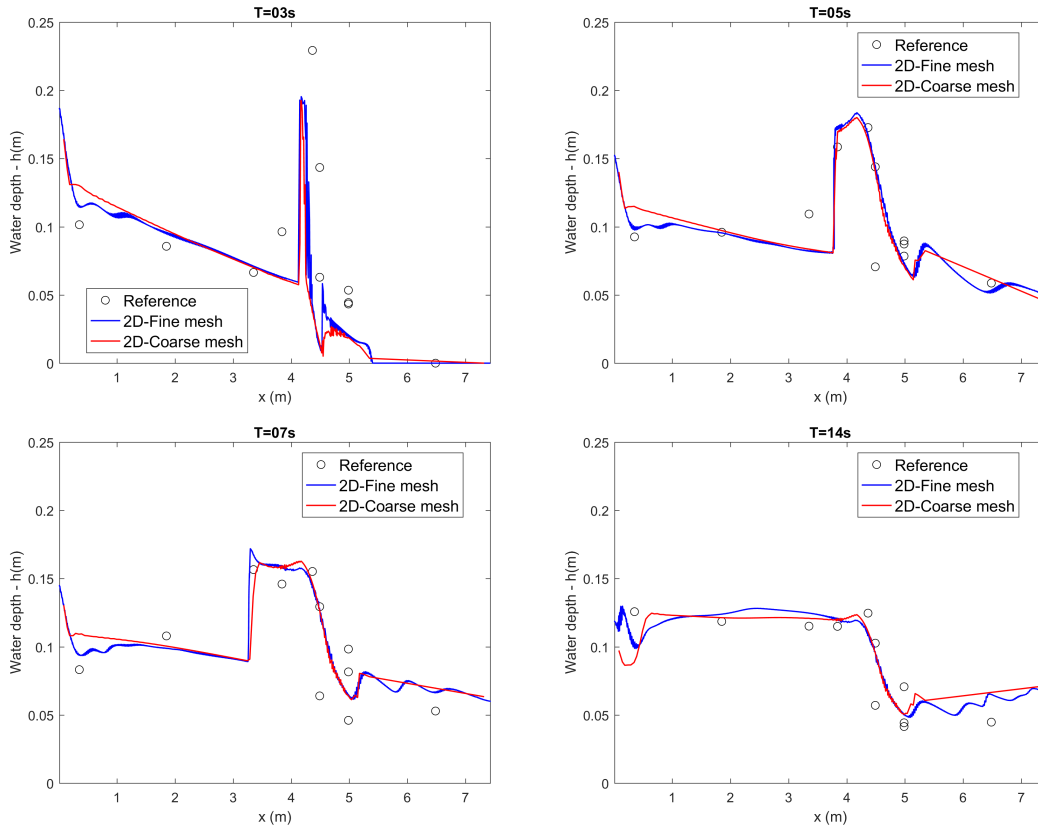


Figure 4.33: Comparison of *Flood1D2D* results (2D fine ( $\Delta x = 0.025\text{m}$ ) or coarse ( $\Delta x = 0.1\text{m}$  except in bend where is  $\Delta x = 0.025\text{m}$ ) triangular mesh) with the experiment provided by Soares-Frazão and Zech (2002): water height along the line A-B-C as illustrated in figure 4.30

- Flux computation at steady state using 1D2D coupling mesh;
- Hydrodynamic computation at highly transient state using 1D2D coupling mesh.

The application of the code in local/district scale for urban flood modeling is presented in chapter 6.

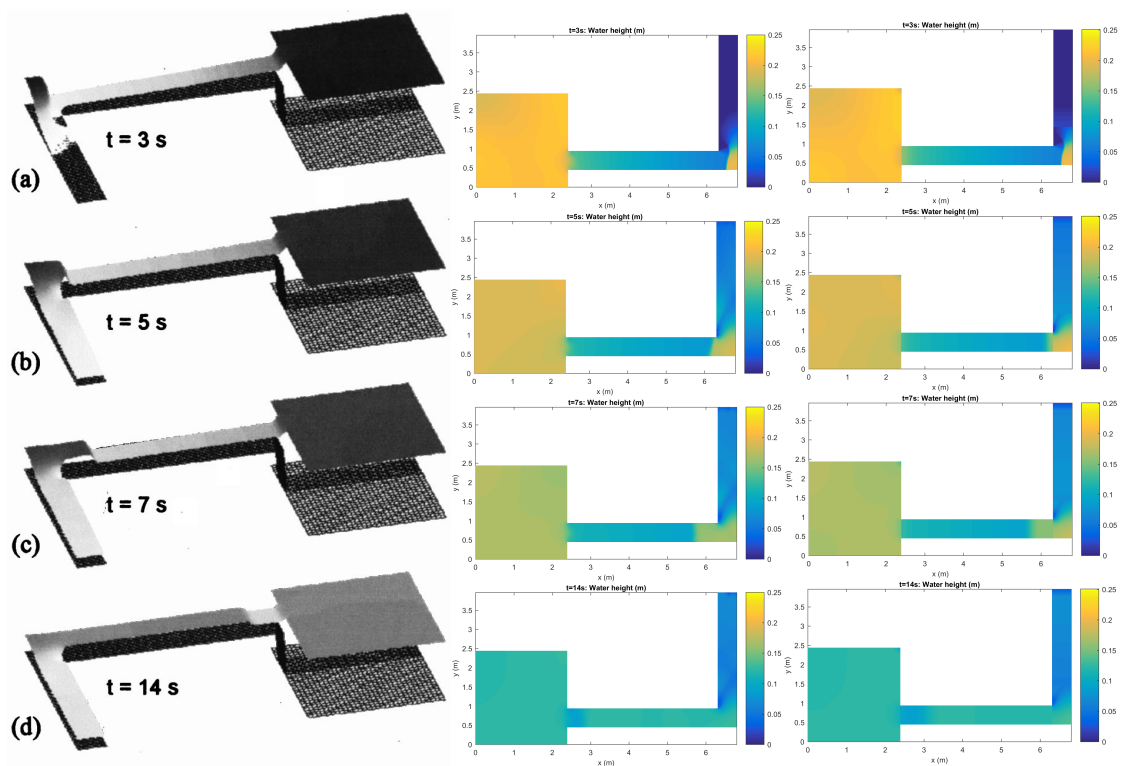


Figure 4.34: Comparison of *Flood1D2D* results (2D water height): left, simulated water height provided by Soares-Frazão and Zech (2002); middle, 2D water height in coarse mesh ( $\Delta x = 0.1\text{m}$  except in bend which is  $\Delta x = 0.025\text{m}$ ); right, 1D2D water height in coarse mesh (see figure 4.30, right side) ( $\Delta x = 0.1\text{m}$  except in bend which is  $\Delta x = 0.025\text{m}$ )

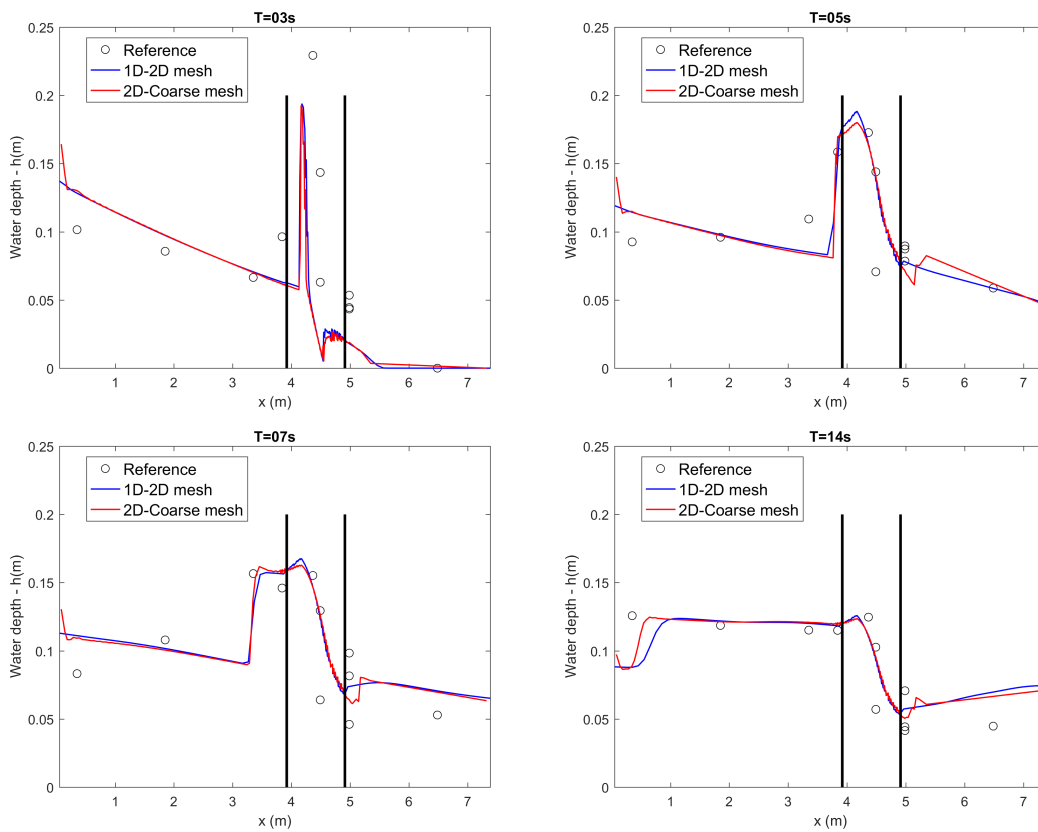


Figure 4.35: Comparison of *Flood1D2D* results (2D or 1D2D mesh) with the experiment provided by Soares-Frazão and Zech (2002): water height along the line A-B-C as illustrated in figure 4.30. 2D mesh is located into two vertical lines

## Chapter 5

# Sensitivity analysis of 1D and 2D shallow water models

The goal of hydraulic modeling is to simulate free surface flows behaviors on a given domain. It is described by predicting spatio-temporal patterns of water elevation and discharge. Depending on the amount of data available and modeling goals, different complexities and parameterizations of hydraulic models can be chosen. Consequently, the uncertainty in model outputs may be related to different sources: data type and observation errors, model structural uncertainties, parametric uncertainties.

Numerical modeling of free surface flows is used to predict flood hydrodynamics especially in the case like branched urban networks in this PhD. This chapter focuses on the sensitivity analysis of 1D and 2D shallow water model outputs. The goal is to bring insight in how water depth and discharge patterns predicted on complex urban flood flows configurations are influenced by model structure, boundary conditions and parameters.

Typical uncertainty sources in hydraulic modeling include inflow and outflow boundary conditions (discharge, height, rating curves...), roughness (uniform or distributed), topography, etc. In this chapter, several uncertainty sources are studied to assess their influence on model output variance using global sensitivity analysis (GSA). The sub-parts are organized as follows:

1. The first section presents an article submitted to the journal “Environmental Modeling and Software”, entitled “Variance based sensitivity analysis of 1D and 2D flood flow hydraulic models”. This paper explores spatial sensitivities of 1D and 2D shallow water (SW) models of branched urban flood flows based on an experimental data-set and a variance decomposition method for various combinations of uncertainty sources. General sensitivity patterns of SW model for fluvial flows are derived in 1D and 2D, for several steady urban floods flows configurations corresponding to those conducted on the ICube urban flood experimental rig. The filtering effect of branched network topography on inflows, the role of large streets as global flow pattern separators and the influence of roughness patterns are investigated.
2. The second section deals with GSA applied to a 2D unsteady hydraulic model of the ICube urban flood experimental rig. A synthetic flood is simulated with uniform roughness. The objectives are to investigate:
  - a) Unsteady flow patterns in the case of flash urban flooding;
  - b) The mechanism of discharge distribution into the experimental rig varied with time;
  - c) The influence of inflow discharge and uniform roughness onto the model output (water height and outlet discharge).

3. In the third section, the sensitivity of model output to different street blockage locations is assessed. Different locations of blockage are described and their influence to discharge distribution and local flow features are studied.

## **5.1 Chen, S., Garambois, P.-A., Finaud-Guyot, P., Dellinger, G., Mose, R., Terfous, A., Ghenaim, A., 2018. Variance based uncertainty quantification for 1d and 2d hydraulic modeling: an experimental urban flood case. Under review for Environmental Modelling & Software.**

### **5.1.1 Introduction**

Flooding is one of the first natural hazard on each continent, and it caused in Europe around 100 billion euros of damage between 1986 and 2006 (Moel et al. (2009)). In the context of climate change and its possible effects on rainfalls regimes and extremes (Pachauri et al. (2014)), an unprecedented urbanization of floodplains increases the vulnerability of human societies (e.g. Werners et al. (2012)). That is why improving the accuracy of flood inundation forecasts and reanalysis combined with uncertainty quantification, especially in urban areas, has become a priority for decision making in civil protection or the insurance industry.

The predictive performances of a model generally depend on model complexity and data availability (e.g. Grayson and Blöschl (2001) for hydrological models). Flood inundation maps are commonly generated with a 2D shallow water (SW) model consisting in depth averaged Navier-Stokes equations (e.g. Hervouet (2007); Arrault et al. (2016); Monnier et al. (2016)) where uncertainty sources can be model structure and parameterization (e.g. basal friction), initial and boundary conditions (bathymetry and source terms). A full shallow water model including inertia terms may be required to capture small scale features and rapidly varying flows over “rural” floodplains (e.g. Neal et al. (2012)), along with appropriate numerical methods for shock capture and wet dry front treatments (e.g. Monnier et al. (2016)). As a matter of facts, the interaction of high energy flows with obstacles triggers 3D flow processes such as crossroads junctions (Mignot et al. (2006)) - which for a realistic representation generally require to solve the Navier-Stokes equations in 3D. Consequently, flow resistance parameterization for a 2D SW model, which is an effective representation of 3D (turbulent) free surface flow structures, may depend on its scale for localized head losses in complex geometries (e.g. Guinot (2012a)) or parietal friction on smooth or macro roughness (e.g. Cassan et al. (2015, 2017)). Another boundary condition that is a well known source of uncertainty is inflow discharge especially in complex urban flood configurations - which can be provided by in situ measurements (involving rating curve uncertainty Delrieu et al. (2005); Paris et al. (2016); Savage et al. (2016)) or simulated by a hydro-meteorological chain involving meteorological model uncertainties (Vié et al. (2011)) and hydrological model uncertainties (e.g. Douinot et al. (2017)).

Given its importance in flood modeling and forecasting, sensitivity analysis (SA) of 1D Saint Venant and 2D SW models to their parameters and boundary conditions are addressed in the present contribution. The study focuses on the case of urban flood flows in a complex streets network, based on a fine and unique laboratory scale experiment while in situ flood data are still rare (Finaud-Guyot et al. (2018)). Remark this streets network is composed of several 4 branch crossroads creating complex patterns of free surface flows confluences and defluences.

Flood simulation accuracy is not necessarily improved by increasing model complexity and resolution (cf. Dottori et al. (2013)) but uncertainty sources may also vary (even interact) as the amount of data required to constrain the model. Sensitivity analysis, that assesses how the

uncertainty in the output of a model can be apportioned to different sources of uncertainty in the model input (Saltelli et al. (2004)), has become a popular tool in environmental modeling (Pianosi et al. (2016)). SA is used in catchment hydrology to explore high dimensional parameter spaces, assess parameter identifiability and understand uncertainty sources (Hornberger and Spear (1981); Beven and Binley (1992); Pushpalatha et al. (2011); Garambois et al. (2013, 2015) among others). Temporal variations of distributed rainfall runoff and simplified hydraulic model parameters sensitivities are analyzed and ranked in the case of Mediterranean flash floods (Garambois et al. (2013)) or large scale conceptual model of the Amazon river (Emery et al. (2016)). Temporal sensitivities of simulated flood response highlight phases and locations of higher sensitivities to runoff production parameters and/or runoff routing depending on rainfall forcing variabilities and drainage network shape among other parameters.

Among the few SA studies in the field of river hydraulic modeling, Roux and Dartus (2008) propose a generalized sensitivity analysis of a 1D Saint Venant model with simplified geometry adapted to remote sensing and ungauged rivers, in the case of flood scenario on the Lèze River, France. The authors show the importance of downstream flow depth in controlling flood extent for a 1.5 km reach of a small river (around 100m bankfull width). Guinot and Cappelaere (2009a) propose local sensitivity equations for the 2D steady state SW equations without shocks and provide some guidelines for model calibration and validation. These sensitivity equations are also derived and implemented for 1D Saint Venant model (Deleenne et al. (2011)). Local sensitivities derived with the adjoint method (2D SW DassFlow model), and involving a cost function, are presented in the case of a high resolution model of a flood on a 2km reach of the Lèze River (Monnier et al. (2016)). The authors find higher sensitivities of water depth to bathymetry and roughness downstream (subcritical regime) of the observation points in the floodplain and in the main channel, roughness sensitivities are higher in the main channel. Recently variance based SA has been applied to 2D hydraulic models in flooding conditions (Abily et al. (2016); Savage et al. (2016)). Abily et al. (2016) present a spatial SA approach of a 2D SW model based on high resolution digital elevation model (DEM). Sensitivity maps of simulated water depth to uncertain parameters including topography are presented for the last 5km of the Var valley, France - November 1994 flood. For a 50km<sup>2</sup> rural floodplain in Sicily, Savage et al. (2016) highlight the sensitivity of simulated flood extent to inflow discharge during flood rising limb then the channel friction parameter during flood peak and the floodplain friction parameter during recession. First order sensitivity of both maximal water depth and flood extent to topography and model resolution is limited whereas interactions of those parameters with others (hydrographs and roughness) increases at the end of the flood given their influence on floodplain flow pathways in this case. These few recent SA studies mostly bring insight on first order hydraulic model sensitivity to its parameters for common subcritical flood flow cases in simple channels on the order of few km and rural floodplains.

Concerning urban floods in a complex branched geometry, the present paper proposes a thorough quantitative sensitivity analysis of the widely used 1D Saint Venant and 2D SW models with a variance based method (Ratto et al. (2007); Saltelli et al. (2008)). It is based on a unique experimental device at the horizontal scale  $1/200$ , able to produce urban flooding with flows corresponding to frequent to rare return periods (Finaud-Guyot et al. (2018)). The originality of this paper is to explore the sensitivities of 1D and 2D SW models of branched urban flood flows based on a detailed experimental data-set in order to assess the relative importance of input parameters and gain insight on modeling uncertainties. Various parameters are investigated including: global and local boundary conditions (water heights and discharge) and spatially uniform or distributed friction coefficient respectively tested in various ranges centered around their calibrated values. For various experimental configurations a variance decomposition method (ANOVA) is used to calculate spatially distributed Sobol sensitivity indices (Si's). The sensitivity

of water height and discharge to input parameters are analyzed on two main streets and the whole experimental rig using respectively 1D and 2D models.

The paper is organized as follows. Section 2 describes the GSA method, experimental device and numerical models used to investigate urban flood flows controls. Spatial patterns of parameter sensitivity are presented in section 3 both for 1D and 2D models. Section 4 presents a detailed discussion around sensitivity patterns in various configurations including the effect of bathymetric slope. Conclusions and perspectives are presented in section 5.

## 5.1.2 Methods and models

### 5.1.2.1 Experimental rig and numerical models

This study is based on the ICube urban flood experimental rig designed and built at the ICube laboratory in Strasbourg (France) (Araud (2012); Finaud-Guyot et al. (2018)). It is supposed to be representative of typical urban geometries at the scale  $1/200$  with street widths of 12.5cm and 5cm and various angles. It is composed of 64 impermeable blocks on a  $5\text{m} \times 5\text{m}$  horizontal plan. The streets network is composed of seven streets in the north-south direction crossed by seven streets in the west-east direction (see figure 5.1 - c). The inflow discharge of each street of the north and west faces is supplied by a volumetric pump, a rectangular weir controls water levels at the outlet of each street and outlet discharges are measured using calibrated weirs relationships (Finaud-Guyot et al. (2018)). The studied configurations correspond to steady state experiments and the corresponding boundary conditions are presented in Appendix (table A.1).

1D and 2D steady models are used for flow simulations under experimental conditions. 1D modeling is performed for widest streets C and 4 using 1D Saint Venant equations which are solved with a finite volume approach (e.g. Guinot (2012b); Brisset et al. (2017)) using a classical HLLC Riemann solver (Guinot and Soares-Frazão (2006)). 2D modeling is performed for the whole experimental rig using Telemac2D (Hervouet (2000)) which solves the 2D shallow water equations coupled to a classical  $k - \varepsilon$  closure turbulence model using a finite volume approach on unstructured triangular mesh.

2D model is run with upstream discharge and downstream water depth determined from experimental data. Roughness is calibrated with a trial and error procedure in order to best match outlet discharges and measured flow lines (cf. figure 5.1 - d and section 5.1.3.2.1). 1D model is run with experimental data for the lateral discharge and downstream water depth, and its roughness is calibrated in order to best match measured flow lines (cf. figure 5.4 - top and section 5.1.3.1.1).

### 5.1.2.2 Background on model sensitivity analysis with variance decomposition methods

Sensitivity analysis is defined as the study of how the uncertainty in the output of a model can be apportioned to different sources of uncertainty in the inputs (Saltelli et al. (2008); Pianosi et al. (2016)). It includes local sensitivity analysis that evaluates the effect on model outputs of a small perturbation of the considered input parameters around a specific value (Guinot and Cappelaere (2009a,b); Delenne et al. (2011); Monnier et al. (2016)); and global sensitivity analysis that explore model behavior over a whole parameter space but that is often more computationally expensive (e.g. Pianosi et al. (2016)).

For a generic model  $f$ , let  $\Omega^k \in \mathfrak{R}^k$  denote the set of all possible values that the model parameters can take. Let  $\underline{X} \in \Omega_k$  be a possible value of the  $k$  model parameters normalized by their variation range. We denote by  $Y = f(\underline{X}) = f(X_1, X_2, \dots, X_k)$  the relationship that links the model inputs to the model output. Following Sobol' (1990); Sobol (1993); Saltelli et al. (2010)

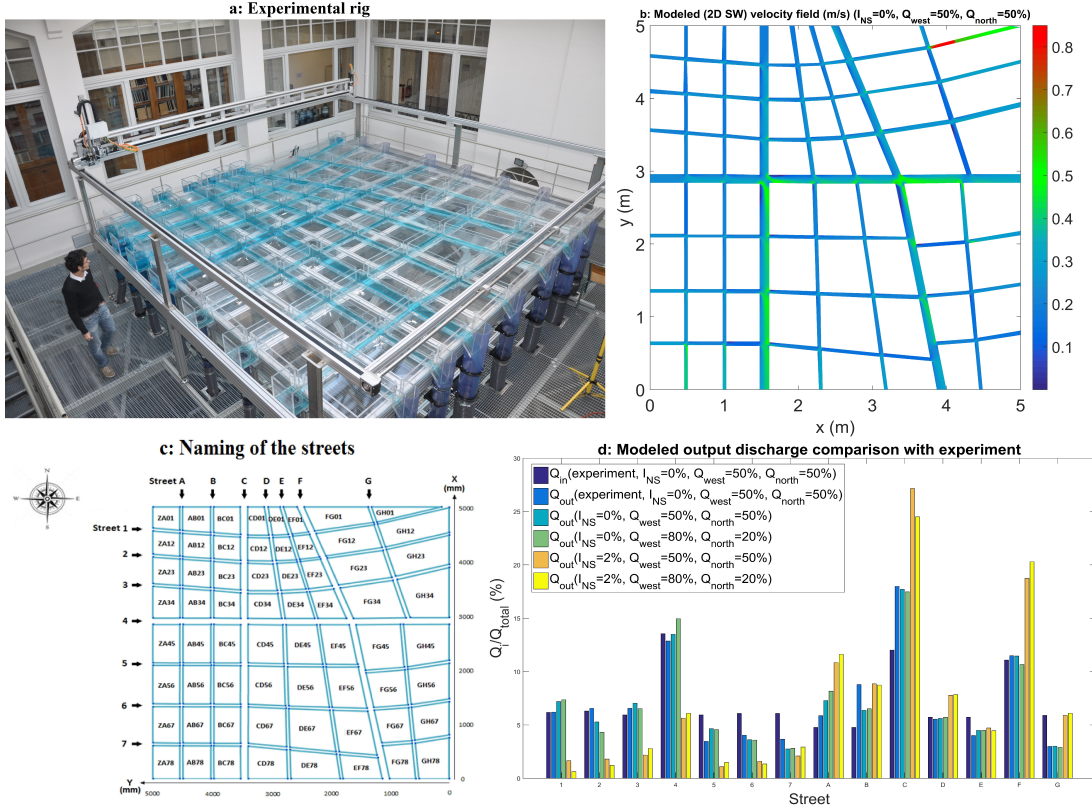


Figure 5.1: (a) Experimental rig, (b) modeled (2D SW) velocity field for  $Q = 80\text{m}^3/\text{h}$  equidistributed between upstream west and north faces, (c) naming of the streets and (d) modeled output discharge comparison with experiment.

and using a high-dimension model representation with functions orthogonal in pairs (in the sense of the scalar product  $\int_{\Omega_k}$  - leading to variances) the so-called functional ANOVA decomposition can be obtained:

$$V(Y) = \sum_i V_i + \sum_i \sum_{j>i} V_{ij} + \dots + V_{1,2,\dots,k} \quad (5.1)$$

where  $V(Y)$  is the total variance,  $V_i = \text{Var}_{X_i}(E_{X \sim i}(Y|X_i))$  is the first-order variance caused by parameter  $X_i$ ,  $V_{ij} = \text{Var}_{X_{ij}}(E_{X \sim ij}(Y|X_i, X_j)) - V_i - V_j$  is the covariance caused by  $X_i$  and  $X_j$  (second-order variance), and higher order terms show the variance contribution from multiple parameters.

The sensitivity index of first-order effect of  $X_i$  on  $Y$  can be defined as:

$$S_{i_1, \dots, i_p} = \frac{V_{i_1, \dots, i_p}}{V} \quad (5.2)$$

where  $S_i$  is the Sobol index, always between 0 and 1. The sum of all Sobol indices is equal to 1:

$$\sum_{i=1}^k S_i + \sum_{i<j}^k S_{ij} + \dots + S_{1,2,\dots,k} = 1 \quad (5.3)$$

### 5.1.2.3 Sobol indices computation method

Variance based (Sobol) sensitivity indices are calculated in this paper for 1D and 2D SW models following the general method presented in figure 5.2. It is based on a large sample of size  $N_s$  of parameters vectors  $\underline{X}^p = (X_1^p, X_2^p, \dots, X_k^p)$ ,  $p \in [1..N_s]$ , considered in this study as a stochastic variables. Sobol indices are computed from the sample of hydraulic model outputs  $Y^p$  using a state dependent parameter metamodeling as proposed by Ratto et al. (2007). It is a simple and computationally effective method for estimating conditional variances of model output with respect to each parameter. The bounds of the variability space of input parameters  $\underline{X}^p$  are defined around their calibrated values. The different tested combinations of hydraulic parameters and boundary conditions along with parameter ranges are explained for each numerical experiment in what follows.

### 5.1.3 Results

This section details sensitivity analysis of 1D and 2D SW models outputs. The sensitivities to their parameters are investigated with the GSA method presented above (cf. section 5.1.2.1) for 1D hydraulic models of the two main streets of the experimental rig and for full 2D models. The spatially distributed variances of model outputs are decomposed with respect to different hydraulic parameters. Each input parameter vector  $\underline{X}^p = (X_1^p, X_2^p, \dots, X_k^p)$ ,  $p \in [1..N_s]$  is formed by:

- Inflow discharges including lateral inflows for 1D model
- Downstream water depths
- Roughness (uniform or spatially distributed)

Different combinations of uncertainty sources, i.e. parameter combinations, and uncertainty ranges are investigated for the 1D model first (section 5.1.3.1). For the 2D model, parameter ranges are chosen such as corresponding to uncertainty ranges from our experimental data-set (cf. Finaud-Guyot et al. (2018)) (section 5.1.3.2).

#### 5.1.3.1 Sensitivity analysis in 1D configuration

**5.1.3.1.1 Model Calibration** Before conducting the GSA, a calibration of the 1D model is needed, it is performed with - uniform or distributed roughness coefficient. The calibration aims at minimizing the Euclidean norm between simulated and measured flow lines. Given the small number of parameters a trial and error procedure is used. The calibrated roughness and 1D model inputs with their variation ranges are presented in table 5.1. For uniform roughness, the Strickler coefficient found for street C is  $K_C^{cal} = 21.5\text{m}^{1/3}.\text{s}^{-1}$  and for street 4  $K_4^{cal} = 21\text{m}^{1/3}.\text{s}^{-1}$ . The calibration results for distributed roughness consist in a roughness value for streets:  $K_{C_s}^{cal} = 26.5\text{m}^{1/3}.\text{s}^{-1}$  for street C and  $K_{4_s}^{cal} = 28.5\text{m}^{1/3}.\text{s}^{-1}$  for street 4 and in a value for crossroads:  $K_{C_c}^{cal} = 9.5\text{m}^{1/3}.\text{s}^{-1}$  for street C and  $K_{4_c}^{cal} = 9\text{m}^{1/3}.\text{s}^{-1}$  for street 4. Figure 5.4 illustrates the simulated water height profiles with uniform and distributed roughness compared with experimental values. Distributed roughness slightly improves simulated water depth profile. Recall that flows are characterized by complex 3D hydrodynamic structures, but this contribution focuses on comparing the sensitivities computed for 1D and 2D modeling approaches in a branched hydraulic network.

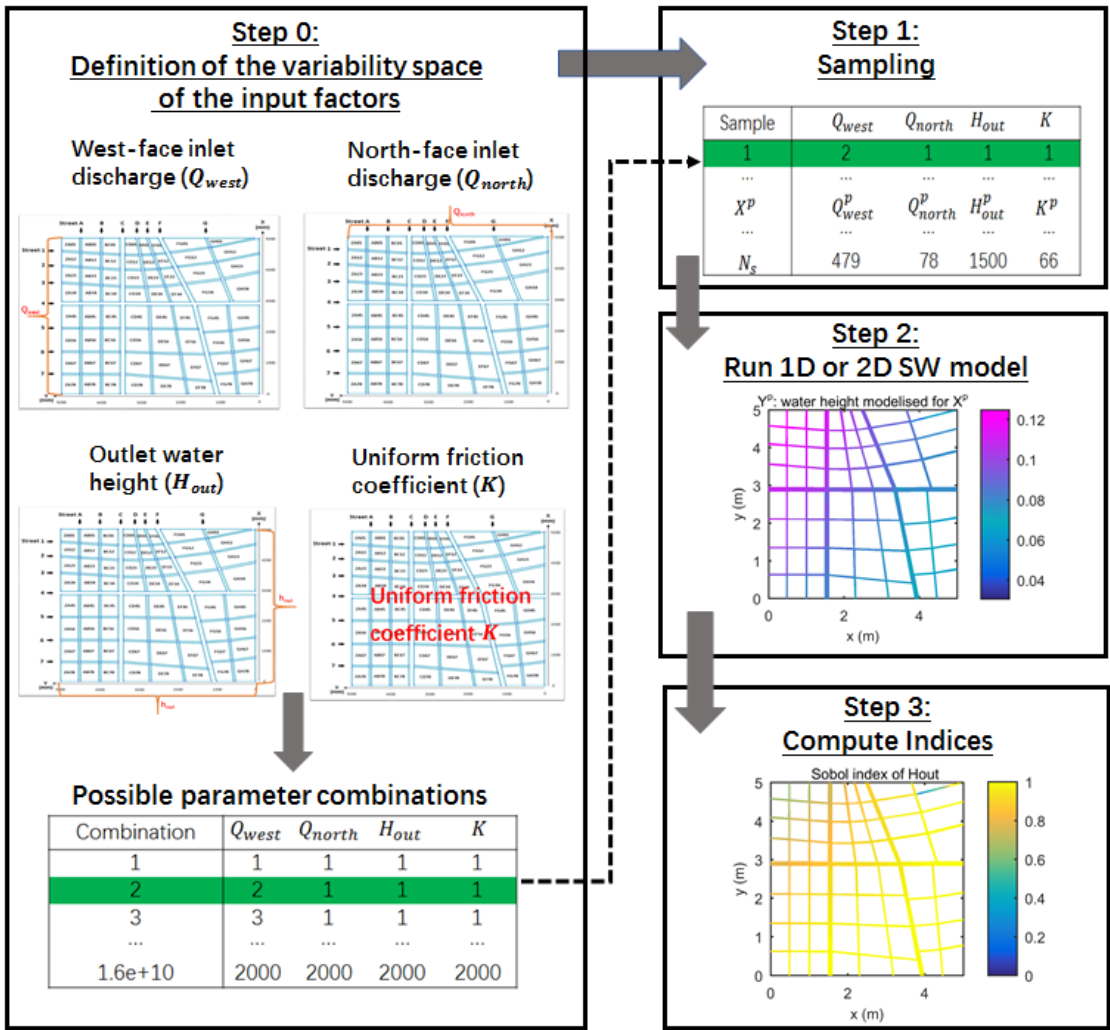


Figure 5.2: Main steps of the methodology used for performing the Global Sensitivity Analysis (GSA) of 1D or 2D hydraulic models. Step 0 consists in choosing the parameters to test and defining their physical bounds hence defining parameter space. Each parameter is sampled randomly in step 1. Next, hydrodynamic model is run for each parameter set in step 2 and sensitivity indices are calculated for all those model realizations in step 3.

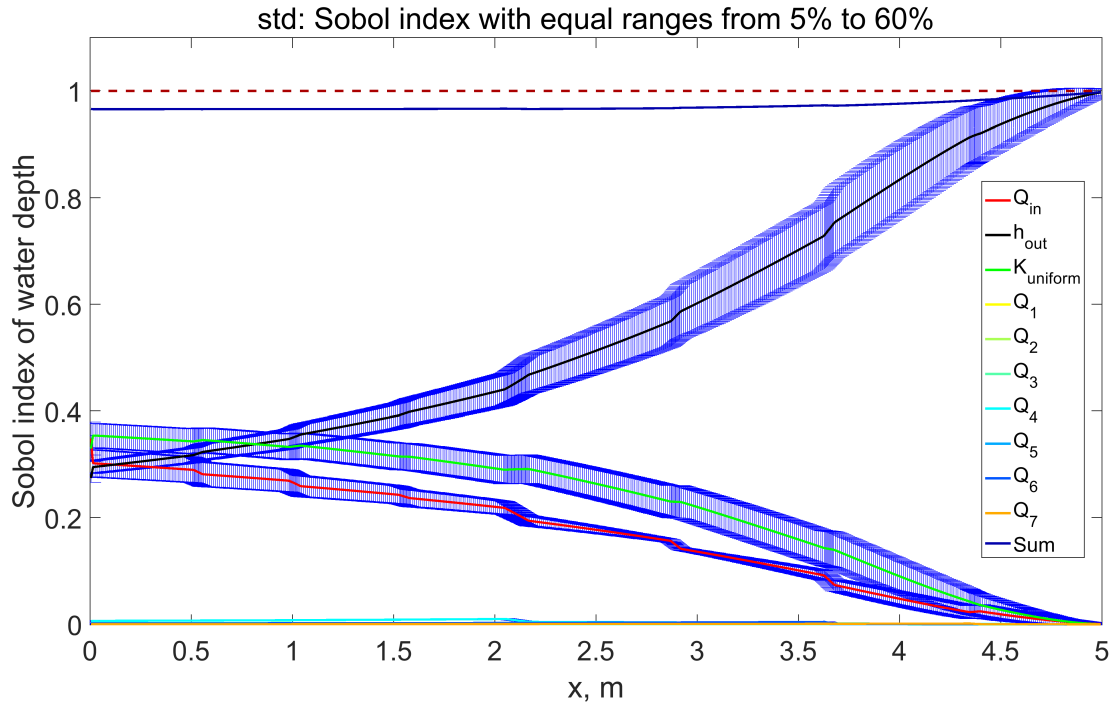


Figure 5.3: Sobol index of water depth for 1D model estimated for parameters sampled on equal ranges of amplitudes various amplitudes ranging from  $\pm 5\%$  to  $\pm 60\%$  each parameter for street C.

**5.1.3.1.2 Sensitivity of GSA on 10 parameters to sampling range** Sensitivity of Sobol indices estimation to parameter sampling range has been tested by applying the same ranges to all tested parameters from 5% to 60%. A limited influence on sensitivity indices values is observed and sensitivity patterns are relatively unchanged (i.e. proportion of the output variable variance explained by each parameter) (cf. figure 5.3). The influence of unequal ranges has also been tested and is presented in following sections for ranges corresponding to experimental uncertainties. The sensitivity to sample size has been investigated  $N_s \in [100; 10000]$ , and the choice is made to use a sufficient number of 2500 parameter sets ensuring good convergence of  $S_i$ s estimation for each following experiment.

Interestingly, figure 5.3 shows the spatial variation of first order sensitivities of 10 parameters. The sum is close to one along the streets highlighting very few interaction effects between the 10 tested parameters in explaining modeled water depth variance. It is mainly explained by three parameters over the (equal) tested ranges: roughness, upstream discharge and downstream water depth. Those three parameters explain about one third of water depth variance upstream of street C. The influence of both upstream discharge and roughness decrease along flow distance whereas the influence of downstream water depth steadily increases to reach more than 95% downstream. This is a reasonable pattern for a subcritical flow.

**5.1.3.1.3 GSA on ten parameters with experimental uncertainties** This section investigates the sensitivity of 1D simulated flow lines to boundary conditions and source terms. Sensitivities are presented for the main streets C and 4 of the urban flood rig, conveying around

Table 5.1: Parameters used and associated perturbation ranges for the 1D street modeling

Symbol	Meaning	Value (street C)	Value (street 4)	Range
$Q_{in}$	Street C (4) inflow discharge	2.671/s	3.011/s	$\pm 5\%$
$h_{out}$	Street C (4) outflow water height	0.083 m	0.078 m	$\pm 10\%$
$Q_1(Q_A)$	Lateral street 1 (A) inflow discharge	0.1711/s	0.0141/s	$\pm 5\%$
$Q_2(Q_B)$	Lateral street 2 (B) inflow discharge	0.1981/s	0.1551/s	$\pm 5\%$
$Q_3(Q_C)$	Lateral street 3 (C) inflow discharge	0.0931/s	-0.1071/s	$\pm 5\%$
$Q_4(Q_D)$	Lateral street 4 (D) inflow discharge	0.4071/s	0.2611/s	$\pm 5\%$
$Q_5(Q_E)$	Lateral street 5 (E) inflow discharge	0.2371/s	0.0771/s	$\pm 5\%$
$Q_6(Q_F)$	Lateral street 6 (F) inflow discharge	0.2961/s	0.3801/s	$\pm 5\%$
$Q_7(Q_G)$	Lateral street 7 (G) inflow discharge	-0.3191/s	-0.5531/s	$\pm 5\%$
$K$	uniform roughness coefficient	$21.5 \text{ m}^{1/3} \cdot \text{s}^{-1}$	$21 \text{ m}^{1/3} \cdot \text{s}^{-1}$	$\pm 50\%$
$L$	Domain length	$5 \text{ m} \times 0.125 \text{ m}$	$5 \text{ m} \times 0.125 \text{ m}$	
$\Delta x$	Cell size	0.02 m	0.02 m	

30% of the total flow (cf. figure 5.1). Ten input parameters are considered including upstream inlet discharge  $Q_{in}$ , outlet water height  $h_{out}$ , uniform roughness  $K$  and seven lateral discharges corresponding to mass exchange at crossroads  $Q_{\{1,\dots,7;A,\dots,G\}}$  (cf. table 5.1). The variation range of each input parameter around its calibrated value ( $^{cal}$ ) is chosen corresponding to the experimental uncertainties. The ranges considered here are:  $Q_{in}^{cal} \pm 5\%$ ,  $h_{out}^{cal} \pm 10\%$ ,  $K^{cal} \pm 50\%$  and  $Q_{\{1,\dots,7;A,\dots,G\}}^{cal} \pm 5\%$ ; note that each lateral discharge is perturbed independently.

The spatial variations of Sobol indices of ten input parameters are presented in figure 5.4 with parametric uncertainty ranges corresponding to experimental ones. In that case, the sum of first order indices  $S_{i \in [1..10]}$  is very close to one indicating very small higher order interactions between parameters. The results for both street C and 4 show that main flow controls over the tested uncertainty ranges are roughness, downstream water depth and upstream discharge. The remaining sensitivities of the seven lateral discharges are very small compared to the three other parameters. Therefore, for the sampled ranges those ten input parameters are studied separately in subsequent sections: three main parameters and seven lateral discharges.

**5.1.3.1.4 GSA on the main three parameters** The spatial variation of Sobol indices of the main three parameters (upstream discharge, downstream water depth and friction) sampled in experimental uncertainty ranges are presented in figure 5.4. Results for both street C and 4 show that the sum of all three parameters is close to 1 highlighting no interactions effects between those three parameters. Modeled water depth variance is mainly explained by roughness and downstream water depth for the whole streets length. Upstream of street C or 4, roughness explains more than 95% of model response and its influence steadily decreases with increasing flow distance. The opposite pattern is obtained for downstream water depth sensitivity with  $S_{h_{out}}$  greater than 95% downstream. Flow in both streets C and 4 is subcritical everywhere and such a pattern is logical. There are no interaction effects between those three parameters along street C and 4, and water depth variance is perfectly explained by their first-order Sobol indices. In magnitude, the influence of inlet discharge can be neglected for the tested ranges compared to water height and friction coefficient.

**5.1.3.1.5 GSA on lateral discharges** We consider here the case where uncertainty sources are only the lateral discharges. The spatial patterns of Sobol indices are presented in figure 5.5. Their sum stays close to one along street C or 4 and again shows no interaction effects.

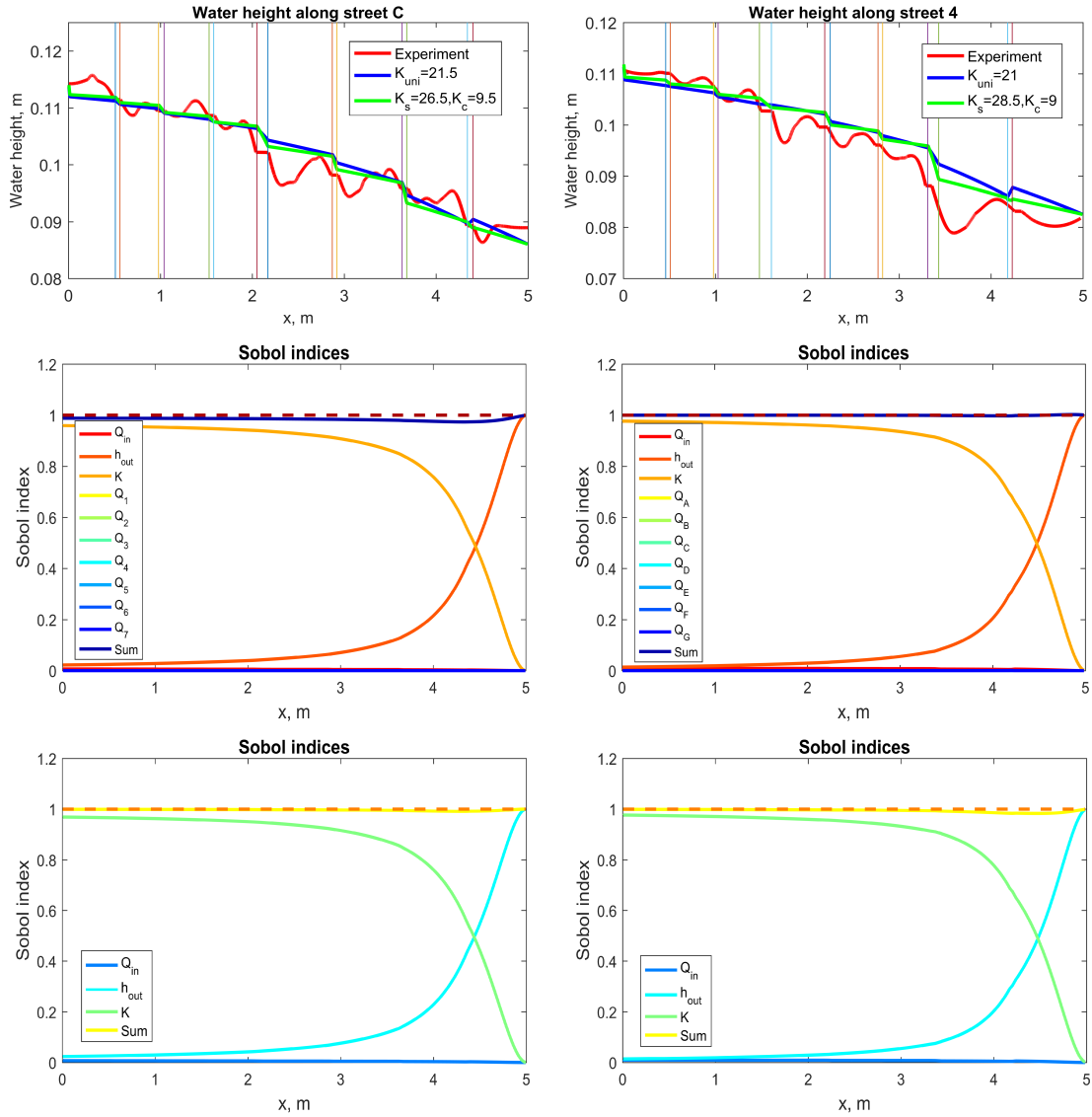


Figure 5.4: Top: Comparison of the computed and measured water height profiles and Sobol indices of ten (Middle) and three (Bottom) main input parameters. The results are plotted for streets C (Left) and 4 (Right). For Sobol index of 10 parameters,  $S_{Q_i} < 0.002$ ,  $\forall i \in [1, 2, 3, 4, 5, 6, 7; A, B, C, D, E, F, G]$ , over experimental uncertainty ranges (cf. table 5.1)

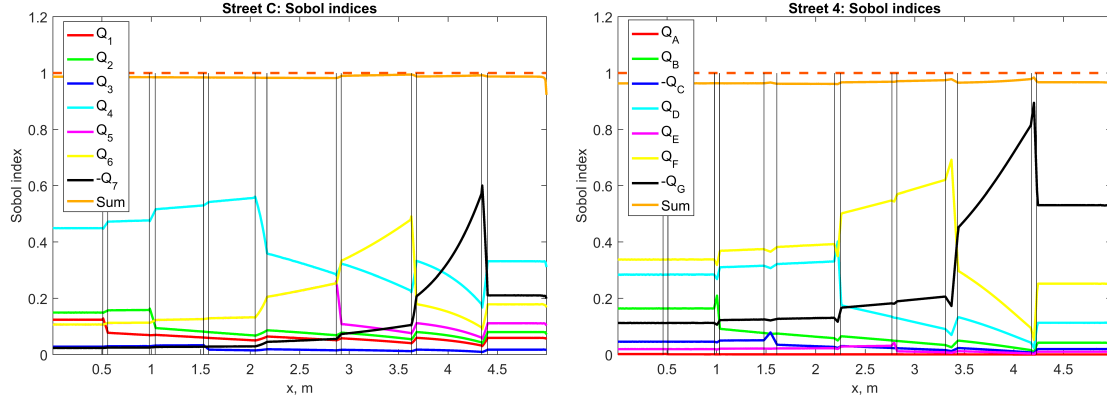


Figure 5.5: Sobol indices of seven lateral discharges with minus signs for flow loss.

The sensitivity of output water depth to a given lateral discharge is maximal at its inflow point (crossroad). Interestingly the influence of a lateral mass flux propagates to the downstream outlet but also upstream in subcritical flow conditions as a downstream control. After the last crossroad, the Sobol indices of lateral discharges stay constant and their values are proportional to lateral discharge values which can be correlated to the prescribed water depth at the downstream end of the street:  $S_{Q_i} = \alpha Q_i^2 \forall i \in [1, 2, 3, 4, 5, 6, 7; A, B, C, D, E, F, G]$  where  $S_{Q_i}$  stands for the Sobol index at the downstream end to the lateral discharge of street  $i$  and  $\alpha$  is a constant factor.

**5.1.3.1.6 GSA on distributed roughness** The spatial pattern of water depth sensitivity to a uniform roughness has been studied in section 5.1.3.1.3 and 5.1.3.1.4. Now the influence of a distributed roughness pattern for streets ( $K_s$ ) and crossroads ( $K_c$ ) is considered. The variation ranges of two roughness are both set to 50% around their calibrated values (cf. section 5.1.3.1.1); the ranges for the other parameters are the same. The results show that no interaction effect exists between those two input parameters since the sum of first order  $S'_i$ s is close to 1 in each street (figure 5.6). For both streets,  $K_s$  has an increasing influence on water depth variance with increasing flow distance contrarily to crossroad roughness sensitivity that decreases.

Interestingly, the sensitivity profile between two crossroads (identified by the vertical dashed lines) evolve from linear upstream to parabolic downstream. This might be explained because the friction term (involving the roughness  $K$ ) is proportional to  $v^2$  and as the water decrease along the street, the velocity increase. Remark also that the magnitude of the sensitivity jump at the crossroads is correlated to the magnitude of the lateral injection.

Interestingly, crossroads roughness plays a larger role (up to 55%) for street 4 than for street C (only up to 34%). This demonstrates that a best effort modeling of the “same” domain (street C or street 4) would not be achieved using the same parameter ( $K_c$  for street 4 and  $K_s$  for street C). This highlights that the importance of the roughness parameter is not related to the area of the modeled domain on which the parameter apply, the crossroads representing 15% of it.

### 5.1.3.2 Sensitivity analysis in 2D configuration

**5.1.3.2.1 2D SW model set up and calibration** 2D steady state SW simulations are performed for the whole experimental rig in order to better reproduce complex flow structures (cf. Arrault et al. (2016); Tran et al. (2016)). The boundary conditions are based on the experimental data-set listed in Appendix table A.1. Constant discharges and water heights are prescribed at

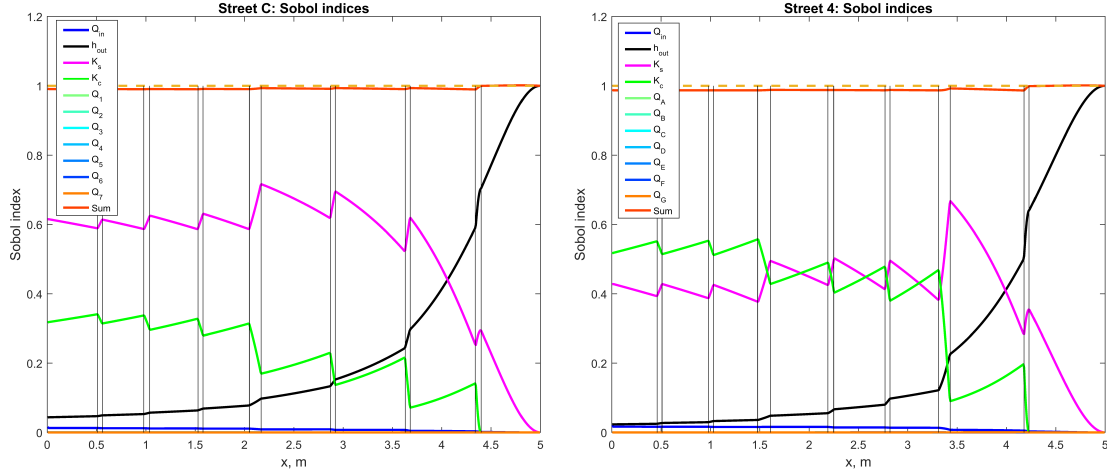


Figure 5.6: Sobol indices of distributed roughness (For street C,  $K_s = 26.5 \text{ m}^{1/3} \cdot \text{s}^{-1}$  and  $K_c = 9.5 \text{ m}^{1/3} \cdot \text{s}^{-1}$ ; For street 4,  $K_s = 28.5 \text{ m}^{1/3} \cdot \text{s}^{-1}$  and  $K_c = 9 \text{ m}^{1/3} \cdot \text{s}^{-1}$ ).

inlets and outlets along with a spatially uniform friction coefficient, since it is only calibrated with measured outlet discharge distribution. Remark that contrarily to 1D model calibrated on measured water depth profiles given known discharge, the 2D model is only calibrated against outlet discharges to reproduce the correct flow pattern within the urban district.

Note that a mesh convergence analysis has been performed for cell sizes ranging between 0.01 and 0.0025m, a grid with 0.005m cells is finally selected. A total inflow discharge of  $80 \text{ m}^3/\text{h}$ , corresponding to rare and high flood flow, is used for steady state simulations with different inflow discharge partitions between west and north face: 1) 50% west and 50% north; 2) 80% west and 20% north. Within a face, the discharge is divided proportionally to the street width. The spatial distributions of simulated water height and Froude number are presented in figure 5.7 for the two inflow repartitions. Water height decreases from west-north corner to south-east corner in both configurations. The flow in the device is subcritical everywhere except in street 1 after the last crossroad between street 1 and G, where supercritical flow occurs. The unequal flow repartition with increased inflow at 80% on west face increases the water height at south-west corner and reduces the region of supercritical flow in street 1 close to the outlet. Interestingly, the outlet street discharges modeled in both configuration (50-50% and 80-20%) are very similar and correspond to the experimental measurements (figure 5.1). This highlights the filtering effect of the experimental rig geometry on inflow discharge as demonstrated in Finaud-Guyot et al. (2018).

**5.1.3.2.2 GSA on water height** Based on previous investigations with 1D model (cf. section 5.1.3.1.3), four main input parameters are tested using GSA, namely west-face discharge  $Q_{west}$ , north-face discharge  $Q_{north}$ , outlet water height  $h_{out}$  and uniform friction coefficient  $K$ . Again their variation ranges are determined based on experimental uncertainties ( $Q_{north}^{cal} \pm 5\%$ ,  $Q_{west}^{cal} \pm 5\%$ ;  $h_{out}^{cal} \pm 10\%$  and  $K^{cal} \pm 50\%$ ). A sample size  $N_s = 2000$  ensures a good convergence of Sobol indices estimation in this 2D SW model configuration (cf. section 5.1.3.1.1). Sensitivity pattern of water depth is presented through 2D maps of Sobol indices along with their sum for the two inflow discharge partitions (figure 5.7). The sum of all Sobol indices is close to 1 for subcritical flow zones (corresponding to Froude number below in figure 5.7) meaning water

depth variance is perfectly explained by the first-order Sobol indices of the tested parameters. Interestingly, the sum  $\sum S_i$  is significantly below 1 in the part of street 1 in which a supercritical flow zone and a hydraulic jump appear for some parameter sets. A detailed investigation of this particular point is made in section 5.1.4.1.

2D maps of first order sensitivities of the water depth to the four tested parameters are presented in figure 5.7b, c, d, e. For the 50-50% hydraulic configuration, roughness and downstream water depth are the most important parameters explaining output water depth variance; as found for the 1D model (cf. section 5.1.3.1.3). Water depth sensitivity to downstream depth  $h_{out}$  and roughness  $K$  evolves globally in the direction from the north-west corner to the south-east corner except in the circle corresponding to supercritical flows; both patterns evolve as for the 1D GSA: decrease (resp. increase) in the direction of the flow for the sensitivity to  $K$  (resp.  $h_{out}$ ). The sensitivity to upstream discharge decreases along effective flow direction, i.e. along the diagonal from north-west to south-east corner; and is almost null in the downstream part of the streets. Interestingly, for the 50-50% configuration the maps show:

- the maximal sensitivity to both upstream discharge (that has the same nominal value and the same range of variation) is almost two time bigger for  $Q_{west}$  than for  $Q_{north}$ ;
- the water depth is more sensitive to upstream discharge in 2D than in 1D. This might be explained by the fact that discharge is more free on the 2D domain than on the 1D. As the modeling is performed in steady state, the water surface profile between two crossroads is described by a classical backwater curve that is function of the discharge (between other parameters). Indeed in 1D, the discharge is totally imposed by the upstream value and the lateral inputs on one street whereas in 2D, the flow repartition between street remains free (driven by the modeled crossroad behavior and mass exchanges between streets).

Histograms presented on figure 5.8 show the sensitivity of water depth to the tested parameters for several precise locations consisting mainly in crossroads within the streets network. They are ordered by increasing hydraulic distance from the upstream north-west corner. It depicts clearly the decrease of water depth sensitivity to upstream controls:  $Q_{west}$ ,  $Q_{north}$ ,  $K$ .

Figure 5.7 shows sensitivity patterns for a 80-20% inflow discharge partition between west and north faces. Spatial Sobol index patterns for this asymmetrical inflow are similar to the ones for the 50-50% configuration. However, the patterns are oriented from the north-west to the south-east corner; i.e. oriented in the direction of the global flow. As expected, the Sobol index of north-face discharge decreases, whereas west-face discharge index increases and explains more than 25% of water depth variance for streets 1 to 4. In that case, the influence of downstream control ( $h_{out}$ ) is lower for the region close to the west and north faces. The supercritical flow region downstream of street 1 is also reduced for less discharge passing by from the north-face.

## 5.1.4 Discussion

### 5.1.4.1 Metamodel error on $S_i$ estimation with hydraulic shocks

As previously shown in section 5.1.3.2.2, the sum of the first order Sobol indices is significantly below 1 in the supercritical region (illustrated by the circles on figure 5.7). Figure 5.9 presents the  $S_i$  profiles along the downstream part of the street 1; figure 5.9 - bottom right shows the range of Froude numbers obtained on the parameter sample, which defines the “shock zone” where supercritical flows ( $Fr > 1$ ) and hydraulic jumps appear for some parameter sets. Figure 5.9 - top right presents all the sampled water surface profile; it highlights that the range of variation of the water depth is almost 3 times larger in the shock zone compared to outside.

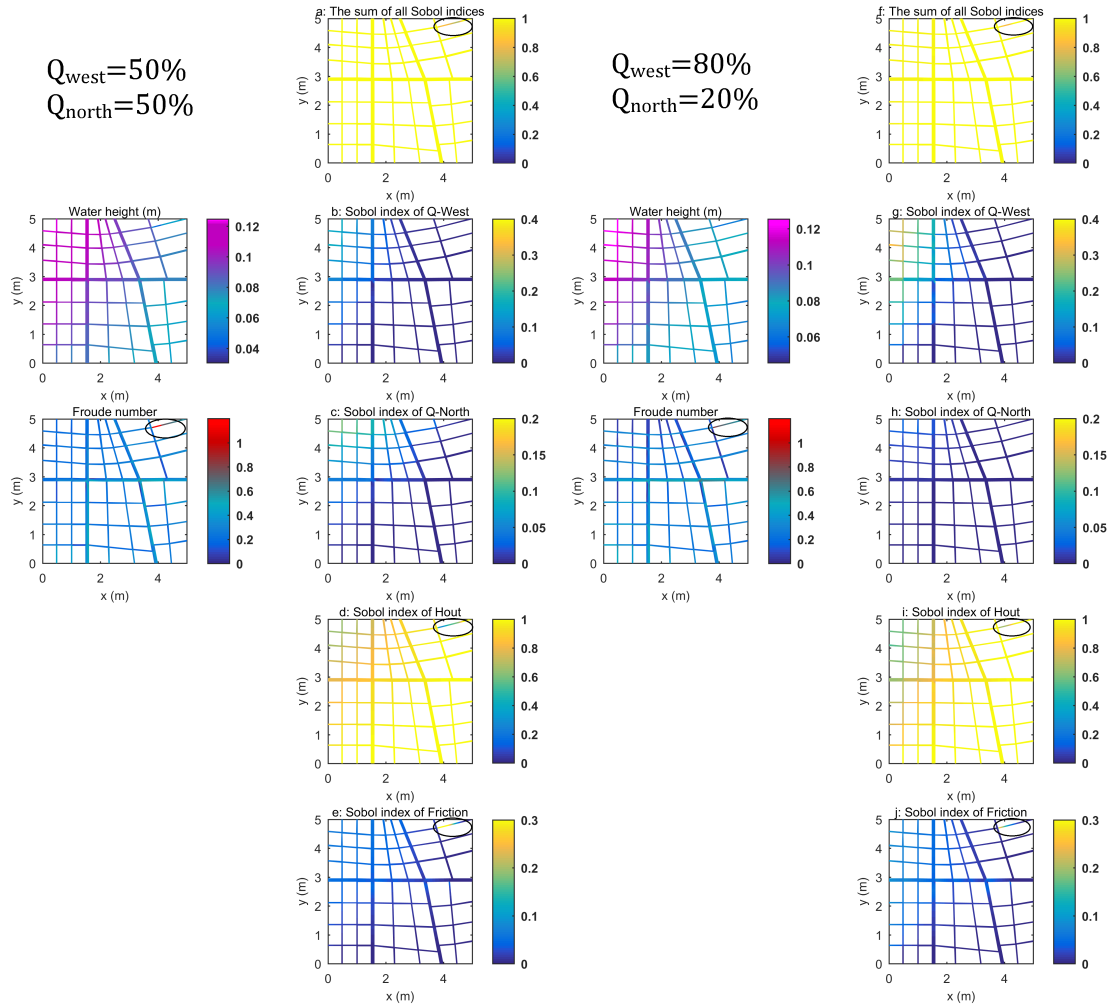


Figure 5.7: 2D maps of Sobol indices for  $80 \text{ m}^3/\text{h}$ : Left, inflow discharge partition at west and north-face 50-50%; Right, inflow discharge partition at west and north-face 80-20%. The circles highlight supercritical flow zones ( $Fr > 1$ ).

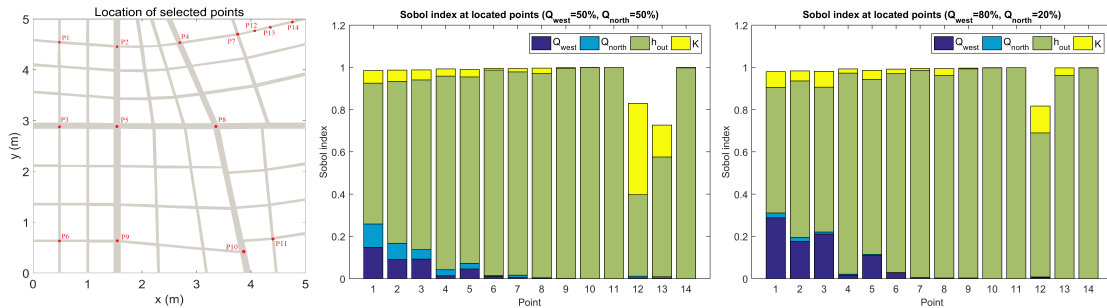


Figure 5.8: Decomposition of local sensitivity of water depth to the tested parameters, experiment without slope. Numbering of points made in function of hydraulic distance to the upstream north-west corner.

Downstream of the shock zone ( $x > 0.9$ ), the variance of the water depth is totally explained by  $h_{out}$  (cf. figure 5.9 - top left); for  $x$  between 0.15 and 0.9, the sensitivity to  $h_{out}$  decreases from downstream to upstream. It can be correlated with the fact that downstream water depth represents a hydraulic control only if the flow is fluvial while the most upstream point is characterized by the highest number of torrential flows over the  $N_s$  flows simulated. The spatial variation of water depth sensitivity to the roughness coefficient  $K$  is barely the negative of the sensitivity pattern to  $h_{out}$ . As presented in section 5.1.3.2.2, the sensitivity of the water depth to the upstream discharge (both  $Q_{north}$  and  $Q_{west}$ ) is almost null along the whole street for the tested ranges.

One cannot ignore that a sum of the first order  $S_i$  lower than one claims for interaction effect between the tested parameters or for metamodel error on Sobol index (e.g. Janon (2012)). The quality of the  $S_i$  estimation with the metamodel is assessed by the correlation coefficient  $r^2$  (cf. figure 5.9). It appears that outside of the shock zone, the  $r^2$  is almost equal to 1 and decreases to 0.7 in the shock zone for which the water depth vary of almost 50%, with respect to 10% outside, around the nominal one (figure 5.9). Moreover, note that metamodel standard deviation is quite narrow as shown for each  $S_i$  profile on figure 5.9 that remain hydraulically coherent.

#### 5.1.4.2 Sensitivity of outlet discharge

In the context of urban flood forecasting, spatial distributions of water height are of great interest but also discharge distribution, at the downstream end of the 14 streets here. The Sobol indices of outlet discharges to 4 main flow controls ( $Q_{north}^{cal} \pm 5\%$ ,  $Q_{west}^{cal} \pm 5\%$ ;  $h_{out}^{cal} \pm 10\%$ ,  $K^{cal} \pm 50\%$ ) in figure 5.10 for different inflow discharge partitions (50-50% and 80-20%); Sobol indices are also calculated for subdistricts as detailed hereafter.

Figure 5.10, top left illustrates the Sobol indices for 14 outlets in south and east face with equal repartition of inflow discharges. For all streets, the sum of all Sobol indices is close to 1, which means no interaction effect exist between the tested parameters controlling the flow distribution at outlets. The outlet discharges in street 1, 5, 6, 7 and G are nearly totally controlled by downstream water height. We retrieve a total dependence between outlet water depth and discharge, in other words a rating curve relationship for those streets. The outlets of street 5, 6, 7 and G are located at the south-east corner of the device, which is far from the inlet at west and north face, and separated by three big streets C, F and 4. Therefore, the influence of upstream discharge distribution on west and north faces can not propagate and is

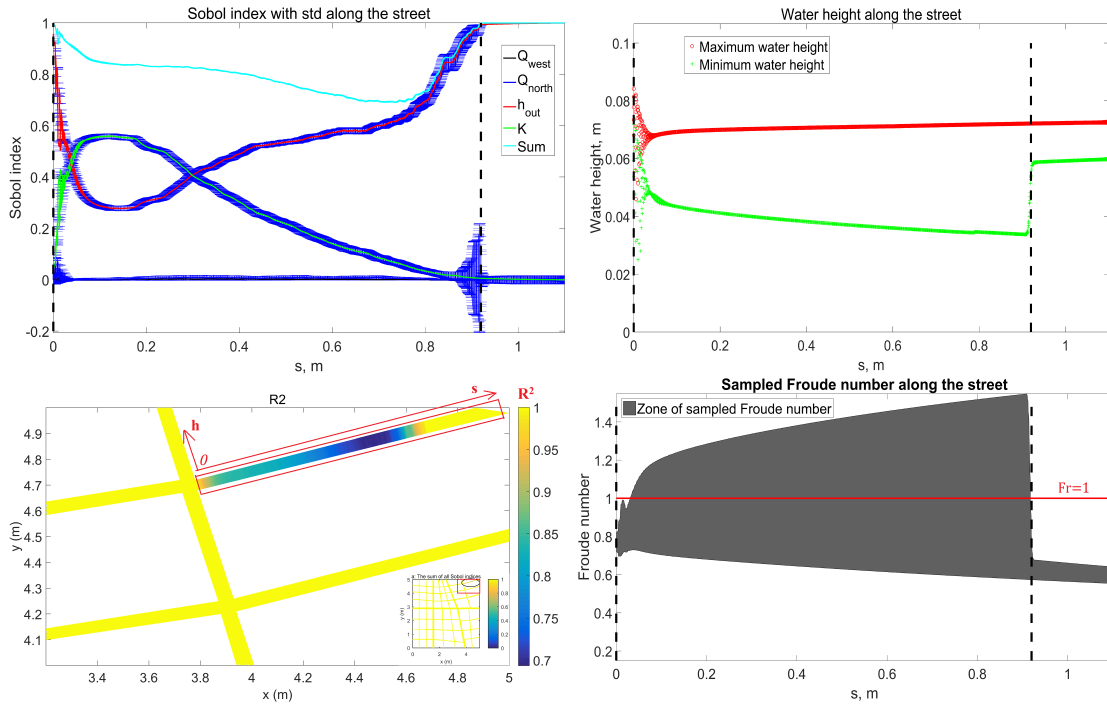


Figure 5.9: Sobol index profiles along the downstream part of street 1 (Top left);  $r^2$  map of the metamodel used to estimate  $S_i^2$ 's (Bottom left); variation range of water surface (Top right) and Froude number profiles (Bottom right) obtained with 2D SW model on the parameter set sample, vertical dashed lines indicates the zone where supercritical flows and hydraulic jumps appear on the sample.

filtered out by those larger streets. This is confirmed by the same sensitivities to  $h_{out}$  for those streets on the 80-20% flow repartition (cf. figure 5.10, bottom). Moreover, concerning street 1 a supercritical flow zone occurs (cf. figures 5.7 and 5.9) hence the flow in street 1 is totally controlled by upstream conditions. Therefore the output discharge of street 1 is not controlled by its downstream water depth but those of other streets. It may be explained by the fact that, applying a stronger downstream control on all streets (i.e. increasing  $h_{out}$ ) reduces the discharge flowing out streets 2 to G thus increases relatively the discharge of street 1.

The outlets of street 2 and 3 (resp. street A, B, D and E) are located close to the inlet on north face (resp. west face), which may be the reason for higher sensitivities to  $Q_{north}$  (resp.  $Q_{west}$ ) for those streets (cf. figure 5.10a). The influence of  $Q_{north}$  (resp.  $Q_{west}$ ) on outlet discharge decreases from street 2 to 3 (resp. street A to E) as their distance to north-face inlet (resp. west-face inlet) increases, whereas the influence of west-face discharge (resp. north-face discharge) increases. Interestingly for streets A to E, the sensitivity of the outlet discharge to  $Q_{west}$  is divided by more than 2 between streets A-B and D-E. This may be related to the influence of the main street C between those two groups of streets.

$h_{out}$  explains around 30% of the outlet discharges of streets A-B and 60% for streets D-E. The first being located closer from the inlet hence more sensitive to inflow discharge than global outlet water height. Moreover flow is conveyed/crossing big streets before reaching streets D-E. For big streets C, F and 4, the influence of west-face discharge and north-face discharge is equal which makes sense given their central locations within the district geometry. Interestingly, outlet

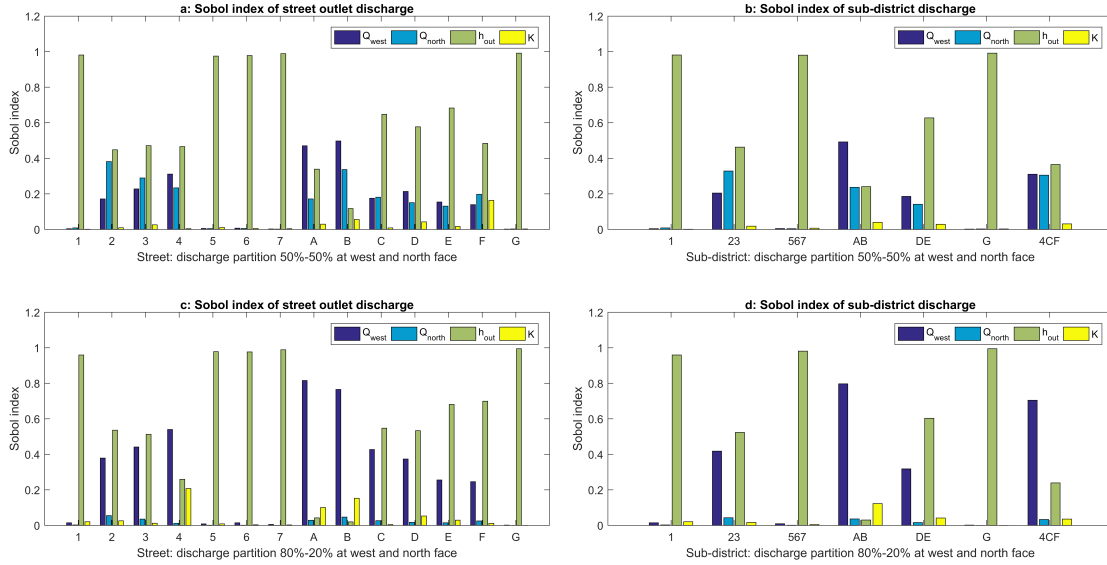


Figure 5.10: Sobol indices of outlet discharges obtained with the 2D SW model (for each test,  $\sum S_i \in [0.97; 1]$ ).

discharge are barely not sensitive to uniform roughness for those steady configurations. However, about 20% of the outlet discharge variance of street F is explained by roughness, which may be linked to its particular orientation north-west to south-east.

As observed by Finaud-Guyot et al. (2018), the 14 outlet discharges can be divided into several sub-districts using big streets, which are sub-district composed of street 1 (for supercritical flow), sub-district 23, sub-district 567, sub-district AB, sub-district DE, sub-district G and sub-district 4CF composed of big streets. The Sobol indices of sub-districts are presented in figure 5.10 for 50-50% and 80-20% inflow repartition. When west-face discharge partition changes from 50% to 80% illustrated in figure 5.10, results show that the influence of west-face discharge increases at sub-district 23, sub-district AB, sub-district DE, and big street sub-district 4CF, where north-face discharge decreases respectively. The Sobol index of outlet water height and friction coefficient is not very sensitive to this change except for streets 4, A, B, C that are less (resp. more) sensitive to  $h_{out}$  (resp.  $K$ ); street F has an opposite trend. The increase of the sensitivity to  $K$  may be related to the increase of the velocity for the concerned streets.

As a conclusion of this section, big streets acts as global flow pattern separators into several sub-district, which can block the influence of upstream inlet discharge and increase the influence of downstream outlet water height.

### 5.1.4.3 Sensitivity to slope

The influence of bottom slope on the simulated free surface flows in the urban district geometry is investigated here. A constant slope in the north-south direction  $I_{NS} = 2\%$  is simulated (the increased elevation of inlets on north face is 0.1 m). The total inlet discharge is  $80\text{m}^3/\text{h}$  with 50-50% and 80-20% discharge partitions at west and north-face. The outlet water height is obtained from 3D model simulations with interface tracking performed using InterFoam and validated on the measured outlet discharge in the “flat configuration” - not presented here. The four input parameters tested previously are investigated here with a bottom slope: west-face discharge

$Q_{west}^{cal} \pm 5\%$ , north-face discharge  $Q_{north}^{cal} \pm 5\%$ , uniform friction coefficient  $K^{cal} \pm 50\%$  and the downstream water height  $h_{out}$  with a range of  $\pm 10\%$  for all streets and configurations except for street 1, 2, 3 and 4 with the 80-20% inflow discharge partition because reverse flow appears at the outlet; the range is thus modified to  $[-10\%, -1\%]$ .

Figure 5.11 presents the results (maps of water depth and Froude number) of the calibrated model with slope for both configurations and the first order Sobol index. The Froude number maps show that by adding a slope in north-south direction, more supercritical flows and hydraulic jumps are generated in streets of north-south direction than in the horizontal case. As presented in section 5.1.3.2.2, the sum of the first order Sobol index is equal to 1 for the whole subcritical flow and smaller than 1 where supercritical flows appear as shown by Froude distribution. The GSA remains consistent for the whole domain as shown in section 5.1.4.1. A comparison of Sobol index maps with and without slope (cf. figure 5.11 and 5.7) shows that the sensitivity patterns are barely the same except in the torrential zones. In the configuration with slope, the influence of  $Q_{west}$  and  $Q_{north}$  (resp.  $h_{out}$ ) on the water depth is almost multiplied (resp. divided) by 2. As in the configuration without slope, the sensitivity to roughness  $K$  becomes non negligible in the torrential zone due to the increase of the velocity.

Histograms presented on figure 5.12 show the sensitivity of water depth to the tested parameters for several precise locations consisting mainly in crossroads within the streets network. They are ordered by increasing hydraulic distance from the upstream north-west corner. It depicts clearly the decrease of water depth sensitivity to upstream controls:  $Q_{west}$ ,  $Q_{north}$ ,  $K$ . However their influence is lower than previously without slope (figure 5.8) because of the occurrence of several super critical flow zones characterized by a higher sensitivity to  $K$  even downstream and acting as a hydraulic disconnection.

Figure 5.13 illustrates the influence of four input parameters on 14 outlet discharges in 50-50% inflow discharge partition with slope. Compared with the results presented in figure 5.10, the sum of first Sobol indices is reduced between 0.8 and 1 for all street except for streets 6 and 7 for where it reduces to almost 0.7. This can be explain by possible parameter interactions but also the occurrence of more supercritical flow zones and hydraulic jumps. Moreover streets 5 to 7 outlets are almost disconnected from upstream (due to torrential flow in streets F and G illustrated in figure 5.11) and corroborates a sensitivity of outlet discharges mainly explained by  $K$  and  $h_{out}$ . The outlet discharges for the streets 5 to 7 and G are also more sensitive to the roughness coefficient  $K$  in the configuration with slope which can be related to the increase of the velocity in the southern streets. The outlet discharge for the streets 2 to 4, B, D and E are significantly less depending on  $Q_{west}$  and  $Q_{north}$  (with a similar  $S_{Q_{west}}/S_{Q_{north}}$  ratio for streets B, D and E) and conversely more depending on  $h_{out}$ . This can be related to north-south slope that deviate the flow in the south and south-east outlets. No significant change can be observed for street 1 and A. The slope has an opposite effect for the main streets C and F outlet sensitivity patterns: the sensitivity to  $h_{out}$  decreases (resp. increases) for street C (resp. F). Street C becomes more sensitive to  $Q_{west}$  whereas street F becomes insensitive to both  $Q_{west}$  and  $Q_{north}$ . Those trends might be explained by more torrential flows appearing in street F than in street C, leading to a more important disconnection from upstream.

### 5.1.5 Conclusions

This study proposes a framework for performing global sensitivity analysis (GSA) in the case of complex free surface flood-flow modeling. It quantifies the influence of the uncertainty of 1D and 2D Shallow water model input parameters on simulated urban flood flows using GSA. For our case study based on the urban flood experimental rig of ICube laboratory Strasbourg different

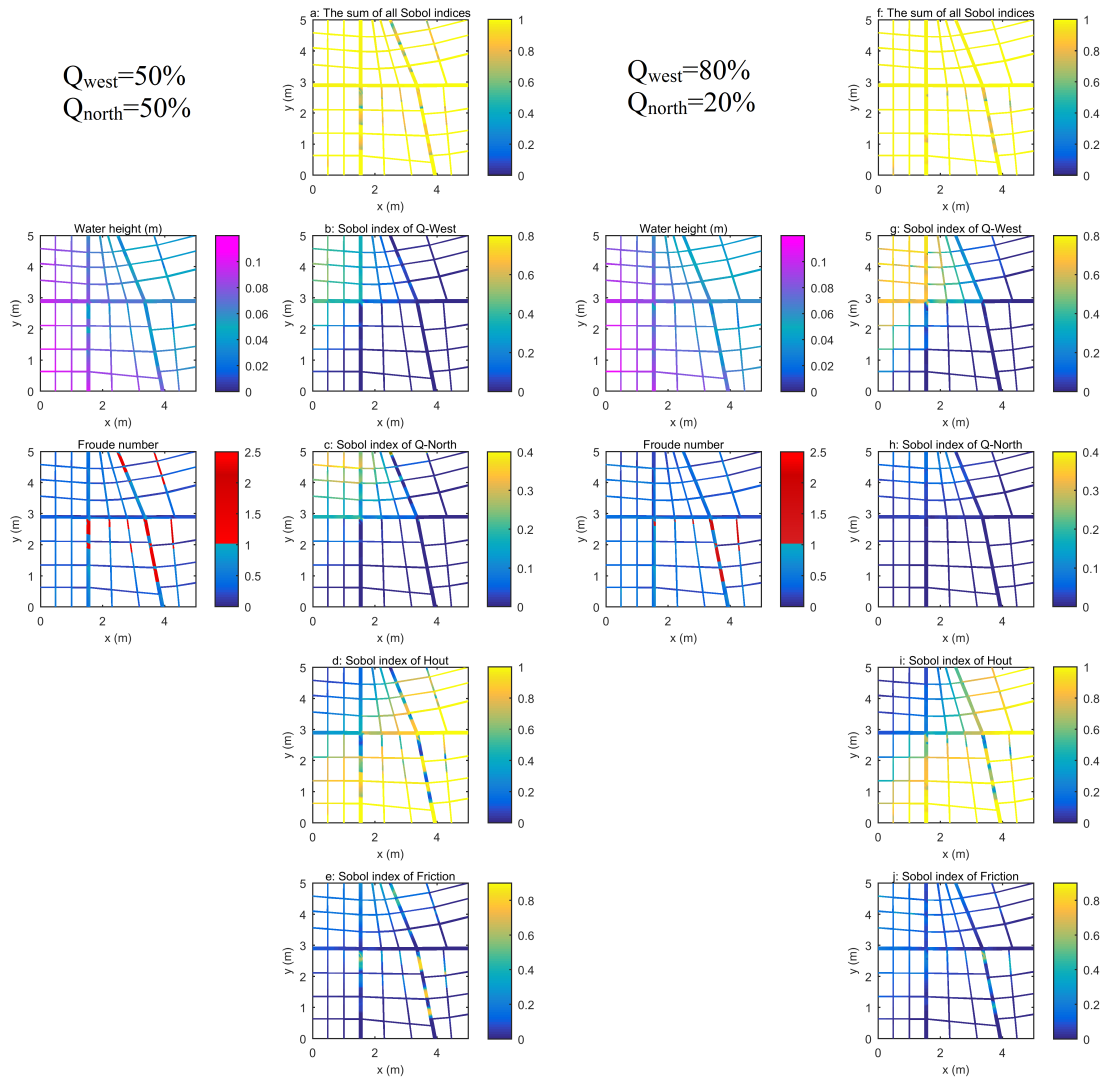


Figure 5.11: 2D maps of Sobol indices for  $80 \text{ m}^3/\text{h}$  with slope: Left, equal 50-50% inflow discharge partition between west and north-face; Right, 80-20% inflow discharge partition between west and north-face

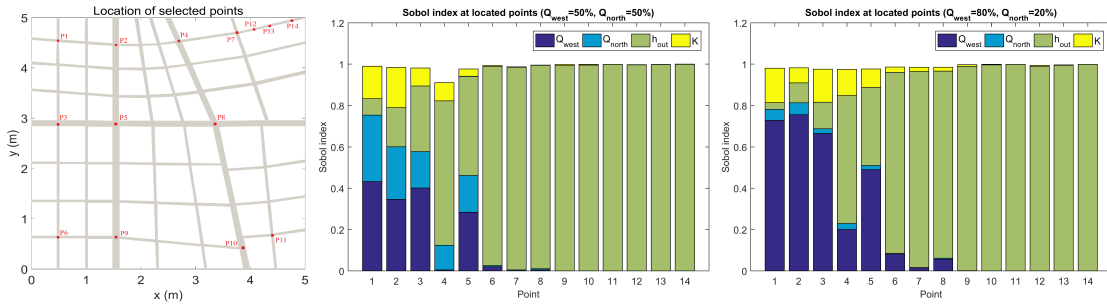


Figure 5.12: Decomposition of local sensitivity of water depth to the tested parameters, experiment with slope. Numbering of points made in function of hydraulic distance to the upstream north-west corner.

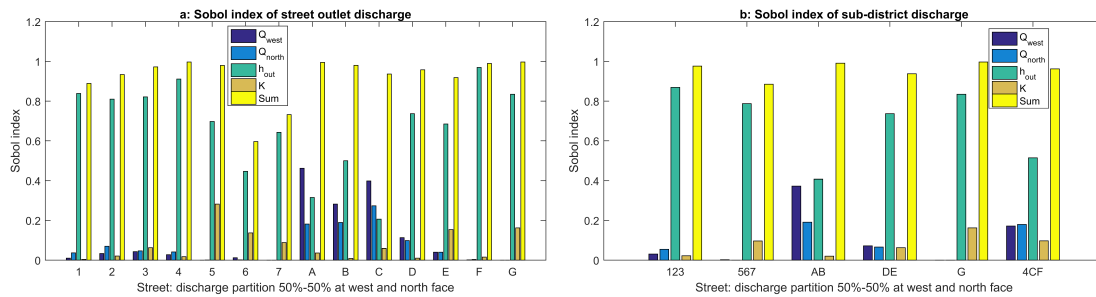


Figure 5.13: Sobol indices of outlet discharges obtained with the 2D SW model with slope

spatial patterns of parameters sensitivity have been found and model output variance explained wrt parameter sensitivities:

- General sensitivity patterns of 1D SW equations have been obtained with parameters sampled on equal ranges. The results show that in 1D configuration, the closer from the downstream boundary condition on water height, the higher the Sobol index as predicted by hydraulic theory for subcritical flow. Interestingly, the sensitivity to friction and upstream discharge are very similar. At a 'far enough' upstream end of the domain, the sensitivity to the downstream water depth is null and both roughness coefficient and upstream discharge explain 50% of the water depth variance.
- 1D Sensitivity patterns corresponding to our experimental uncertainties are similar to previous ones with a lower influence of the upstream discharge that is less uncertain. Water depth variance is mostly explained by friction and downstream water depth showing opposite spatial variations. The sensitivity analysis to the lateral discharges highlight that the main (resp. smaller) streets of the experimental rig explain 30 to 45% (resp. 0 to 15%) of the water depth variance with a higher sensitivity close to the crossroads at which the flow is injected. Sensitivity to distributed (street and crossroad) friction coefficient has shown that the water depth variance is not proportional to the domain size on which a friction coefficient (either crossroad and street) is applied and that similar parameterization for different streets produce variables sensitivity responses. This highlights the need of identifying the strongest hydraulic controls during a calibration process.

- Maps of Sobol indices are provided for 2D SW model with two different upstream discharge partitions. The results are in agreement with the findings in 1D but in different proportions: the water depth variance is explained at almost 70% by the downstream water depth, to less than 10% by the friction coefficient and to less than 25% by the upstream discharge. This highlights that the friction coefficient plays a different role in the energy dissipation at 2D scale. Moreover it quantifies the filtering effect of the topography on the discharge distribution through the whole district as suggested by Finaud-Guyot et al. (2018) which is confirmed by the downstream discharge sensitivity to upstream inflow that is barely null. Concerning the street outlet discharge, different sensitivity patterns are obtained with a variance explained at 100% by the downstream water depth, or almost equally explained by the downstream water depth and the upstream faces discharge; the friction coefficient being only involved in some particular streets. The key findings is that larger streets acts as global flow pattern separators into several sub-district, which can block the influence of upstream inlet discharge and increase the influence of downstream outlet water height.
- Sensitivity maps are also presented for hydraulic regime changes and flows with a positive bottom slope triggering more supercritical flow in the district. The global sensitivity patterns remains similar but with an increased role of the friction coefficient, a water depth distribution that is less downstream dependent (especially in the sub-district that is closer of the inlets), and an asymmetrical sensitivity to the upstream discharge (with an increased sensitivity to the north discharge).

This work highlights and somehow quantifies the nonlinearities of these complex free surface flow patterns and dependencies. Subsequent works could investigate unsteady aspects of urban flood flows for other geometries, flood magnitude and source terms such as street/underground networks or building interactions. The sensitivity of 1D/2D coupled models could also be investigated along with other parametrizations of flow resistance. Note that the results presented involve a significant number of model runs - on the order of  $10^4$  2D model ( $4 \cdot 10^5$  cells) evaluations were needed corresponding 35 days of calculation on 256 cores. New methods for computing Sobol indices at a lower cost could also be of interest.

## 5.2 Variance based sensitivity analysis of 2D unsteady flood flow hydraulic model

Many flood hazard studies and predictions are performed with steady state models, including flood hazard mapping for different return period. However unsteady models (see e.g. Mignot et al. (2006); Schubert and Sanders (2012); Skinner et al. (2015); Arrault et al. (2016); Guinot et al. (2017a)) simulate spatio-temporal hydrodynamic patterns and consequently the variations of flood hazard throughout the passage of a flood wave. In this part, GSA of an unsteady urban flood model is conducted. The uncertainty of inflow hydrograph defined hereafter and uniform roughness are considered. First the input factors and especially the hydrograph shape are defined, then the resulting “calibrated model” outputs are analyzed (subsection 5.2.1). Next, Sobol variation ranges are defined and Monte Carlo simulations with sampling size 200 are conducted to check time-varied Sobol index to different uncertainty sources (inflow discharge and uniform roughness).

### 5.2.1 Calibration of the rating curve

Unsteady simulation on the whole ICube urban flood experimental rig illustrated in figure 5.1, considered without bottom slope, is conducted with a time-varied inflow hydrograph (see figure 5.14) defined for each street on north and west inlet faces and rating curves for each street on east and south outlet faces. The latest being calibrated with respect to the steady experiment with total inflow discharge  $80 \text{ m}^3 \cdot \text{h}^{-1}$  (respectively  $0.02222 \text{ m}^3 \cdot \text{s}^{-1}$  as presented in figure 5.14). Currently, the ICube urban flood experimental rig is not equipped to measure water depth in transient configuration at the downstream end of the streets. No experimental values can then be used to provide downstream boundary conditions for the modeling. A stage discharge relationship has then been used (Bos (1976); Gharahjeh et al. (2015)):

$$Q = \frac{2}{3} C_d B \sqrt{2g} h^{3/2} \quad (5.4)$$

where  $Q$  is the total discharge,  $B$  is the weir width (channel width in this configuration),  $h$  is the water depth above weir crest elevation and  $C_d$  is the discharge coefficient. The stage-discharge relationship is calibrated such as a nil water depth in the street corresponds to a nil discharge. This implies that the weir height is assumed to be nil in the numerical modeling. The discharge coefficient  $C_d$  is calibrated for each street using the steady state experimental value: the water depth and associated discharge measured in the downstream part of each street. The calibrated discharge coefficient is listed in table 5.2.

Table 5.2: Calibrated discharge coefficient of rating curve

Street	$C_d$	Street	$C_d$
1	2.8	A	1.2
2	1.2	B	1.2
3	1.65	C	1.15
4	1.05	D	1.2
5	1.8	E	1.2
6	1.2	F	1.25
7	1.75	G	1.2

## 5.2.2 Transient 2D modeling

A synthetic inflow hydrograph is considered (figure 5.14) with a total simulation time of 350s such as being 35 times bigger to the average relaxation time of the urban flood device estimated at 10s as found in next section. A simple shape with a piecewise linear function is defined such as  $Q(t = 0) = Q(t = 350) = 0 \text{ m}^3 \cdot \text{h}^{-1}$  and  $Q(t) = 80 \text{ m}^3 \cdot \text{h}^{-1}$ ,  $t \in [100; 150]$ , hence defining a rising limb of 100s a steady state of 50s and a falling limb of 200s. The inflow discharge is equally distributed at west and north face and proportional to the channel width for each street. The maximum inflow discharge of  $80 \text{ m}^3 \cdot \text{h}^{-1}$  corresponds to a typical flood discharge tested experimentally in steady state (cf. chapter 5 section 5.1).

Full 2D depth-averaged shallow water equations are solved and discretized on a triangular mesh grid with a resolution of 0.005m. The mesh convergence analysis has been conducted as mentioned above (see section 5.1.3.2.1). Finite volume method and HLLC Riemann solver are used to calculate the fluxes between neighboring cells. The initial water depth over the whole domain is set to 1.5mm before flash flood simulation starts.

## 5.2.3 Analysis of the direct run

The resulting spatial and temporal patterns of water depth and Froude number are presented in figures 5.15 and 5.16.

Figure 5.15 shows spatially distributed water height maps every 20s from 0s (starting of the flash flood) to 350s (end of the flash flood). The water height increases and decreases at rising and falling limb following the inflow hydrograph variations and spreads from north-west corner to east-south corner along the diagonal. The water height reaches the maximum at steady state of total inflow discharge  $80 \text{ m}^3 \cdot \text{h}^{-1}$  from 100s to 150s which has been analyzed in the steady simulation of section 5.1. Remark that for all snapshots of this unsteady simulation the water depth is higher upstream than downstream.

Figure 5.16 presents the time-varied Froude number on the whole device. More supercritical zones can be observed for this unsteady flash flood case. One reason can be the outlet weir height set to 0m instead of weir height of 0.05m in previous studies in steady state. Interestingly, maps of the distributed Froude number are very similar during rising limb (0s–100s) and steady state (100s–150s) and only decreases at the end of the falling limb (300s–350s), when the areas of supercritical flow reduce. The supercritical zones are located:

- Around outlets for  $t > 40\text{s}$ ;
- Inside the urban flood device and mostly during flood rising limb. The resulting hydraulic jumps downstream of those supercritical flow zones when a fluvial zone exists may affect the spread of the flash flood within the geometry.

As a matter of facts, the torrential zones located in downstream ends of each street tend to impose a critical depth for upstream fluvial flow lines. This may explain the general decrease of water depth along the apparent flow direction (NW-SE diagonal).

The time-varied outlet discharges of the 14 streets and their ratios to total discharge  $\frac{Q_i}{Q_{total,out}}$  ( $Q_{total,out}$ , total outlet discharges) are presented in figure 5.17. The temporal variations of outlet discharges follow the same trend than inflow hydrograph with a delay of about 10s, which is the propagation time needed to cross the whole device. The three biggest streets (street C, F and 4 having a width 0.125m) have the biggest outlet discharges compared to the small streets with a width 0.05m. To estimate if those biggest outlet discharges are related to the particular role of those streets or mainly due to their larger width, the discharges of larger streets have been computed and divided by  $\frac{0.125\text{m}}{0.05\text{m}} = 2.5$  to allow a simple comparison with

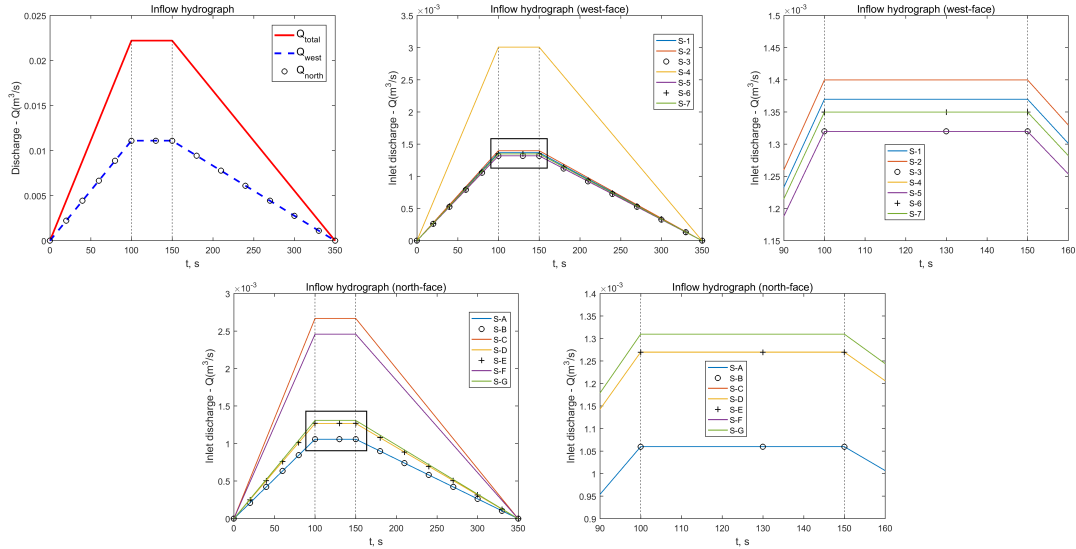


Figure 5.14: Inflow hydrograph on west and north face of each street

the discharges of smaller streets:  $Q_{equiv,4} = 0.001204 \text{ m}^3 \cdot \text{s}^{-1}$ ,  $Q_{equiv,C} = 0.001068 \text{ m}^3 \cdot \text{s}^{-1}$  and  $Q_{equiv,F} = 0.000984 \text{ m}^3 \cdot \text{s}^{-1}$ . Those equi-value discharges are in the range for the smaller streets. It indicates that the more water in streets 4, C and F is due to their widths.

The ratios between each outlet discharge  $Q_i$  and the total discharge  $Q_{total,out}$  are presented in figure 5.17 right. For all the streets, the relative discharge is constant between 0s and 5s. This corresponds to the contained water depth within the domain that flow out by the downstream weir. After 60s (dash line in figure 5.17 right), the relative discharges are barely constant. Before (respectively after) 350s, the biggest streets (4, C and F) represent almost 48% (respectively 42%) of the total discharge. Focusing on the trends of variation of the relative discharge around  $t = 350$ s, several groups of streets can be identified:

- Streets (1, 2, 3) and (A, B) that have a reduction of the relative discharge;
- Streets (D, E) that have a barely constant relative discharge;
- Streets (5, 6, 7) and (G) that have an increase of the relative discharge.

Interestingly, these groups of streets are the same than the one proposed by Finaud-Guyot et al. (2018) based on steady state experiment. This highlights the role of the streets network geometry to redistribute the discharge between streets.

It appears that during the falling limb of the flood, the streets that become more important are further from the inlet (NW corner).

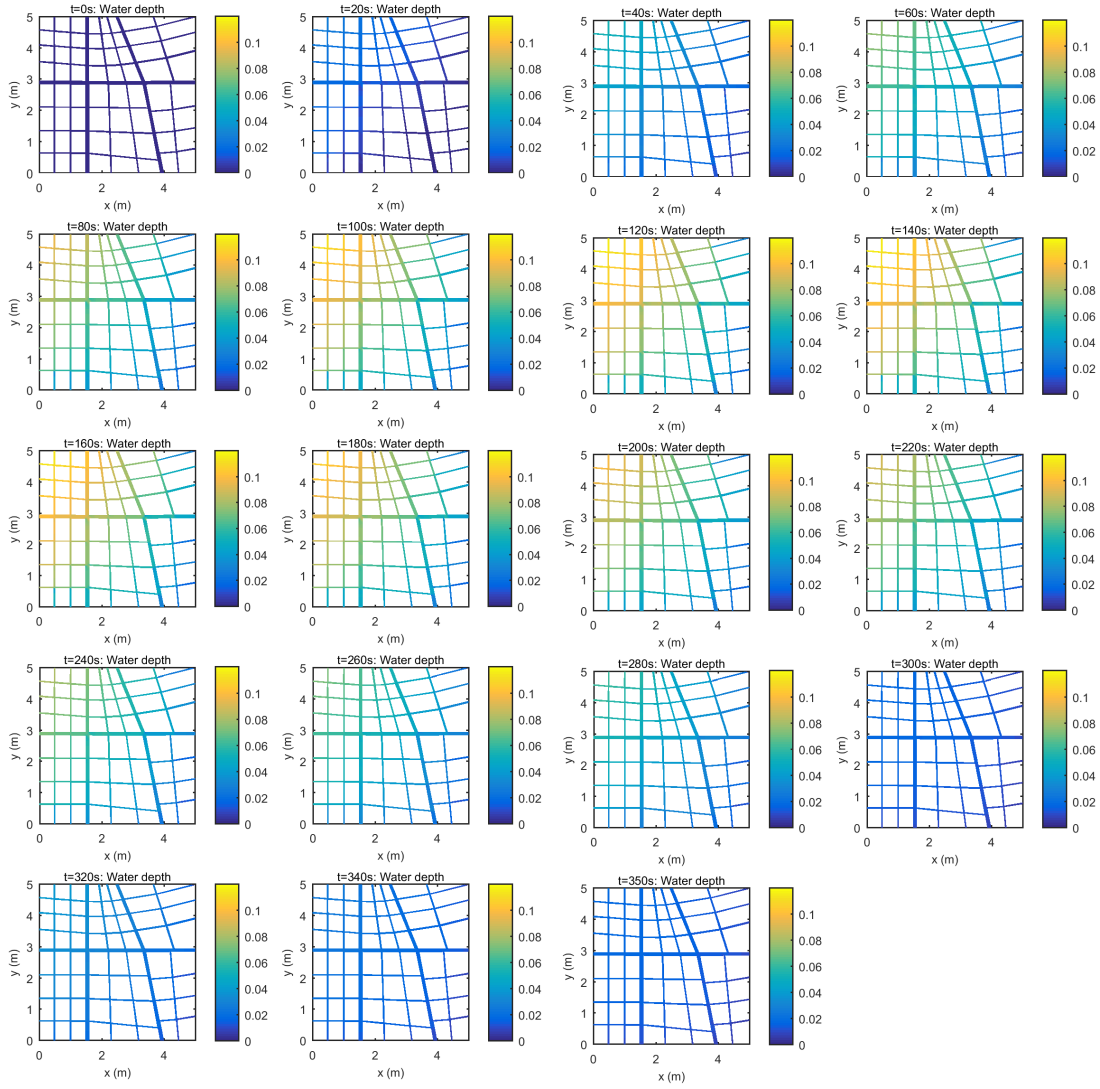


Figure 5.15: Time-varied spatially distributed water height

Table 5.3: Maximum inlet discharge for each street

Street	Inlet discharge	Street	Inlet discharge
1	0.00137 $\text{m}^3 \cdot \text{s}^{-1}$	A	0.00106 $\text{m}^3 \cdot \text{s}^{-1}$
2	0.00140 $\text{m}^3 \cdot \text{s}^{-1}$	B	0.00106 $\text{m}^3 \cdot \text{s}^{-1}$
3	0.00132 $\text{m}^3 \cdot \text{s}^{-1}$	C	0.00267 $\text{m}^3 \cdot \text{s}^{-1}$
4	0.00301 $\text{m}^3 \cdot \text{s}^{-1}$	D	0.00127 $\text{m}^3 \cdot \text{s}^{-1}$
5	0.00132 $\text{m}^3 \cdot \text{s}^{-1}$	E	0.00127 $\text{m}^3 \cdot \text{s}^{-1}$
6	0.00135 $\text{m}^3 \cdot \text{s}^{-1}$	F	0.00246 $\text{m}^3 \cdot \text{s}^{-1}$
7	0.00135 $\text{m}^3 \cdot \text{s}^{-1}$	G	0.00131 $\text{m}^3 \cdot \text{s}^{-1}$

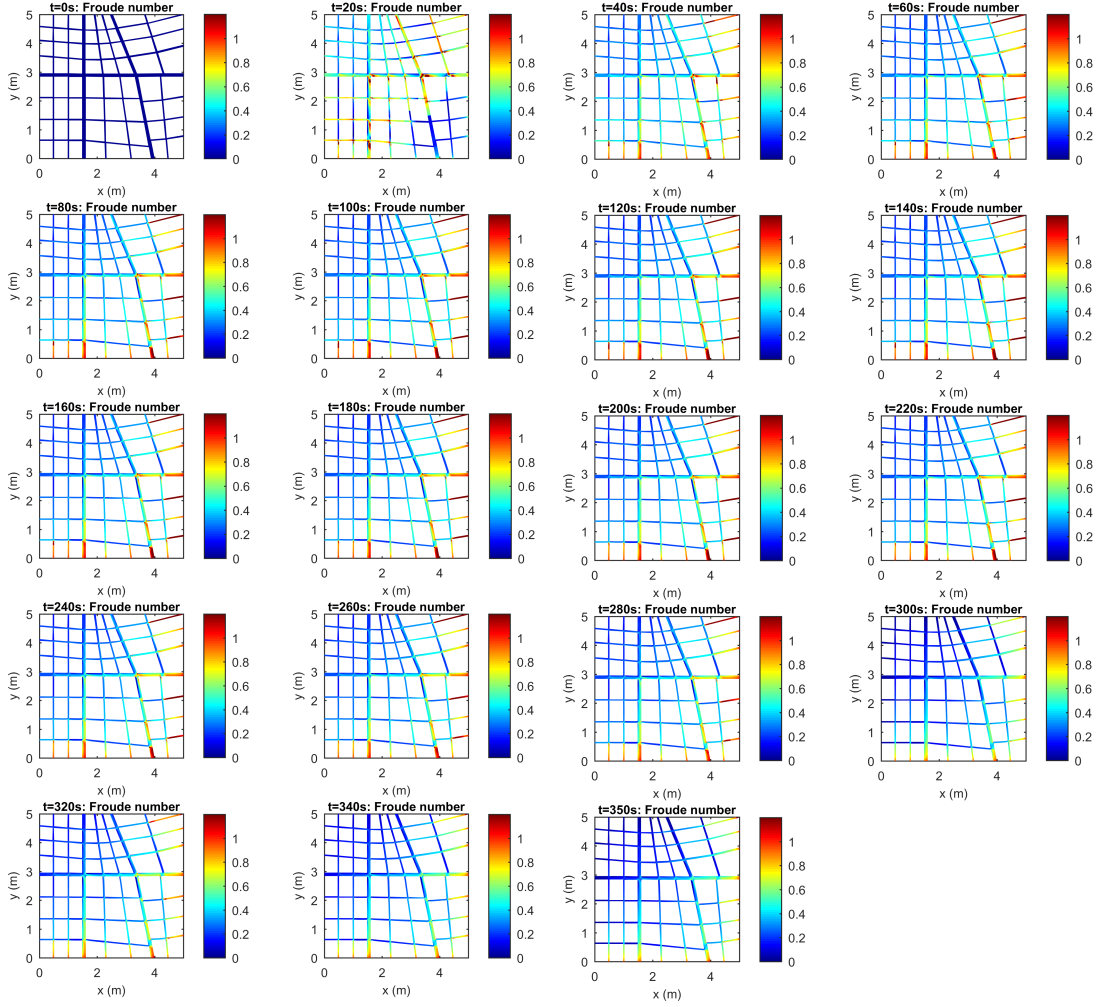


Figure 5.16: Time-varied spatially distributed Froude number

## 5.2.4 Global sensitivity analysis

Global sensitivity analysis (GSA) described in section 5.1.2 is applied to unsteady flash flood to determine the influence of uncertainty sources on unsteady model outputs. Two input parameters are analyzed: inflow discharge and uniform roughness  $K$ . The sampling range for inflow discharge is set to  $Q_{i,in}^{cal} \pm 25\%$  (see figure 5.14 for  $Q_{i,in}^{cal}$ ), hence maximum total inflow discharge  $Q_{in,total}^{cal}$  ranges from  $60\text{m}^3.\text{h}^{-1}$  to  $100\text{m}^3.\text{h}^{-1}$ . The sampling range for uniform roughness is set to  $K^{cal} \pm 50\%$ , which corresponds to roughness ranging between  $50\text{m}^{1/3}.\text{s}^{-1}$  and  $150\text{m}^{1/3}.\text{s}^{-1}$ . The outlet BC, rating curve, is not considered in this study. The sampling size is set to 200 given the computational cost of 1.5h on 32 processors of a forward run for each parameter set. The convergence of sampling size is reached based on the Sobol indices of  $R^2$  and  $S_i - std$  presented in figure 5.19. The standard deviation of the water depth Sobol index to  $Q_{in}$  and  $K$  is very low on the whole domain.  $R^2 \sim 1$  on the main part of the domain except where the flow hydraulic jump appears. In what follows, we present the Sobol maps of sensitivity of water depth to

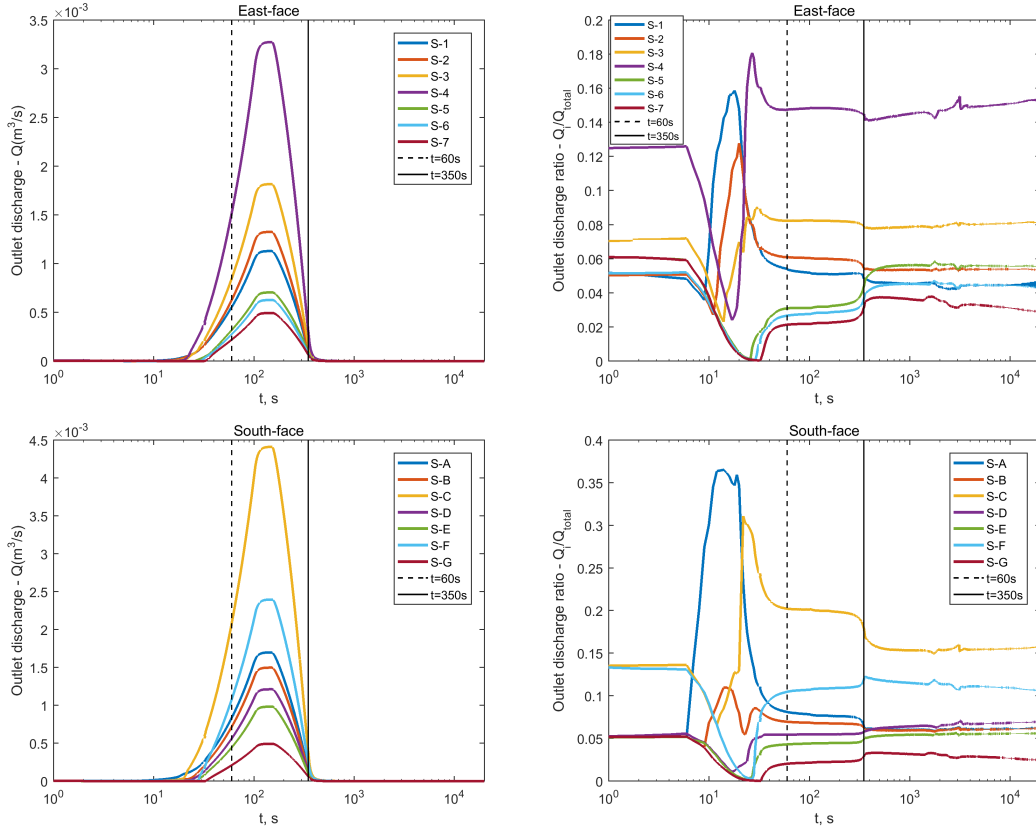


Figure 5.17: Time-varied outlet discharge (left side) and ratio  $\frac{Q_i}{Q_{total,out}}$  (right side) of 14 streets (top, east-face; bottom, south-face)

inflow discharge for 3 states (rising limb, steady peak state and falling limb) in figure 5.18. The sensitivity of outlet discharges to considered parameters is also provided in figure 5.20.

#### 5.2.4.1 Sensitivity analysis on spatially varied water height

The influence of uncertain inflow discharge and uniform roughness on the spatially distributed water height during a flash flood is studied. Sobol indices maps for inflow discharge, uniform roughness and their sum are presented in figure 5.18 for 9 different times equally sampling the three hydrograph phases (rising limb, steady peak state and falling limb).

Figure 5.18 left shows the sum of all Sobol indices  $S_{sum}$  that are close to 1 except at some locations where hydraulic jump and interaction effects exist. Such zones are reduced with increasing simulation time since hydraulic jumps tend to vanish throughout the device as explained in section 5.2.1 (see for instance, the map at  $t = 20s$  and  $t = 40s$ , street 4 between  $t = 160s$  and  $t = 220s$  and street F between  $t = 220s$  and  $t = 280s$ ). Again this shows water depth variance pattern is mainly explained at first order by the two parameters investigated (inflow discharge and uniform roughness), except at hydraulic jump locations as shown for steady state in previous section (see section 5.1.4.1).

Figure 5.18 middle shows the Sobol index of inflow discharge, which extends and decreases

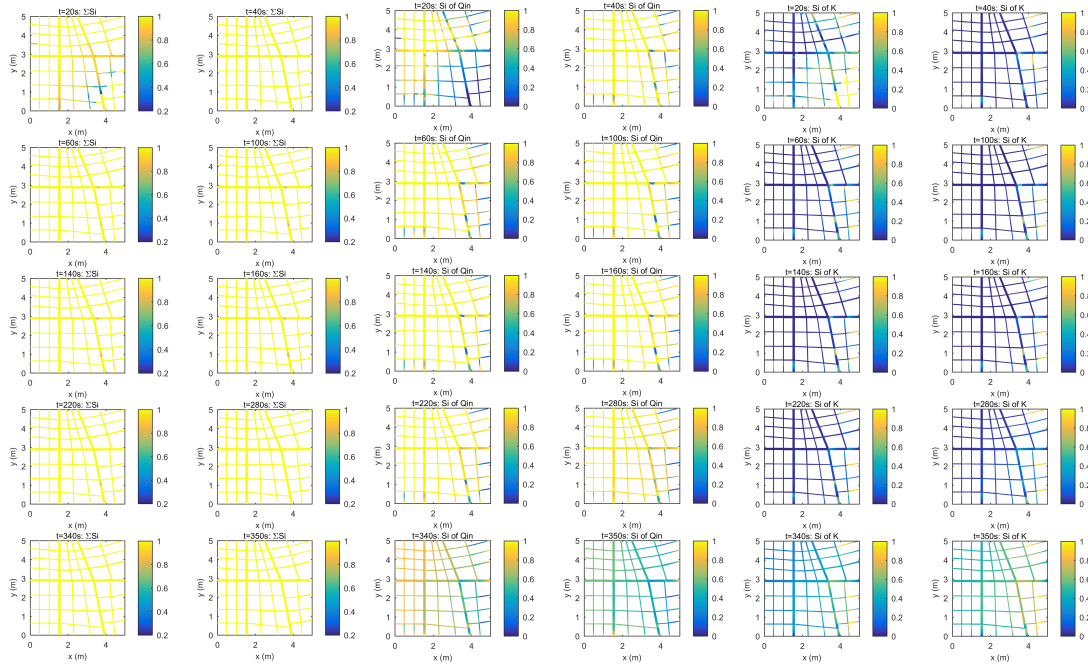


Figure 5.18: 2D maps of time-varied Sobol indices calculated on distributed water height: left, the sum of all Sobol indices; middle, Sobol index of inflow discharge; right, Sobol index of roughness

from north-west corner to the east-south corner along the diagonal. It spreads from the beginning of the flood (0s) and nearly has dominant control on the whole device at 40s except at the locations of supercritical flows where roughness plays a more important role. At the end of the flash flood ( $t=350s$ ) where inflow discharge has decreased to  $0m^3.h^{-1}$  but water still propagates, the inflow discharge and roughness has similar effect on water height except for supercritical zones.

The Sobol index of uniform roughness has an opposite trend compared to inflow discharge as illustrated in figure 5.18 right. In supercritical flow zones where no hydraulic jump exists, the Sobol index of roughness is close to 1 and roughness has dominant control instead of inflow discharge for the increase of velocity. For the supercritical zones followed by a hydraulic jump inside the device, interaction effect exist and the function of roughness on the water height decreases as explained in section 5.1.4.1.

#### 5.2.4.2 Sensitivity analysis on outlet discharge

Another output of interest is outlet discharge for the 14 outlet streets. Considering the Sobol estimation is approximately correct in terms of shape and  $R^2$  and  $S_i - std$  illustrated in figure 5.21 and sum always lower than 1.0577. Time-varied Sobol indices of outlet street discharges to the tested parameters (inflow discharge and uniform roughness) are presented in figure 5.20 at every 20s from 20s to 350s.

First of all, the sum of Sobol indices, for each outlet street, is close to 1 after 60s until to the end of the flash flood. Note that the sum of Sobol indices is lower than one during submersion but not during flow recession phase. This may suggest higher order interactions between the tested parameters. This could either be order two or more interactions between parameters, which could give insight for modifying model parameterization along with improving the accuracy of Sobol

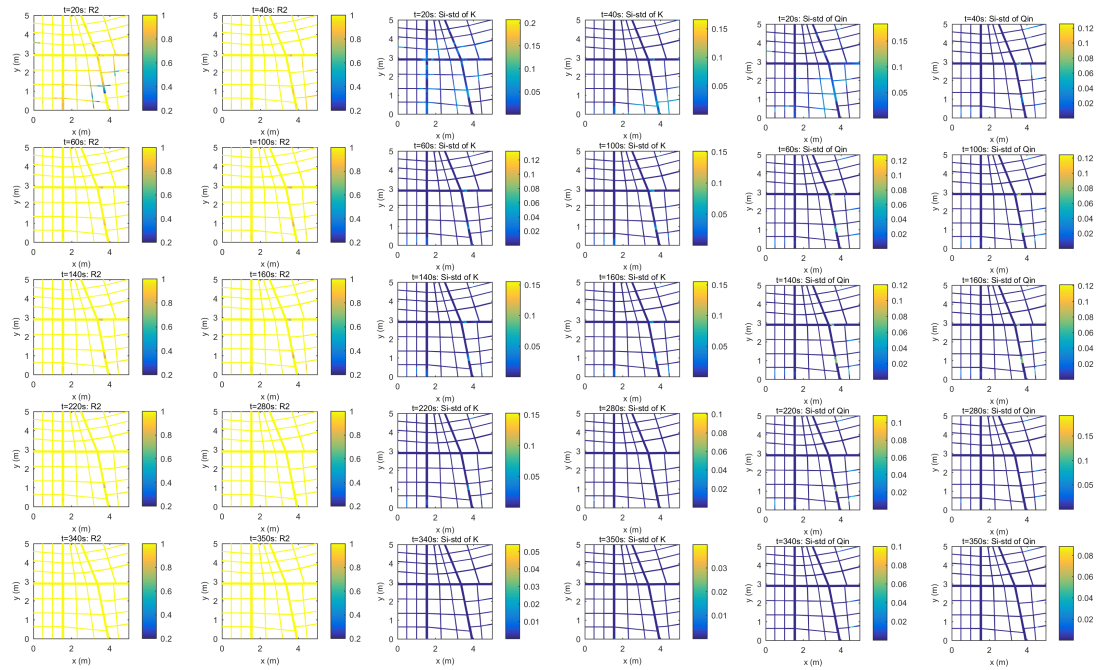


Figure 5.19: 2D maps of time-varied Sobol indices calculated on distributed water height: left,  $R^2$ ; middle,  $S_i - std$  of  $Q_{in}$ ; right,  $S_i - std$  of  $K$

indices estimation - higher sample size which is costly or other new effective estimation method (see e.g. Janon (2012)). The influence of total inflow discharge variation explains more than 80% of the outflow discharge variance of each outlet street except for the first point ( $t = 20s$ ) for which the outlet discharge is also influenced by the drainage of the initial water depth (see section 5.2.3). Sobol index of streets 5 and 7 show that those streets are less sensitive to  $Q_{in}$  (cf. figure 5.20 middle). This may either be due to their particular geometry (“broken street” at crossroads E5 and E7) or high Froude numbers. The other parameter considered is uniform roughness which explains on the order of 10% or less of the outflow discharge variance of each outlet street. Interestingly, the sensitivity to roughness is higher for streets 5 and 7 (cf. figure 5.20 right).

### 5.2.5 Conclusions on temporal sensitivities

This temporal sensitivity analysis investigated the influence of two input parameters (inflow discharge and uniform roughness) on 2D shallow water model response. The case of a synthetic “flash” flood has been simulated on ICube urban flood experimental rig geometry. The results show that:

1. Water spreads from north-west corner to the south-east corner along the diagonal and the variation of water depth is comparable to the inflow hydrograph shape;
2. Discharge distribution into the device reaches stable state at 60s during submersion flow phases and changes at the end of flash flood ( $t=350s$ );

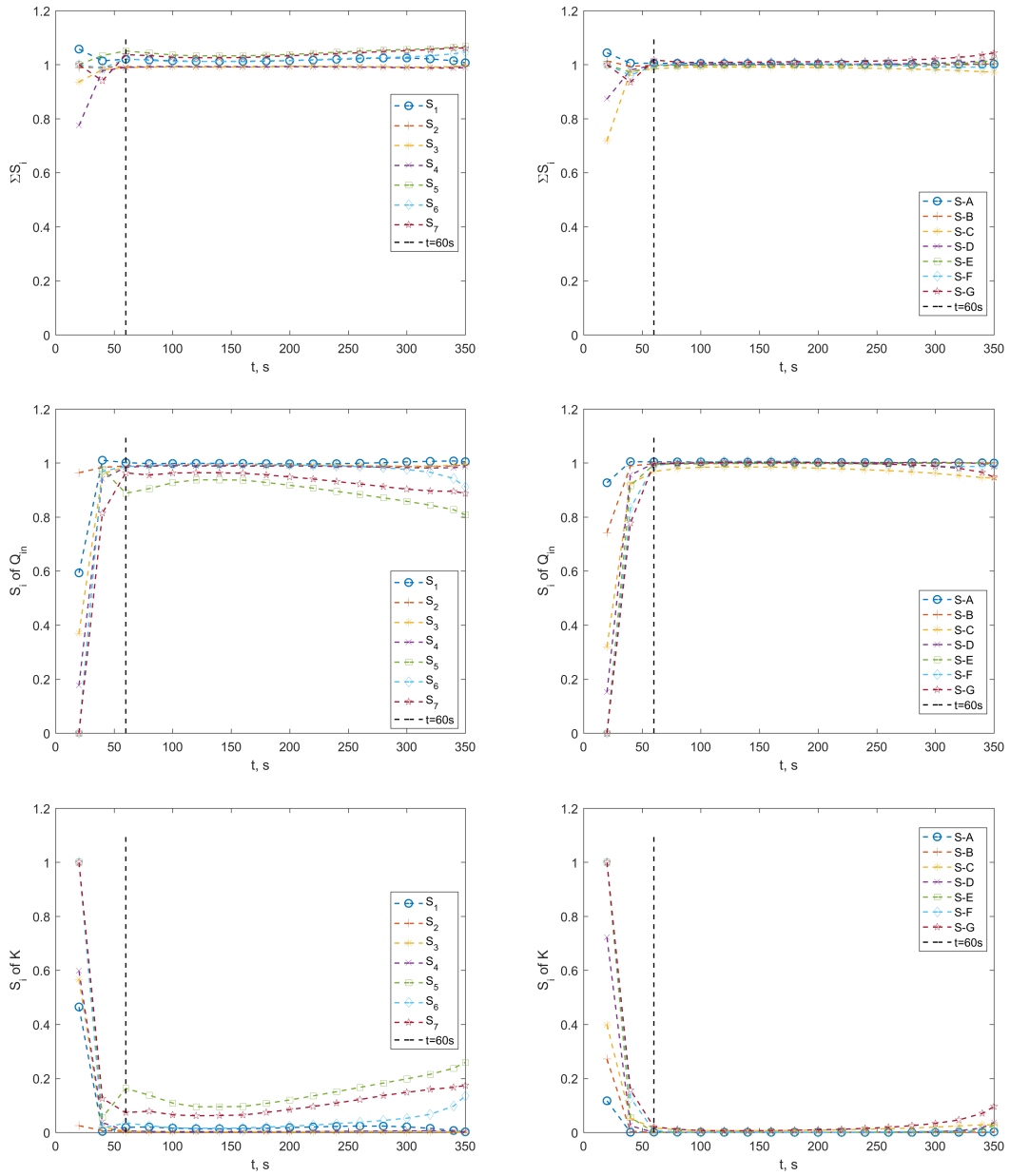


Figure 5.20: Time-varied Sobol indices on outlet discharge (left, east-face; right, south-face): top, the sum of all Sobol indices; middle, Sobol index of inflow discharge; bottom, Sobol index of roughness

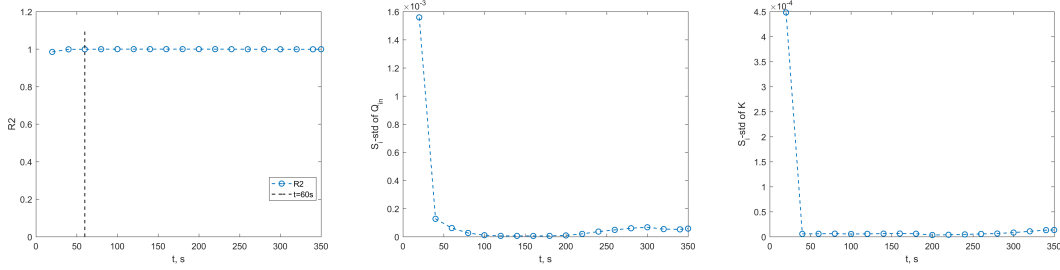


Figure 5.21: Time-varied Sobol indices on outlet discharge: left,  $R^2$ ; middle,  $S_i - std$  of  $Q_{in}$ ; right,  $S_i - std$  of  $K$

3. Supercritical flow zones appear during the submersion phase inside the domain and vanish when discharge distribution reaches stable state ( $t=60s$ );
4. From GSA it appears that inflow discharge has a dominant control on water depth (outlet discharge, respectively) except during “dynamic” submersion where roughness plays a larger role and higher order interactions may exist.

### 5.3 Sensitivity of global flow pattern to street blockage

During urban floods, blockage in the street might happen due to obstructions such as cars and fallen trees, especially in small streets. This induce a change of the local flow features (water height and velocity field) and might have impact on the global flow direction and the discharge distribution at outlets. To test the sensitivity of the urban model to the blockage, nine configurations are set to study their influence to flow features and discharge distribution. The blockages are considered for various street width and flow directions across the whole device. Their locations are presented in figure 5.22, which can be classified as: 1) blockage in small streets (blockage 1, 2, 3, 4, 5, 8 and 9, width 0.05m); 2) blockage in big street C (blockage 6, width 0.125m); 3) half-blockage in big street 4 (blockage 7, width 0.125m). The reference is the steady state simulation studied in section 5.1 without blockage.

To assess the influence of the tested blockage, we define  $\epsilon_f$  as:

$$\epsilon_f = \frac{1}{N} \sum_{i=1}^N \left| \frac{f_i^{sim} - f_i^{ref}}{f_i^{ref}} \right| \quad (5.5)$$

where  $N$  is the number of cells; subscript  $f$  is either  $h$  (for the water depth),  $Fr$  (for the Froude number) or  $Q$  (for the outlet discharge);  $f_i^{sim}$  stands for the simulated value of  $f$  in cell  $i$  and  $f_i^{ref}$  is the reference of this same variable in the same cell.  $\epsilon_f$  is thus a measure of the relative variation on  $f$  induced by a blockage.

Figure 5.23 illustrates  $\epsilon_h$  and  $\epsilon_{Fr}$  on 9 blockages compared with normal setting. Results show that water height is more sensitive to blockage 6, whereas Froude number is less sensitive to blockage 3, 4 and 5 compared with other settings. Figure 5.24 presents the evolution of  $\epsilon_Q$  for different blockage. Compared with other settings, outlet discharge is more sensitive to blockage 6 and 7.

The sensitivity analysis conducted above shows that full blockage (Blockage 6) on the wider street has bigger effect on both water height and Froude number distribution and outlet discharge.

Whereas for half blockage (Blockage 7) on the wider street, it only has bigger effect on Froude number and outlet discharge distribution, but not on water height. Full blockage on narrow streets (Blockage 1, 2, 3, 4, 5, 8 and 9) has limited influence on distributed water height whatever the street's location and direction. Simulated Froude number is sensitive to full blockage of narrow streets only if the street is located rather upstream or downstream as illustrated in figure 5.23 (right side).

## 5.4 Conclusions

This chapter proposed global sensitivity analysis (GSA) in the case of complex free surface flood-flow steady and unsteady modeling which based on the urban flood experimental rig of ICube laboratory Strasbourg. The influence of uncertainty sources of 1D and 2D Shallow water model input parameters on steady and unsteady model outputs is assessed in the case of urban flood flows using GSA with presented spatial and temporal sensitivity indices. The sensitivity of model output to street blockage is also assessed:

- Spatial Sobol index of steady 1D or 2D SW models has provided the guidelines for the calibration on input parameters before simulation to improve the model output accuracy. Input parameters studied are inflow discharge, outlet water height and uniform and distributed roughness based on the experimental ranges. The sensitivity to equal range is also tested to obtain the general sensitivity patterns. The sensitivity to bottom slope is conducted for special cases.
- Temporal and spatial Sobol index in 2D scale is provided to study the development of input parameter sensitivity along the time. Inflow discharge obtained from classical flash flood and uniform roughness are studied. The mechanism of discharge distribution into the device varied with time is studied. The Sobol index of inflow discharge spreads and disappears on the whole device as the same trend of inflow hydrograph of a flash flood.
- The sensitivity of flow features to the location of street blockage is conducted. Undoubtedly, the variation of flow features and outlet discharge caused by blockage in big streets (width 0.125m) is much bigger than small streets (0.05m). However, the role of small street is correlated with the location and direction of the street. This study can be used to identify the key small streets to the whole feature and discharge distribution into the device.

The presented sensitivity analysis can be the guidelines on model calibration and data collection before urban flood simulation.

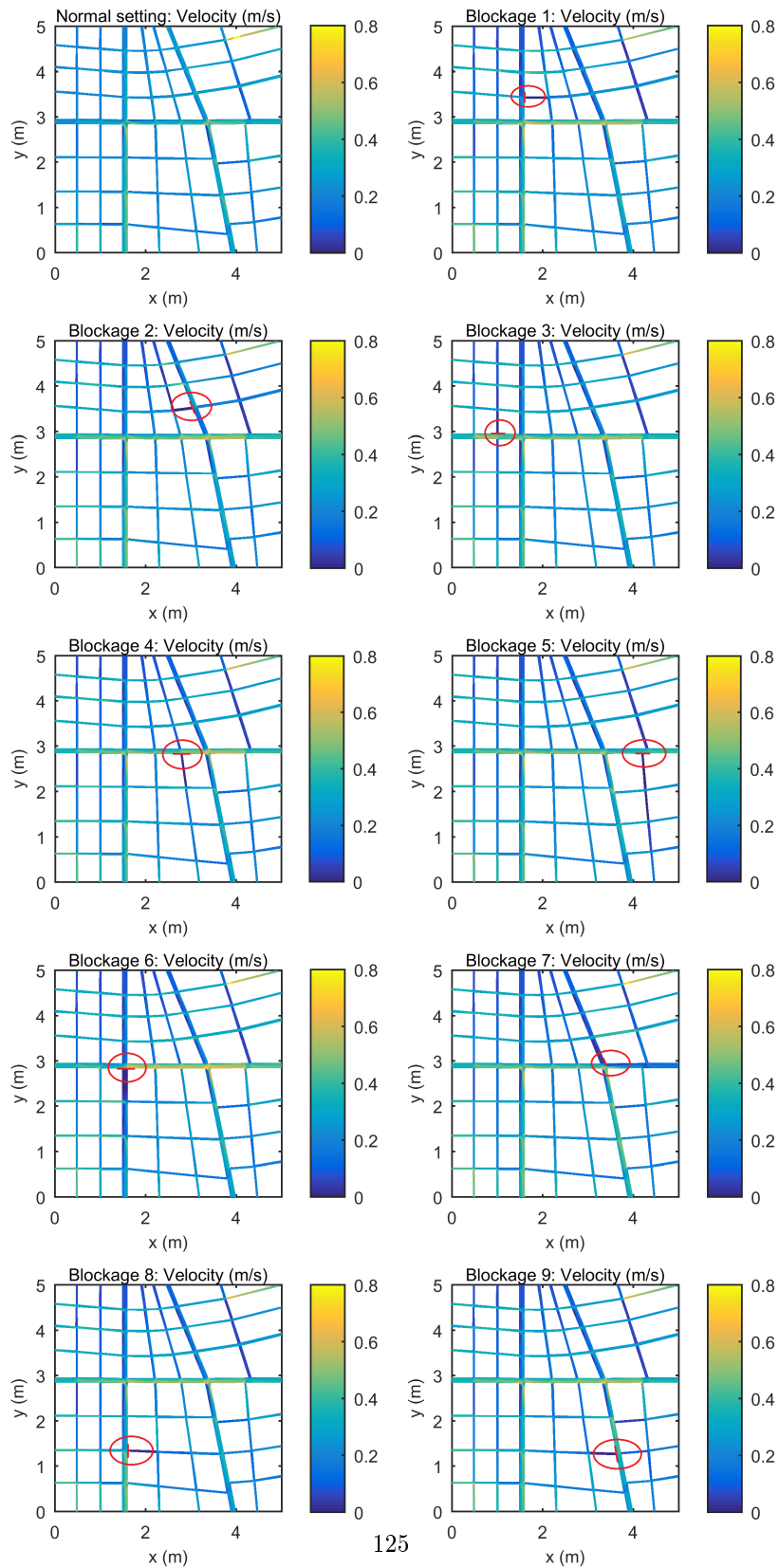


Figure 5.22: Simulated velocity field with/without blockages

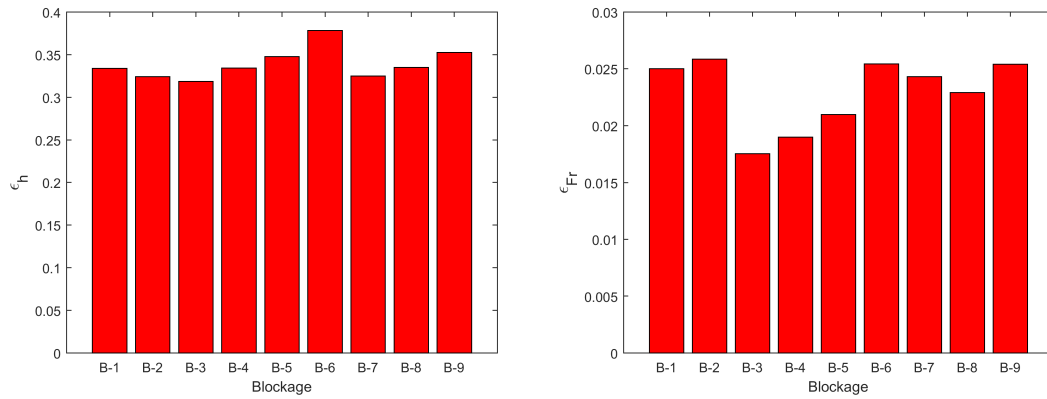


Figure 5.23:  $\epsilon$  on water height and Froude number for 9 blockages: left, water height; right, Froude number

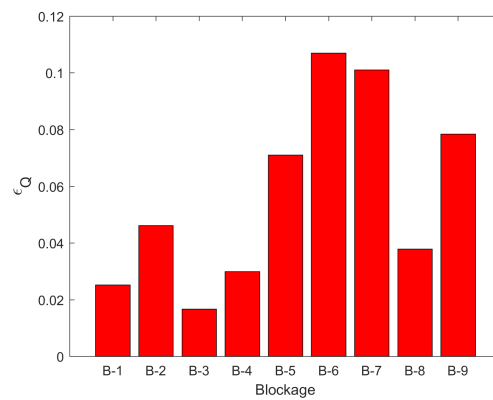


Figure 5.24:  $\epsilon$  on outlet discharge  $Q_{out}$  for 9 blockages

## Chapter 6

# Model applications

The numerical model *Flood1D2D* using cut-cell technique to account for the effect of recirculation zones downstream of crossroads has been derived in chapter 3 and validated in chapter 4 for various hydraulic configurations. In this chapter, the *Flood1D2D* model is applied on urban flood configurations using 1D2D coupling to reproduce flow patterns expecting performances comparable to those of a classical 2D model.

In view to tailor 1D2D shallow water model (*Flood1D2D*) to urban flood flow simulations the following points are investigated in this chapter:

- In the first section, the impact of different modeling options of the friction term is assessed. The modification of the friction slope due to the introduction of the recirculation effect through the porosity parameter is highlighted and the sensitivity of the  $S_f$  computation to hydraulic radius formulation is assessed for similar geometrical and hydraulic parameterisation;
- In the second section, the response surfaces of existing laws for predicting recirculation shape downstream of three branch intersections computed and compared, to give idea of the reasonable porosity on four branch intersections;
- In the third section, “real like” recirculation dimensions are estimated, with various methods, from 2D modeling (full 2D shallow water with turbulence) on a four branch crossroad configuration taken from an experimental dataset of Nanía et al. (2011);
- In the fourth section, the sensitivity of the simulated recirculation zone dimensions to input parameters of the full 2D SW model is investigated with GSA applied on a four branch crossroad;
- In the fifth section, *Flood1D2D* is parameterized and tested on the four branch crossroad configuration of Nanía et al. (2011). The influence of the porosity parameterisation and roughness on flow lines is tested;
- In the sixth section, the sensitivity of *Flood1D2D* on parameterisation is investigated with GSA;
- Finally, the model is applied to a district for reproducing experimental configurations of the ICube urban flood experimental rig.

## 6.1 Influence of the friction effect parameterization

The friction drag force is an essential physical effect that is accounted in the shallow water equations (see section 3.1.2). In this work, a classical Manning-Strickler parameterisation is used to compute the friction slope  $S_f$  (equation 3.54) involving the computation of the hydraulic radius. In classical 1D approaches, the hydraulic radius  $R_h$  involves the computation of the full wetted perimeter whereas in 2D, the hydraulic radius is classically approximated by the water depth in the computational cell to simplify the implementation. The friction slope  $S_f$  thus writes  $S_{f,1D}$  in 1D or  $S_{f,2D}$  in 2D:

$$S_{f,1D} = \frac{u^2}{K^2 R_h^{4/3}} \quad R_h = \frac{S}{\chi} \quad (6.1a)$$

$$S_{f,2D} = \begin{cases} \frac{u\sqrt{u^2 + v^2}}{K_x^2 R_h^{4/3}} & \text{along } Ox \\ \frac{v\sqrt{u^2 + v^2}}{K_y^2 R_h^{4/3}} & \text{along } Oy \end{cases} \quad R_h = h \quad (6.1b)$$

where  $K$  is the Strickler coefficient ( $K_x$  (respectively  $K_y$ ) being the Strickler coefficient in the  $x$  (respectively  $y$ ) direction),  $u$  (respectively  $v$ ) is the depth-average velocity in the  $x$  (respectively  $y$ ) direction.

The 1D cells in *Flood1D2D* represent the full street width (as it would be in a classical 1D model) but the classical 2D shallow water equations are computed on it (equations (3.56)). It thus seems logical in the context of 1D2D hydraulic modeling to wonder how to compute the hydraulic radius.

### 6.1.1 Approximations of hydraulic radius

For the implementation in *Flood1D2D*, the friction effect in the so-called 2D cells is computed using the classical  $R_h = h$  assumption for the 2D modeling tools. In the case of the 1D cells, the question of the hydraulic radius  $R_h$  computation remains. Indeed, the hydraulic radius  $R_h = S/\chi$  traduces the fact that the friction effect is induced by the contact length between the flow and the soil (represented by the wetted perimeter  $\chi$ ) that imposes a nil velocity and that this effect impacts the whole wetted cross section  $S$ .

In the particular case of a 1D cell, a part of the total wetted cross-section is assumed to be a recirculation for which the flow velocity is nil in average and thus for which the friction effect can be accounted to be also nil in average. The friction effect on the whole wetted cross section thus reduces to the part on the flow vein with three zones of contact between the flow and a nil velocity (see figure 6.1): the bottom, the solid wall and the interface between the flow vein and the recirculation zone.

Three different approaches have been proposed to estimate the wetted perimeter  $\chi$  and thus the hydraulic radius  $R_h$ . Considering 1D cells with recirculation zone (thus a porosity  $\phi$  a priori

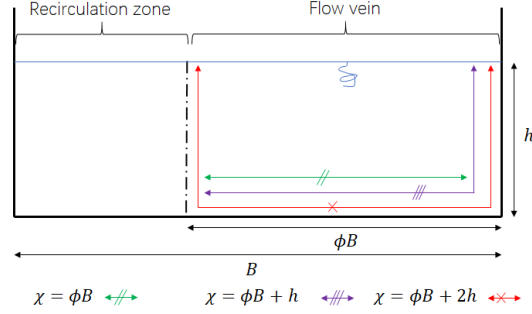


Figure 6.1: Scheme of the considered cross-section with recirculation

smaller than 1),  $\chi(h, \phi)$  and  $R_h(h, \phi)$  can be written:

$$\chi_{SW} = \phi B \qquad R_{h,SW}(\phi, h, B) = \frac{\phi B h}{\phi B} = h \qquad (6.2a)$$

$$\chi_{wall} = \phi B + h \qquad R_{h,wall}(\phi, h, B) = \frac{\phi B h}{\phi B + h} \qquad (6.2b)$$

$$\chi_{full} = \phi B + 2h \qquad R_{h,full}(\phi, h, B) = \frac{\phi B h}{\phi B + 2h} \qquad (6.2c)$$

where subscripts  $_{SW}$  stands for “shallow water” as the water depth is neglected in front of the effective width  $\phi B$  of the flow vein,  $_{wall}$  indicates that the friction is only accounted on the bottom and the side wall of the flow vein and  $_{full}$  corresponds to a full and classical computation of the wetted perimeter.

Introducing the definition of the discharge  $Q = u \times \phi \times B \times h$  in equation (6.1a) leads to:

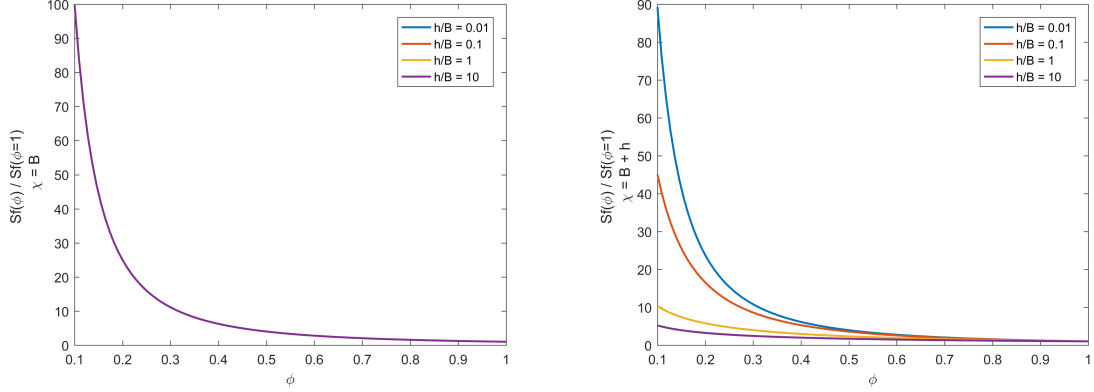
$$S_f(\phi, h, B) = \frac{Q^2}{\phi^2 B^2 h^2 K^2 R_h^{4/3}(\phi, h, B)} \qquad (6.3)$$

A comparison of the different estimation of the hydraulic radius is thus performed hereafter and the sensitivity of the friction slope to hydraulic approximations is explored.

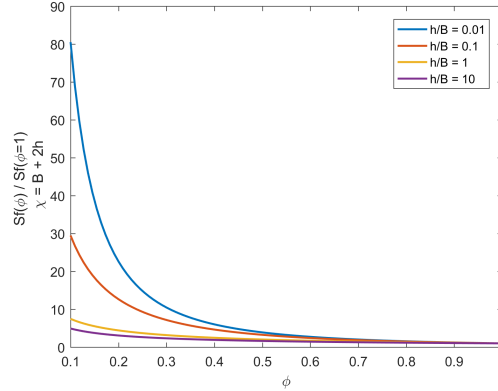
### 6.1.2 Sensitivity of the $S_f$ computation to porosity

This section aims to highlight the modification of the friction slope due to the introduction of the recirculation effect through the porosity parameter. For a chosen hydraulic radius formulation, the friction slope  $S_{f,\{SW,wall,full\}}(\phi, h, B)$  is adimensionalised by the friction slope  $S_{f,\{SW,wall,full\}}(\phi = 1, h, B)$  computed for the same hydraulic radius formulation with  $\phi = 1$ :

$$\begin{aligned} \frac{S_{f,\{SW,wall,full\}}(\phi, h, B)}{S_{f,\{SW,wall,full\}}(\phi = 1, h, B)} &= \frac{Q^2}{\phi^2 B^2 h^2 K^2 R_{h,\{SW,wall,full\}}^{4/3}(\phi, h, B)} \frac{B^2 h^2 K^2 R_{h,\{SW,wall,full\}}^{4/3}(\phi = 1, h, B)}{Q^2} \\ &= \frac{1}{\phi^2} \left( \frac{R_{h,\{SW,wall,full\}}(\phi = 1, h, B)}{R_{h,\{SW,wall,full\}}(\phi, h, B)} \right)^{4/3} \end{aligned} \qquad (6.4)$$



(a) Adimensionalised friction slope for the “shallow water” estimation equation (6.5a) (b) Adimensionalised friction slope for the “wall” estimation equation (6.5b)



(c) Adimensionalised friction slope for the “full” estimation equation (6.5c)

Figure 6.2: Evolution of the friction slope  $S_f$  due to the porosity parameter  $\phi$ . For the sake of clarity, the porosity  $\phi$  starts at  $\phi = 0.1$  as the plotted formulas are in  $1/\phi^2$  leading to vertical asymptote and infinite value of the relative friction slope for  $\phi = 0$ .

Introducing equation (6.2) for the each formulation of the hydraulic radius into equation (6.4) leads to:

$$\frac{S_{f,sw}(\phi, h, B)}{S_{f,sw}(\phi = 1, h, B)} = \frac{1}{\phi^2} \quad (6.5a)$$

$$\frac{S_{f,wall}(\phi, h, B)}{S_{f,wall}(\phi = 1, h, B)} = \frac{1}{\phi^2} \left( \frac{\phi B + h}{\phi B + \phi h} \right)^{4/3} = \frac{1}{\phi^{7/3}} \left( \frac{\phi B + h}{B + h} \right)^{4/3} \quad (6.5b)$$

$$\frac{S_{f,full}(\phi, h, B)}{S_{f,full}(\phi = 1, h, B)} = \frac{1}{\phi^2} \left( \frac{\phi B + 2h}{\phi B + 2\phi h} \right)^{4/3} = \frac{1}{\phi^{7/3}} \left( \frac{\phi B + 2h}{B + 2h} \right)^{4/3} \quad (6.5c)$$

Figure 6.2 presents equation (6.5) for different hydraulic radius formulations as a function of porosity  $\phi$ . For every hydraulic radius formulation  $R_{h,\{SW,wall,full\}}$ , the adimensionalised friction slope decreases to 1 as the porosity get closer to 1. For the smaller porosity ( $\phi = 0.1$ ), the friction slope with the porosity is, at most, 100 times bigger than the friction slope without porosity ( $\phi=1$ ). As highlighted by figure 6.2a and equation (6.5a), the adimensionalised friction slope for the “shallow water” estimation of the hydraulic radius  $R_{h,SW}$  does not depend on  $h/B$ . For the “wall” (respectively “full”) estimation of the hydraulic radius  $R_{h,wall}$  (respectively  $R_{h,full}$ ), the adimensionalised friction slope decreases when  $h/B$  increases from 0.01, 0.1, 1 to 10 (whatever the porosity).

As highlighted by Araud (2012); Finaud-Guyot et al. (2018), the typical water depth in the ICube urban flood experimental rig is in the range  $1\text{cm} \leq h_{XP} \leq 15\text{cm}$ , for street width  $B_{XP}$  in the range  $5\text{cm} \leq B_{XP} \leq 12.5\text{cm}$ . The scaling of the experimental rig being  $\lambda_h = B_{XP}/B_{Real} = 1/200$  in the horizontal direction and  $\lambda_v = h_{XP}/h_{Real} = 1/20$  in the vertical direction, the corresponding water depth and velocity in real world configurations are respectively  $0.2\text{m} \leq h_{Real} \leq 3\text{m}$  and  $5\text{m} \leq B_{Real} \leq 25\text{m}$ . The ratio  $h/B$  is thus in the range  $0.2 \leq h_{XP}/B_{XP} \leq 1.2$  (respectively  $0.02 \leq h_{Real}/B_{Real} \leq 0.12$ ) for the experimental (respectively real) configuration. Let us consider that a significant effect of the porosity is defined by a friction slope computed with recirculation ( $\phi < 1$ ) 10% bigger than the friction slope computed without recirculation. In the real configurations (thus considering  $h/B = 0.1$ ), figure 6.2 shows the recirculation introduces a significant effect for  $\phi < 0.95$  (whatever the estimation chosen for the computation of the hydraulic radius). Similar reasoning for the experimental configuration ( $h/B = 1$ ) shows that the recirculation introduces a significant effect from a similar threshold  $\phi < 0.95$ .

For a given friction slope formulation (either the “shallow water”, the “wall” or the “full”), the friction slope appears to be significantly modified when introducing a recirculation (by decreasing the porosity). The recirculation reducing the size of the flow vein for a given discharge, the velocity is thus increased leading as highlighted here to a higher friction effect. However, this does not account for the potential effect of the recirculation on the discharge distribution in a street network that should be investigated more deeply (see section 6.6). Indeed, the parametrisation (using either the Strickler coefficient  $K$  or the porosity  $\phi$ ) is defined at the computational cell scale. However, those parameters effects on the hydrodynamic are much global (see for instance Guinot and Cappelaere (2009b)), especially in branched network for which the flowpaths are not easy to define.

### 6.1.3 Sensitivity of the $S_f$ computation to hydraulic radius

In this section, the sensitivity of the  $S_f$  computation to hydraulic radius formulation is assessed for similar geometrical and hydraulic parameterisation. For a chosen hydraulic radius formulation, the friction slope  $S_{f,\{SW,wall\}}$  is adimensionalised by the friction slope  $S_{f,full}$  computed using the full and classical computation of the wetted perimeter:

$$\begin{aligned} \frac{S_{f,\{SW,wall\}}}{S_{f,full}} &= \frac{Q^2}{\phi^2 B^2 h^2 K^2 R_{h,\{SW,wall\}}^{4/3}} \frac{\phi^2 B^2 h^2 K^2 R_{h,full}^{4/3}}{Q^2} \\ &= \left( \frac{R_{h,full}}{R_{h,\{SW,wall\}}} \right)^{4/3} \end{aligned} \quad (6.6)$$

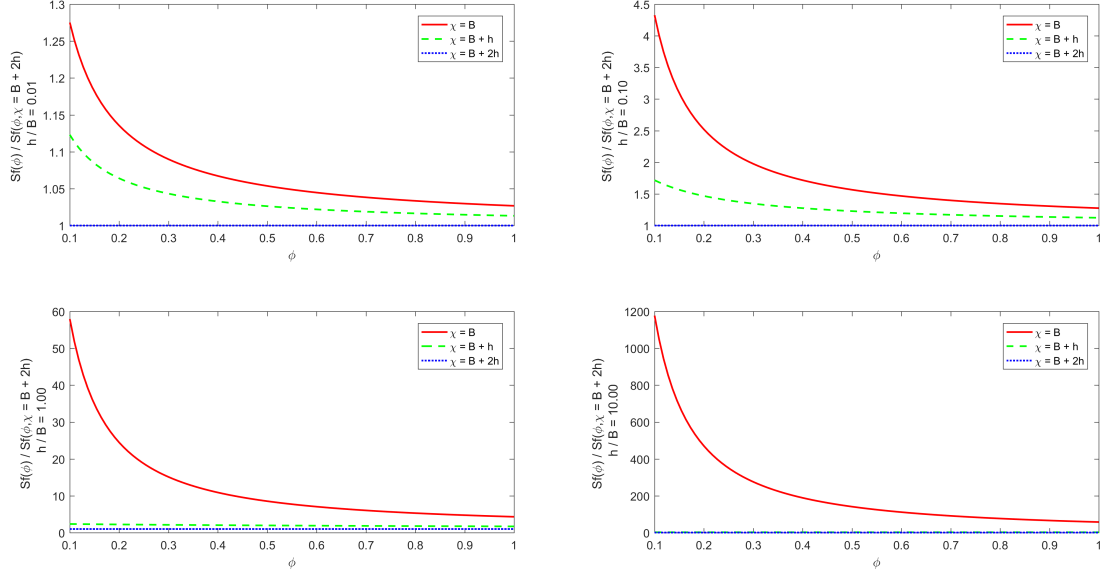


Figure 6.3: Influence of the friction slope  $S_f$  formulation for different aspect ratio  $h/B$ . Top left:  $h/B = 0.01$ , top right:  $h/B = 0.1$ , bottom left:  $h/B = 1$ , bottom right:  $h/B = 10$ . For the sake of clarity, the porosity  $\phi$  starts at  $\phi = 0.1$  as the plotted formulas are in  $1/\phi^2$  leading to vertical asymptote and infinite value of the relative friction slope for  $\phi = 0$ . Note that for  $h/B = 10$  (bottom right), line  $\chi = B + h$  is hidden by the line  $\chi = B + 2h$

Introducing equation (6.2) into equation (6.6) for the different formulations of the hydraulic radius, leads to:

$$\frac{S_{f,sw}}{S_{f,full}} = \left( \frac{\phi B}{\phi B + 2h} \right)^{4/3} \quad (6.7a)$$

$$\frac{S_{f,wall}}{S_{f,full}} = \left( \frac{\phi B + h}{\phi B + 2h} \right)^{4/3} \quad (6.7b)$$

Figure 6.3 presents equation (6.7) for different geometries (characterized by various  $h/B$  ratio) as a function of the porosity  $\phi$ . For every geometry ( $h/B$  in  $[0.01, 0.1, 1, 10]$ ), the adimensionalised friction slope decreases as the porosity get closer to 1. The adimensionalised friction slope for the “shallow water” estimation of the hydraulic radius  $R_{h,sw}$  is always bigger than the one for the “wall” estimation of the hydraulic radius  $R_{h,wall}$ . As the geometrical ratio  $h/B$  decreases the difference between the adimensionalised friction slopes (whatever the porosity) reduces.

As explained above, the ratio  $h/B$  is in the range  $0.2 \leq h_{XP}/B_{XP} \leq 1.2$  (respectively  $0.02 \leq h_{Real}/B_{Real} \leq 0.12$ ) for the experimental (respectively real) configuration. In the real configurations (thus considering  $h/B = 0.1$ ), figure 6.3 shows that the friction slope computed with the “shallow water” (respectively “wall”) is 4.36 (respectively 1.72) times bigger than using the “full” estimation for the smaller considered porosity ( $\phi = 0.1$ ); 1.566 (respectively 1.23) times bigger for  $\phi = 0.5$  and only 1.275 (respectively 1.123) times bigger without recirculation ( $\phi = 1$ ). Similar reasoning for the experimental configuration ( $h/B = 1$ ) shows that the friction slope computed with the “shallow water” (respectively “wall”) is 57.94 (respectively 2.37) times

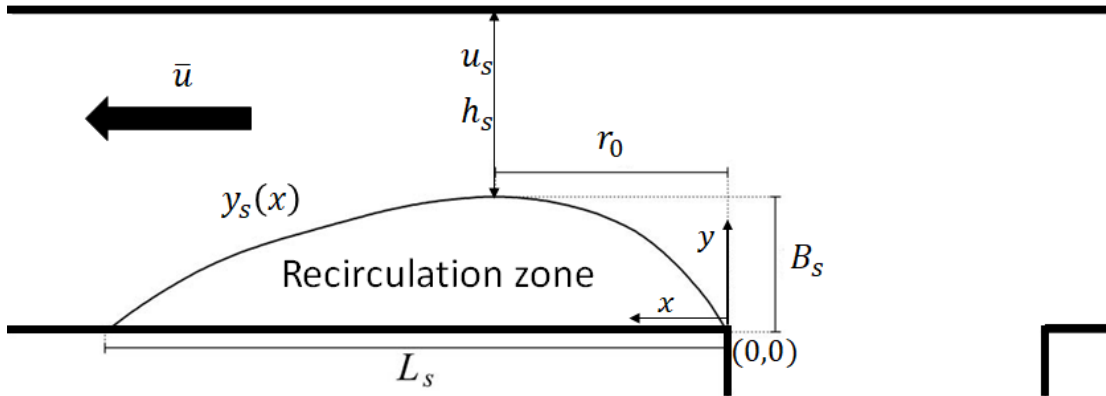


Figure 6.4: Definition of the dimensions of the recirculation zone adapted from Schindfessel et al. (2017)

bigger than using the “full” estimation for the smaller considered porosity ( $\phi = 0.1$ ); 8.55 (respectively 1.976) times bigger for  $\phi = 0.5$  and only 4.326 (respectively 1.717) times bigger without recirculation ( $\phi = 1$ ).

For a given geometrical and hydraulic configuration, the friction slope appears to be significantly influenced by the friction computation formulation (either “shallow water” or “wall” compared to “full”). Interestingly, the friction slope is up to 60 times bigger than the one with a full computation for the experimental configuration ( $h/B = 1$ ). This ratio has the same order of magnitude than taking into account the recirculation effect (as highlighted in section 6.1.2). In the real-world configuration, this ratio decreases to 4 which is smaller than the influence of the recirculation.

The choice of the friction slope formulation is thus much more important for the experimental configuration than for modeling real-world domain. Moreover and as highlighted in section 3.1.2, this study only focuses on the friction slope but shallow water flows are known to be influenced by several other parameters (like porosity, initial and boundary condition et al.).

## 6.2 Response surface of existing three branches recirculation laws

As presented in section 2.2, only few studies have been performed on four branch intersections especially on a recirculation zone downstream of a crossroad. Ming (2017) proposed in his thesis that a four branch intersection can be seen as a combination of a three branch confluence and bifurcation. It seems feasible to study the recirculation zone in four branch intersections from the results on three branch intersections. Therefore, to delineate the dimensions of separation zone in four branch intersections, results on three branch intersections quantifying the dimensions of recirculation zone are reviewed, compared and analyzed in this section.

Figure 6.4 illustrates the recirculation zone in three branch intersections.  $y_s(x)$  delineates the shape of recirculation zone.  $L_s$  is the length of the recirculation zone, and  $B_s$  the maximum value of  $y_s$  for all  $x$  between 0 and  $L_s$ . The length  $r_0$  corresponds to the distance from the downstream corner to the  $x$ -coordinate of the maximum contraction. At maximum contraction point,  $u_s$  is the longitudinal velocity outside the recirculation zone and  $h_s$  is the averaged water height perpendicular to the flow direction.

Three empirical relationships quantifying the dimensions of the recirculation zone are rewritten here and adapted for comparison:

- Best and Reid (1984) established for T-confluence:

$$\frac{B_s}{B} = 0.506 + 0.205 \ln q \quad (6.8a)$$

$$\frac{L_s}{B} = 2.587 + 1.025 \ln q \quad (6.8b)$$

where  $B$  is the channel width,  $q = Q_L/Q_d$  is the discharge ratio with  $Q_L$  and  $Q_d$  the lateral and downstream discharges. Those empirical relationships are determined with a downstream Froude number  $F_d$  in the range 0.1 to 0.3 and  $q$  in the range 0.2 to 1.  $q = 1$  corresponds to a  $90^\circ$  bend and  $q = 0$  would correspond to a straight channel. The recirculation zone is thus expected to be maximal for  $q = 1$ .

- Gurram et al. (1997) established for T-confluence:

$$\frac{B_s}{B} = \frac{1}{2} \times \left( F_d - \frac{2}{3} \right)^2 + 0.45q^{1/2} \quad (6.9a)$$

$$\frac{L_s}{B} = \begin{cases} 3.8 \times \left( 1 - \frac{1}{2} F_d \right) \times q^{1/2} & \text{for } F_d < 1 \\ 1.04q^{1/2} & \text{for } F_d = 1 \end{cases} \quad (6.9b)$$

where  $B$  is the channel width;  $q = Q_L/Q_d$  is the discharge ratio,  $Q_L$  and  $Q_d$  are lateral and downstream discharges;  $F_d$  is the downstream Froude number, which varies from 0.1 to 0.99 for subcritical flow regime. Qualitative analysis of equations (6.9a) and (6.9b) shows that, as for equations (6.8a) and (6.8b), the maximal recirculation zone might appear for  $q = 1$ .

Gurram et al. (1997) also suggest to compute the shape of the recirculation zone:  $Y_s = [\sin(90^\circ X_s)]^{2/3}$  where  $Y_s = f(B_s)$  and  $X_s = f(L_s)$ .

- Kasthuri and Pundarikanthan (1987) established for T-bifurcation:

$$\frac{B_s}{B} = 0.504 \times (q')^2 - 0.893 \times (q') + 0.861 \quad (6.10a)$$

$$\frac{L_s}{B} = 6.49 \times (q')^2 - 8.44 \times (q') + 4.45 \quad (6.10b)$$

where  $q' = Q_L/Q$  (in range 0.2 to 1),  $Q_L$  and  $Q$  being the lateral and total inlet discharges. Despite  $q'$  has not the same definition as  $q$ , it appears to be quite similar as (i) for  $q' = 0$  it corresponds to the straight channel configuration (with thus no recirculation) and  $q' = 1$  corresponds to a  $90^\circ$  bend (with a priori the maximal recirculation zone).

The comparison of the three relationships for the computation of the ratio  $\frac{B_s}{B}$  is presented in figure 6.5b. It shows that when the discharge ratio  $q$  increases, the ratio  $\frac{B_s}{B}$  increases for T-confluence (corresponding to equations (6.8a) and (6.9a)) and decreases for T-bifurcation (equation (6.10a)). For T-branch confluence flow, downstream Froude number has small influence on  $\frac{B_s}{B}$  and limited difference is observed between Best and Reid (1984) and Gurram et al. (1997). Interestingly for T-bifurcation flow, the recirculation appears to be maximal for  $q' \rightarrow 0$  (corresponding to no discharge in the lateral branch). That can be understood by reversing the reasoning: to have all

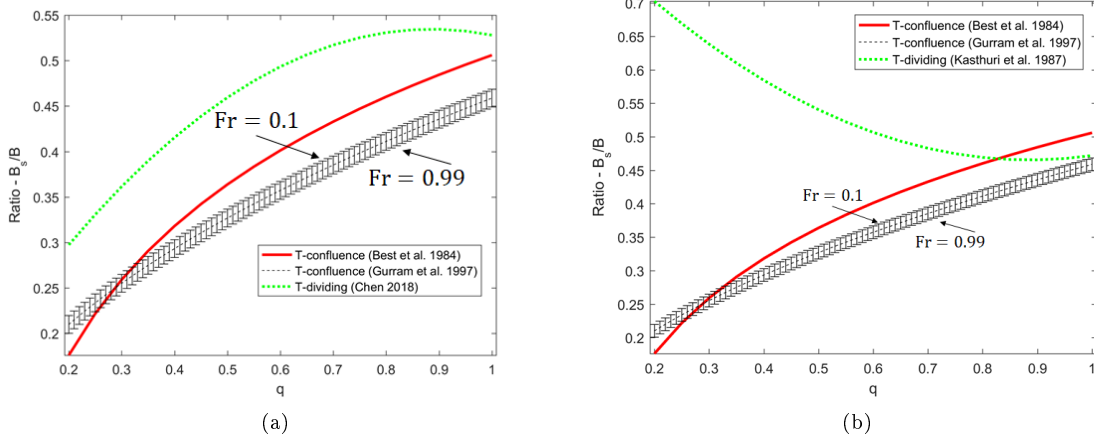


Figure 6.5: Comparison of three empirical relationships quantifying the maximum recirculation width

the flow going straight, the recirculation in the branched street has to be maximal and occupy the full lateral street. For  $q' \rightarrow 1$ , the value of  $B_s/B$  computed using the three formulation tends to the same asymptotic value:  $B_s/B = 0.5$ . A new relation, based on the relation of Kasthuri and Pundarikanthan (1987) (equation (6.10a)), is proposed:

$$\frac{B_s}{B} = 1 - \left( \frac{B_s}{B} \right)_{\text{Kasthuri}} \quad (6.11)$$

This equation is plotted on figure 6.5a and interestingly, the shape is very similar to the one observed for equations (6.8a) and (6.9a). On the basis of the relations (6.8a), (6.9a) and (6.11), it appears that  $\frac{B_s}{B}$  evolves in the range 0.18 to 0.54 as  $q$  changes from 0.2 to 1.

Figure 6.6a presents the variations of the ratio  $\frac{L_s}{B}$  for the different above-mentioned formulations in function of  $q$  (respectively  $q'$ ). It shows that when the discharge ratio  $q$  increases, the ratio  $\frac{L_s}{B}$  increases for T-confluence (corresponding to equations (6.8b) and (6.9b)). Interestingly, the curve corresponding to the formulation proposed in Kasthuri and Pundarikanthan (1987) seems different from what was published (see figure 6.6b). Indeed, for  $q' = 1$ , equation (6.10b) gives  $L_s/B = 6.49 \times (1)^2 - 8.44 \times (1) + 4.45 = 2.5$  which is quite different from the value of 2 plotted by Kasthuri and Pundarikanthan (1987). It also gives a minimal length of the recirculation for  $q' = 0.65$  of 170% of the channel width. For T-branch confluence flow,  $F_d$  has big influence on  $\frac{L_s}{B}$  compared with  $\frac{B_s}{B}$ .

### 6.3 2D hydrodynamic analysis of a four branch crossroad

In chapter 5, 1D and 2D steady and transient hydrodynamics have been analyzed in the configurations of the ICube urban flood experimental rig. In this section, similar analysis is conducted at the local scale on a four branch crossroad. The flow patterns on a four branch crossroad are analyzed, and especially the dimensions of the recirculation zone downstream of the crossroad.

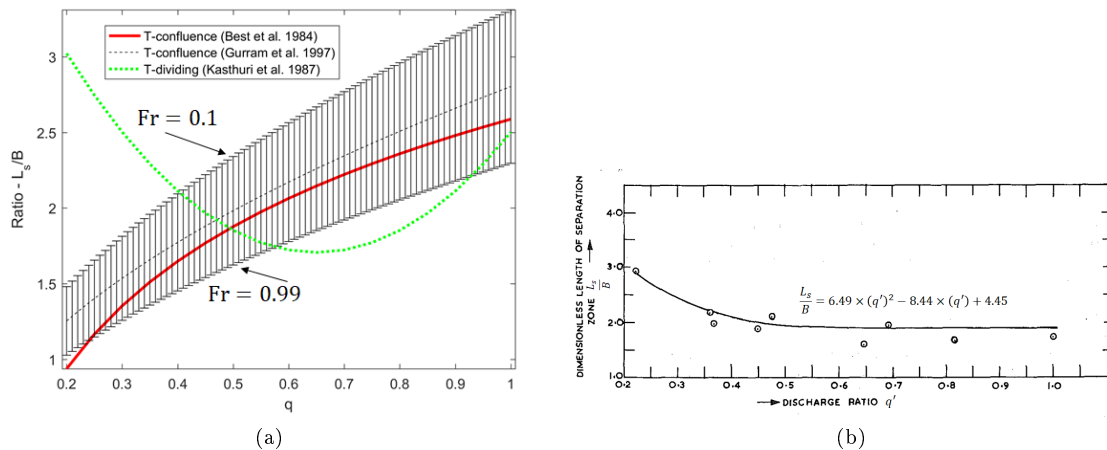


Figure 6.6: Left, comparison of three empirical relationships quantifying the total recirculation length; Right, dimensionless length of separation zone taken from Kasthuri and Pundarikanthan (1987)

### 6.3.1 Classical 2D modeling of a four branch crossroad

The tested configuration of four branch crossroad corresponds to the experiment of Nanía et al. (2011) with two inlets (north and west streets) and two outlets (south and east streets). The channels have a rectangular cross-section of 1.5m width and 0.35m height. Input and output channels are respectively 2m and 5m long. At the junction, channels cross with an angle of  $90^\circ$  and thus form a  $1.5\text{m} \times 1.5\text{m}$  square. The channels and the junction are in the horizontal plane. The experimental setup and dimensions are illustrated in figure 6.7a.

A reference simulation is performed with a fine mesh and a 2D SW model accounting for turbulence. The goal is to simulate a realistic flow pattern recirculation zones just downstream of the crossroad for this four branch crossroad flow. In the  $x$  and  $y$  directions, symmetrical boundaries are used so that analysis can be focused on one direction only. The inlet discharges are set to  $Q_{in,x} = Q_{in,y} = 0.075\text{m}^3.\text{s}^{-1}$  and outlet water height is  $h_{out,x} = h_{out,y} = 0.1\text{m}$  so that  $Fr_{outlet} = 0.5$  ensuring fluvial flow conditions over the whole domain - inlet Froude number is fluvial and there is no hydraulic jumps. The Strickler coefficient is set to  $K = 100\text{m}^{1/3}.\text{s}^{-1}$  in order to be consistent with the study in chapter 5. Initial water surface elevation is set to 0.1m and velocity in  $x$  and  $y$  directions are set to  $0\text{m}.\text{s}^{-1}$ . The modeling is performed using Telemac2D with a finite element method with a  $k - \varepsilon$  turbulence model. Grid size is set to 0.06m (ensuring convergence) using an unstructured triangular mesh (see figure 6.7b). The parameters are listed in table 6.1.

Simulated results water height and velocity field are presented respectively in figures 6.8a and 6.8b. Water height along the line A-B-C-D in  $x$  direction is also presented (see figure 6.8c). This water height profile along line A-B and C-D is the averaged water height perpendicular to the street direction. Between B and C, the plotted values correspond to the computed water depth values at the cell corner being in a 0.03m buffer around the segment BC.

Water height decreases from inlet to outlet and a sharp decrease occurs across the crossroad (see figure 6.8c, between B-C). After the crossroad, averaged water height first decreases and then increases along the flow direction, which corresponds to the effect of the recirculation zone contracting the flow vein hence increasing flow speed. Indeed, the shape of the recirculation

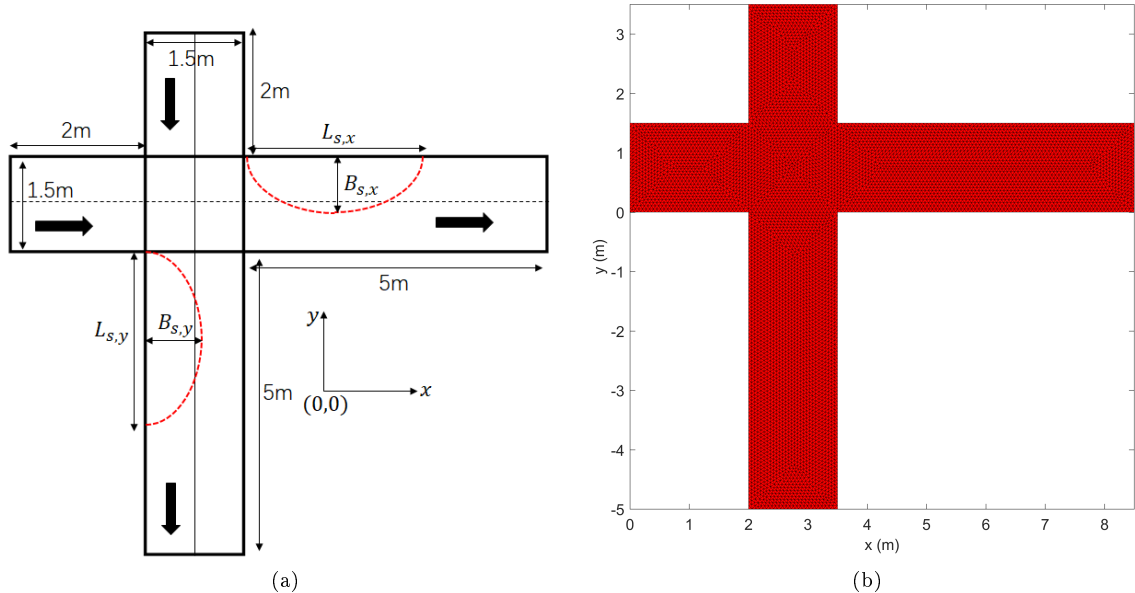


Figure 6.7: Left: illustration of a four branch crossroad with dimensions:  $B_{s,x}$  and  $L_{s,x}$  (respectively  $B_{s,y}$  and  $L_{s,y}$ ) are the maximum width and total length of the recirculation zone in  $x$  (respectively  $y$ ) direction downstream of the crossroad (Nanía et al. (2011)); right, unstructured triangular mesh on a four branch crossroad

Table 6.1: Parameters used on a four branch crossroad modeling

Symbol	Meaning	Value
$g$	Gravitational acceleration	$9.81\text{m}\cdot\text{s}^{-2}$
$Q_{in,x}$	Inlet discharge in $x$ direction	$0.075\text{m}^3\cdot\text{s}^{-1}$
$Q_{in,y}$	Inlet discharge in $y$ direction	$0.075\text{m}^3\cdot\text{s}^{-1}$
$h_{out,x}$	Outlet water height in $x$ direction	0.1m
$h_{out,y}$	Outlet water height in $y$ direction	0.1m
$\Delta x$	Cell size	0.06m
$K$	Strickler coefficient	$100\text{m}^{1/3}\cdot\text{s}^{-1}$
$h_{ini}$	Initial water level over the domain	0.1m

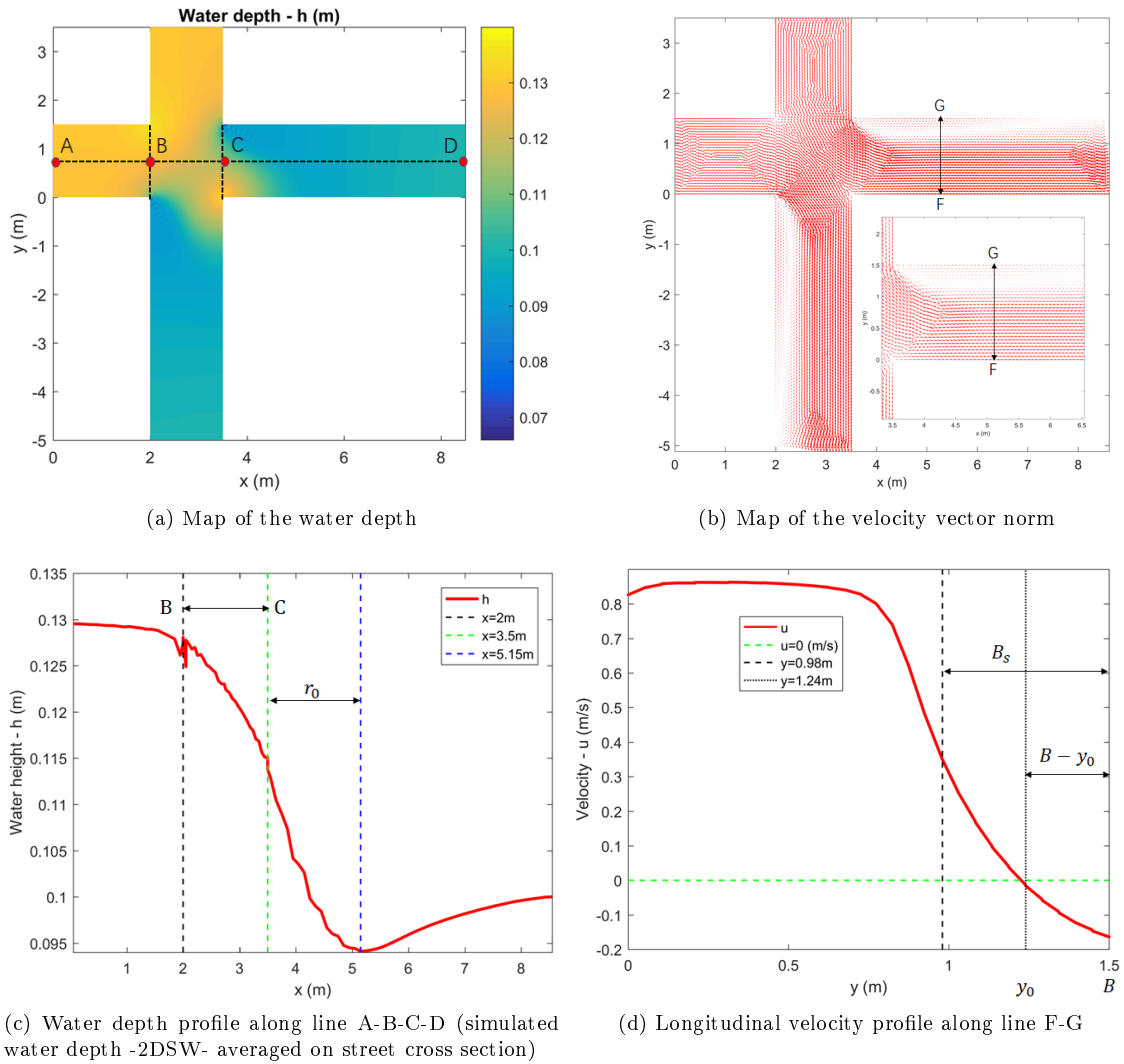


Figure 6.8: Telemac2D results on a four branch crossroad

zone can be observed on the map of the 2D velocity field (see figure 6.8b). In the  $x$  direction, recirculation zone starts from the north-east corner of the crossroad and develops along the east channel until the outlet. Recirculation zone induces a reduction of the flow vein area hence increasing the velocity as in a Venturi canal (Finaud-Guyot et al. (2018)), and consequently making water height decreases. After the maximum contraction point, water height increases and velocity decreases.

### 6.3.2 Characterization of the recirculation zone

Three methods are presented in this section to quantify the dimensions of recirculation zone.

### 6.3.2.1 Zero-discharge method

The first method is referred to as the “*zero-discharge method*” (Schindfessel et al. (2017)). In the recirculation area, the discharge is assumed to be nil in a cross-section (i) in the normal direction to the street axis; (ii) starting from the bank attached to separation zone and ending at  $y_s$  the limit between the recirculation and the flow vein (see figure 6.4). The width of the recirculation is thus defined as:

$$\int_0^{y_s(x)} \bar{u}(x) dy = 0 \quad (6.12)$$

where  $\bar{u}(x)$  represents the average on the water depth of the longitudinal velocity and  $y_s(x)$  is the distance to the bank attached to separation zone at which the recirculation ends.

Using this method, the determination of  $L_s$  (the total length of the recirculation zone) and  $B_s$  (the maximum value of  $y_s$  for all  $x$  between 0 and  $L_s$ ) requires thus to compute  $y_s$  along the downstream street (at least until  $L_s$ ) and then to detect the value of  $B_s$ . This method appears to be quite time consuming especially in view of the determination of  $B_s$  and  $L_s$  in lots of modeling.

### 6.3.2.2 Zero-velocity method

The “*zero-velocity method*” is a simplified approach, compared to the “*zero-discharge method*” (see section 6.3.2.1), to determine  $B_s$  and  $L_s$ . The maximum contraction profile (for which the recirculation width is  $B_s$ ) is located at the minimal water depth on the longitudinal profile (see figure 6.8c). The value of  $r_0$  can thus be obtained from the downstream corner to the maximum contraction point featured by localized minimum water height, which is named as recirculation radius. As illustrated in figure 6.8c,  $r_0 = 1.65\text{m}$ . Assuming symmetrical recirculation shape (as proposed by Gurram et al. (1997)) leads to  $L_s = 2r_0 = 3.3\text{m}$ .

For a given cross-section, the center of the recirculation is assumed to correspond to the point where the longitudinal velocity is nil. At maximum contraction point, velocity is depicted along the direction perpendicular to the flow as in figure 6.8d (line F-G,  $x = 5.15\text{m}$ ). Velocity  $u$  decreases from point F to G, and stays almost constant outside the recirculation zone and then decreases when entering the recirculation zone reaching a symmetrical profile with negative velocities on half of this recirculation width. The center of the recirculation is thus located (assuming  $u = 0\text{m}\cdot\text{s}^{-1}$ ) for  $y_0 = 1.24\text{m}$ . This leads to the following estimation of  $B_s$ :  $B_s = 2 \times (B - y_0) = 0.52\text{m}$ .

This methodology is less time-consuming than the “*zero-discharge method*” (see section 6.3.2.1), as it only requires to compute the longitudinal water depth profile and one transversal velocity profile to determine both  $B_s$  and  $L_s$ .

### 6.3.2.3 Approximated zero-velocity method

Finally, the “*approximated zero-velocity method*” is proposed to allow the computation of both  $B_s$  and  $L_s$  with smaller computational cost than with the “*zero-velocity method*”.  $L_s$  is computed as for the “*zero-velocity method*”. To avoid the determination and the analysis of the longitudinal velocity along the transversal cross-section, the mass equation is written for the maximal contraction profile:

$$Q = (B - B_s) h_s u_s \quad (6.13)$$

where  $Q$  is the total discharge,  $u_s$  the longitudinal velocity outside the recirculation zone and  $h_s$  is the averaged water height perpendicular to the flow direction.  $h_s$  is estimated from the longitudinal water depth profile as it is the water depth in  $r_0$ .  $u_s$  is computed as the average of

Table 6.2: Variation range of boundary conditions provided by Nanía et al. (2011)

Symbol	Meaning	Min	Max	Variation range
$Q_{in,x}$	Inlet discharge at $x$ direction	$0.012\text{m}^3.\text{s}^{-1}$	$0.075\text{m}^3.\text{s}^{-1}$	$\pm 72.5\%$
$Q_{in,y}$	Inlet discharge at $y$ direction	$0.012\text{m}^3.\text{s}^{-1}$	$0.075\text{m}^3.\text{s}^{-1}$	$\pm 72.5\%$
$w_{out,x}$	Outlet weir height at $x$ direction	0.02m	0.08m	$\pm 60\%$
$w_{out,y}$	Outlet weir height at $y$ direction	0.02m	0.08m	$\pm 60\%$

the computed value in a circle of radius  $0.033B$  having its center in  $(r_0, 0.167B)$ . Indeed, close to a distance of  $0.167B$  to the street side, the longitudinal velocity is barely constant (see figure 6.8d).  $B_s$  is thus computed as:

$$B_s = B - \frac{Q}{u_s \times h_s} \quad (6.14)$$

Using this method, the obtained  $B_s = 0.5747\text{m}$ . In this section,  $B_s = 0.52\text{m}$  using the zero-velocity method used as reference. The difference can be explained because the estimation of  $u_s$  is not exactly the averaged velocity outside the recirculation zone. A correction factor  $C$  is thus introduced:  $B_{s,c} = CB_s$  where  $B_s$  is estimated using equation (6.14),  $C = 0.9$  and  $B_{s,c}$  is the final width of the recirculation area.

For the sake of clarity,  $B_{s,c}$  will also be denoted as  $B_s$  in the following sections. In the following sections, the dimensions  $B_s$  and  $L_s$  of the recirculation will be estimated using the “*approximated zero-velocity method*”.

## 6.4 GSA of a full 2D SW model applied to crossroad modeling

Global sensitivity analysis (GSA) used to quantify the influence of input parameters on model outputs has been studied at the district scale in chapter 5. In this section, GSA is applied at a more local scale on a four branch crossroad. The sensitivity of the hydraulic variables and recirculation dimensions to input parameters is assessed using GSA as described in section 5.1.2.

### 6.4.1 Variation range of input parameters

The geometry of the four branch crossroad has been presented in figure and an unstructured 2D triangular mesh is used for simulation (see figure 6.7b). Boundary conditions and their variation ranges are based on the experiment provided by Nanía et al. (2011) (see table 6.2).  $Q_{in,x}$  and  $Q_{in,y}$  are modified in the range  $0.012\text{m}^3.\text{s}^{-1}$  to  $0.075\text{m}^3.\text{s}^{-1}$  corresponding to a perturbation of 72.5%. Experimentally, the downstream water height is controlled by weirs of variable height ( $w_{out,x}$  and  $w_{out,y}$ ) in the range 2cm - 8cm corresponding to a perturbation of 60%. For the sake of simplicity, the simulation is performed with imposed downstream water height perturbed of 60% around the nominal value of 5cm. Friction coefficient  $K$  is set to  $100\text{m}^{1/3}.\text{s}^{-1}$  with a variation range of 50% as done in chapter 5. The parameters for the nominal simulation are listed in table 6.3.

### 6.4.2 GSA on the four branch crossroad flow

With the configuration of the four branch crossroad described in section 6.4.1, the global sensitivity analysis (GSA) is conducted to assess the influence of the input parameters on the outputs of interest (namely spatially varied water height and outlet discharge). Preliminary tests using the nominal values and different perturbations of the outlet water heights  $h_{out,x}$  and  $h_{out,y}$  result

Table 6.3: Nominal parameters of the four branch crossroad modeling

Symbol	Meaning	Value
$g$	Gravitational acceleration	$9.81\text{m}\cdot\text{s}^{-2}$
$Q_{in,x}$	Inlet discharge in $x$ direction	$0.0435\text{m}^3\cdot\text{s}^{-1}$
$Q_{in,y}$	Inlet discharge in $y$ direction	$0.0435\text{m}^3\cdot\text{s}^{-1}$
$h_{out,x}$	Outlet water height in $x$ direction	0.05m
$h_{out,y}$	Outlet water height in $y$ direction	0.05m
$K$	Strickler coefficient	$100\text{m}^{1/3}\cdot\text{s}^{-1}$
$\Delta x$	Cell size	0.06m
$h_{ini}$	Initial water level over the domain	0.1m

Table 6.4: Parameters used and associated perturbation range for the four branch crossroad flow

Symbol	Meaning	Value	Range
$Q_{in,x}$	Inlet discharge in $x$ direction	$0.0435\text{m}^3\cdot\text{s}^{-1}$	$\pm 72.5\%$
$Q_{in,y}$	Inlet discharge in $y$ direction	$0.0435\text{m}^3\cdot\text{s}^{-1}$	$\pm 72.5\%$
$h_{out}$	Outlet water height	0.05m	$\pm 60\%$
$K$	Strickler coefficient	$100\text{m}^{1/3}\cdot\text{s}^{-1}$	$\pm 50\%$

in highly variable hydrodynamics. Indeed, incoming water by the “outlet” streets with the highest imposed water depth is observed. Computing the sensitivity with such a variable response surface would require an important number of runs. To avoid too expensive computations, only four input parameters are tested: both inlet discharges in  $x$  and  $y$  directions ( $Q_{in,x}$  and  $Q_{in,y}$ ), the friction coefficient  $K$  and  $h_{out}$  the outlet water height for both  $x$  and  $y$  directions.

The nominal values for all the tested parameters and their variation ranges are listed in table 6.4. 2000 Monte Carlo simulations are conducted with input parameter sets randomly sampled following the chosen variation ranges.

Figure 6.9 presents the Sobol index of the simulated water height to the tested parameters. Maps of the water height variance to the inlet discharges  $Q_{in,x}$  and  $Q_{in,y}$  are symmetrical with main effects in the inlet channels and at the crossroad. Then they decrease from crossroad to outlet as explained by Chen et al. (2018). Interestingly, the upstream discharge  $Q_{in,x}$  explains 35% of the variance of the street west (corresponding to the street in which the discharge is injected) and up to 55% for the lateral upstream street (north street). This shows that the discharge of west street creates a backwater control on street north as the flow regime is subcritical on the whole computed domain. A local peak of sensitivity can also be identified where the flow coming from the west street and deviated by the north discharge meets the upstream part of the left side of the south street. Similar trends are visible for  $Q_{in,y}$ .

Concerning outlet water height (see figure 6.9), they have biggest influence at outlet and decreases from downstream to upstream. However, their influence is limited at channels downstream of the crossroad and has barely no effect upstream of and into the crossroad. Friction has similar effect as inlet discharge and also decreases from upstream inlet to downstream outlet. Interestingly, friction has big influence at recirculation zone both in  $x$  and  $y$  direction just after the crossroad. This may be explained by the contraction effect caused by the recirculation zone, which caused the increase of flow velocity.

The sum of all Sobol indices is greater than 0.9 indicating no significant interaction effects between the tested parameters for this is completely subcritical flow.

Sobol indices of outlet discharges are presented in figure 6.10. Results show that the sum of

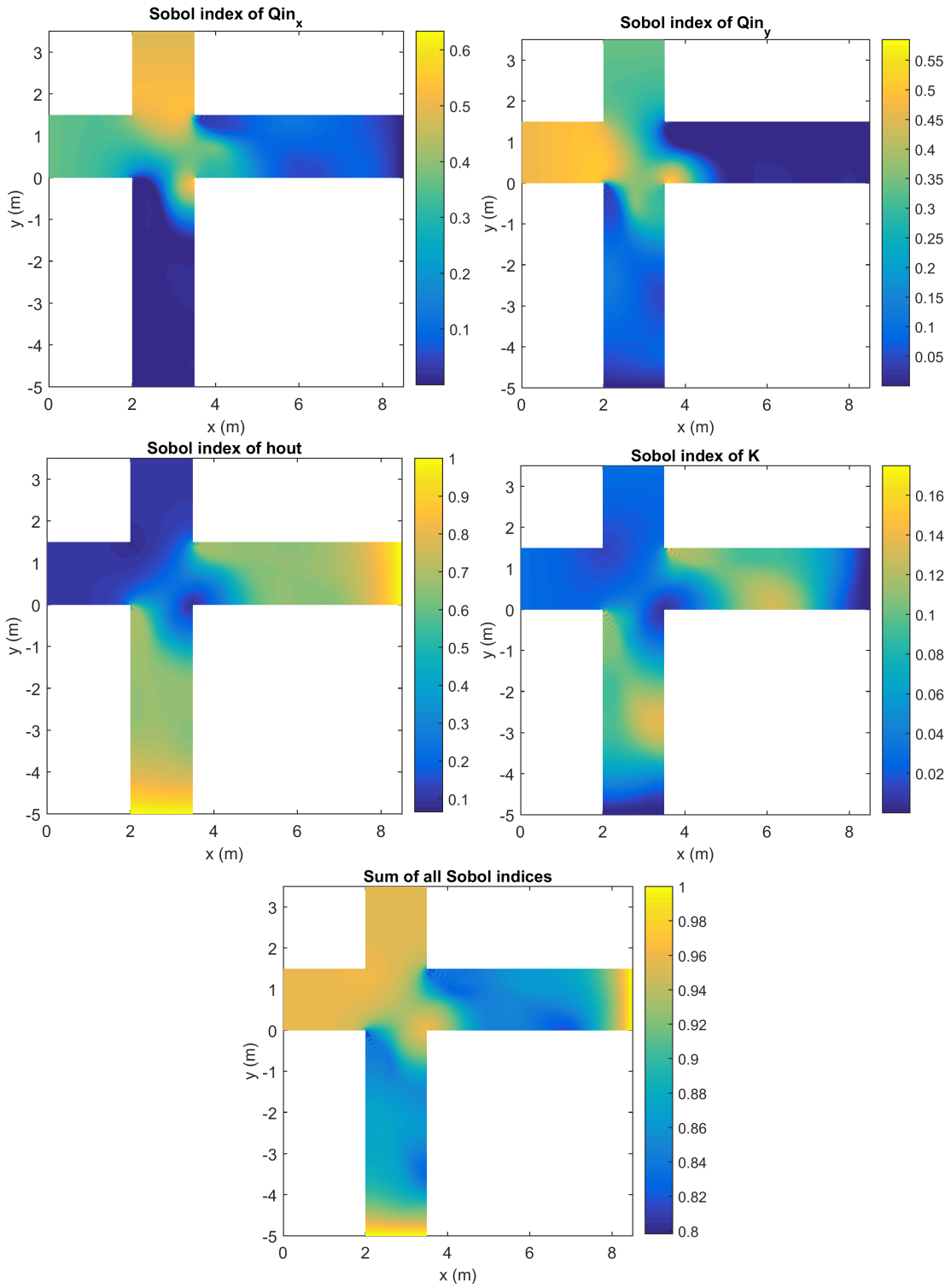


Figure 6.9: Sobol indices of spatially distributed water height simulated with Telemac2D to input parameters on a four branch crossroad flow

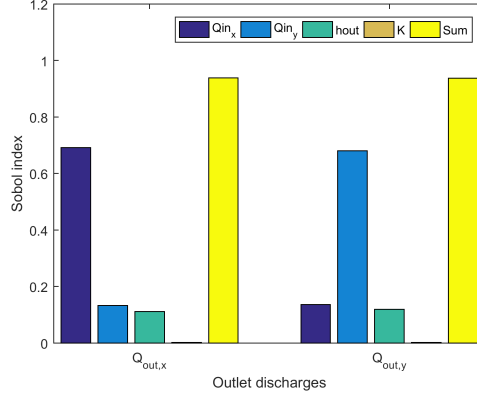


Figure 6.10: Sobol indices of outlet discharges simulated with Telemac2D to input parameters

Table 6.5: Extreme values (maximum or minimum) and associated perturbation range of recirculation dimensions

Symbol	Meaning	Min	Max	Range
$B_{s,x}$	Maximum recirculation width at $x$ direction	0.16m	0.86m	$\pm 68.6\%$
$L_{s,x}$	Recirculation length at $x$ direction	2.1m	5.1m	$\pm 41.7\%$
$B_{s,y}$	Maximum recirculation width at $y$ direction	0.16m	0.86m	$\pm 68.6\%$
$L_{s,y}$	Recirculation length at $y$ direction	2.1m	5.1m	$\pm 41.7\%$

all Sobol indices is close to 1 again indicating no significant interaction effect between the tested parameters both  $Q_{out,x}$  and  $Q_{out,y}$ .  $Q_{in,x}$  and  $Q_{in,y}$  have similar effects on discharge distribution downstream of the crossroad for this symmetrical boundary conditions. Compared with the other parameters, friction has limited effect on discharge distribution at crossroad, which is in contrast with its influence on water height.

### 6.4.3 Variation range of the recirculation dimensions

The 2000 Monte Carlo simulations are used in this section to obtain the variation range of the recirculation dimensions, namely  $B_s$  and  $L_s$ . As detailed at section 6.2, dimensions of a recirculation zone can be affected by inlet discharge ratio and outlet Froude number. With the variation range of boundary conditions listed in table 6.4, variation ranges of  $B_s$  and  $L_s$  can be obtained. For symmetrical boundary conditions, only recirculation dimensions at  $x$  direction are studied.

Using the “*approximated zero-velocity method*” presented in section 6.3.2.3, variation ranges are obtained for  $B_s$  and  $L_s$  from 2000 Monte Carlo simulations.  $B_s$  changes from 0.16m to 0.86m with variation range 68.6% and  $L_s$  changes from 2.1m to 5.1m with variation range 41.7%, cf. table 6.5. Their frequency distribution curves are also presented in figure 6.11. The distribution of  $B_s$  is close to normal distribution and sampled around  $B_s = 0.4$ m. For  $L_s$ , its frequency increases from 2.1m to 5.1m and reaches a maximum at  $L_s = 5.1$ m, which is due to the limited length of the channel for which the recirculation zone just ends at channel outlet. The ranges of recirculation dimensions obtained from 2D simulation results are compared with empirical relationships presented at section 6.2. Results in figure 6.12 show that two analysis have similar results.

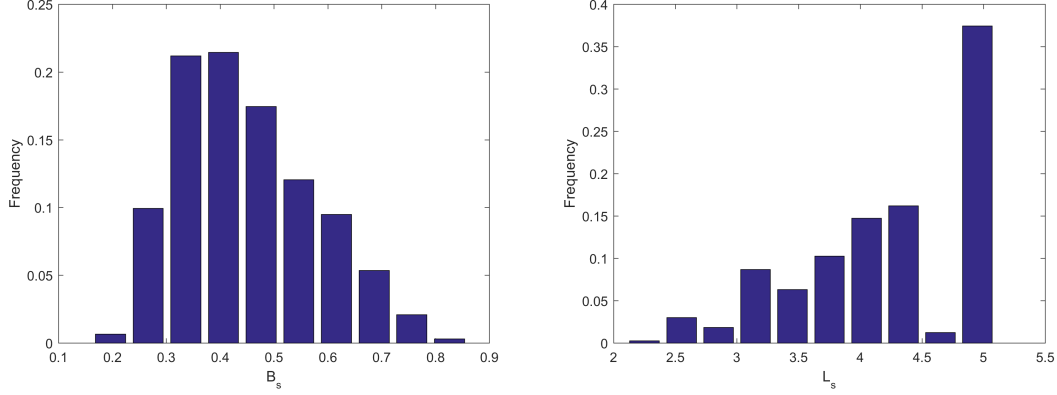


Figure 6.11: Distribution curve of frequency of  $B_s$  and  $L_s$

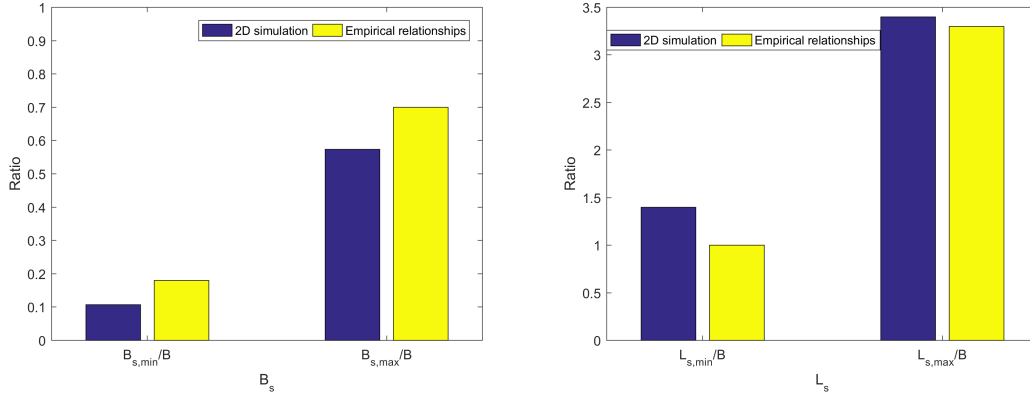


Figure 6.12: Comparison of recirculation dimensions between 2D simulation results and empirical relationships presented in section 6.2

## 6.5 Application of the *Flood1D2D* model

The coupled and effective 1D2D model (*Flood1D2D*) tailored for urban flood flows requires reasonable computational costs and is based on a relatively parsimonious parameterisation. The set of equations and the numerical methods are detailed in chapter 3 and validated in chapter 4. Recall that the code *Flood1D2D* is designed to:

- Take advantage of the relative accuracy of a 2D shallow water model for describing flood flows patterns at crossroad;
- Take advantage of low computational cost of 1D in streets;
- Use a porosity function in 1D cell to account for sub-grid scale recirculation effect identified at section 2.2, which is the main novelty of the code.

In what follows, the parameterization of the code is presented, including the calibration of porosity function  $\phi$  and roughness. The application of the code on a four branch crossroad is presented with and without porosity.

### 6.5.1 Parameterisation of the code *Flood1D2D*

The code *Flood1D2D* is expected to reproduce the flow patterns both in streets and crossroad. As *Flood1D2D* is parameterized using both a Strickler coefficient in all cells and a porosity in the 1D cells, this parameterization has to be defined prior to the computation. The Strickler coefficient can be classically estimated based on the wall materials. The definition of the porosity represents the proportion of the street width available for the flow vein (see section 3.3.1):  $\phi(s) = 1 - B_{recirc}(s)/B$ ,  $B_{recirc}(s)$  being the width of the recirculation at  $s$  where  $s$  is the curvilinear axis along the street ( $s = 0$  being located by convention at the junction between the upstream crossroad and the street). Three different approaches are proposed to estimate  $B_{recirc}(s)$ :

- The recirculation shape proposed by Gurram et al. (1997):

$$\frac{B_{recirc}(s)}{B_s} = \left[ \sin \left( 90^\circ \frac{s}{L_s/2} \right) \right]^{2/3} \quad (6.15)$$

where  $B_s$  is the maximum width and  $L_s$  is the total length of recirculation zone.

- An hypothetical shape assumed to be a second order polynomial:

$$B_{recirc}(s) = as^2 + bs + c \quad (6.16)$$

such as  $B_{recirc}(0) = B_{recirc}(L_s) = 0$  and  $B_{recirc}(L_s/2) = B_s$  hence  $a = -\frac{4B_s}{L_s^2}$ ,  $b = \frac{4B_s}{L_s}$  and  $c = 0$ .

- A piecewise function:

$$B_{recirc}(s) = \begin{cases} as^2 + bs + c & \text{for } 0 \leq s \leq r_0 \\ ds + e & \text{for } r_0 \leq s \leq L_s \end{cases} \quad (6.17)$$

such as  $B_{recirc}(0) = B_{recirc}(L_s) = 0$ ,  $B_{recirc}(r_0) = B_s$  and  $L_s = 3r_0$  hence  $a = -\frac{4B_s}{r_0^2}$ ,  $b = \frac{2B_s}{r_0}$ ,  $c = 0$ ,  $d = \frac{B_s}{-2r_0}$  and  $e = \frac{3}{2}B_s$ .

For every formulation, the recirculation shape can be defined using only two parameters:  $B_s$  and  $L_s$ . For similar  $B_s = 0.26\text{m}$  and  $L_s = 3.3\text{m}$ , the three proposed shapes are plotted in figure 6.13.

One approach would have been to estimate  $B_s$  and  $L_s$  using Best and Reid (1984); Gurram et al. (1997); Kasthuri and Pundarikanthan (1987) empirical models. However, those models are proposed for three branch junction flows with a discharge ratio parameter  $q$  smaller than unity for every experiment that is greater than 1 for the four branch crossroad of Nanía et al. (2011). The Telemac2D results have been preferred to estimate those parameters.

### 6.5.2 Results comparison using *Flood1D2D* with and without porosity

In this section, *Flood1D2D* results using various parameterizations are compared on the configuration used in section 6.3.1. The four branch crossroad presented in figure 6.7a is used to show the influence of the porosity parameterization. The crossroad is meshed using 2D cells and the four streets are meshed using 1D cells (see figure 6.14). In the  $x$  and  $y$  directions, symmetrical boundary conditions are used with inlet discharges  $Q_{in,x} = Q_{in,y} = 0.075\text{m}^3.\text{s}^{-1}$  and outlet

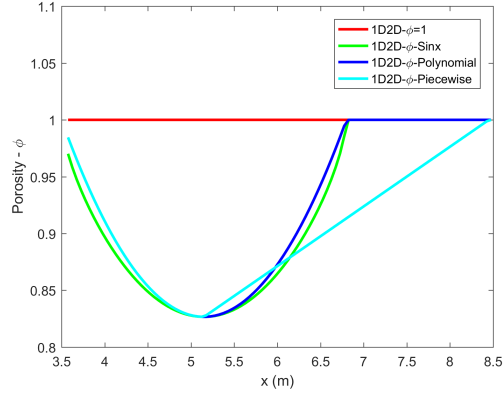


Figure 6.13: Distribution of porosity  $\phi$  after crossroad both in  $x$  and  $y$  directions

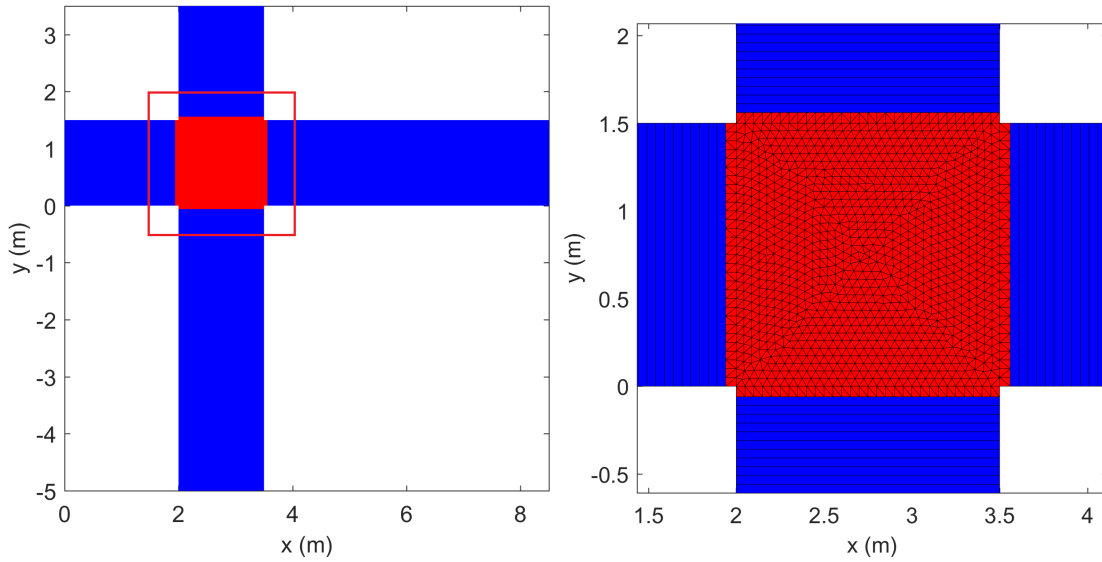


Figure 6.14: 1D2D coupling mesh on four branch crossroad (blue is 1D and red is 2D mesh). Right is a zoom on crossroad.

water height  $h_{out,x} = h_{out,y} = 0.1\text{m}$ , which listed in table 6.1 as section 6.3. Initial water surface elevation is  $0.1\text{m}$  and velocity in  $x$  and  $y$  directions are set to  $0\text{m}\cdot\text{s}^{-1}$ . PorAS Riemann solver is used for the flux computation. The simulation is carried out until steady flow conditions are reached over the computed domain.

Simulated 1D2D results are compared with 2D results to test in which extent it can reproduce the 2D flow features (water height). For symmetrical boundary conditions, discharge distribution at crossroad is not considered and water height is only presented along the  $x$  direction (line A-B-C-D see figure 6.8a).

### 6.5.2.1 Influence of the minimal porosity value

In this section, the influence of porosity parameterization in reproducing contracted flow profiles is tested. 1D2D simulations with and without porosity are performed using uniform roughness. The Strickler coefficient is set to  $100\text{m}^{1/3}.\text{s}^{-1}$  for both 1D and 2D cells.  $B_s = 0.52\text{m}$  and  $r_0 = 1.65\text{m}$  are obtained from 2D simulation results using the “*approximated zero-velocity method*” presented in section 6.3.2.3. Polynomial relationship (6.16) is used to reproduce the recirculation shape and  $L_s = 2r_0 = 3.3\text{m}$ .  $\phi_{min}$  is calculated by  $B_s$ :

$$\phi_{min} = 1 - \frac{B_s}{B} \quad (6.18)$$

Computed water depth profiles for variations  $B_s$  are compared with the reference (Telemac2D) on figure 6.15. For any positive  $B_s$ , results show that downstream of the crossroad, because of the recirculation, the flow vein is contracted, hence accelerated, and the free surface presents an inflection for  $x \in [3.5; 5.15]$  as in the reference.

When  $B_s = 0.52\text{m}$ , the flow accelerates to supercritical flow after the crossroad and a hydraulic jump occurs at the end of the recirculation zone. The hydraulic jump is not modelised in the reference obtained with Telemac.. The above difference can be explained by an overestimation of the flow contraction by calculating  $B_s$  from a 2D simulation. Indeed, the size in plane of a real 3D recirculation may be variable on the vertical and even in 2D scale it may not be fully isolated from the flow. However the porosity represents a zone that is totally separated from the main stream with no flux exchange between them. Therefore,  $B_s$  calculated from 2D simulation may be overestimated compared to the one necessary to perform an effective modeling of the flow contraction in 1D.

By decreasing  $B_{s,\phi}$  (0.3m, 0.26m, 0.2m, and 0m) the calculated profiles presented in figure 6.15 remain subcritical. Compared to the reference,  $B_{s,\phi} = 0.26\text{m}$  is the value for which the effective flow is better reproduced at the maximum contraction point, which is the half of the value calculated from 2D results  $B_{s,\phi} = \frac{B_s}{2}$ . Therefore,  $B_{s,\phi} = 0.26\text{m}$  is used in 1D model to reproduce the 2D flow lines and  $\phi_{min}$  is calculated by  $B_{s,\phi}$ :

$$\phi_{min} = 1 - \frac{B_{s,\phi}}{B} = 1 - \frac{B_s}{2B} = 82.7\% \quad (6.19)$$

When  $B_{s,\phi} = 0\text{m}$ , corresponding to no porosity and friction only, the flow line modeled with *Flood1D2D* is linear, hence not reproducing flow contraction behavior. Note that even with a distributed friction coefficient such contracted flow profiles cannot be reproduced using a 1D approach as the friction coefficient is embedded in the source term  $S_f$  of the SW equation, only able to dissipate energy. Indeed this term is of the opposite sign of the velocity which remains monotonous in a prismatic reach as water depth profile.

The hydraulic jump is triggered by the parameter values creating high flow velocity, namely a flow contracting at  $B_s = 0.52$  combined to a low roughness value  $K = 100\text{m}^{1/3}.\text{s}^{-1}$ . Moreover, the roughness value used in *Flood1D2D* in 1D mesh does not account for the head loss due to turbulence modeled in Telemac2D. This explains why no hydraulic jump appears in Telemac2D results.

### 6.5.2.2 Influence of the porosity shape

In order to test the influence of the porosity shape on reproducing water depth profile, three relationships proposed at section 6.5.1 are tested: Gurram et al. (1997) relationship (6.15), polynomial relationship (6.16) and piecewise relationship (6.17) as plotted in figure 6.13.

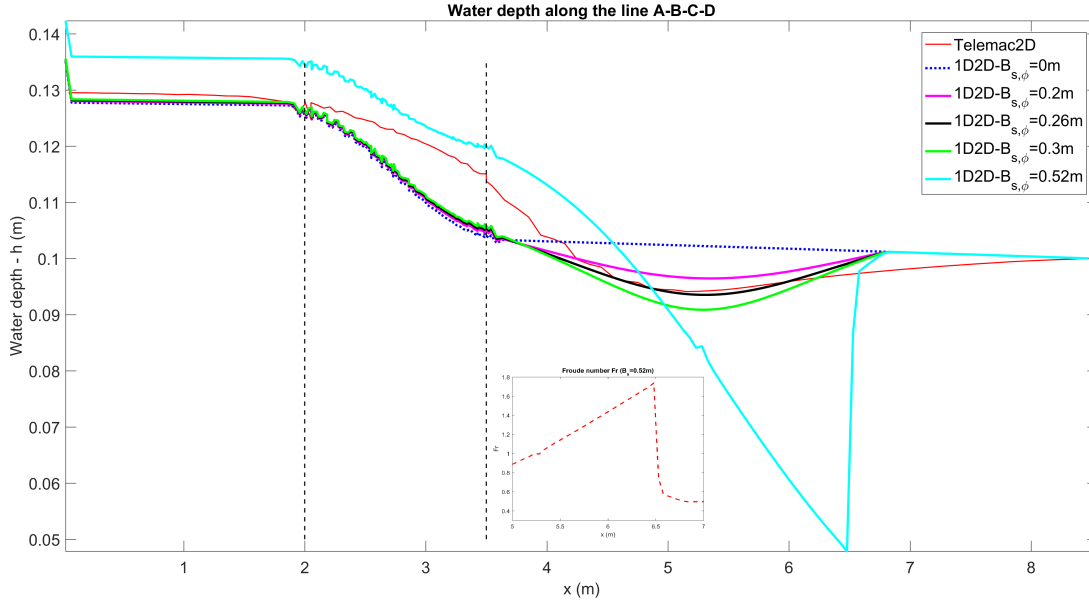


Figure 6.15: Comparison of simulated water height between Telemac2D and *Flood1D2D* using different  $B_{s,\phi}$

Water depth profiles along the line A-B-C-D in  $x$  direction are compared with the 2D reference profile. A uniform roughness  $K = 100\text{m}^{1/3}.\text{s}^{-1}$  is applied both on 1D and 2D cells. Water depth results are presented in figure 6.16. The water depth profiles using both the Gurram et al. (1997) and the polynomial relationships are very similar along the whole A-D profile. Downstream of the crossroad ( $x > 3.5\text{m}$ ), all the 1D effective water depth profiles present similar trends including a flow profile contraction as the 2D profile (with a local minimum at  $x \approx 5.1\text{m}$ ) with more or less good agreement depending on the flow zones. Piecewise relationship produces a profile that is closer from the reference, especially after the maximum contraction point compared with the two others.

However, at street inlet just downstream the crossroad, the water depth profile is still lower than the 2D profile. The energy loss modeled in 2D is not fully accounted by the 1D model parameterized with a uniform roughness especially downstream of the crossroad. Therefore, distributed roughness is considered in what follows to improve the performance of the 1D2D model.

### 6.5.2.3 Influence of non-uniform Strickler coefficient

To account for 2D energy loss caused by 2D flow feature in 1D2D model and improve the agreement between the flow profiles, a distributed roughness is used in 1D2D modeling. The whole domain has been divided into several sections:

- At crossroad, which is meshed using 2D grid, the Strickler coefficient is set to  $K = 100\text{m}^{1/3}.\text{s}^{-1}$  without modification;
- For the the street portion located upstream of the crossroad, and the one downstream of the maximum contraction point, where uniform flow is dominating, the Strickler coefficient is set to  $K = 100\text{m}^{1/3}.\text{s}^{-1}$  without modification;

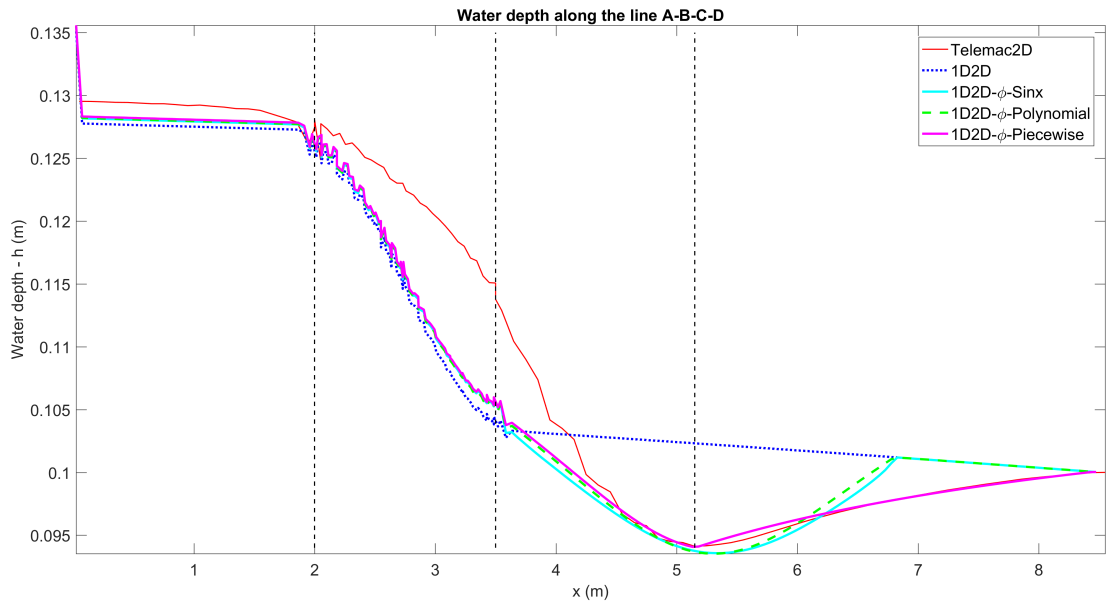


Figure 6.16: Comparison of simulated water height between Telemac2D and *Flood1D2D* using  $\phi = 1$ , trigonometric, polynomial and piecewise relationships

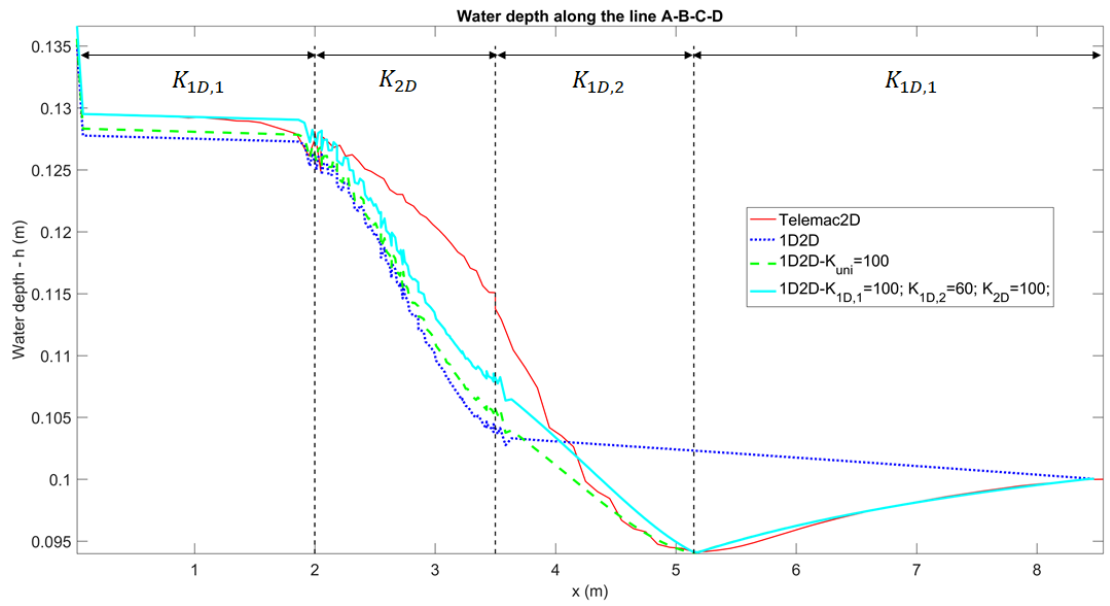


Figure 6.17: Comparison of simulated water height between Telemac2D and *Flood1D2D* using uniform and distributed roughness

- At section just downstream of the crossroad but before the maximum contraction point, which is characterized by 2D streamlines curvature an effective modeling is obtained by increasing the Strickler coefficient to  $K = 60\text{m}^{1/3}\cdot\text{s}^{-1}$ .

Figure 6.17 shows the calculated water height using distributed roughness compared with uniform roughness. Result show that the curve fitting has been improved especially at inlet channel using distributed roughness to account for the extra energy loss caused by 2D flow features.

### 6.5.3 Conclusion

The proposed model uses an effective 1D approach with a porosity able to account for flow contraction, recall acceleration and water depth decrease, due to a recirculation zone. Simulating such a hydraulic behavior may be impossible to perform with friction (energy dissipation) only for which water depth steadily decreases from upstream to downstream. The previous calibration of the porosity shape and of a spatially variable roughness shows that *Flood1D2D* is able to reproduce a 2D reference. However there may exist multiple sets of those parameters that could produce comparable flow lines. In the following section, the sensitivity of water height and discharge distribution to recirculation dimensions is assessed.

## 6.6 GSA of *Flood1D2D* using porosity parameterization

In this section, global sensitivity analysis (GSA) is applied to all the parameters of *Flood1D2D* (roughness and recirculation zone dimensions) to assess their influence on water height and discharge distribution. In *Flood1D2D*, the recirculation zones are parameterised with the porosity function  $\phi(s) = 1 - B_{recirc}(s)/B$  where  $B_{recirc}(s)$  is the width of the recirculation at a distance  $s$  of the crossroad.

The piecewise polynomial/linear relationship is chosen to reproduce the recirculation shape. As discussed at section 6.5.2, porosity function  $\phi$  implemented into the code *Flood1D2D* to account for the effect of the recirculation  $\phi_{min} = 1 - \frac{B_{s,\phi}}{B} = 1 - \frac{B_s}{2B}$  and the length of the recirculation  $L_s = 3r_0$ .

The GSA is used to estimate the sensitivity of water depth and discharge to  $Q_{in}$ ,  $h_{out}$ ,  $K$  and the recirculation dimensions ( $B_s$  and  $r_0$ ), in the four branch crossroad configuration described in section 6.3. The variation ranges for  $Q_{in}$ ,  $h_{out}$ ,  $K$  are equal to the one used for the 2D GSA (see section 6.4) and the one determined from 2000 Monte Carlo simulations described in section 6.4 for  $B_s$  and  $r_0$ .

### 6.6.1 GSA on main controls and recirculation dimensions

In this section, 8 parameters are tested on the four branch crossroad flow, including four main control parameters ( $Q_{in,x}$ ,  $Q_{in,y}$ ,  $h_{out}$  and  $K$ ) and four parameters on recirculation dimensions ( $B_{s,x}$ ,  $r_{0,x}$ ,  $B_{s,y}$  and  $r_{0,y}$ ). The nominal parameters values and their variation ranges are listed in table 6.6, 5000 runs are performed in order to sample extensive the parameter space.

Sobol indices of outlet discharges to all input parameters are presented in figure 6.18. Results show that the sum of all Sobol indices is close to 1, indicating very few interaction effect between parameters in explaining discharge partition caused by the crossroad. For outlet discharges, inlet discharges ( $Q_{in,x}$  and  $Q_{in,y}$ ) have dominant influence compared with the other parameters that can thus be neglected. For outlet discharge at  $x$  (respectively  $y$ ) direction,  $Q_{in,x}$  (respectively  $Q_{in,y}$ ) has dominant influence. Compared to a full 2D model (see figure 6.10), the influence of the outlet water height on discharge distribution is significantly reduced for *Flood1D2D*. The

Table 6.6: Parameters used and associated perturbation range for the four branch crossroad flow

Symbol	Meaning	Value	Range
$Q_{in,x}$	Inlet discharge in $x$ direction	$0.0435\text{m}^3.\text{s}^{-1}$	$\pm 72.5\%$
$Q_{in,y}$	Inlet discharge in $y$ direction	$0.0435\text{m}^3.\text{s}^{-1}$	$\pm 72.5\%$
$h_{out,x}$	Outlet water height in $x$ direction	0.05m	$\pm 60\%$
$h_{out,y}$	Outlet water height in $y$ direction	0.05m	$\pm 60\%$
$K$	friction coefficient	$100\text{m}^{1/3}.\text{s}^{-1}$	$\pm 50\%$
$B_{s,x}$	Maximum recirculation width in $x$ direction	0.225m	$\pm 68.6\%$
$r_{0,x}$	Recirculation radius in $x$ direction	1.8m	$\pm 41.7\%$
$B_{s,y}$	Maximum recirculation width in $y$ direction	0.225m	$\pm 68.6\%$
$r_{0,y}$	Recirculation radius in $y$ direction	1.8m	$\pm 41.7\%$

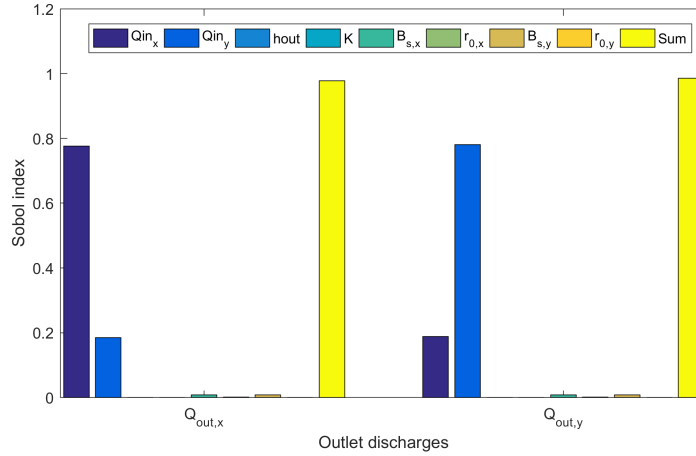


Figure 6.18: Sobol indices of outlet discharges simulated with Flood1D2D to the main controls including recirculation dimensions

recirculation zones (parameterised using the porosity function through  $B_{s,x}$ ,  $r_{0,x}$ ,  $B_{s,y}$  and  $r_{0,y}$ ) have very low influence on the discharge distribution at crossroad for the tested parameter ranges. Larger ranges of variation could be explored (avoiding incoherent configuration such as a porosity of 0 in one street would correspond to a full blockage and thus  $Q_{out} = 0$ ).

Figure 6.19 illustrates the Sobol index of water height to the main control parameters. The sum of all Sobol indices shows that no interaction effects exist at the inlet channels and into crossroad. However, at the zone where porosity varies after the crossroad, the sum of all Sobol indices is around 0.8 and less than 1. The friction coefficient explains at most 10% of the water height variance and reaches 16% where the flow vein has a reduced width (thus corresponding to a higher velocity zone). The sensitivity of the water height to the height at the downstream boundary decreases from 70% at the downstream end of the streets to less than 10% in the crossroad and upstream. The water height is sensitive to the west upstream discharge  $Q_{in,x}$ . This sensitivity is (i) smaller than 10% in the south street, (ii) between 45% and 10% from the upstream to the downstream end of the east street (iii) equal to 35-40% in the west street and (iv) equal to 45-55% in the north street. The northern part of the crossroad is sensitive to  $Q_{in,x}$  at barely 55% whereas the sensitivity in the south west corner decreases to few percent. The

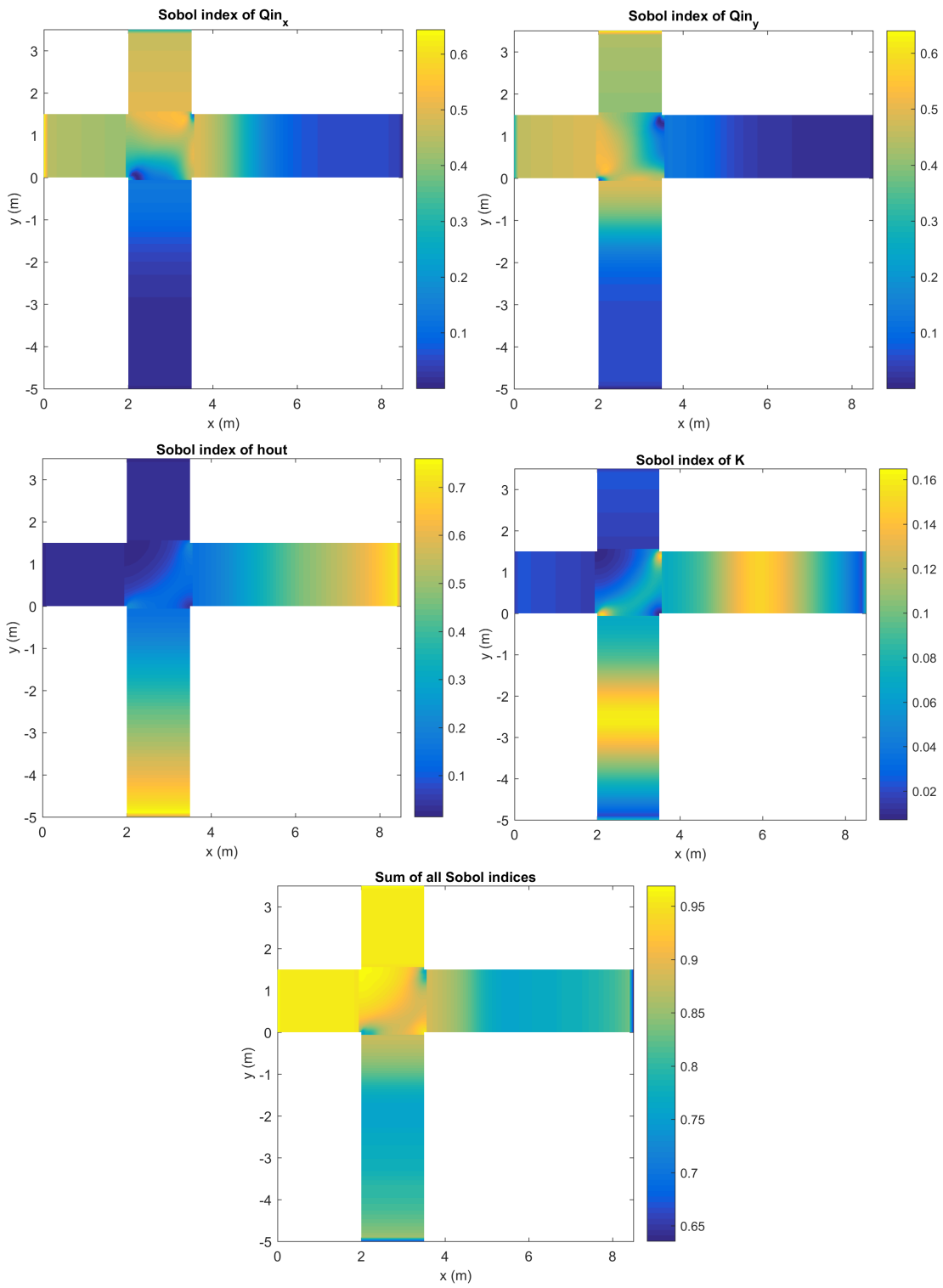


Figure 6.19: Sobol indices of spatially distributed water height simulated with *Flood1D2D* on a four branch crossroad (main controls considered in the full parameter set are  $Q_{in,x}$ ,  $Q_{in,y}$ ,  $h_{out}$  and  $K$ )

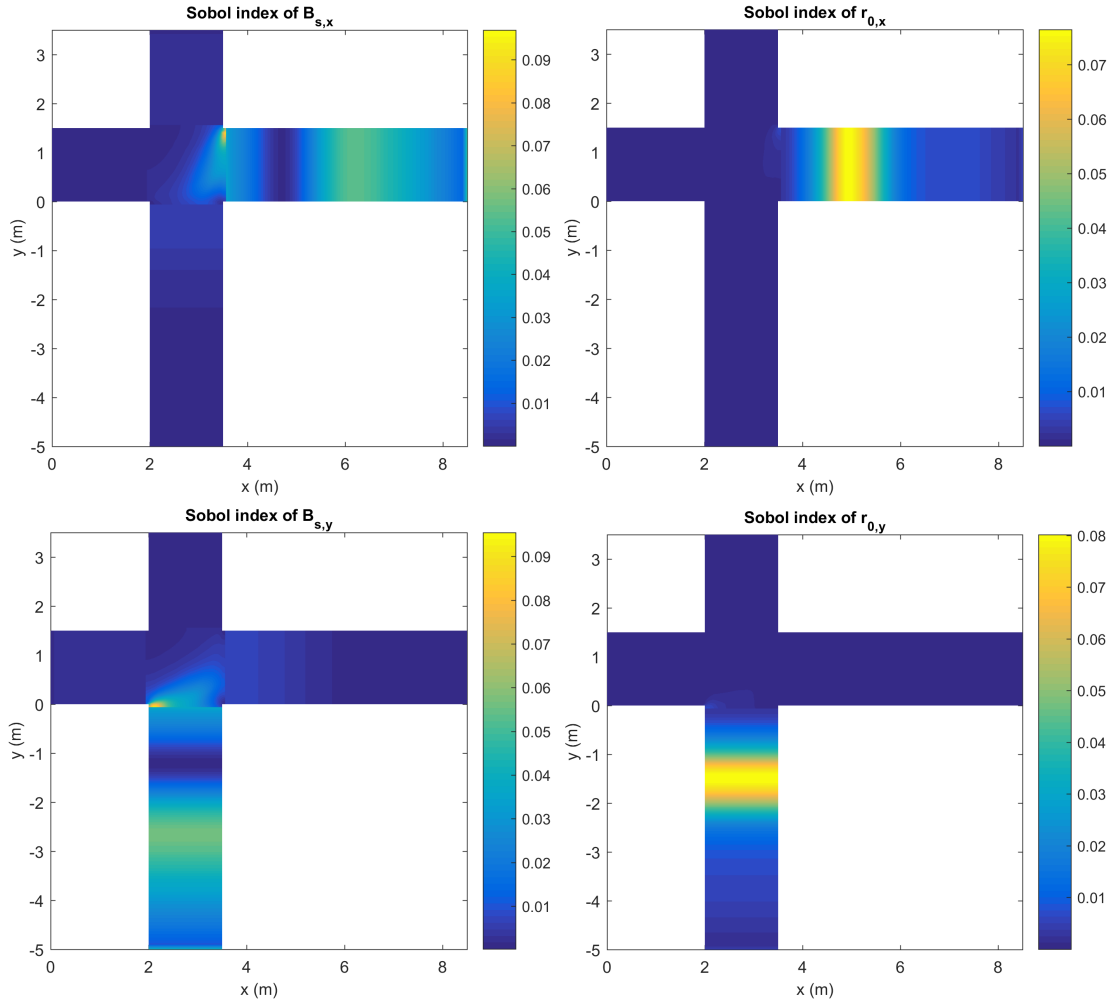


Figure 6.20: Sobol indices of spatially varied water height simulated with *Flood1D2D* to recirculation dimensions (considered in full parameter sets composed of  $B_{s,x}$ ,  $r_{0,x}$ ,  $B_{s,y}$  and  $r_{0,y}$ ): top left, sensitivity of the water depth to the maximum recirculation width in x direction; top right, to the recirculation radius in x direction; bottom left, to the maximum recirculation width in y direction; bottom right, to the recirculation radius in y direction

sensitivity of the water height to the upstream discharge in street north  $Q_{in,y}$  is symmetrical to the sensitivity to  $Q_{in,x}$  around the north-west to south-east direction. Interestingly, the water height in the north street is more sensitive to the upstream discharge in the west street than in the north street. This might be explained by the fact that increasing the discharge in street west would create a bigger blockage on the south output of the crossroad. The blockage creates an increase of the water height that creates on the north street a backwater effect as the flow is subcritical. The influence of classical parameters on water height has thus similar effect as in full 2D analysis conducted in section 6.4.

Figure 6.20 shows the Sobol index of water height to recirculation dimensions ( $B_{s,x}$ ,  $r_{0,x}$ ,  $B_{s,y}$  and  $r_{0,y}$ ).  $B_{s,x}$  the cross sectional recirculation width (respectively  $B_{s,y}$ ) has an effect on

Table 6.7: Parameters used and associated perturbation range for the four branch crossroad flow

Symbol	Meaning	Value	Range
$B_{s,x}$	Maximum recirculation width at $x$ direction	0.225m	$\pm 68.6\%$
$r_{0,x}$	Recirculation radius at $x$ direction	1.8m	$\pm 41.7\%$
$B_{s,y}$	Maximum recirculation width at $y$ direction	0.225m	$\pm 68.6\%$
$r_{0,y}$	Recirculation radius at $y$ direction	1.8m	$\pm 41.7\%$
$K$	Strickler coefficient	$100\text{m}^{1/3}.\text{s}^{-1}$	$\pm 50\%$

the water height only at the north east corner of the crossroad (respectively south west) and in the outlet channel at  $x$  direction (respectively  $y$  direction). In both of the downstream streets, the sensitivity to  $B_{s,x}$  (respectively  $B_{s,y}$ ) appears to be minimal at the nominal value of  $r_{0,x}$  (respectively  $r_{0,y}$ ). The variance of the water height to  $r_{0,x}$  (respectively  $r_{0,y}$ ) is nil except in the east (respectively south) street. The maximum of sensitivity is located around the nominal value of  $r_0$ . Compared with main control parameters ( $Q_{in,x}$ ,  $Q_{in,y}$ ,  $h_{out}$  and  $K$ ), recirculation parameters have limited influence on water height. However the influence of flow contractions in each streets has a clear effect on water height upstream, within the crossroad and with a maximal sensitivity at the angle from which the recirculation, hence the contraction is represented.

### 6.6.2 GSA on recirculation dimensions and roughness

In this section, the main control parameters ( $Q_{in,x}$ ,  $Q_{in,y}$ ,  $h_{out}$ ) are kept constant to their nominal values in order to exhibit the influence of recirculation dimensions and friction on the four branch crossroad flow features. Five parameters are tested including  $B_{s,x}$ ,  $r_{0,x}$ ,  $B_{s,y}$  and  $r_{0,y}$  and roughness  $K$ . The boundary conditions are listed in table 6.3. The nominal values of recirculation dimensions and their variation ranges for sampling are listed in table 6.7. The Sobol index on water height and outlet discharges are presented in figures 6.21 and 6.22.

Figure 6.21 illustrates the sensitivity of the water height to the five input parameters and their sum. The sum of all Sobol indices is close to 1 except at the zones after the crossroad as explained at section 6.6.1.  $B_{s,x}$  (respectively  $B_{s,y}$ ) has effect on the inlet channels and on the east (respectively south) face of the crossroad. For  $r_{0,x}$  and  $r_{0,y}$ , they only have influence at porosity variation zone. For friction coefficient, it has main effect at inlet channels before the crossroad and decreases from upstream to downstream as explained by Chen et al. (2018). In the downstream streets, friction coefficient is higher in the low porosity zones for which the velocity is increased.

Figure 6.22 presents Sobol indices of input parameters on outlet discharges. Results show that recirculation width has main effect on discharge distribution at crossroad compared with length of recirculation and roughness.

## 6.7 Application of *Flood1D2D* at the district scale

As illustrated in section 6.5.2: modeling the street with a pseudo-1D approach only parameterised with a friction coefficient fails to reproduce, at the local scale, realistic contracted water depth profiles. Adding a new parameterization representing the reduction of the flow vein allows to handle those difficulties and is shown to influence discharge distribution downstream of a hydraulic intersection. This section aims at characterizing the effect of the porosity on the flow pattern at a more global scale: the district scale which consists in a branched network composed of several crossroads.

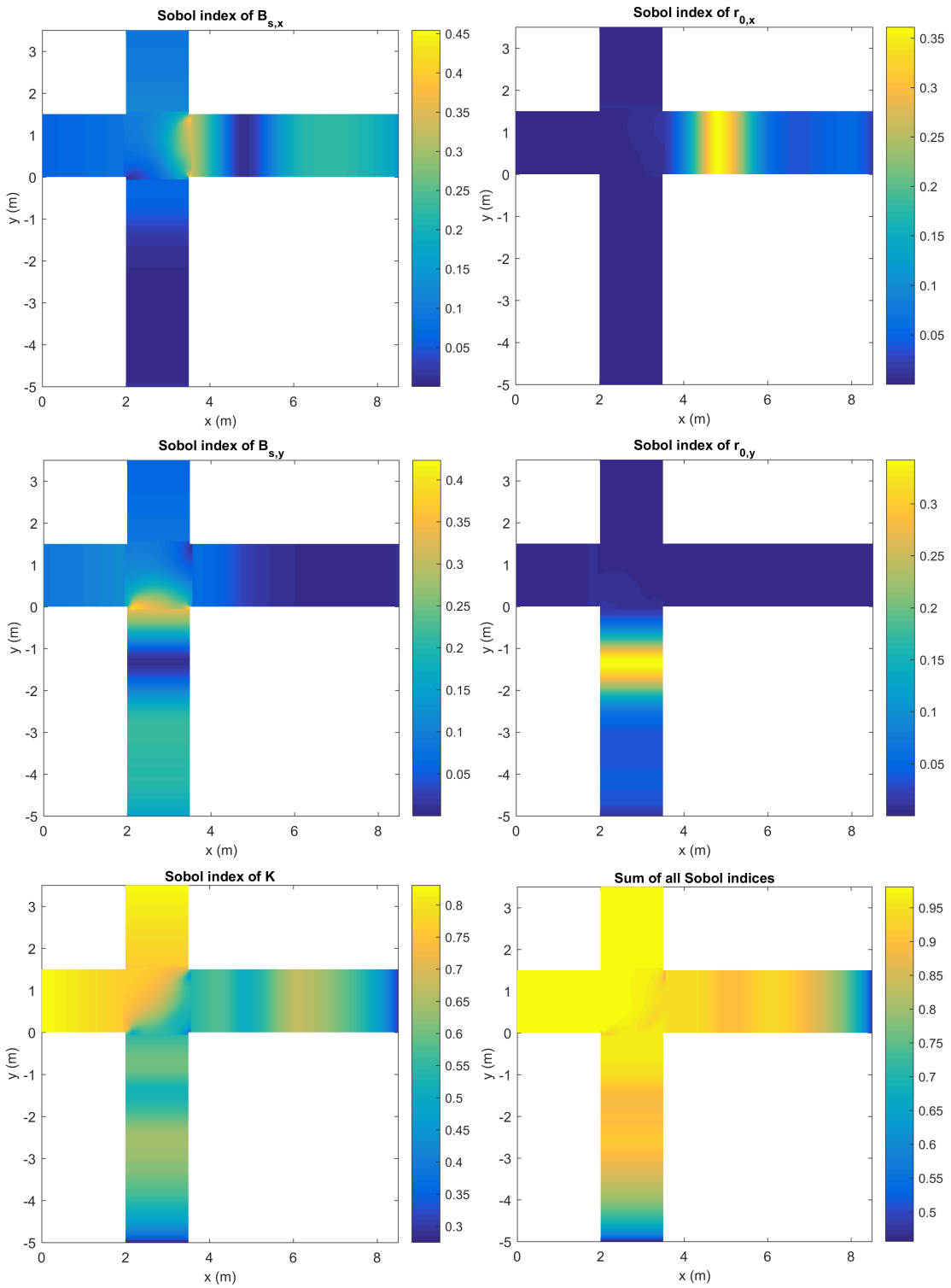


Figure 6.21: Sobol indices of spatially distributed water height simulated with *Flood1D2D* to recirculation dimensions on a four branch crossroad.

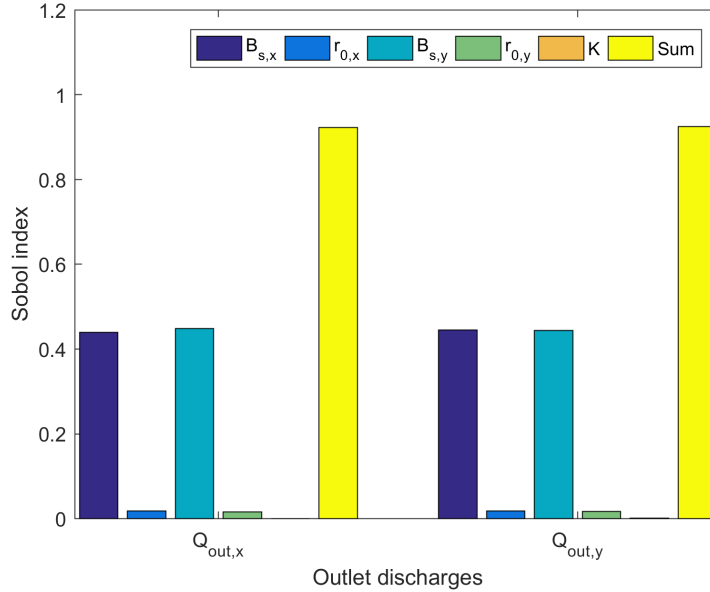


Figure 6.22: Sobol indices of outlet discharges simulated with *Flood1D2D* to recirculation dimensions on a four branch crossroad.

### 6.7.1 Modeled crossroads network

The sensitivity of *Flood1D2D* is determined on a sub-part of the ICube urban flood experimental rig developed in Strasbourg. A study on the full experimental rig would have implied a modeling with a high number of parameters and thus a very expensive computational cost for a sensitivity study in view of calibration. The sub-part chosen includes four crossroads with streets of various widths and orientations located into the center of the rig. It includes streets 3 and 4 along west-east direction and streets E and F along north-south direction (see figure 6.23). Streets E and 3 (respectively F and 4) are small (respectively large) streets. The total width of the large street is barely 12.5cm and 5cm for the small streets. For the sake of clarity, a crossroad is identified by the name of the two streets crossing: 'E3' is thus the crossroad between street E and street 3. A subpart of street is named using the two crossroads upstream and downstream: 'E3E4' designs the portion of street E between crossroad 'E3' and 'E4'.

Steady-state experimental data-set (Araud (2012); Arrault et al. (2016); Finaud-Guyot et al. (2018)) allows to know the discharge and the water depth patterns in each street. The discharge is measured into the street between two crossroads and water depth is obtained along the two side walls of the channel. The network is modeled using a 1D2D unstructured mesh with a discretization step  $\Delta x = 0.025\text{m}$  (see figure 6.23). The streets are modeled using 1D cells and the crossroads are represented using 2D. The boundary conditions are set to upstream discharge in streets E, F, 3 and 4 (corresponding to the experimental values) and rating curves are computed for each downstream end. Those rating curves are computed based on the experimental data: the discharge and the water at the downstream end of the last streets. PorAS Riemann solver is used for flux computation. In every configuration, the simulation is run during 1000s to ensure steady state flow over the whole domain.

This geometrical configuration is used to highlight the sensitivity of *Flood1D2D* to three

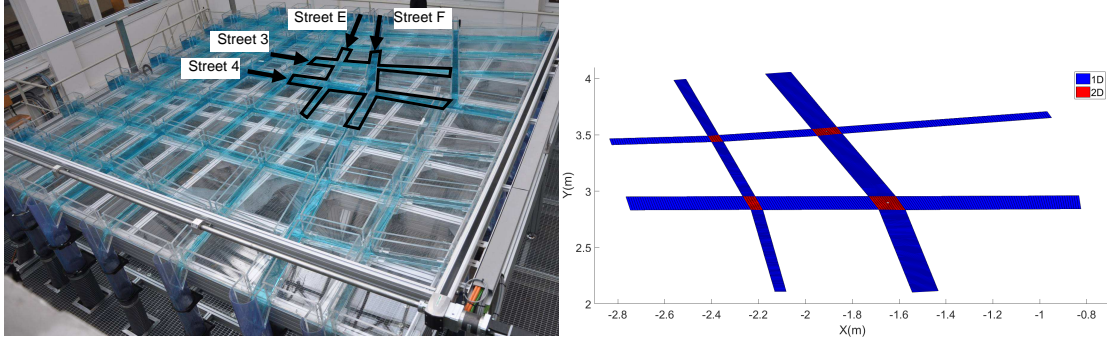


Figure 6.23: Experimental rig and illustration of the modeled zone (left side) and 1D2D mesh (right side). The white dot in the south east crossroad is a plotting artefact.

different parameterizations:

- No porosity and a spatially varied Strickler coefficient;
- A uniform Strickler coefficient and a spatially varied porosity based on the street width;
- A uniform Strickler coefficient and a spatially varied porosity based on the street width. The porosity in the streets 'E3E4' and 'E3F3' are weighted in order to influence the flow repartition at the 'E3' crossroad.

### 6.7.2 Characterization in $K_{street}/K_{cross}$

The model is parameterized using two uniform values of the Strickler coefficient:  $K_{street}$  in streets and  $K_{cross}$  in crossroads. Each parameter is taken in the set of values [25, 50, 75, 100, 125, 150] and all combinations are tested, that is 36 in total. The relative variation of the water depth in cell  $i$   $\tilde{h}_i$  is defined as:

$$\tilde{h}_i = 100 \times \frac{\max(h_i^k) - \min(h_i^k)}{h_{exp}(x_i, y_i)} \quad (6.20)$$

where  $h_{exp}(x_i, y_i)$  represents the experimental water depth at the coordinate of the gravity center of cell  $i$ ,  $\min(h_i^k)$  and  $\max(h_i^k)$  are the minimal and the maximal water depth in cell  $i$  computed in simulation  $k$ .  $\tilde{h}_i$  is presented in figure 6.24 and is smaller than 6% showing that the water depth is barely not influenced by the Strickler coefficient as highlighted in section 6.6.

The street outlet discharge is compared to the experimental value on figure 6.25. For each street, the first bar corresponds to the experimental value. Whatever the parameterization of the model, each discharge flowing out from streets E and F (respectively 3 and 4) is systematically under- (respectively over-) estimated. Interestingly,  $K_{street}$  seems to impose an averaged street discharge value (look for instance the shift in the outlet discharge for street F when  $K_{street}$  varies from 25 to 50).  $K_{cross}$  has a smaller impact on outflow discharge repartition (with always the same trend around the value imposed by  $K_{street}$ ).

It appears that *Flood1D2D* parameterized only with a Strickler coefficient is unable to correctly reproduce the water depth profile (see section 6.5.2) and the downstream discharge repartition.

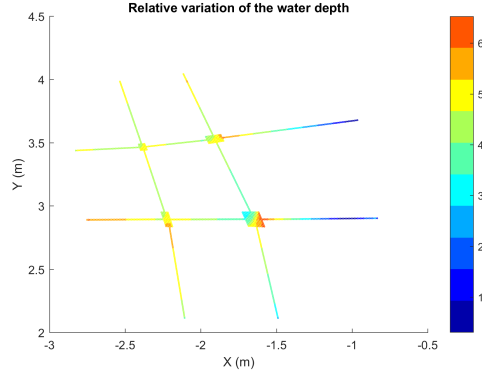


Figure 6.24: Relative variation of water depth to a parameterization with  $K_{street}$  and  $K_{cross}$

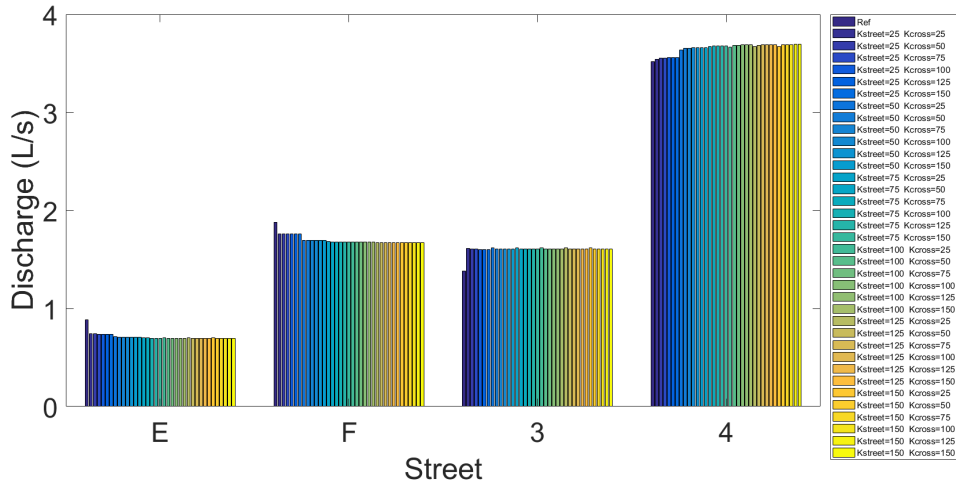


Figure 6.25: Outlet discharge sensitivity to a parameterization with  $K_{street}$  and  $K_{cross}$

### 6.7.3 Parameterization in $K_{unif} / \phi_{large} / \phi_{narrow}$

The model is parameterized using a uniform value of the roughness coefficient  $K = 75\text{m}^{1/3}.\text{s}^{-1}$  since few sensitivity to both  $K_{street}$  and  $K_{cross}$  is found in the previous section on outlet discharges. A distributed porosity is defined for all streets downstream of crossroads following a parabolic profile:

$$\phi(s) = \begin{cases} as^2 + bs + c & \text{for } 0 \leq s \leq 0.5 \\ 1 & \text{elsewhere} \end{cases} \quad \text{with } \phi(0) = \phi(1/2) = 1 \quad \text{and} \quad \phi(1/4) = \phi_r \quad (6.21)$$

where  $s$  is the adimensional curvilinear abscissa (0 (respectively 1) at the upstream (respectively downstream) end of each street). The model is parameterized, by adjusting  $a$ ,  $b$  and  $c$ , with two values of  $\phi_{r,l}$  in large streets (F and 4) and  $\phi_{r,n}$  in narrow streets (E and 3). In order to sample *Flood1D2D* response surface, all the combinations of values of  $\phi_{r,l}$  and  $\phi_{r,n}$  in  $[0.25, 0.50, 0.75, 1.00]$  are tested, that is 16 in total.

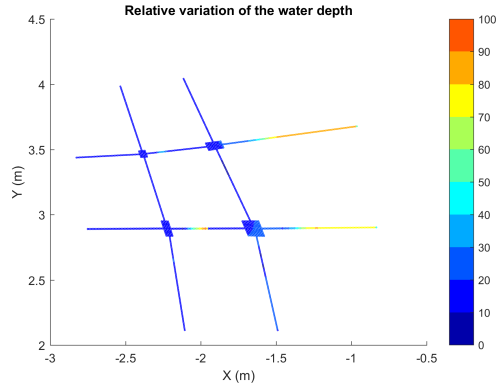


Figure 6.26: Relative variation of water depth to a parameterization with  $\phi_{r,n}$  and  $\phi_{r,l}$

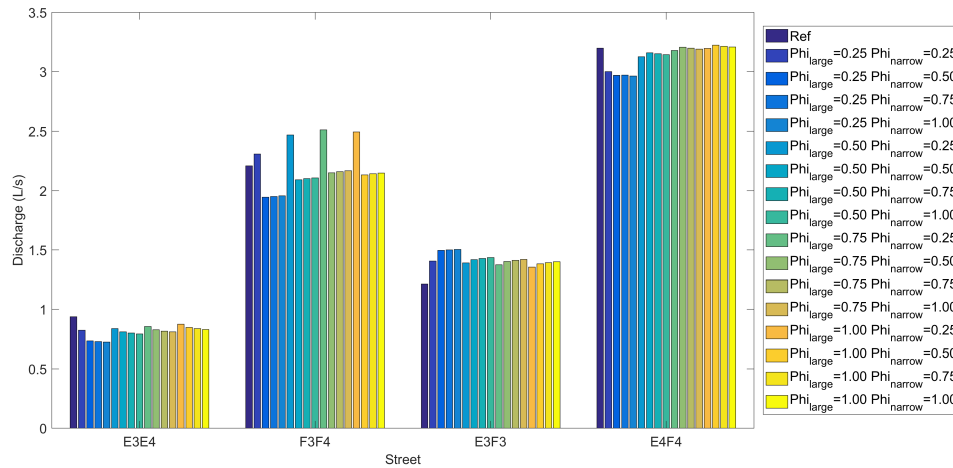


Figure 6.27: Street discharge sensitivity to a parameterization with  $\phi_{r,n}$  and  $\phi_{r,l}$

The relative variation of water depth is presented in figure 6.26, which ranges from 0 to 100. The important variations of the water depth are localized in streets E4F4, F3G3 and F4G4. Hydraulic jumps are localized in those streets and move at a small velocity, which claims for quasi-steady state results. Increased simulations would have been required but would have leads to unaffordable computational costs.

The outlet street discharges and those in the four streets between crossroads are compared to the experimental values on figure 6.27 and 6.28. For each street, the first bar corresponds to the experimental value. For each street and all parameter sets tested, there are both under and over estimations of street outlet discharge which was not possible with roughness only. Despite the sparse sampling of this wide parameter space, the spread of model response quite centered around discharge measurements suggests that there may exist parameter sets reproducing those values. It clearly shows the ability of the proposed model and parameterization to model various non monotonous flow patterns and potentially realistic local discharge and global discharge distributions.

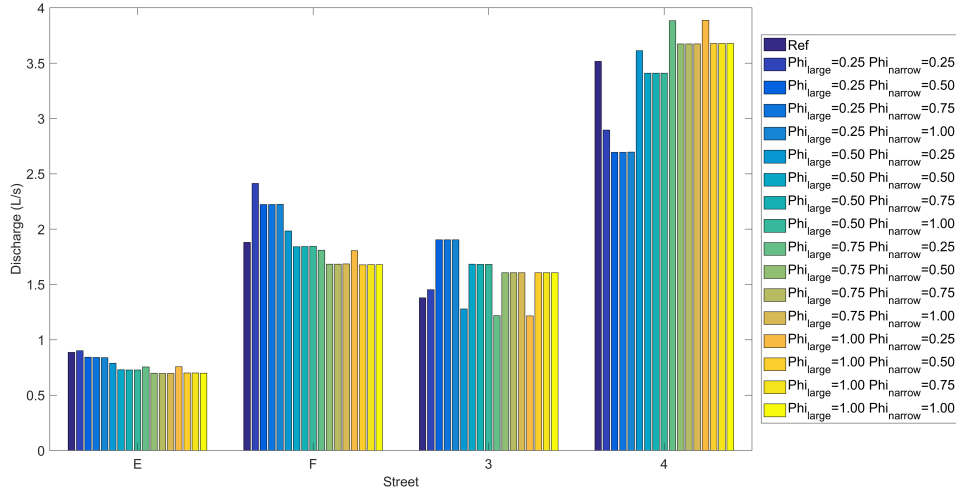


Figure 6.28: Outlet discharge sensitivity to a parameterization with  $\phi_{r,n}$  and  $\phi_{r,l}$

#### 6.7.4 Parameterization in $K_{unif} / \phi_{large} / \phi_{narrow} / Ratio$

In this section, the model is parameterized using a uniform roughness  $K = 75\text{m}^{1/3}.\text{s}^{-1}$  and distributed porosity as described in section 6.7.3:  $\phi_{large}$  is applied to large streets,  $\phi_{narrow}$  to the street E and to subpart F3G3 of street 3. Subpart E3F3 of street 3 is parameterised with  $r \times \phi_{narrow}$ . The set of values for the different parameters are  $[0.6, 0.75, 0.9]$  for  $\phi_{large}$ ,  $[0.7, 0.8, 0.9, 1]$  for  $\phi_{narrow}$  and  $[0.3, 0.475, 0.65, 0.825, 1]$  for  $r$ . Choosing  $r \leq 1$  allows to impose a porosity in street E3F3 smaller than in street E3E4. It is expected that it would increase the discharge in street E3E4 as figure 6.27 highlights that the discharge is overestimated (respectively underestimated) in street E3F3 (respectively E3E4). In order to sample *Flood1D2D* response surface, all the combinations of values of  $\phi_{large}$ ,  $\phi_{narrow}$  and *Ratio* are tested, that is 60 in total.

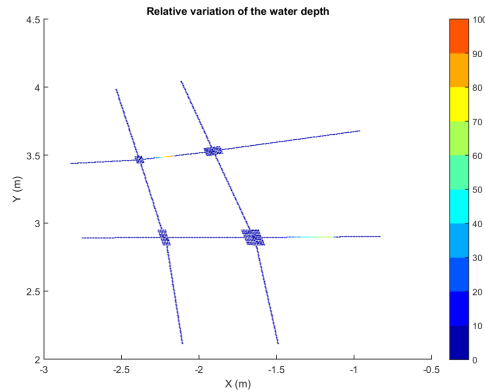


Figure 6.29: Relative variation of water depth to a parameterization with  $\phi_{narrow}$  and *Ratio*

The relative variation of water depth is presented in figure 6.29, which ranges from 0 to 100.

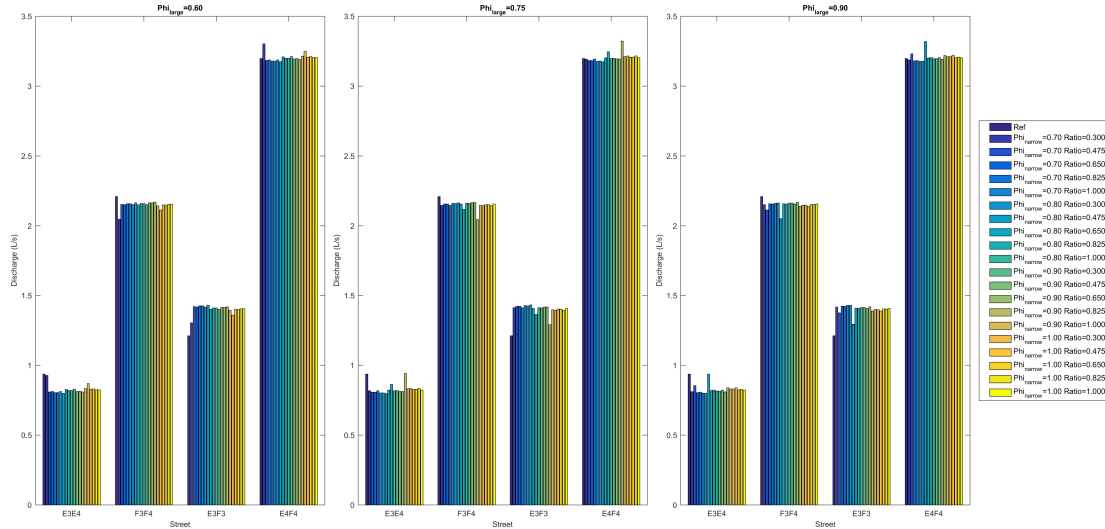


Figure 6.30: Street discharge sensitivity to a parameterization with  $\phi_{narrow}$  and Ratio

The important variations of the water depth are localized in streets E3F3 and F4G4. Again hydraulic jumps are localised in those streets and a quasi-steady state is reached. Increased simulations would have been required but would have lead to unaffordable computational costs.

The outlet street discharges and those in the four streets between crossroads are compared to the experimental values on figure 6.30 and 6.31. For each street, the first bar corresponds to the experimental value. Figure 6.30 shows that the ratio parameter  $r$  allows to slightly improve the discharge repartition between streets E3F3 and E3E4. Interestingly, the outlet discharge of each street is almost kept constant with varied street discharges combining different  $\phi_{large}$  and  $\phi_{narrow}$  (whatever the ratio parameter  $r$ ). It highlights that the mechanism of discharge redistribution into the street networks. The discharge distribution at the district scale is  $Q_{in}$  dependent but results in a comparable outlet discharge partition.

The issues related to the calibration of spatially distributed  $K$  and  $\phi$  parameters should be further studied, especially equifinality problems in the light of their influence on discharge repartition at large scale in branched networks.

## 6.8 Conclusions

In this chapter, the application of *Flood1D2D* at local and district scale has been studied for urban flood modeling. Result of this chapter shows the ability of *Flood1D2D* using parameter porosity  $\phi$  in reproducing 2D flow lines and the function of recirculation zone on water height and discharge distribution at local and district scales.

Firstly, the sensitivity of friction slope calculation to recirculation effect parameterization is assessed and provide advice for choosing different hydraulic radius formulations. The friction slope formulation is significantly modified when recirculation effect is introduced.

Then, *Flood1D2D* is applied at local scale, a four branch crossroad. Simulated flow lines are compared with 2D simulation results (Telemac2D). Result shows the ability of *Flood1D2D* to account for the recirculation effect using porosity  $\phi$ , which can't be explained using roughness only. The function of recirculation zone on water height and discharge distribution is also assessed

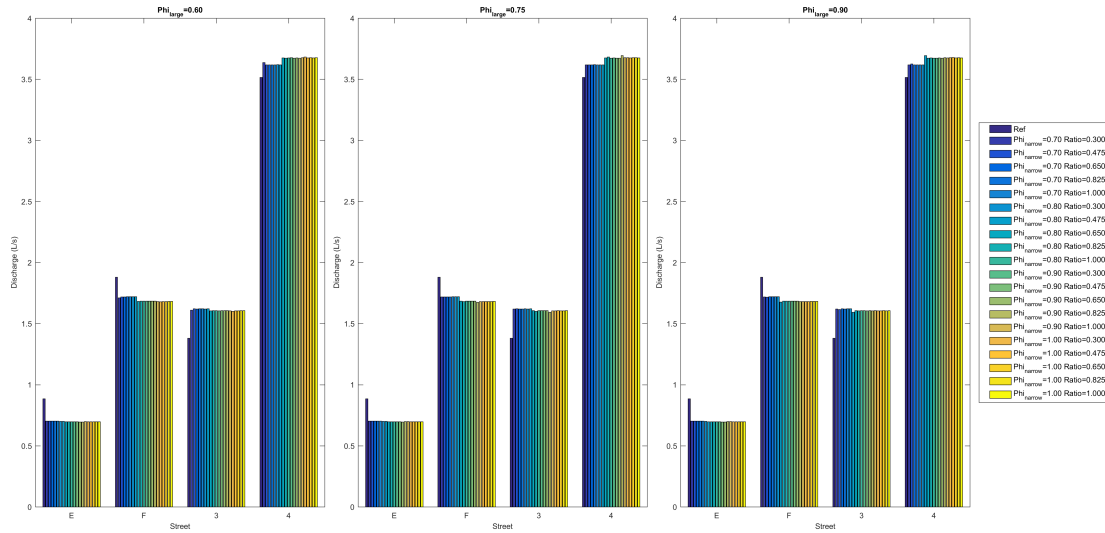


Figure 6.31: Outlet discharge sensitivity to a parameterization with  $\phi_{narrow}$  and Ratio

using GSA. Result shows that recirculation dimensions ( $B_s$  and  $L_s$ ) have limited influence on flow patterns compared with main flow controls ( $Q_{in}$ ,  $h_{out}$  and  $K$ ).  $B_s$  has bigger influence on discharge distribution compared with  $L_s$  and  $K$ , which are negligible.

Finally, *Flood1D2D* is applied at district scale, consists in a branched network composed of several crossroads. Result shows the ability of the code on discharge redistribution into the network, whereas distributed roughness not. The stability of outlet discharge is observed whatever the variation of street discharges into the network.

## Chapter 7

# General conclusions and perspectives

### 7.1 General conclusions

This thesis proposes a new effective modeling approach based on SW equations with an original parameterization adapted to urban flood modeling at the local and the district scale. This PhD work is based on a new C code *Flood1D2D*. The work is based on experimental datasets from the ICube urban flood experimental rig located in Strasbourg. A particular attention is paid to recirculation areas downstream of crossroads, their local effective modeling and their effect on the flow pattern at the district scale.

A detailed state of art on urban floods and the application of shallow water models in such configurations has been presented, in chapter 1, highlighting the need for new effective and computationally affordable modeling approaches. The governing equations, relying on a 2D shallow water model with isotropic porosity and an original use of a cut-cell technique for effective 1D2D coupling and its discretization in finite volumes, are presented in chapter 2. The model is validated on classical synthetic test cases and reference datasets from laboratory experiments. It includes classical synthetic test cases (including bottom slope and friction effect) and specific modeling features (1D2D and porosity function). The predictive capability and accuracy of the *Flood1D2D* are highlighted both for steady and unsteady configurations.

Then, chapter 4 presents a thorough sensitivity analysis of classical 1D and 2D shallow water (SW) models response to its inputs using a GSA method. In the case of urban flood flows, the influence of uncertain parameters of 1D and 2D shallow water model input parameters on steady and unsteady model outputs (h,Q) is quantified. Spatial and temporal Sobol indices of h and Q to the input parameters have highlighted the locations of the main flow controls along their temporal variation during a flood. The role of the streets network geometry on water partitioning is underlined. Results show that subcritical or supercritical flow can be fully accounted by first-order Sobol index. Moreover, it is shown that for a hydraulic jump the calculation of Sobol indices may require further attention as the possible higher order interactions between classical hydraulic model parameters.

The new parameterization proposed for an effective urban flood modeling in 1D2D, accounting for the flow contraction due to recirculation zones, with a porosity like approach is studied in chapter 5. An isotropic porosity  $\phi$ , implemented into the code *Flood1D2D* and it is parameterized from recirculation dimensions  $B_s$  (maximum recirculation width) and  $L_s$  (recirculation length) estimate from classical 2D simulations, assuming a simple geometrical shape. This new parameterization leads to correct 1D effective simulated flow lines in the contracted flow veins, which is impossible with a roughness only. The effect of recirculation zone parameters on the water height and discharge distribution simulated with *Flood1D2D* is assessed using GSA on a four branched

crossroad.  $B_s$  is shown to have a bigger influence on discharge distribution compared to  $L_s$  and  $K$ . Finally, *Flood1D2D* is also applied at the district scale, for a branched network composed of several crossroads taken from ICube experimental dataset. The few parameter sets tested show the ability of the new parameterization, using both roughness and porosity, to influence both water depth at the local scale and the discharge distribution at the global scale.

## 7.2 Perspectives

The purpose of this thesis was to develop a parsimonious 1D2D coupling method adapted to urban district configuration, taking into account recirculation effects on urban flood flow patterns. The application of the code, at a larger scale, for example at the scale of the full ICube urban flood rig should be investigated along with the question of spatialized parameters calibration on existing datasets. Moreover, further studies could tackle the problem of unsteady urban flood flows and the necessary parameterization complexities by paying attention to potential equifinality problems. The mechanism of discharge distribution, including transient phenomena, at the crossroad scale would also be interesting for further research as the generalization at the district scale.

# Bibliography

- Abderrezzak, K. E. K., Paquier, A., Mignot, E., 2009. Modelling flash flood propagation in urban areas using a two-dimensional numerical model. *Natural Hazards* 50 (3), 433–460.
- Abily, M., Bertrand, N., Delestre, O., Gourbesville, P., Duluc, C.-M., 2016. Spatial global sensitivity analysis of high resolution classified topographic data use in 2d urban flood modelling. *Environmental Modelling & Software* 77, 183–195.
- Anderson, J. D., Wendt, J., 1995. *Computational fluid dynamics*. Vol. 206. Springer.
- Araud, Q., 2012. Simulations des écoulements en milieu urbain lors d'un évènement pluvieux extrême. Ph.D. thesis, Université de Strasbourg.
- Arrault, A., Finaud-Guyot, P., Archambeau, P., Bruwier, M., Erpicum, S., Pirotton, M., Dewals, B., 2016. Hydrodynamics of long-duration urban floods: experiments and numerical modelling. *Natural Hazards and Earth System Sciences* 16 (6), 1413–1429.
- Bachmat, Y., Bear, J., 1986. Macroscopic modelling of transport phenomena in porous media. 1: The continuum approach. *Transport in porous media* 1 (3), 213–240.
- Bellos, V., Kourtis, I. M., Moreno-Rodenas, A., Tsihrintzis, V. A., 2017. Quantifying roughness coefficient uncertainty in urban flooding simulations through a simplified methodology. *Water* 9 (12), 944.
- Best, J. L., Reid, I., 1984. Separation zone at open-channel junctions. *Journal of Hydraulic Engineering* 110 (11), 1588–1594.
- Beven, K., Binley, A., 1992. The future of distributed models: model calibration and uncertainty prediction. *Hydrological processes* 6 (3), 279–298.
- Bladé, E., Gómez-Valentín, M., Dolz, J., Aragón-Hernández, J., Corestein, G., Sánchez-Juny, M., 2012. Integration of 1d and 2d finite volume schemes for computations of water flow in natural channels. *Advances in Water Resources* 42, 17–29.
- Bos, M. G., 1976. Discharge measurement structures. Tech. rep., Ilri.
- Bradbrook, K., Biron, P., Lane, S., Richards, K., Roy, A., 1998. Investigation of controls on secondary circulation in a simple confluence geometry using a three-dimensional numerical model. *Hydrological Processes* 12 (8), 1371–1396.
- Brisset, P., Garambois, P., Monnier, J., Roux, H., 2017. Identifiability and assimilation of sparse altimetry data in 1d saint-venant river models. revised.

- Bruwier, M., 2017. Advanced porosity-based models to assess the influence of urban layouts on inundation flows and impact of urban evolution on flood damage. Ph.D. thesis, Université de Liège, Liège, Belgique.
- Bruwier, M., Archambeau, P., Erpicum, S., Pirotton, M., Dewals, B., 2017. Shallow-water models with anisotropic porosity and merging for flood modelling on cartesian grids. *Journal of Hydrology* 554, 693–709.
- Cassan, L., Belaud, G., Baume, J. P., Dejean, C., Moulin, F., 2015. Velocity profiles in a real vegetated channel. *Environmental Fluid Mechanics* 15 (6), 1263–1279.
- Cassan, L., Roux, H., Garambois, P.-A., 2017. A semi-analytical model for the hydraulic resistance due to macro-roughnesses of varying shapes and densities. *Water* 9 (9), 637.
- Chen, A. S., Evans, B., Djordjević, S., Savić, D. A., 2012a. A coarse-grid approach to representing building blockage effects in 2d urban flood modelling. *Journal of hydrology* 426, 1–16.
- Chen, A. S., Evans, B., Djordjević, S., Savić, D. A., 2012b. Multi-layered coarse grid modelling in 2d urban flood simulations. *Journal of Hydrology* 470, 1–11.
- Chen, S., Garambois, P.-A., Finaud-Guyot, P., Dellinger, G., Mose, R., Terfous, A., Ghenaim, A., 2018. Variance based uncertainty quantification for 1d and 2d hydraulic modeling: an experimental urban flood case. Under review for *Environmental Modelling & Software*.
- Creëlle, S., Schindfessel, L., De Mulder, T., 2016. Modelling of the tributary momentum contribution to predict confluence head losses. *Journal of Hydraulic Research*, 1–15.
- Cunge, J. A., 1975. Two dimensional modeling of flood plains. *Unsteady flow in open channels* 2, 705–762.
- Defina, A., 2000. Two-dimensional shallow flow equations for partially dry areas. *Water resources research* 36 (11), 3251–3264.
- Delenne, C., Finaud-Guyot, P., Guinot, V., Cappelaere, B., 2011. Sensitivity of the 1d shallow water equations with source terms: Solution method for discontinuous flows. *International Journal for Numerical Methods in Fluids* 67 (8), 981–1003.
- Delrieu, G., Nicol, J., Yates, E., Kirstetter, P.-E., Creutin, J.-D., Anquetin, S., Obled, C., Saulnier, G.-M., Ducrocq, V., Gaume, E., et al., 2005. The catastrophic flash-flood event of 8–9 September 2002 in the Gard Region, France: a first case study for the Cévennes–Vivarais Mediterranean hydrometeorological observatory. *Journal of Hydrometeorology* 6 (1), 34–52.
- Dottori, F., Di Baldassarre, G., Todini, E., 2013. Detailed data is welcome, but with a pinch of salt: Accuracy, precision, and uncertainty in flood inundation modeling. *Water Resources Research* 49 (9), 6079–6085.
- Douinot, A., Roux, H., Dartus, D., 2017. Modelling errors calculation adapted to rainfall–runoff model user expectations and discharge data uncertainties. *Environmental Modelling & Software* 90, 157–166.
- Emery, C. M., Biancamaria, S., Boone, A., Garambois, P.-A., Ricci, S., Rochoux, M. C., Decharme, B., 2016. Temporal variance-based sensitivity analysis of the river-routing component of the large-scale hydrological model isba–trip: Application on the amazon basin. *Journal of Hydrometeorology* 17 (12), 3007–3027.

- Fan, Y., Ao, T., Yu, H., Huang, G., Li, X., 2017. A coupled 1d-2d hydrodynamic model for urban flood inundation. *Advances in Meteorology* 2017.
- Fernandez-Nieto, E. D., Marin, J., Monnier, J., 2010. Coupling superposed 1d and 2d shallow-water models: Source terms in finite volume schemes. *Computers & Fluids* 39 (6), 1070–1082.
- Finaud-Guyot, P., 2009. Modélisation macroscopique des inondations fluviales et urbaines-prise en compte des écoulements directionnels et des échanges lit majeur-lit mineur. Ph.D. thesis, Université Montpellier II-Sciences et Techniques du Languedoc.
- Finaud-Guyot, P., Delenne, C., Guinot, V., 2010a. Coupling of 1d and 2d models for river flow modelling. In: *SimHydro 2010: Hydraulic modeling and uncertainty*.
- Finaud-Guyot, P., Delenne, C., Guinot, V., 2011. Coupling of 1d and 2d models for river flow modelling. *La Houille Blanche* (3), 23–28.
- Finaud-Guyot, P., Delenne, C., Lhomme, J., Guinot, V., Llovel, C., 2010b. An approximate-state Riemann solver for the two-dimensional shallow water equations with porosity. *International Journal for Numerical Methods in Fluids* 62 (12), 1299–1331.
- Finaud-Guyot, P., Garambois, P.-A., Araud, Q., Lawniczak, F., François, P., Vazquez, J., Mosé, R., 2018. Experimental insight for flood flow repartition in urban areas. *Urban Water Journal*, 1–9.
- Fletcher, T., Andrieu, H., Hamel, P., 2013. Understanding, management and modelling of urban hydrology and its consequences for receiving waters: A state of the art. *Advances in water resources* 51, 261–279.
- Garambois, P.-A., 2012. Etude régionale des crues éclair de l’arc méditerranéen français. Elaboration de méthodologies de transfert à des bassins versants non jaugés. Ph.D. thesis, Université de Toulouse.
- Garambois, P.-A., Roux, H., Larnier, K., Castaings, W., Dartus, D., 2013. Characterization of process-oriented hydrologic model behavior with temporal sensitivity analysis for flash floods in mediterranean catchments. *Hydrology and Earth System Sciences* 17, 2305–2322.
- Garambois, P.-A., Roux, H., Larnier, K., Labat, D., Dartus, D., 2015. Parameter regionalization for a process-oriented distributed model dedicated to flash floods. *Journal of Hydrology* 525, 383–399.
- Gejadze, I. Y., Monnier, J., 2007. On a 2d zoom for the 1d shallow water model: Coupling and data assimilation. *Computer methods in applied mechanics and engineering* 196 (45-48), 4628–4643.
- Gharahjeh, S., Aydin, I., Altan-Sakarya, A., 2015. Weir velocity formulation for sharp-crested rectangular weirs. *Flow Measurement and Instrumentation* 41, 50–56.
- Ghostine, R., Hoteit, I., Vazquez, J., Terfous, A., Ghenaïm, A., Mose, R., 2015. Comparison between a coupled 1d-2d model and a fully 2d model for supercritical flow simulation in crossroads. *Journal of Hydraulic Research* 53 (2), 274–281.
- Grayson, R., Blöschl, G., 2001. Spatial patterns in catchment hydrology: observations and modelling. CUP Archive.

- Guinot, V., 2012a. Multiple porosity shallow water models for macroscopic modelling of urban floods. *Advances in Water Resources* 37, 40–72.
- Guinot, V., 2012b. *Wave propagation in fluids: models and numerical techniques*. John Wiley & Sons.
- Guinot, V., 2017b. A critical assessment of flux and source term closures in shallow water models with porosity for urban flood simulations. *Advances in Water Resources* 109, 133–157.
- Guinot, V., 2017c. Consistency and bicharacteristic analysis of integral porosity shallow water models. explaining model oversensitivity to mesh design. *Advances in Water Resources* 107, 43–55.
- Guinot, V., Cappelaere, B., 2009a. Sensitivity analysis of 2d steady-state shallow water flow. Application to free surface flow model calibration. *Advances in Water Resources* 32 (4), 540–560.
- Guinot, V., Cappelaere, B., 2009b. Sensitivity equations for the one-dimensional shallow water equations: Practical application to model calibration. *Journal of Hydrologic Engineering* 14 (8), 858–861.
- Guinot, V., Sanders, B. F., Schubert, J. E., 2017a. Dual integral porosity shallow water model for urban flood modelling. *Advances in Water Resources* 103, 16–31.
- Guinot, V., Soares-Frazão, S., 2006. Flux and source term discretization in two-dimensional shallow water models with porosity on unstructured grids. *International Journal for Numerical Methods in Fluids* 50 (3), 309–345.
- Gurram, S. K., Karki, K. S., Hager, W. H., 1997. Subcritical junction flow. *Journal of Hydraulic Engineering* 123 (5), 447–455.
- Hager, W. H., 1987. Discussion of separation zone at open-channel junctions by James L. Best and Ian Reid (november, 1984). *Journal of Hydraulic Engineering* 113 (4), 539–543.
- Hager, W. H., 1989. Transitional flow in channel junctions. *Journal of Hydraulic Engineering* 115 (2), 243–259.
- Hervouet, J.-M., 2000. Telemac modelling system: an overview. *Hydrological Processes* 14 (13), 2209–2210.
- Hervouet, J.-M., 2007. *Hydrodynamics of free surface flows: modelling with the finite element method*. John Wiley & Sons.
- Hervouet, J. M., Samie, R., Moreau, B., 2000. Modelling urban areas in dam-break flood-wave numerical simulations.
- Hornberger, G. M., Spear, R. C., 1981. Approach to the preliminary analysis of environmental systems. *J. Environ. Mgmt.* 12 (1), 7–18.
- Hsu, C.-C., Tang, C.-J., Lee, W.-J., Shieh, M.-Y., 2002. Subcritical 90° equal-width open-channel dividing flow. *Journal of Hydraulic Engineering* 128 (7), 716–720.
- Hsu, C.-C., Wu, F.-S., Lee, W.-J., 1998. Flow at 90° equal-width open-channel junction. *Journal of Hydraulic Engineering* 124 (2), 186–191.

- Huang, J., Weber, L. J., Lai, Y. G., 2002. Three-dimensional numerical study of flows in open-channel junctions. *Journal of Hydraulic Engineering* 128 (3), 268–280.
- Ishigaki, T., Toda, K., Inoue, K., 2003. Hydraulic model tests of inundation in urban area with underground space. In: *Proc. of XXX IAHR Congress, Theme B*. pp. 487–493.
- Janon, A., 2012. Analyse de sensibilité et réduction de dimension. Application à l’océanographie. Ph.D. thesis, Université de Grenoble.
- Jia, Y., Zhu, T., Riahi-Nezhad, C. K., Zhang, Y., 2010. Numerical modeling of flow through a breached levee and during levee closure. In: *World Environmental and Water Resources Congress 2010: Challenges of Change*. pp. 1304–1316.
- Kasthuri, B., Pundarikanthan, N., 1987. Discussion of separation zone at open-channel junctions by James L. Best and Ian Reid (november, 1984). *Journal of Hydraulic Engineering* 113 (4), 543–544.
- Kim, B., Sanders, B. F., Famiglietti, J. S., Guinot, V., 2015. Urban flood modeling with porous shallow-water equations: a case study of model errors in the presence of anisotropic porosity. *Journal of Hydrology* 523, 680–692.
- Lhomme, J., 2006. Modélisation des inondations en milieu urbain: approches unidimensionnelle, bidimensionnelle et macroscopique. Ph.D. thesis, Université Montpellier II-Sciences et Techniques du Languedoc.
- Lhomme, J., Guinot, V., 2007. A general approximate-state Riemann solver for hyperbolic systems of conservation laws with source terms. *International journal for numerical methods in fluids* 53 (9), 1509–1540.
- Li, C., Zeng, C., 2009. 3d numerical modelling of flow divisions at open channel junctions with or without vegetation. *Advances in Water Resources* 32 (1), 49–60.
- Li, C., Zeng, C., 2010. Flow division at a channel crossing with subcritical or supercritical flow. *International journal for numerical methods in fluids* 62 (1), 56–73.
- MacCormack, R., Paullay, A., 1972. Computational efficiency achieved by time splitting of finite difference operators. In: *10th Aerospace Sciences Meeting*. p. 154.
- Mamedov, A. S., 1989. Hydraulic calculation of a confluence. *Power Technology and Engineering (formerly Hydrotechnical Construction)* 23 (9), 553–556.
- Marin, J., Monnier, J., 2009. Superposition of local zoom models and simultaneous calibration for 1d–2d shallow water flows. *Mathematics and Computers in Simulation* 80 (3), 547–560.
- Mignot, E., Paquier, A., Haider, S., 2006. Modeling floods in a dense urban area using 2d shallow water equations. *Journal of Hydrology* 327 (1), 186–199.
- Mignot, E., Paquier, A., Rivière, N., 2008a. Experimental and numerical modeling of symmetrical four-branch supercritical. *Journal of Hydraulic Research* 46 (6), 723–738.
- Mignot, E., Rivière, N., Perkins, R., Paquier, A., 2008b. Flow patterns in a four-branch junction with supercritical flow. *Journal of Hydraulic Engineering* 134 (6), 701–713.
- Mignot, E., Vinkovic, I., Doppler, D., Riviere, N., 2014. Mixing layer in open-channel junction flows. *Environmental Fluid Mechanics* 14 (5), 1027–1041.

- Ming, X., 2017. Experimental and numerical study of open channel intersections. Ph.D. thesis, Ecole Centrale de Lyon.
- Modi, P. N., Dandekar, M. M., Ariel, P. D., 1981. Conformal mapping for channel junction flow. *Journal of the Hydraulics Division* 107 (12), 1713–1733.
- Moel, H. D., Alphen, J. V., Aerts, J., 2009. Flood maps in Europe—methods, availability and use. *Natural Hazards and Earth System Sciences* 9 (2), 289–301.
- Momplot, A., Lipeme Kouyi, G., Mignot, E., Rivière, N., Bertrand-Krajewski, J.-L., 2017. Typology of the flow structures in dividing open channel flows. *Journal of Hydraulic Research* 55 (1), 63–71.
- Monnier, J., Couderc, F., Dartus, D., Larnier, K., Madec, R., Vila, J.-P., 2016. Inverse algorithms for 2d shallow water equations in presence of wet dry fronts: Application to flood plain dynamics. *Advances in Water Resources* 97, 11–24.
- Nanía, L. S., Gómez, M., Dolz, J., 2004. Experimental study of the dividing flow in steep street crossings. *Journal of Hydraulic Research* 42 (4), 406–412.
- Nanía, L. S., Gómez, M., Dolz, J., Comas, P., Pomares, J., 2011. Experimental study of subcritical dividing flow in an equal-width, four-branch junction. *Journal of Hydraulic Engineering* 137 (10), 1298–1305.
- Neal, J., Villanueva, I., Wright, N., Willis, T., Fewtrell, T., Bates, P., 2012. How much physical complexity is needed to model flood inundation? *Hydrological Processes* 26 (15), 2264–2282.
- Neary, V. S., Odgaard, A. J., 1993. Three-dimensional flow structure at open-channel diversions. *Journal of Hydraulic Engineering* 119 (11), 1223–1230.
- Neary, V. S., Sotiropoulos, F., Odgaard, A., 1999. Three-dimensional numerical model of lateral-intake inflows. *Journal of Hydraulic Engineering* 125 (2), 126–140.
- Noh, S. J., Lee, S., An, H., Kawaike, K., Nakagawa, H., 2016. Ensemble urban flood simulation in comparison with laboratory-scale experiments: Impact of interaction models for manhole, sewer pipe, and surface flow. *Advances in Water Resources* 97, 25–37.
- Özgen, I., Liang, D., Hinkelmann, R., 2016a. Shallow water equations with depth-dependent anisotropic porosity for subgrid-scale topography. *Applied Mathematical Modelling* 40 (17), 7447–7473.
- Özgen, I., Zhao, J., Liang, D., Hinkelmann, R., 2016b. Urban flood modeling using shallow water equations with depth-dependent anisotropic porosity. *Journal of Hydrology* 541, 1165–1184.
- Pachauri, R. K., Allen, M. R., Barros, V. R., Broome, J., Cramer, W., Christ, R., Church, J. A., Clarke, L., Dahe, Q., Dasgupta, P., et al., 2014. Climate change 2014: synthesis report. Contribution of Working Groups I, II and III to the fifth assessment report of the Intergovernmental Panel on Climate Change. IPCC.
- Paquier, A., Mignot, E., Bazin, P.-H., 2015. From hydraulic modelling to urban flood risk. *Procedia Engineering* 115, 37–44.
- Paris, A., Dias de Paiva, R., Santos da Silva, J., Medeiros Moreira, D., Calmant, S., Garambois, P.-A., Collischonn, W., Bonnet, M.-P., Seyler, F., 2016. Stage-discharge rating curves based on satellite altimetry and modeled discharge in the amazon basin. *Water Resources Research* 52 (5), 3787–3814.

- Pianosi, F., Beven, K., Freer, J., Hall, J. W., Rougier, J., Stephenson, D. B., Wagener, T., 2016. Sensitivity analysis of environmental models: A systematic review with practical workflow. *Environmental Modelling & Software* 79, 214–232.
- Pushpalatha, R., Perrin, C., Le Moine, N., Mathevet, T., Andréassian, V., 2011. A downward structural sensitivity analysis of hydrological models to improve low-flow simulation. *Journal of Hydrology* 411 (1), 66–76.
- Qing-Yuan, Y., Xian-Ye, W., Wei-Zhen, L., Xie-Kang, W., 2009. Experimental study on characteristics of separation zone in confluence zones in rivers. *Journal of Hydrologic Engineering* 14 (2), 166–171.
- Ramamurthy, A. S., Qu, J., Vo, D., 2007. Numerical and experimental study of dividing open-channel flows. *Journal of Hydraulic Engineering* 133 (10), 1135–1144.
- Ratto, M., Pagano, A., Young, P., 2007. State dependent parameter metamodeling and sensitivity analysis. *Computer Physics Communications* 177 (11), 863–876.
- Rivière, N., Perkins, R., Chocat, B., Lecus, A., 2006. Flooding flows in city crossroads: experiments and 1-d modelling. *Water Science and Technology* 54 (6-7), 75–82.
- Rivière, N., Travin, G., Perkins, R., 2013. Transcritical flows in three and four branch open-channel intersections. *Journal of Hydraulic Engineering* 140 (4), 04014003.
- Rivière, N., Travin, G., Perkins, R. J., 2011. Subcritical open channel flows in four branch intersections. *Water Resources Research* 47 (10).
- Roux, H., Dartus, D., 2008. Sensitivity analysis and predictive uncertainty using inundation observations for parameter estimation in open-channel inverse problem. *Journal of Hydraulic Engineering* 134 (5), 541–549.
- Saltelli, A., Annoni, P., Azzini, I., Campolongo, F., Ratto, M., Tarantola, S., 2010. Variance based sensitivity analysis of model output. Design and estimator for the total sensitivity index. *Computer Physics Communications* 181 (2), 259–270.
- Saltelli, A., Ratto, M., Andres, T., Campolongo, F., Cariboni, J., Gatelli, D., Saisana, M., Tarantola, S., 2008. *Global sensitivity analysis: the primer*. John Wiley & Sons.
- Saltelli, A., Tarantola, S., Campolongo, F., Ratto, M., 2004. *Sensitivity analysis in practice: a guide to assessing scientific models*. John Wiley & Sons.
- Salvadore, E., Bronders, J., Batelaan, O., 2015. Hydrological modelling of urbanized catchments: A review and future directions. *Journal of Hydrology* 529, 62–81.
- Sanders, B. F., Schubert, J. E., Gallegos, H. A., 2008. Integral formulation of shallow-water equations with anisotropic porosity for urban flood modeling. *Journal of Hydrology* 362 (1), 19–38.
- Sattar, A. M., Kassem, A. A., Chaudhry, M. H., 2008. Case study: 17th street canal breach closure procedures. *Journal of Hydraulic Engineering* 134 (11), 1547–1558.
- Savage, J. T. S., Pianosi, F., Bates, P., Freer, J., Wagener, T., 2016. Quantifying the importance of spatial resolution and other factors through global sensitivity analysis of a flood inundation model. *Water Resources Research* 52 (11), 9146–9163.

- Schindfessel, L., Créëlle, S., De Mulder, T., 2017. How different cross-sectional shapes influence the separation zone of an open-channel confluence. *Journal of Hydraulic Engineering* 143 (9), 04017036.
- Schubert, J. E., Sanders, B. F., 2012. Building treatments for urban flood inundation models and implications for predictive skill and modeling efficiency. *Advances in Water Resources* 41, 49–64.
- Seity, Y., Brousseau, P., Malardel, S., Hello, G., Bénard, P., Bouttier, F., Lac, C., Masson, V., 2011. The arome-france convective-scale operational model. *Monthly Weather Review* 139 (3), 976–991.
- Seyoum, S. D., Vojinovic, Z., Price, R. K., Weesakul, S., 2011. Coupled 1d and noninertia 2d flood inundation model for simulation of urban flooding. *Journal of hydraulic engineering* 138 (1), 23–34.
- Skamarock, W. C., Klemp, J. B., Dudhia, J., Gill, D. O., Barker, D. M., Wang, W., Powers, J. G., 2005. A description of the advanced research WRF version 2. Tech. rep., National Center For Atmospheric Research Boulder Co Mesoscale and Microscale Meteorology Div.
- Skinner, C. J., Coulthard, T. J., Parsons, D. R., Ramirez, J. A., Mullen, L., Manson, S., 2015. Simulating tidal and storm surge hydraulics with a simple 2d inertia based model, in the Humber Estuary, UK. *Estuarine, Coastal and Shelf Science* 155, 126–136.
- Soares-Frazão, S., Lhomme, J., Guinot, V., Zech, Y., 2008. Two-dimensional shallow-water model with porosity for urban flood modelling. *Journal of Hydraulic Research* 46 (1), 45–64.
- Soares-Frazão, S., Zech, Y., 2002. Dam break in channels with 90° bend. *Journal of Hydraulic Engineering* 128 (11), 956–968.
- Soares-Frazão, S., Zech, Y., 2008. Dam-break flow through an idealised city. *Journal of Hydraulic Research* 46 (5), 648–658.
- Sobol', I. M., 1990. On sensitivity estimation for nonlinear mathematical models. *Matematicheskoe modelirovanie* 2 (1), 112–118.
- Sobol, I. M., 1993. Sensitivity estimates for nonlinear mathematical models. *Mathematical modelling and computational experiments* 1 (4), 407–414.
- Song, X., Zhang, J., Zhan, C., Xuan, Y., Ye, M., Xu, C., 2015. Global sensitivity analysis in hydrological modeling: Review of concepts, methods, theoretical framework, and applications. *Journal of hydrology* 523, 739–757.
- Southard, J., 2006. *Introduction to Fluid Motions, Sediment Transport and Current-Generated Sedimentary Structures*.
- Stokes, G. G., 1845. On the theories of internal friction of fluids in motion. *Trans. Camb. Philos. Soc.* 8, 287–305.
- Taylor, E. H., 1944. Flow characteristics at rectangular open-channel junctions. In: *Proceedings of the American Society of Civil Engineers*. Vol. 68. ASCE, pp. 1521–1530.
- Teng, J., Jakeman, A., Vaze, J., Croke, B., Dutta, D., Kim, S., 2017. Flood inundation modelling: A review of methods, recent advances and uncertainty analysis. *Environmental Modelling & Software* 90, 201–216.

- Testa, G., Zuccala, D., Alcrudo, F., Mulet, J., Soares-Frazão, S., 2007. Flash flood flow experiment in a simplified urban district. *Journal of Hydraulic Research* 45 (sup1), 37–44.
- Thanh, M. D., Kimura, I., Shimizu, Y., Hosoda, T., 2010. Numerical simulation of flow at an open-channel confluence using depth-averaged 2d models with effects of secondary currents. *Journal of Applied Mechanics* 13, 769–780.
- Thual, O., 2010. Hydrodynamique de l’environnement. Ecole polytechnique.
- Tran, T. D., Chorda, J., Laurens, P., Cassan, L., 2016. Modelling nature-like fishway flow around unsubmerged obstacles using a 2d shallow water model. *Environmental Fluid Mechanics* 16 (2), 413–428.
- Van Emelen, S., Soares-Frazão, S., Riahi-Nezhad, C. K., Chaudhry, M., Imran, J., Zech, Y., Feb. 2012. Simulations of the New Orleans 17th Street Canal breach flood. *Journal of Hydraulic Research* 50 (1), 70–81.
- Velickovic, M., Zech, Y., Soares-Frazão, S., 2017. Steady-flow experiments in urban areas and anisotropic porosity model. *Journal of Hydraulic Research* 55 (1), 85–100.
- Velickovic, M., et al., 2012. Macroscopic modeling of urban flood by a porosity approach. Ph.D. thesis, Université catholique de Louvain.
- Vié, B., Nuissier, O., Ducrocq, V., 2011. Cloud-resolving ensemble simulations of mediterranean heavy precipitating events: uncertainty on initial conditions and lateral boundary conditions. *Monthly Weather Review* 139 (2), 403–423.
- Vitturi, M. d., Engwell, S., Neri, A., Barsotti, S., 2016. Uncertainty quantification and sensitivity analysis of volcanic columns models: Results from the integral model plume-mom. *Journal of Volcanology and Geothermal Research* 326, 77–91.
- Wahlstrom, M., Guha-Sapir, D., 2015. The human cost of weather-related disasters 1995–2015. Geneva: United Nations International Strategy for Disaster Reduction.
- Webber, N. B., Greated, C., 1966. An investigation of flow behaviour at the junction of rectangular channels. *Proceedings of the Institution of Civil Engineers* 34 (3), 321–334.
- Weber, L. J., Schumate, E. D., Mawer, N., 2001. Experiments on flow at a 90° open-channel junction. *Journal of Hydraulic Engineering* 127 (5), 340–350.
- Werners, S., Ludwig, F., et al., 2012. Water resources in Europe in the context of vulnerability. Tech. rep., European Environment Institute.
- Yu, D., Lane, S. N., 2006a. Urban fluvial flood modelling using a two-dimensional diffusion-wave treatment, part 1: mesh resolution effects. *Hydrological Processes* 20 (7), 1541–1565.
- Zech, Y., Soares-Frazão, S., 2007. Dam-break flow experiments and real-case data. A database from the European IMPACT research. *Journal of Hydraulic Research* 45 (sup1), 5–7.



## Appendix A

## Appendix

Table A.1: Boundary conditions for device simulation

Street	Inlet discharge	Outlet water height	Street	Inlet discharge	Outlet water height
1	1.37 l/s	6.5 cm	A	1.06 l/s	8.3 cm
2	1.40 l/s	7.8 cm	B	1.06 l/s	8.0 cm
3	1.32 l/s	7.8 cm	C	2.67 l/s	8.3 cm
4	3.01 l/s	7.8 cm	D	1.27 l/s	7.3 cm
5	1.32 l/s	6.4 cm	E	1.27 l/s	7.1 cm
6	1.35 l/s	6.5 cm	F	2.46 l/s	7.1 cm
7	1.35 l/s	6.5 cm	G	1.31 l/s	6.4 cm

# Modèle effectif par une approche de Saint-Venant pour les écoulements complexes lors d'inondations urbaines

## Résumé

Les inondations représentent le premier danger naturel sur chaque continent, avec des préoccupations particulières centrées sur les inondations urbaines pour l'urbanisation sans précédent, qui augmente la vulnérabilité des sociétés humaines aux inondations. Pour les difficultés d'accès aux données en temps réel, la méthode numérique semble être une approche puissante pour la prévision des inondations et l'atténuation des dommages. Dans cette thèse, un nouveau logiciel Flood1D2D pour la modélisation des crues urbaines a été proposé en utilisant le maillage de couplage 1D2D, avec 1D dans la rue et 2D appliqué au carrefour. Le logiciel est conçu sur la base de l'installation située dans ICube Strasbourg et validée à l'aide de cas de tests synthétiques. La nouveauté du modèle est de rendre compte de l'effet de recirculation en utilisant la fonction de porosité, et de reproduire la convexité dans les profils de profondeur le long de la rue en aval de chaque carrefour où une zone de recirculation apparaît. Une analyse de sensibilité basée sur la variance est également réalisée pour les modèles classiques d'eau peu profonde 1D et 2D pour l'étalonnage de modèles et la collecte de données.

**Mots clés : Inondation urbaine, 1D / 2D, porosité, analyse de sensibilité, équations de Saint-Venant**

## Résumé en anglais

Flooding represents the first natural hazard on each continent, with special concerns are focused on urban flooding for the unprecedented urbanization, which increases the vulnerability of human societies to floods. For the accessing difficulties of real-time data, numerical method seems to be a powerful approach for flood forecasting and damage mitigation. In this thesis, a new software Flood1D2D for urban flood modeling has been proposed using 1D2D coupling mesh, with 1D on the street and 2D applied on the crossroad. The software is designed based on the rig located in ICube Strasbourg and validated using synthetic test cases. The novelty of the model is to account for the recirculation effect using porosity function, and it can reproduce the convexity in water depth profiles along the street downstream each crossroad where a recirculation zone appears, which can't be accounted using roughness only. Variance based sensitivity analysis is also performed for classical 1D and 2D shallow water models for model calibration and data collections.

**Keywords : Urban flood, 1D/2D, porosity, sensitivity analysis, Saint-Venant equations**